DISS ETH Nr. 19320

DETERMINATION OF THE ACTIVE SITES IN SUPPORTED PLATINUM CATALYSTS BY MEANS OF X-RAY ABSORPTION AND EMISSION SPECTROSCOPY

A dissertation submitted to

ETH ZURICH

for the degree of

Doctor of Sciences

presented by

JAGDEEP SINGH

Master of Technology, Indian Institute of Technology Roorkee

03.10.1983

citizen of India

accepted on the recommendation of

Prof. Dr. Jeroen A. van Bokhoven

Prof. Alexander Wokaun

Dr. Pieter Glatzel

2010

Table of contents

Abstract

Zusammenfassung

Table of contents

Chapter 4: Electronic structure of alumina-supported platinum catalysts

Chapter 5: Generating highly active partially oxidized platinum during oxidation of carbon monoxide over Pt/Al_2O_3

Table of contents

Table of contents

Abstract

Supported platinum catalysts are of great interest because of their high activity in reactions like preferential oxidation of CO (PROX) in fuel cell industry and in automobile industry as part of the three-way catalyst. The properties of these supported platinum catalysts depend on the size of the particles, the support, and the reaction conditions. In this thesis, CO oxidation was studied over platinum catalysts supported on various supports, of different particle sizes, and under dynamic reaction conditions. The aim of the thesis was to establish the structure-performance relationship over supported platinum catalysts during CO oxidation. Newly developed methods based on X-ray absorption and emission spectroscopy were employed.

The structure of a catalyst is prone to change during different stages of a catalytic process and, to understand the functioning of the catalyst and the chemical processes on its surface, needs to be determined under actual working conditions. This requires the use of techniques that reveal the electronic and geometric structures of the catalyst under in situ conditions. X-ray absorption spectroscopy (XAS), X-ray emission spectroscopy (XES) and infra red (IR) spectroscopy were used in the research described in this thesis. When an adsorbate is chemically adsorbed on a catalyst surface, new bonding and anti-bonding states are formed, which can be probed by XAS and XES respectively, along with the geometric structure that is obtained from EXAFS (extended X-ray absorption fine structure) and XANES (X-ray absorption near edge structure). In situ IR spectroscopy provides complimentary information about the adsorbed species on the metal surface. In this thesis, HERFD (high-energy resolution fluorescence detected) XAS was extensively used because of its excellent spectral resolution compared to conventional XAS. Quick-extended X-ray absorption fine structure (QEXAFS) is a technique that is capable of revealing the dynamic structure of a catalyst in the sub-second time regime. In situ resonant inelastic X-ray scattering (RIXS), which is one type of XES, was explored to reveal the detailed electronic structure of the supported platinum catalyst. In situ time- and space-resolved X-ray absorption spectroscopy was combined with mass spectrometry and infrared spectroscopy to derive a spatially resolved understanding of the dynamic structure-performance relationships in a reactor during total and preferential CO oxidation.

The potential of RIXS to probe the electronic structure of 5d elements was examined on various platinum and gold compounds. The combination of XAS and XES

Abstract

provided a comprehensive map of the occupied and unoccupied 5d density of states. RIXS revealed the valence band structure of these compounds. The experimental spectra were modeled using multiple scattering calculations using the FEFF8 code. The technique also revealed the electronic structure of nano-particles of gold, where the d band was shifted toward lower binding energy in comparison to that of bulk gold. The change in the structure of platinum after alloying with tin was investigated by Pt L_3 HERFD XAS and RIXS. The changes in the structure rendered the bimetallic particles less active for hydrogen and carbon monoxide adsorption due to tin enrichment at the surface. The platinum d band of platinum-tin particles was narrower and shifted down relative to the Fermi level in comparison to that of platinum particles. The difference in electronic structure, which was clearly observed between pure and alloyed particles persisted after adsorption of hydrogen, however after CO adsorption, the structure became very similar.

In situ HERFD XAS, QEXAFS, combined with IR spectroscopy and kinetic measurements revealed the catalytically active species during CO oxidation over supported platinum catalysts. Regardless of the particle size and support, CO oxidation occurred in two reaction regimes: a regime of low rate and one of high rate, depending on temperature and CO and O_2 concentration. These regimes were separated by a sudden switch called ignition respectively extinction. In the regime of low rate, the catalyst surface was covered by CO, which poisoned the catalyst, and in the regime of high rate, partially oxidized platinum was present. At the onset of the ignition, an increasing amount of platinum oxide was observed, which autocatalytically increased the conversion. The structure of the oxide was highly defective and platinum was likely under-coordinated to oxygen. High temperature and high concentration of oxygen were beneficial to achieving the highly active oxidic platinum. Smaller platinum particles supported on alumina reached high activity at lower temperature than the larger particles. The ignition temperature and the amount of oxidized platinum depended on the support.

The structural changes that occurred during the kinetic oscillations of CO oxidation over alumina-supported platinum catalyst were elucidated by combining in situ space- and time-resolved XAS, IR spectroscopy, and kinetic measurements. The structure of the catalyst varied as function of position in the plug flow reactor. The structure of the catalytically active phase was identified; oscillations occur because of local changes in the catalyst structure inside the reactor. The kinetic oscillations during

Abstract

CO oxidation were paralleled with the reduction and CO poisoning, and re-oxidation of the surface.

Ceria-supported platinum nano-clusters and platinum-doped ceria were studied during PROX by means of HERFD XAS. The ceria-supported platinum catalyst was leached using a cyanide solution and a platinum-doped ceria was thus obtained. The platinum-doped ceria consisted of platinum mostly in its cationic form. HERFD XAS revealed the changing oxidation state of platinum during the reaction, where along with preferential oxidation of CO (PROX), water gas shift (WGS), and methanation were also observed. Ceria-supported platinum nano-clusters were more active than platinum-doped ceria during oxidation of both H_2 and CO. The metal-doped ceria with supported platinum particles was the most selective for PROX. As soon as oxygen was depleted in the gas phase, the cationic platinum irreversibly reduced to form supported platinum particles. This generated the more active, but less selective catalyst.

In summary, the research done in this thesis derived a time- and space-resolved understanding of the dynamic structure-performance relationships in a reactor during total and preferential CO oxidation using in situ time- and space- resolved X-ray absorption and emission spectroscopy combined with mass spectrometry and IR spectroscopy. The exclusive use of hard X-rays enabled performing these studies under catalytic conditions. Recently developed techniques of HERFD XAS and in situ RIXS revealed the structure of the catalysts with excellent resolution, which gave deeper insights into the active species of supported platinum catalysts.

Abstract

Zusammenfassung

Heterogene Platinkatalysatoren sind wegen ihrer hohen Aktivität in solchen Reaktionen wie selektive Oxidation (PROX) von Kohlenstoffmonoxid als Teil der Drei-Wege-Katalysatoren in Brennstoffzellen- und Automobilindustrie vom grossen Interesse. Die Eigenschaften der heterogenen Platinkatalysatoren hängen von der Partikelgrösse, dem Träger und den Reaktionsbedingungen ab. In dieser Dissertation wurde CO-Oxidation über Platinkatalysatoren auf verschiedenen Trägern, von unterschiedlichen Partikelgrössen und unter dynamischen Reaktionsbedingungen untersucht. Das Ziel dieser Doktorarbeit war, die Korrelation zwischen der Struktur der heterogenen Platinkatalysatoren und deren katalytischen Eigenschaften in der CO-Oxidation aufzustellen. Neulich entwickelte spektroskopische Methoden, die auf Röntgenabsorption oder -emission basieren, wurden dafür zur Hilfe gezogen.

Die Struktur eines Katalysators ist anfällig für Änderungen bei verschiedenen Stufen eines katalytischen Prozesses. Um das Funktionieren eines Katalysators und die chemischen Prozesse auf deren Oberfläche zu verstehen, muss der Katalysator unter realen Reaktionsbedingungen untersucht werden. Das erfordert die Verwendung von solchen Methoden, die die elektronischen und geometrischen Eigenschaften des Katalysators *in situ* bestimmen können. Bei der in dieser Dissertation dargelegten Forschungsarbeit wurden Röntgenabsorptionsspektroskopie (XAS), Röntgenemissionsspektroskopie (XES) und IR-Spektroskopie verwendet. Wenn ein Molekül auf der Oberfläche chemisch adsorbiert wird, werden neue bindende und antibindende Zustände gebildet. Diese können mit XAS, respektive mit XES, untersucht werden; die geometrische Struktur wird mittels EXAFS (Extended X-ray Absorption Fine Structure) und XANES (X-ray Absorption Near Edge Structure) bestimmt. *In situ* IR-Spektroskopie liefert zusätzliche Information über die auf der Metalloberfläche adsorbierte Spezies. In dieser Dissertation wurde HERFD (High-Energy Resolution Fluorescence Detected) XAS wegen ihrer besseren spektralen Auflösung im Vergleich zu herkömmlicher XAS verwendet. QEXAFS (Quick-Extended X-ray Absorption Fine Structure) ist eine Methode, die es ermöglicht, die dynamische Struktur eines Katalysators im Sub-Sekunden-Bereich zu untersuchen. *In situ* RIXS (Resonant Inelastic X-ray Scattering) ist eine Art von XES, mit der sich die detaillierte elektronische Struktur des heterogenen Platinkatalysators untersuchen lässt. *In situ* Röntgenabsorptionsspektroskopie mit hoher räumlicher und zeitlicher Auflösung wurde

Zusammenfassung

mit Massenspektrometrie und Infrarotspektroskopie kombiniert, um räumlich aufgelöste Information zur dynamischen Struktur-Leistungs-Beziehung bei der Total- und Selektivoxidation von Kohlenstoffmonoxid zu gewinnen.

Das Potenzial von RIXS, die elektronische Struktur von 5d-Elementen zu untersuchen, wurde an verschiedenen Platin- und Goldverbindungen geprüft. Eine Kombination von XAS und XES hat ein umfassendes Verständnis über die besetzte und unbesetzte 5d Zustandsdichte geliefert. Mit RIXS konnte die Struktur des Valenzbandes dieser Verbindungen bestimmt werden. Die aufgenommenen Spektren wurden mit Hilfe von Mehrfachstreuung mit dem FEFF8-Programm modelliert. Mit diesem Verfahren liess sich auch die elektronische Struktur von Goldnanopartikeln bestimmen, wobei das d-Band im Vergleich zum Bulk zu niedrigeren Bindungsenergien verschoben war. Die Strukturänderung von Platin nach Legierung mit Zinn wurde mit Pt L_3 HERFD XAS und RIXS untersucht. Die Strukturänderungen haben erwiesen, dass die bimetallischen Partikel wegen Oberflächenanreicherung von Zinn weniger aktiv für die Adsorption von Wasserstoff und Kohlenstoffmonoxid sind. Das d-Band von Platin bei Platin-Zinnpartikeln war schmaler und relativ zu Fermi-Niveau nach unten verschoben im Vergleich zu Platinpartikeln. Nach Wasserstoffadsorption war der Unterschied in der elektronischen Struktur der reinen und legierten Partikeln klar sichtbar, aber nach Adsorption von Kohlenstoffmonoxid ist die Struktur sehr ähnlich geworden.

Mit *in situ* HERFD XAS und QEXAFS, kombiniert mit IR-Spektroskopie und kinetischen Messungen, liess sich die katalytisch aktive Spezies bei CO-Oxidation an heterogenen Platinkatalysatoren bestimmen. Ungeachtet der Partikelgrösse und des Trägers, erfolgte die Oxidation von Kohlenstoffmonoxid in zwei Bereichen: im Bereich der niedrigen und der hohen Reaktionsgeschwindigkeit, abhängig von Temperatur und CO- sowie O_2-Konzentration. Diese zwei Bereiche waren durch eine abrupte Reaktionsgeschwindigkeitsänderung getrennt, auch genannt „Zündung" und „Extinktion". Bei geringer Reaktionsgeschwindigkeit bedeckte CO die Oberfläche und vergiftete den Katalysator. Bei hoher Reaktionsgeschwindigkeit wurde Platin partiell oxidiert. Zu Beginn der Zündung war eine steigende Menge von Platinoxid zu beobachten, das den Umsatz autokatalytisch erhöht hat. Die Struktur des Oxids war sehr defektreich und Platin war wahrscheinlich unterkoordiniert. Hohe Temperatur und Konzentration von Sauerstoff waren vorteilhaft, um ein sehr aktives Platinoxid zu erhalten. Kleinere Platinpartikel auf Aluminiumoxidträger haben eine höhere Aktivität

Zusammenfassung

bei geringerer Temperatur erwiesen, als grössere Partikel. Die Zündungstemperatur und die Menge des oxidierten Platins waren vom Träger abhängig.

Die Strukturänderungen, die sich während der kinetischen Oszillationen von CO-Oxidation über Platin auf Aluminiumoxid ereignet haben, konnten durch eine Kombination von XAS mit hoher räumlicher und zeitlicher Auflösung, IR-Spektroskopie und kinetischen Messungen aufgeklärt werden. Die Struktur des Katalysators hing von der Position im Pfropfenströmugsreaktor ab. Da die Oszillationen durch die lokalen Veränderungen in der Katalysatorstruktur im Inneren des Reaktors hervorgerufen werden, konnte die Struktur der katalytisch aktiven Phase bestimmt werden. Die kinetischen Oszillationen bei CO-Oxidation wurden mit Reduktion, CO-Vergiftung und Reoxidation der Oberfläche in Verbindung gebracht.

Platin-Nanocluster auf Ceroxid und Platin-dotiertes Ceroxid wurden bei PROX mit Hilfe von HERFD XAS untersucht. Platin-Ceroxid-Katalysator wurde mit Zyanidlösung behandelt, um Platin-dotiertes Ceroxid zu erhalten. Das Platin-dotierte Ceroxid hat Platin hauptsächlich in kationischer Form enthalten. Mit HERFD XAS wurde der Oxidationszustand von Platin, der sich während der Reaktion verändert hat, bestimmt, wobei ausser der selektiven Oxidation von CO auch Wassergas-Shift-Reaktion (WGS) und Methanisierung beobachtet wurden. Platin-Nanocluster auf Ceroxid waren aktiver bei Oxidation von Wasserstoff und CO als Platin-dotiertes Ceroxid. Das Metall-dotierte Ceroxid mit geträgerten Platinpartikeln hat sich als am meisten selektiv für PROX erwiesen. Sobald der Sauerstoff in der Gasphase aufgebraucht wurde, wurde das kationische Platin reduziert und es bildeten sich metallische Platinpartikel. Dies erzeugte einen aktiven, aber weniger selektiven Katalysator.

Die in dieser Dissertation dargestellten Forschungsergebnisse tragen zum besseren Verständnis der dynamischen Struktur-Leistungs-Korrelationen bei der Total- und Selektivoxidation von Kohlenstoffmonoxid bei. *In situ* Röntgenabsorptions- und Emissionsspektroskopie, kombiniert mit Massenspektrometrie und IR-Spektroskopie, lieferten räumlich aufgelöste Information zur Katalysatorstruktur und dem Reaktionsablauf. Die Anwendung von harter Röntgenstrahlung hat es ermöglicht, diese Studien unter katalytischen Bedingungen durchzuführen. Mit Hilfe der neulich entwickelten Methoden, wie HERFD XAS und *in situ* RIXS, konnte die Struktur des Katalysators mit ausgezeichneter Auflösung bestimmt werden, was einen tieferen

Zusammenfassung

Einblick in die Struktur der aktiven Spezies des heterogenen Platinkatalysators ermöglicht hat.

Chapter 1

Introduction

Chapter 1

1.1 Supported metal catalysts

Catalysis[1] is the enabling technology for bulk chemicals production, the synthesis of fine chemicals, and pollution abatement. Catalysis can be divided into two classes depending on the phase of the system: 1. heterogeneous catalysis and 2. homogeneous catalysis. In heterogeneous catalysis the catalyst and the reactants are in different phases; in homogeneous catalysis, both catalyst and the reactants are in the same phase. All heterogeneous catalytic processes proceed via the following three basic steps:

1. adsorption of reactants on the catalyst surface

2. reaction on the catalyst surface

3. desorption of products from the catalyst surface.

Therefore, the catalyst surface plays a very important role in the activity and selectivity for any particular reaction. One way to increase the number of active sites is to increase the surface area through decreasing the size of catalyst particles. Therefore, heterogeneous catalysts often consist of small metal particles, which are deposited and stabilized on a support. The structure of nano-sized metal particles, and in turn their physical and chemical properties, differs from that of bulk metal. For example, gold, which has long been considered as an inert metal and inactive for catalysis, exhibits a very high activity and selectivity for oxidation and hydrogenation reactions, when highly dispersed over metal oxides.[2] The support ensures that the particles remain dispersed to maintain stable catalytic performance. Often a second function of the support is to participate in the reaction and perform one or more reaction steps. Supported metal catalysts have shown their superiority in different reactions such as CO oxidation,[3] the water gas shift reaction,[4] hydrogenation[3d,5] methanation,[6] and hydrolysis.[7] The crystallite size is one of the most important parameters determining the activity of supported metal catalysts for most of these reactions. There exists a classification of supported metals depending on the metal particle size:[8] (a) metal particles with size exceeding 5 to 10 nm, which have a surface structure similar to that of bulk metals, (b) metal particles between one and five nm, which are of great interest due to their size-dependent properties affecting the reaction rate, and (c) metal particles below one nm. The catalytic properties for many reactions are influenced by metal particle size,[2,9] support,[9,10] and pretreatment conditions.[11] The support, which cannot be considered an inert material, strongly affects activity, selectivity, and long-term stability of the catalyst.[11,12] It has been proposed and debated that the metal-

support interaction alters the available reactive area and changes the electronic properties of metal and thus, the catalytic behavior. It exists due to the formation of metal-proton adduct in case of acidic supports,[13] due to charge transfer between the metal and the oxygen from the support,[14] and due to the polarization of metal by the support.[15] The pre-treatment conditions also play an important role in determining the activity of supported metal catalysts.[11] The pre-treatment conditions have a direct influence on structure of support and metal and their interaction.

Platinum is the metal of interest in this thesis, because it is an important industrial metal. The preferential oxidation (PROX) of carbon monoxide in a hydrogen-rich mixture over platinum catalysts is of considerable interest for the technical purification of the hydrogen feed gas.[16] Furthermore, because platinum is an active component of automotive three-way catalysts, studying and understanding the catalysis occurring on these platinum catalysts is essential.[3b] While platinum belongs to the family of noble metals because of its rarity in the earth's crust and its resistance to corrosion, it has a different chemical behavior than the other noble metals such as copper, silver and gold, which have filled d-bands. Platinum has an unfilled d-band that crosses the Fermi level making it active for catalysis. It has an extended d-orbital that enables chemisorption of adsorbates that subsequently react and desorb. At the platinum step sites and (100)-(1x1) surface, the presence of unsaturated d-orbitals, which are free to interact with symmetry-conserving orbitals of impinging gas phase reactants, is responsible for the high catalytic activity[17]. The structure sensitivity of platinum single crystals under high vacuum conditions, and for catalysts with varying platinum nanoparticle sizes under realistic conditions,[18,19] are well established, which amongst others has been related to the higher reaction rate on terrace sites in comparison to the defect sites (steps and kinks). *One of the aims of this thesis is to relate the activity and the structure of supported platinum catalysts during CO oxidation.* In this thesis, the structure of platinum catalysts with different particle size and different supports was determined during CO oxidation. Alloying two different metals is a common practice in heterogeneous catalysis to improve the activity, selectivity, and stability. The addition of tin is a classical way to modify the catalytic performance of platinum catalysts. The synergistic effect in bimetallic catalysts has been shown to depend on the precise particle composition, feed composition and operating temperature.[20] The changes in the performance of bimetallic catalysts are

often related to their different electronic and geometric structures.[21] Many experimental[22] and theoretical[23] studies have shown a higher activity for the bimetallic alloys compared to monometallic materials due to electronic modification of the primary metal sites after alloying. However, there are very few experimental studies to quantitatively relate the performance of the catalytic systems to their structure.[21,24] The differences in electronic structure of alumina-supported platinum particles (monometallic system) and alumina-supported platinum-tin particles (bimetallic system) have been established in this work.

1.2 Structure exploration

To understand the origin of the activity and reactivity of supported metal catalysts, an elucidation of the geometric and electronic structure of the ensemble of atoms forming the catalytically active site is essential. Moreover, it is important to track the dynamic structure of the catalyst under operating conditions to determine the structure-performance relationships, which requires in situ techniques.[25] There are many techniques to determine the structure, all with pros and cons; their application depends on the required information and the conditions of measurement. Because of the large penetration depth of X-rays, the interaction of X-rays with matter has been applied extensively. X-ray absorption spectroscopy (XAS) is one of the most popular techniques for determining the structure of materials without long-range order.[26] An XAS spectrum can be divided into three regions, namely the pre-edge, the X-ray absorption near edge structure (XANES), and the extended X-ray absorption fine structure (EXAFS). These regions are shown in Figure 1.1. The shape of XANES spectra gives the electronic structure and the local geometry around the atom that absorbs the X-ray radiation. It reflects the empty density of states (DOS) of the electronic transition. EXAFS spectroscopy provides the coordination geometry, such as bond length (with an accuracy of about 0.01 Å), the number of neighboring atoms, which indicates the size and shape of the nanoparticles, and the Debye-Waller factor.[27] XAS is used in this thesis to explore the structure of catalysts under real catalytic conditions.
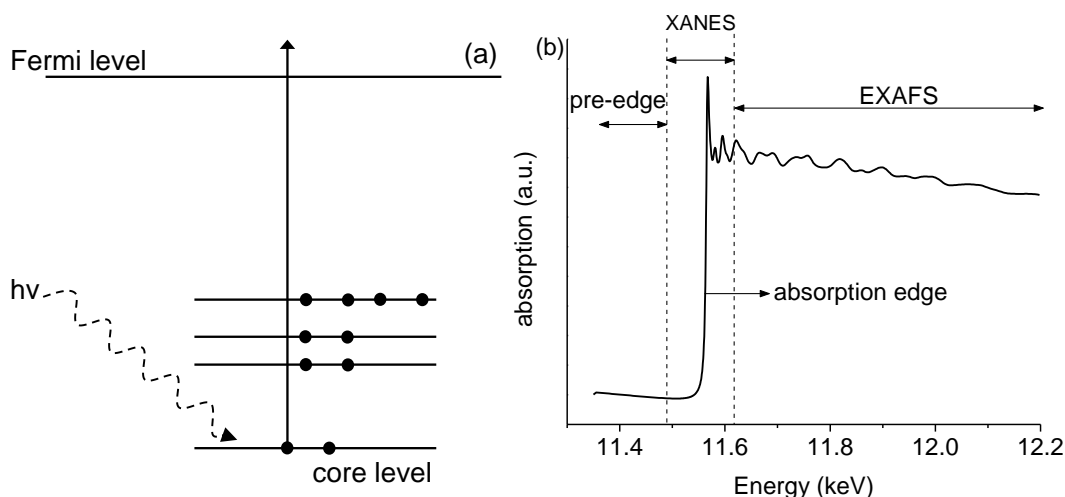
Figure 1.1: (a) excitation process of core-electron by X-rays (b) regions of an XAS spectrum.

In an XAS experiment, an electron from a core level is excited through the absorption of a photon of the incoming X-rays. The excited electron is pushed above the Fermi level and obtains a kinetic energy equal to the difference in the energy of the incoming X-ray and the bonding energy of the excited electron. As the energy of the incoming X-rays increases, the excitation occurs when the energy of the incoming X-rays exceeds the binding energy of the core-electron, causing a sharp increase in the absorption signal. This energy is referred to as the absorption edge (Figure 1.1). XAS is an element-specific technique because the energy of an absorption edge correlates directly to the core-level energy, which is unique for each element and core-electron level.[28] As the core electron is excited above the Fermi level, XAS reveals information about the unoccupied DOS. For example, the K edge probes the transition of a 1s electron to np and the $L_{2,3}$ edges, that of a 2p to (n-1)d. As a result, the L_3 edge is sensitive to the d DOS and directly probes the oxidation state of a transition metal. The first intense feature, also referred to as whiteline, in the L_3 edge spectrum thus, also reveals an anti-bonding state that forms after adsorption of reactants.[29] The shape and intensity provides information about the electronic and geometric structure of the absorbing atom.[30] The $\Delta\mu$ XANES technique emphasizes these characteristics.[31]

Although XAS and especially EXAFS are well understood and often applied experimental techniques along with full theoretical support,[32] they still have limitations. The technique does not distinguish neighboring atoms of similar atomic number such as N and O. Furthermore, because an XAS spectrum records the contribution of all the atoms in the sample and gives an average signal, it is difficult to

resolve the various geometric and electronic states. This limitation of traditional XAS can be overcome in part by valence-selective XAS[33] and spin-selective XAS.[34] Another limitation of XAS is the life-time broadening of the core hole, leading to intrinsically broad XAS spectra, and thus, hindering a detailed interpretation of the spectra. A partial solution has, however, been found.[34a] The method, high-energy resolution fluorescence detected XAS (HERFD XAS), for recording spectra with smaller life-time broadening will be further explored and applied in this thesis (section 2.4.3).

X-ray emission spectroscopy (XES), a relatively old technique to determine the catalyst structure, has strongly developed in recent years due to developments of high-flux beamlines at third-generation synchrotrons using high-brilliance and tunable X-ray sources.[35] XES will be discussed in detail in section 2.4 of this thesis. In contrast to XAS, XES yields the occupied orbitals. Because in many cases, both the excited and emitted X-rays are hard X-rays, the in situ electronic structure of the specific elements of materials can be investigated.[36] This is in contrast to X-ray photoemission spectroscopy (XPS)[37] and ultra-violet photoemission spectroscopy (UPS),[38] which generally require high vacuum. XES clearly distinguishes ligands such as nitrogen and oxygen,[39] which is hardly possible with XAS. The peculiarity of the ligand can be revealed, even in the liquid phase when working with organic materials.[40] The technique of resonant XES, also referred to as resonant inelastic X-ray scattering (RIXS) or X-ray resonance Raman spectroscopy, combines XAS and XES. In chapter 4 of this thesis, in situ XES has been applied to better understand the processes occuring at the catalyst surface.

Infra red (IR) spectroscopy is another technique, which is used often to probe the molecules adsorbed on the surface of a catalyst.[41] IR spectroscopy is one of the oldest techniques in the field of in situ spectroscopy with its application dating back to early 60's.[42] IR spectroscopy yields the surface species,[43] log-lived indermediate species,[44] and indirectly characterizes the surface and active sites of a working catalyst.[45] This technique gives information that is complimentary to X-ray spectroscopy, because IR is an indirect method to determine the structure of catalyst. Many studies had applied IR spectroscopy to probe the active sites during the oxidation of CO. Despite these extensive studies,[46] there is little agreement concerning the role of carbonyl species. There are reports where linear and bridged adsorbed CO are suggested to be active[46b,47] Also, the existence of islands of CO on the catalyst

surface has been shown[3c,48] to be relevant for CO oxidation, the formation of which is dependent on the particle morphology and size.[49] Therefore, combining XAS and IR spectroscopy is attractive to obtain an overall picture

1.3 CO oxidation

CO oxidation is one of the most-studied reactions in the field of heterogeneous catalysis. It is the key reaction during the preferential oxidation of CO in a hydrogen feed gas mixture in fuel cells, where it is crucial to decrease the CO concentration below 50 ppmv.[50] As stated above, CO oxidation is also one of the reactions occurring in a three-way catalytic converter, where the pollutant gases are transformed into less harmful ones. CO oxidation over noble metals is considered to be structure-insensitive at high partial pressure of CO and structure-sensitive in excess of oxygen.[51] Although CO oxidation seems to be straightforward, the reaction mechanism and the structure of the catalytically active species are still debated. Most researchers claim that metallic platinum is the active surface species for oxidation of carbon monoxide even in an oxygen-rich environment.[52] Recent surface diffraction studies on surfaces of platinum single crystals[53] on the other hand, indicate that the rate of oxidation of carbon monoxide is higher when the surface is oxidized. Finally, it has been suggested that the active structure is a combination of metallic and oxidic phases on the supported metal catalysts.[54] Theoretical calculations have shown the possible role played by partially oxidized surfaces in generating high catalytic activity.[55] Scanning tunneling microscopy revealed the high reactivity of an oxidized platinum surface in CO oxidation.[56]

The CO oxidation over single crystals[52a,53,57] and supported platinum catalysts[3e,58] occurs in two reaction regimes respectively with low and high reaction rates at O_2 to CO ratios greater than stoichiometric. The low activity state is characterized by the adsorbed CO that poisons the active surface.[3c,e,46a,b] Desorption of the carbon monoxide is the rate-limiting step in the low-activity regime. The high activity state is characterized by the presence of a surface oxide.[53,58c,d] The type of platinum oxide depends on particle size[59] and affects catalytic CO oxidation.[60] On supported platinum catalysts, catalytic CO oxidation activity was found to increase with increasing particle size.[52c,61] One explanation was that this is due to the increasing planar sites on larger particles, which were thought to be more catalytically active than

edge and corner sites[61,62] in contrast to earlier findings that the flat surfaces and steps have identical oscillation properties over a single crystal of platinum[63] and a more recent observation that the concave surface of a mesoporous platinum has a higher ability to activate oxygen and thus enhance CO oxidation.[64] Another suggestion was a lower fraction of oxidized platinum with increasing particle size. There was an increase in the turn-over frequency (TOF) of CO oxidation with increasing particle size. The increase in TOF was linked to less oxidation, which was the basis for saying that during CO oxidation the active surface is metallic platinum.[52c] Oxidation resistance is tuned by the acidity of the support.[65] The support, thus, plays an active role during catalysis. Its composition induces a modification of the catalytic activity of the metal particle.[66] Therefore, the important concepts for catalytic activity over platinum are particle size, support, and the active phase. *One of the goals of this thesis was to determine the structure of the active species CO oxidation over supported platinum catalysts with different particle size and supports*.

One interesting phenomenon that occurs during CO oxidation over single crystals[3a,67] and supported metal catalysts[3c,46b,58b,68] is the existence of self-sustained kinetic oscillations under specific conditions. On a single crystal of Pt(100) under UHV,[63,69] a transformation occurs from a hexagonal phase to a (1x1) phase with islands of *c*(2x2) when going from a low to high CO surface concentration. This surface phase transition has been identified to be the driving force for the kinetic oscillations[69,70] in catalytic CO oxidation, when the adsorption properties of the surface switch with the transition. Other explanations of these oscillations relate to the formation of islands of carbon monoxide.[3c,46a,71] The carbon monoxide islands form preferentially on faceted centers and lower the reaction rate by blocking active sites. In this thesis, these kinetic oscillations are studied over nano-sized platinum particles within a plug-flow reactor and a possible mechanism for oscillations is proposed.

1.4. Scope of the thesis

The goal of this thesis is to establish the structure-performance relationship for supported platinum catalysts during CO oxidation and highlight the possibilities of X-ray absorption and explore those of X-ray emission spectroscopy to perform in situ catalytic studies.

The thesis starts with experimental chapter, which describes the various techniques used in the work done in this thesis. The synthesis of supported platinum particles of

different size and on different supports is also given in Chapter 2. A detailed description of the kinetic measurements is given and it is explained how the in situ studies are performed. The major part of Chapter 2 deals with X-ray absorption and emission spectroscopy highlighting the modifications done in conventional XAS to gain higher spectral resolution. The resonant XES or RIXS planes are also explained in this chapter, which are relatively new tools to probe the filled DOS for 5d transition metals.

The goal of assessing the ability of RIXS to probe the electronic structure of a real catalyst starts with evaluating the structure of known reference compounds. This is done in Chapter 3. It deals with determining the electronic structure of various platinum and gold compounds by means of XAS and RIXS at the Pt and Au L_3-edges. The experimental spectra are compared to theoretical ones obtained by FEFF calculations. The good agreement between theory and experiment and the use of hard X-rays in experiments present a promising use of RIXS for in situ catalytic studies for real catalysts. RIXS and HERFD XAS are utilized to determine the structure of supported platinum and platinum-tin particles on alumina in Chapter 4. The alloying with tin results in the changed electronic structure of platinum. This in turn changes the adsorption properties of platinum towards hydrogen and CO, which is described in this chapter. It is shown how the structure of the catalysts changes after adsorption of adsorbants. These studies aid in understanding the actual catalytic process over catalyst surface.

Chapters 5, 6, and 7 deal with the CO oxidation over supported platinum catalysts. Various techniques are applied and combined to determine the dynamic structure of platinum under the reacting conditions. HERFD XAS describes the structure in the two distinct regimes during CO oxidation and quick EXAFS enables determining the rapid change in the structure of a catalyst during the switch between the two reactivity regimes. Full EXAFS analysis of the spectra reveals the detailed geometric structure of the catalyst in these regimes. The research has been done on various supports such as silica, titania, and alumina. The particle size effect of platinum is also addressed and shown to affect the activity of the catalyst for CO oxidation. IR helps to reveal the adsorbates on the catalyst surface during the reaction and corroborates the results of XAS.

Chapter 8 builds on the previous chapters and deals with the phenomenon of kinetic oscillations over platinum catalysts during CO oxidation. The successful combination of QEXAFS, IR and kinetic measurements shows the dynamic structure of alumina-supported platinum catalyst in a reactor during the oscillations. The mechanism for these oscillations has been proposed on supported platinum catalyst and a successful attempt is made to bridge the pressure and material gaps between the single crystal studies and the real catalyst studies.

As the commercial application of CO oxidation is found in the fuel cells where the CO content has to be below certain critical levels, PROX of CO has been investigated in the presence of hydrogen over ceria- and alumina-supported catalysts in Chapter 9. HERFD XAS reveals the changing structure of the catalyst under reaction conditions. The thesis is compiled at the end with an overall conclusion in Chapter 10, which also gives an outlook.

References

1 (a) G. C. Bond, Heteogeneous Catalysis: Principles and Applications, Oxford Science Publications, Clarendon Press, Oxford, 1987; (b) G. Ertl, H, Knözinger, Handbook of Heterogeneous Catalysis, ed. J. Vertkamp, Wile-VCH, Weinheim, 1997.

2 (a) M. Haruta, Catal. Today, 36 (1997) 153; (b) M. Haruta, Catal. Surv. Japan, 1 (1997) 61.

3 (a) G. Ertl, Adv. Catal., 37 (1990) 213; (b) R. J. Farrauto, R. M. Heck, Catal. Today, 51 (1999) 351; (c) P. T. Fanson, W. N. Delgass, J. Lauterbach, J. Catal., 204 (2001) 35; (d) M. Haruta, M. Date, Appl. Catal. A: General, 222 (2001) 427; (e) P.-A. Carlsson, L. Oesterlund, P. Thormaehlen, A. Palmqvist, E. Fridell, J. Jansson, M, Skoglundh, J. Catal., 226 (2004) 422; (f) N. Lopez, T. V. W. Janssens, B. S. Clausen, Y. Xu, M. Mavrikakis, T. Bligaard, J. K. Nørskov, J. Catal., 223 (2004) 232.

4 (a) D. S. Newsome, Catal. Rev. - Sci. Eng., 21 (1980) 275; (b) D. Andreeva, V. Idakiev, T. Tabakov, A. Andreev, J. Catal., 158 (1996) 354; (c) H. Sakurai, A. Ueda, T. Kobayashi, M. Haruta, J. Chem. Soc. Chem. Commun., 271 (1997); (d) T. Bunluesin, R. J. Gorte, G. W. Graham, Appl. Catal. B-Eniron., 15 (1998) 107; (e) T. Tabakova, V. Idakiev, D. Andreeva, I. Mitov, Appl. Catal. A: General, 202 (2000) 336; (f) M. Mokhtar, T. M. Salama, M. Ichikawa, J. Colloid Interface Sci., 224 (2000) 336; (g) S. Hilaire, X. Wang, T. Luo, R. J. Gorte, J. Wagner, Appl. Catal. A: General, 215 (2001) 271; (h) Q. Fu, A Weber, M. Flytzani-Stephanopoulos, Catal. Lett., 77 (2001) 87.

5 (a) G. C. Bond, P. A. Sermon, J. Chem. Soc. Chem. Commun., 444 (1973); (b) Z. Xu, F.-S. Xiao, S. K. Purnell, O. Alexeev, S. Kawi, S. E. Deutsh, B. C. Gates, Nature, 372 (1994) 346; (c) P. Claus, A. Brückner, C. Mohr and H. Hofmeister, J. Am. Chem. Soc., 122 (2000) 11430; (d) Y. H. Niu, L. K. Yeung, R. M. Crooks, J. Am. Chem. Soc., 123 (2001) 6840; (e) A. Corma, P. Serna, Science, 313 (2006) 332; E. Bus, R. Prins, J. A. van Bokhoven, Catal. Commun., 8 (2007) 1397.

6 (a) M. A. Vannice, J. Catal., 37 (1975) 462; (b) M. Araki, V. Ponec, J. Catal., 44 (1976) 439; (c) R. A. Demmin, R. J. Gorte, J. Catal., 105 (1987) 373; (d) J. G. Xu, G. F. Froment, AICHE J., 35 (1989) 88; (e) R. A. Lemons, J. Power Sources, 29 (1990) 251; (f) M. J. Kahlich, H. A. Gasteiger, R. J. Behm, J. Catal., 171 (1997) 93.

7 (a) C. Bianchi, F. Porta, L. Prati, M. Rossi, Topics in Catal., 13 (2000) 231; (b) F. Porta, L. Prati, M. Rossi, S. Coluccia, G. Martra, Catal. Today, 61 (2000) 165.

8 M. Boudart, J. Mol. Catal., 30 (1985) 27.

9 (a) J. Wei, E. Iglesia, J. Phys. Chem. B, 108 (2004) 4094; (b) X. Wang, S. M. Sigmon, J. J. Spivey, H. H. Lamb, Catal. Today, 96 (2004) 11; (c) K. S. Han, O. H. Han, P. K. babu, J. Electrochem. Soc., 152 (2005) J131; (d) P. Panagiotopoulou, A. Christodoulakis, D. I. Kondarides, S. Boghosian, J. Catal., 240 (2006) 114.

10 (a) P. Denton, A. G. Fendler, H. Praliaud, M. Primet, J. Catal., 189 (2000) 410; (b) D. E. Ramaker, G. E. van Dorssen, B. L. Mojet, D. C. Konningsberger, Top. Catal., 10 (2000) 157; (c) M. L. Toebes, Y. Zhang, J. Hajek, T. A. Nijhuis, J. H. Bitter, A. J. van Dillen, D. Y. Murzin, D. C. Koningsberger, K. P. de Jong, J. Catal., 226 (2004) 215.

11 (a) S. R. De Miguel, J. A. M. Correa, G. T. baronetti, A. A. Castro, O. A. Scelza, Appl. Catal. 60 (1990) 47; (b) R.-M. Jao, L.-J. Leu, J.-R. Chang, Appl. Catal. A: Gen., 135 (1996) 301; (c) R. Zanella, C. Louis, Catal. Today, 107 (2005) 768; (d) G. J. Hutchings, M. S. Hall, A. F. Carley, P. Landon, B. E. Solsona, C. J. Kiely, A. Herzing, M. Makkee, J. A. Moulijn, A. Overweg, J. C. F.-Gonzalez, J. Guzman, B. C. Gates, J. Catal., 242 (2006) 71; (e) E. Bus, R. Prins, J. A. van Bokhoven, Phys. Chem. Chem. Phys., 9 (2007) 3312.

12 (a) M. M. Schubert, V. Plzak, J. Garche, R. J. Behm, Catal. Lett., 76 (2001) 143; (b) M. Haruta, Gold Bull., 37/1-2 (2004) 27.

13 (a) Z. Zhang, T. T. Wong, W. M. H. Sachtler, J. Catal., 128 (1991) 13; (b) Z. Karpinski, S. N. Gandhi, W. M. H. Sachtler, J. Catal., 141 (1993) 337.

14 (a) G. Larsen, G. L. Haller, Catal. Lett., 3 (1989) 103; (b) A. de Mallmann, D. Barthomeuf, Stud. Surf. Sci. Catal., 46 (1989) 429; (c) A. de Mallmann, D. Barthomeuf, J. Chem. Phys., 87 (1990) 535.

15 (a) A. P. Jansen, R. A. van Santen, J. Phys. Chem., 94 (1990) 6764; (b) E. Sanchez-Marcos, A. P. J. Jansen, R. A. van Santen, Chem. Phys. Lett., 16 (1990) 399.

16 (a) A. J. Appleby, F. R. Foulkes, Fuel Cell Handbook, Van Nostrand Reinhold, New York, 1989; (b) C. D. Dudfield, R. Chen, P. L. Adock, Int. J. Hydrogen Energy, 26 (2001) 763.

17 A.C. Balazs, and K.H. Johnson. Molecular-orbital Models for the Catalytic Activity and Selectivity of Coordinatively Unsaturated Platinum Surfaces and Complexes. Surface Science 114 (1982) 197.

18 (a) J. L. Gland, M. R. McClellan, F. R. McFeely, J. Chem. Phys., 79 (1983) 6349; (b) A. Szabo, M. A. Henderson, J. T. Yates, J. Chem. Phys. 96 (1992) 6191; (c) D. W. Goodman, C. H. F. Peden, G. B. Fisher, S. H. Oh, Catal. Lett., 22 (1993) 271; (d) M. Bowker, Q. Guo, Y. Li, R. W. Joyner, Catal. Lett., 22 (1993) 275; (e) J. Z. Xu, J. T. Yates, J. Chem. Phys., 99 (1993) 725

19 (a) H. Hopster, H. Ibach, G. Comsa, J. Catal., 46 (1977) 37; (b) E. C. Akubuiro, X. E. Verykios, L. Lesnick, Appl. Catal., 14 (1985) 215; (c) D. N. Belton, S. J. Schmieg, Surf. Sci., 202 (1988) 238; (d) G. S. Zafiris, R. J. Gorte, Surf. Sci., 276 (1992) 86; (e) I. Stará, V. Nehasil, V. Matolín, Surf. Sci., 331–333 (1995) 173; (f) V. Nehasil, I. Stará, V. Matolín, Surf. Sci., 352–354 (1996) 305; (g) U. Heiz, A. Sanchez, S. Abbet, W. D. Schneider, J. Am. Chem. Soc., 121 (1999) 3214; (h) I. Meusel, J. Hoffmann, J. Hartmann, J. Libuda, H. J. Freund, J. Chem. Phys. B, 105 (2001) 3567; (i) A. K. Santra, D. W. Goodman, Electrochim. Acta, 47 (2002) 3595.

20 Y. Cai, H. G. Stenger, Jr., C. E. Lyman, J. Catal., 161 (1996) 123.

21 E. Nikolla, J. Schwank, S. Linic, J. Am. Chem. Soc., 131 (2009) 2747.

22 (a) M. T. Paffett, S. C. Gebhard, R. G. Windham, B. E. Koel, J. Phys. Chem., 94 (1990) 6831; (b) F. Buatier de Mongeot, M. Scherer, B. Gleich, E. Kopatzki, R. J. Behm, Surf. Sci., 411 (1998) 249; (c) M. M. Schubert, M. J. Kahlich, G. Feldmeyer, M. Hüttner, S. Hackenberg, H. A. Gasteiger, R. J. Behm, Phys. Chem. Chem. Phys., 3 (2001) 1123.

23 (a) R. M. Watwe, R. D. Cortright, M. Mavrikakis, J. K. Nørskov, J. A. Dumesic, J. Chem. Phys., 114 (2001) 4663; (b) C. J. Zhang, R. J. Baxter, P. Hu, A. Alavi, M. H. Lee, J. Chem. Phys., 115 (2001) 5272; (c) M. T. M. Koper, Surf. Sci., 548 (2004) 1.

24 (a) A. Nilsson, L. G. M. Pettersson, B. Hammer, T. Bligaard, C. H. Christensen, J. K. Norskov, Catal. Lett., 100 (2005) 111; (b) V. R. Stamenkovic, B. S. Mun, M. Arenz, K. J. J. Mayrhofer, C. A. Lucas, G. F. Wang, P. N. Ross, N. M. Markovic, Nat. Mater., 6 (2007) 241.

25 (a) J. M. Thomas, Angew. Chem. Int. Ed., 38 (1999) 3589; (b) B. M. Weckhuysen, Phys. Chem. Chem. Phys., 5 (2003) 4351.

26 D. C. Koningsberger, R. Prins, X-ray absorption: principles, applications, techniques of EXAFS, SEXAFS, and XANES, Wiley, New York, (1988).

27 E. A. Stern, D. E. Sayers, F. W. Lytle, Phys. Rev. B, 11 (1975) 4836.

28 (a) D. C. Koningsberger, B. L. Mojet, G. E. van Dorssen, D. E. Ramaker, Top. Catal., 10 (2000) 143; (b) J. A. van Bokhoven, T. Ressler, F. M. F. de Groot, G. Knopp-Gericke, in In-situ spectroscopy of catalysts, ed. B.M. Weckhuysen, American Scientific Publishers, California, (2004) 123.

29 (a) D. E. Ramaker, D. C. Koningsberger, Phys. Rev. Lett., 89 (2002) 139701; (b) A. L. Ankudinov, J. J. Rehr, J. J. Low, A. R. Bare, Phys. Rev. Lett., 89 (2002) 139702.

30 (a) D. E. Ramaker, B. L. Mojet, M. T. G. Oostenbrink, J. T. Miller, D. C. Koningsberger, Phys. Chem. Chem. Phys., 1 (1999) 2293; (b) A. L. Ankudinov, J. J. Rehr, J. Low, S. R. Bare, Phys. Rev. Lett., 86 (2001) 1642; (c) M. K. Oudenhuijzen, J. A. van Bokhoven, J. T. Miller, D. E. Ramaker, D. C. Koningsberger, J. Am. Chem. Soc., 127 (2005) 1530; (d) N. Weiher, E. Bus, L. Delannoy, C. Louis, D. E. Ramaker, J. T. Miller, J. A. van Bokhoven, J. Catal., 240 (2006) 100; (e) E. Bus, D. E. Ramaker, J. A. van Bokhoven, J. Am. Chem. Soc., 129 (2007) 8094.

31 D. E. Ramaker, D. C. Koningsberger, Phys. Chem. Chem. Phys., 12 (2010) 5514.

32 (a) B. K. Teo, P. A. Lee, J. Am. Chem. Soc., 101 (1979) 2815; (b) J. J. Rehr, J. Mustre de Leon, S. I. Zabinsky, R. C. Albers, J. Am. Chem. Soc., 113 (1991) 5135; (c) A. Filipponi, A. DiCicco, C. R. Natoli, Phys. Rev. B, 52 (1995) 15122.

33 P. Glatzel, L. Jacquamet, U. Bergmann, F. M. F. de Groot, S. P. Cramer, Inorg. Chem., 41 (2002) 3121.

34 (a) K. Hämäläinen, D. P. Siddons, J. B. Hastings, L. E. Berman, Phys. Rev. Lett., 67 (1991) 2850; (b) X. Wang, F. M. F. de Groot, S. P. Cramer, Phys. Rev. B, 56 (1997) 4553.

35 (a) G. Materlik, C. J. Sparks, K. Fischer, in Resonant Anomalous X-Ray Scattering: Theory and Applications, North-Holland, Amsterdam (1994); (b) D. L. Ederer and J. H. McGuire, in Raman Emission by X-Ray Scattering, World Scientific, Singapore (1996); (c) J. Nordgren, E. Z. Kurmaev, J. Electron Spectrosc. Relat. Phenom., 110-111 (2000) 1; (d) A. Kotani, S. Shin, Rev. Mod. Phys., 73 (2001) 203; (e) N. Wassdahl, A. Nilsson, T. Wiell, H. Tillborg, L. C. Duda, J. Guo, N. Mårtensson, J. Nordgren, J. N. Andersen, R. Nyholm, Phys. Rev. Lett., 69 (1992) 812.

36 P. Glatzel, J. Singh, K. O. Kvashnina, J. A. van Bokhoven, J. Am. Chem. Soc., 132 (2010) 2555.

37 (a) K. Siegbahn, C. Nordling, G. Johansson, J. Hedman, P.F. Heden, K. Hamrin, U. Gelius, T. Bergmark, L. O. Werme, R. Manne, Y. Baer, in ESCA Applied to Free

Molecules, North-Holland, Amsterdam (1969); (b) S. Hufner, in Photoelectron Spectroscopy, Springer-Verlag, Berlin (1995); (c) N. Mårtensson, A. Nilsson, in Applications of Synchrotron Radiation: High Resolution Studies of Molecules and Molecular Adsorbates, ed. W. Eberhardt, Springer-Verlag, Berlin, vol. 35 (1995).

38 S. D. Kevan, in Angle-Resolved Photoemission, Elsevier, Amsterdam (1992).

39 U. Bergmann, C. R. Horne, T. J. Collins, J. M. Workman, S. P. Cramer, Chem. Phys. Lett., 302 (1999) 119.

40 V. A. Safonova, L. N. Vykhodsteva, Y. M. Polukarov, O. V. Safonova, G. Smolentsev, M. Sikora, S. G. Eeckhout, P. Glatzel, J. Phys. Chem. B, 110 (2006) 23192.

41 J. Ryczkowsky, Catal. Today, 68 (2001) 263.

42 R. P. Eischens, W. A. Pliskin, Adv. Catal., 10 (1958) 1.

43 P. Maetz, J. Saussey, J. C. Lavalley, R. Thouroude, J. Cataly., 147 (1994) 48.

44 (a) F. Le Peltier, P. Chaumette, J. Saussey, M. M. Bettahar, J. C. Lavalley, J. Mol. Catal. A: Chem., 122 (1997) 131; (b) J-L. Freysz, J. Saussey, J. C. Lavalley, P. Bourges, J. Catal., 197 (2001) 131.

45 (a) J. Saussey, J. C. Lavalley, J. Mol. Catal., 50 (1989) 343; (b) J.F. Joly, N. Zanier-Szydlowski, S. Colin, F. Raatz, J. Saussey, J.C. Lavalley, Catal. Today, 9 (1991) 31; (c) L. Savary, J. Saussey, G. Costentin, M. M. Bettahar, J. C. Lavalley and M. Gubelmann-Bonneau, Catal. Lett., 38 (1996) 197.

46 (a) D. M. Haaland, F. L. Williams, J. Catal., 76 (1982) 450; (b) T. H. Lindstrom, T. T. Tsotsis, Surf. Sci., 150 (1985) 487; (c) Y. Barshad, X. Zhou, E. Gulari, J. Catal., 94 (1985) 128; (d) N. W. Cant, D. E. Angove, J. Catal., 97 (1986) 36; (e) Y-E. Li, D. Boecker, R. D. Gonzalez, J. Catal. 110 (1988) 319.

47 J. Sarkany, R. D. Gonzalez, Appl. Catal. 5 (1983) 85.

48 J. Sarkany, M. Bartok, R. D. Gonzalez, J . Catal. 81 (1983) 347.

49 J. A. Anderson, Catal. Lett. 13 (1992) 363.

50 J. M. Zalc, D.G. Löfter, J. Power Sources, 111 (2002) 58.

51 (a) E. McCarthy, J. Zahradnik, G. C. Kuczynski, J. J. Carberry, J. Catal., 39 (1975) 29; (b) T. Engel, G. Ertl, Adv. Catal., 28 (1979); (c) N. W. Cant, J. Catal., 62 (1980) 173; (d) S. Ladas, H. Poppa, M. Boudart, Surf. Sci., 102 (1981) 151; (e) S. H. Oh, C.

C. Eickel, J. Catal., 128 (1991) 526; (f) D. R. Rainer, M. Koranne, S.M. Vesecky, D. W. Goodman, J. Phys. Chem. B, 101 (1997) 10769.

52 (a) J. A. Anderson, J. Chem. Soc. Faraday Trans., 88 (8) (1992) 1197; (b) R. Burch, P. K. Loader, Appl. Catal., A 122 (1995) 169; (c) F. J. Gracia, L. Bollmann, E. E. Wolf, J. T. Miller, A. J. Kropf, J. Catal., 220 (2003) 382.

53 M. D. Ackermann, T. M. Pedersen, B. L. M. Hendriksen, O. Robach, S. C. Bobaru, I. Popa, C. Quiros, H. Kim, B. Hammer, S. Ferrer, J. W. M. Frenken, Phys. Rev. Lett., 95 (2005) 255505.

54 (a) R. Burch, P. K. Loader, Appl. Catal. B, 5 (1994) 149; (b) S. Yang, A. M. Valiente, M. B. Gonzalez, I. R. Ramos, A. G. Ruiz, Appl. Catal. B, 28 (2000) 223.

55 (a) C. Stampfl, M. Scheffler, Phys. Rev. Lett., 78 (1997) 1500; (b) X.-G. Wang, A. Chaka, M. Scheffler, Phys. Rev. Lett., 84 (2000) 3650; (c) K. Reuter, M. Scheffler, Phys. Rev. B. 65 (2002) 035406; (d) K. Reuter, M. Scheffler, Phys. Rev. B. 68 (2003) 045407.

56 B. L. M. Hendriksen, J. W. M. Frenken, Phys. Rev. Lett., 89 (2002) 046101.

57 X. Su, P. S. Cremer, Y. R. Shen, G. A. Somorjai, J. Am. Chem. Soc., 119 (1997) 3994.

58 (a) F. J. Gracia, S. Guerrero, E. E. Wolf, J. T. Miller, A. J. Kropf, J. Catal., 233 (2005) 372; (b) P.-A. Carlsson, V.P. Zhdanov, M. Skoglundh, Phys. Chem. Chem. Phys., 8 (2006) 2703; (c) J. Singh, E. M. Alayon, M. Tromp, O. Safonova, P. Glatzel, M. Nachtegaal, R. Frahm, J. A. van Bokhoven, Angew. Chem. Int. Ed. 47 (2008) 9260; (d) E. M. Alayon, J. Singh, M. Nachtegaal, M. Harfouche, J. A. van Bokhoven, J. Catal. 263 (2009) 228.

59 C. Wang, H. Lin, S. Hsu. T. Huang, H. Chiu, J. Mol. Catal. A: Chemical, 188 (2002) 201.

60 N. Seriani, W. Pompe, L. C. Ciacchi, J. Phys. Chem. B, 110 (2006) 14860.

61 B. Atalik, D. Uner, J. Catal., 241 (2006) 268.

62 J. Yang, V. Tschamber, D. Habermacher, F. Garin, P. Gilot, Appl. Catal. B: Environmental, 83 (2008) 229.

63 G. Ertl, P. R. Norton, J. Rustig, Phys. Rev. Lett., 49 (1982) 177.

64 A. Saramat, P. Thormählen, M. Skoglundh, G. Attard, A. E. C. Palmqvist, J. Catal., 253 (2008) 253.

65 (a) Y. Yazawa, H. Yoshida, T. Hattori, Appl. Catal. A: General, 237 (2002) 139; (b) M. Kobayashi, A. Morita, M. Ikeda, Appl. Catal. B: Environmental, 71 (2007) 94.

66 A. Y. Stakheev, L. M. Kustov, Appl. Catalysis A: General, 188 (1999) 3.

67 (a) G. Ertl, Surf. Sci., 287-288 (1993) 1; (b) J. Lauterbach, H. H. Rotermund, Catal. Lett., 27 (1994) 27; (c) G. Ertl, H. Rotermund, Surf. Sci., (1996) 617; (d) J. Lauterbach, G. Bonilla, T. D. Pletcher, Chem. Eng. Sci., 54 (1999) 4501; (e) M. Bertram, C. Beta, H. H. Rotermund, G. Ertl, J. Phys. Chem. B, 107 (2003) 9610.

68 Y. Deng, T. G. Nevell, Farad. Dis., 105 (1996) 33.

69 R. Imbihl, M. P. Cox, G. Ertl, J. Chem. Phys., 84 (1986) 3519.

70 F. van Neer, A. Bliek, Chem, Eng. Sci., 54 (1999) 4483.

71 D. Boecker, E. Wicke, Ber. Buseng. Phys. Chem. 89 (1986) 629.

Chapter 1

Chapter 2

Experimental techniques

Chapter 2

2.1 Synthesis of supported platinum catalysts

Supported platinum catalysts were synthesized by either incipient-wetness impregnation or deposition-precipitation method, depending on the support. Incipient-wetness impregnation method acquired its name, because the volume of the solution used to impregnate the catalyst precursor onto the support is equal or less than that of the pore volume of the support. The metal-precursor solution is added to the support and pores of the support are filled by capillary forces. The maximum loading of the metal is limited by the solubility of the precursor in the solution and the pore volume of the support. Deposition-precipitation is a method where the metal hydroxide is supposed to precipitate on the support as a result of the gradual increase of the pH of the solution in which the support is suspended. The support surface acts as a nucleating agent for the precipitate and under proper conditions of temperature, pH and stirring, the active phase gets attached to the support. The ultimate dispersion of the metal depends on the conditions of drying and further pretreatment.[1] The ligands of the precursor are removed by calcination, generally in air, at elevated temperatures. The maximum temperature and the duration of calcination affect the particle size and its distribution on the support.

Gold nano-particles supported on alumina, used in chapter 3, were supported using deposition-precipitation. An aqueous solution of 0.151 g of hydrated gold hydrochloric acid in 2.55 ml of distilled water was added to 5 g of alumina, which was dried at 393 K overnight. The obtained sample was mixed thoroughly for 30 minutes and then heated for about 2h at 423-433 K. The pH of the solution was maintained at an approximate value of 8 using 1M sodium hydroxide solution. The solution was filtered and the precursor was recovered after washing with de-ionized water at 353 K and dried at 363 K overnight. The sample was then reduced in pure hydrogen flow while increasing the temperature to 523 K.

1.90 wt% Pt/Al_2O_3, called Pt/Al_2O_3 in chapters 4, 8, and 9, was synthesized using incipient-wetness impregnation method. 1.0 g $Pt(NH_3)_4(NO_3)_2$ in 14 ml deionized water was added to 25g of γ-alumina (surface area of 180 m^2/g). 2 mL saturated NH_4OH was then added to the above mixture. This sample was dried overnight at 398 K, at 498 K for 3 h, and reduced at 523 K in a flow of pure hydrogen (100 mL/min) at atmospheric pressure. The platinum elemental composition was determined by inductively coupled plasma method. The catalyst was dried at 498 K afterward.

For synthesis of 1 wt% Pt 0.25 wt% Sn, on Al_2O_3, called $PtSn/Al_2O_3$ in chapter 4, first platinum was grafted on γ-Al_2O_3 by wetness impregnation. An aqueous solution was made from 128 mg of $Pt(NH_3)_4(NO_3)_2$ in 3.3 mL de-ionized H_2O, and then mixed with 6.34 g of γ-Al_2O_3. The obtained solid was dried at 423 K for 1 h followed by calcination in flowing air at 573 K for 5 h. The resulting powder was treated with an aqueous solution of 45 mg Bu_3SnOAc in 3.4 mL pentane. After drying at room temperature, the catalyst was heated in flowing air at 373 K for 1 h and later at 673 K for 3 h.

2 wt% Pt/Al_2O_3 catalyst, which was used in work presented in chapters 5 and 6, was prepared by incipient-wetness impregnation. 0.197 g tetra amine platinum nitrate was dissolved in 2.55 ml water and then impregnated on 5 g of alumina, which was dried at 393 K, to give 2 wt% Pt/Al_2O_3 samples. The resulting powder was dried at room temperature for four hours. Calcination was performed in flowing air in two steps; heating to 473 K, left for four hours, and then heating to 673 K and left for four hours. The heating rate during both ramps was 5 K/min. The catalyst was subsequently reduced in a flow of pure hydrogen at 723 K for two hours to yield 2 wt% platinum nano-particles supported on alumina.

3 wt% Pt/TiO_2, which was used in work presented in chapter 6, was also prepared by deposition-precipitation. A solution of 0.3 g of H_2PtCl_6 in 70 mL water, with the pH adjusted to 4 - 5 using NaOH, was added to 4 g of TiO_2. The solution was stirred for 2 hours at 70°C. The obtained paste was filtered and washed with 1 L of warm water (343 K) and dried under vacuum. The catalyst was calcined in a flow of air: heated at 5 K/min to 393 K, remained at this temperature for 4 hours, heated again at 5 K/min to 673 K, remained at this temperature for another 4 hours, and cooled to room temperature in a flow of air. The catalyst was reduced in a flow of 50 mL/min hydrogen for 2 hours at 473 K and cooled down to room temperature in 10 mL/min of flowing helium.

2 wt% Pt/SiO_2 catalyst, which was used in work presented in chapter 6, was synthesized by deposition-precipitation. 40 mL water was added to 0.197 g of $Pt(NH_3)_4(NO_3)_2$. NaOH was added to adjust the pH to 10. The solution was mixed with 5 g of dried SiO_2 and stirred for 2.5 hours, was filtered, washed with 1 L of warm water (343 K), and dried at 373 K for 5 hours. The calcination was done in a similar way as for Pt/TiO_2 described above. The catalyst was reduced in 50 mL/min of flowing hydrogen for 2 hours at 523 K and cooled to room temperature in hydrogen flow.

1.90 wt% Pt/Al_2O_3, which was used in work presented in chapter 7, was synthesized using the incipient-wetness impregnation method, similar to that as used in chapter 4. Instead of drying at 498 K, one batch of the catalyst was calcined at 623 K and another batch at 773 K, both in the presence of static air. The catalysts calcined at 623 K and 773 K are mentioned as Pt-623 and Pt-773 respectively in chapter 7.

4.4 wt% $Pt/Ce(La)O_x$, called $Pt/Ce(La)O_x$ in chapter 9, was synthesized using an incipient-wetness impregnation method. La doped ceria was synthesized using coprecipitation method. 13.7 g of $(NH_4)_2Ce(NO_3)_2$ was mixed with 0.9 g of hydrated lanthanum nitrate in 200 ml of deionized water along with 24 g of urea. The solution was heated to 373 K under constant stirring. After coprecipitation, the obtained gel was heated for about 8 h at 373 K, filtered, washed with hot water and dried at 373 K in a vacuum oven. The obtained powder was then calcined at 923 K for 8 h in air resulting in the final support material for supporting platinum. 0.44 g of H_2PtCl_6 was dissolved in deionized water, the volume of which was equal to the pore volume of lanthanum-doped ceria. The powder was then dried at 383 K for 10 h under vacuum, and then calcined in air for 10 h at 673 K. Afterward, the leaching of $Pt/Ce(La)O_x$ was done using 2% aqueous solution of NaCN at room temperature for 24 h. The leaching resulted in 2 wt% $Pt/Ce(La)O_x$, where the platinum content was approximated from energy-dispersive X-ray spectroscopy (EDX). The sample is called $L-Pt/Ce(La)O_x$ in chapter 9.

2.2 Electron microscopy

To characterize the particle size and size distribution of the metal particles, electron microscopy is used. The information about the structure, morphology, and composition can be derived by analyzing the interaction of the electron beam with a sample.[2] Transmission electron microscopy (TEM) is one of the techniques which allows the visualization of the particles, sometimes even smaller than 1 nm. TEM has the advantage of being able to detect electron diffraction patterns, which allows structural characterization even when the normal image contrast is very low. The supported metal particles, as synthesized in this thesis, can be visualized by high-resolution TEM (HRTEM). The metal has generally a high atomic number and is thus a stronger electron scatterer than the support such as silica, alumina. In this case, Z-contrast imaging or high-angle annular dark field detector scanning TEM (HAADF-STEM) is beneficial to reveal the metal particles clearly. An electron beam is scanned over a defined area of the sample. The image is constructed by simultaneously recording the signal generated by

the interaction of electrons with the sample using selected detectors. An energy-dispersive X-ray (EDX) spectrum can be measured by localizing the electron beam on a particular area in the image. These spectra help in revealing the actual constituents present in that specific area of the image. For example, in case of alloys, EDX is beneficial to reveal the presence of different metals.

In the work in this thesis, the particle size distribution was determined by STEM. The sample was mounted on a carbon foil after the evaporation of ethanol, and a copper grid was used to support the sample. The measurements were performed using a Tecnai F30 microscope operating with a field-emission cathode at 300 kV and a high-angle annular dark-field (HAADF) detector. Elemental analysis of bright spots in the STEM micrographs was done by EDX.

2.3 X-ray absorption spectroscopy

2.3.1   XANES and EXAFS

As stated in chapter 1, XAS is a well-established technique to determine the electronic and geometric structure of materials. When the X-rays hit a material, they are scattered and/or absorbed by the material. Therefore, the intensity of the incoming beam reduces after passing through the matter and is given by the Lambert's law:

$$I_t = I_0 \exp (\mu.x) \tag{1}$$

where,

I_t = intensity of transmitted X-rays

I_0 = intensity of incoming X-rays

x = path length through which the X-ray travel

μ = linear absorption coefficient

The linear absorption coefficient, μ, depends on the type of atoms comprising the material and their density. The absorption through the matter decreases with increasing energy of the incoming X-rays, because with increasing incoming energy the probability of absorption decreases. At a certain energy, a sharp increase in the absorption is observed as shown in Figure 2.1(a). At these energies, there is absorption of the incoming photons to excite an electron from a core level to the lowest empty state above the Fermi level. This sharp increase in the absorption is called the absorption edge. As the core electrons in each element have their own characteristic binding energy, XAS is

23

element-specific technique. Figure 2.1(a) shows three different absorption edges, namely L_3, L_2, and L_1 for platinum and they arise from the excitation of core electrons from respectively $2p_{3/2}$, $2p_{1/2}$, and 2s core levels. Similarly, when the core electrons are excited from 1s core level, the absorption edge is called K edge. These excitations or transitions follow the quantum mechanical selection rules. The transitions where the orbital quantum number of the excited (final) state differs from the initial state by 1 ($\Delta L = \pm 1$) and 2 ($\Delta L = \pm 1$) are called dipole and quadrupole transitions respectively. The dipole transitions dominate the quadrupole transitions. Therefore, K and L_1 edges probe the p density of states (DOS) and L_3, and L_2 edges probe mainly d DOS and s DOS to much less extend. The quadrupole transitions are often observed in the pre-edge region as explained below. In case of solids and molecular structure, the smooth background, as observed in Figure 2.1(a), is not observed and instead many peaks are originated after the absorption edge (Figure 2.1(b)). The origin of these peaks will be explained in the later part of this section. The XAS spectrum, as shown in Figure 2.1(b), can be divided into three regions: the pre-edge region, the X-ray absorption near-edge structure (XANES), and the extended X-ray absorption fine structure (EXAFS).
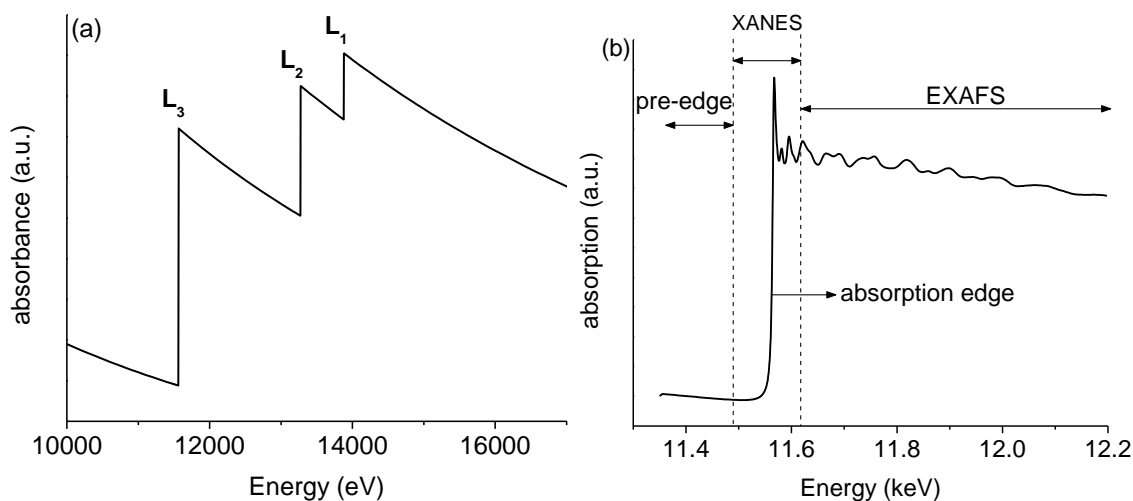
Figure 2.1: (a) The three L edges of platinum. (b) Pt L_3 edge spectrum of platinum foil.

The first intense feature in the XANES region after the absorption edge is called the whiteline. The intensity of the whiteline, the energy position of the absorption edge, and shape of the XANES spectra can be exploited to determine structure of catalysts during reaction. The shape and intensity of XANES is determined by the oxidation state and local structure of the absorbing element. As mentioned above, it represents the spin

selective empty density of state. The altered DOS after adsorption of reactants on a metal can be probed in L_3 and L_2 edges. Adsorption sites of hydrogen atoms,[3] oxygen atoms,[4] carbon monoxide,[3a,5] and ethylene[6] have thus been observed. Therefore, XANES spectroscopy is a very powerful tool to study element specifically the catalyst surfaces with different adsorbates. The intensity of the whiteline in L_3 edge spectra (2p→nd transition) is highly sensitive to the oxidation state of the element under investigation. This characteristic feature has been utilized in this work for supported platinum catalysts during CO oxidation because one of the most important features of the electronic structure of the active element is the number of d-electrons. When platinum is oxidized, a more intense whiteline is observed because of the increase in the number of holes in the d-band above the Fermi level. The advantage of calculating XANES using different programs such as FEFF,[7] GNXAS,[8] DFT with local spin density (LSD) approximation,[9] multiplet theory,[10] helps in identifying the catalyst structure and adsorption sites probed by the different shape and intensities of the XANES spectra.

To explain the origin of the wiggling pattern of X-ray absorption spectrum at photon energy above an absorption edge, one must consider the kinetic energy of the photoelectron that is created by the absorption of incoming photons. If the energy of the incoming X-rays (hν) is higher than the binding energy (E_0) of a core electron, then the extra energy is transferred to the excited photo-electron as kinetic energy (E_{kin}) and the energy balance is given by following equation:

$$E_{kin} = h\nu - E_0 \qquad\qquad (2)$$

This photo-electron can be mathematically treated as a spherical electronic wave. In solids, this electronic wave originating from the absorbing atom, referred as outgoing wave, $\psi_{outgoing}$, interacts with the neighboring atoms and result in backscattered wave, $\psi_{backscattered}$. These two waves can interfere with each other constructively or destructively, resulting in the final state, ψ_{final} as following:

$$\psi_{final} = \psi_{outgoing} + \psi_{backscattered} \qquad\qquad (3)$$

ψ_{final} depends on the local environment of the absorbing atom. The probability of photoelectric absorption, P, which is proportional to the absorption co-efficient, µ, is given by Fermi's Golden Rule as following:

$$\mu \propto P = \frac{2\pi^2 e^2}{\omega c^2 m} \left| \langle \psi_{final} | \boldsymbol{E} \cdot r | \psi_{initial} \rangle \right|^2 \rho(E_f) \tag{4}$$

ω = the angular frequency

e = the electron charge

ψ_{final}= the final state wave function (equation 3)

$\psi_{initial}$= the initial state wave function

$\boldsymbol{E}$ = the electric field polarization vector

r = the position vector of the scatterer with respect to the absorber atom

$\rho(E_f)$ = the density of allowed states at the final energy E_f

The electric field and the position vector determine whether the transition is dipole allowed or not. This explains why instead of a smooth background as in Figure 2.1(a), there are peaks observed in Figure 2.1(b) in the EXAFS region, because the final state, ψ_{final} is a function of two interfering contributions (equation 3), which are a function of the energy of the incoming photon. Therefore, the wiggles observed in the EXAFS region are due to the formation of maxima and minima originated from the interference of outgoing and backscattered electronic waves. The wiggling part of the EXAFS region can be expressed using EXAFS function, χ(k), as following:

$$\mu(k) = \mu_0(k) \, [1 + \chi(k)] \tag{5}$$

μ_0 = atomic background, representing the X-ray absorption of a single free atom

k = photo-electron wave vector

The EXAFS function, χ(k), is described mathematically by the following equation if the photo-electron is assumed to scatter only once, i.e. in the single scattering approximation.

$$\chi(k) = \sum_{j=0}^{j} A_j(k) \sin(2kR_j + \varphi_j(k)) \tag{6}$$

j refers to the jth coordination shell, which consists of atoms of same element at the same distance, R_j, from the absorbing atom.

$A_j(k)$ = the backscattering amplitude

$\varphi_j(k)$ = phase shift experienced by the photo-electron in the scattering process

The backscattering amplitude is given as:

$$A_j(k) = \frac{S_0^2 e^{\frac{-2R_j}{\lambda}}}{kR_j^2} \times e^{-2\sigma_j^2 k^2} \times N_j F_j(k) \tag{7}$$

S_0^2 = amplitude reduction factor, signifying the incomplete transfer of photon energy to the photo-electron, which is due to many body effects and shake-up/shake-off processes in the absorber atom. The value of S_0^2 varies between 0.75 and 0.95.[11]

λ = mean free path defined as $\lambda = 2\pi/k$

σ_j^2 = Debye-Waller factor, representing the structural disorder including thermal and static disorder

N_j = number of neighboring atoms in the jth shell

F_j = scattering power of neighbor j

F_j and φ_j are typical of absorber-scatterer pairs and are tabulated or can be calculated.

As explained by equation 3, the final state, and thus, the EXAFS function, is a result of interference of two contributions, thus, the absorption process depends on the contributions from both wave functions. The type of neighbor atoms (Z), the number of neighbor atoms (N) and the distance of the neighbor atoms (R) determine the backscattered wave and thus analyzing the EXAFS function gives information about all these parameters, which in turn constitute the structural information of the material under study. To obtain the structural information, the EXAFS data needs to be analyzed with any of the many available programs.[12] In this work, XDAP software[13] is used to analyze the EXAFS data. The first step involved in the data analysis is to subtract the monotonically decreasing background. Then the edge position is determined, and

afterward the atomic background. This atomic background is subtracted and spectrum is normalized. In the last step, the EXAFS data is fitted using the references to obtain the above-mentioned parameters.

2.3.1.1 Experimental

XANES and EXAFS spectra collected during CO oxidation for different supported platinum catalysts, as shown in chapter 6 of this thesis, were collected at the X10DA (superXAS) beamline at the Swiss Light Source, Villigen, Switzerland. Energy scans were performed with a Si-111 double crystal monochromator. Beam size was approximately 100 μm by 115 μm. Spectra were collected either in fluorescence or transmission geometry depending on the support. The first ionization chamber was filled with helium to detect the initial intensity; the second ionization chamber with a mixture of helium and nitrogen to detect the transmitted x-rays. A platinum foil was placed between the second ion chamber and a silicon diode for internal energy calibration. In fluorescence mode, a 13-channel Germanium detector was used. EXAFS data analysis was performed using standard procedure as explained. Previously generated reference files[14] were used to fit the EXAFS data. These were generated from the known unit cell parameters of platinum metal and platinum oxide using Atoms,[15] calculated using the FEFF8 code[16] and fitted to actual XAS measured data of platinum foil and platinum oxide.

2.3.2   Quick EXAFS (QEXAFS)

The dynamic nature of a catalytic process requires the collection of XAS spectra with high repetition rate in the order of a fraction of seconds. In the conventional XAS experiment, the data collection requires 15-30 min for one full EXAFS scan. In this conventional step-by-step method of data collection, the typical integration time for a single data point is 1 sec. The monochromator is then moved to the next position for the adjacent energy and the data collection is delayed by 0.5-1 sec considering the settling of the mechanical vibrations. The movement of monochromator itself requires time. These time requirements to move the monochromator mechanics and wait for mechanical vibrations to settle as well as to read the data by the detectors, lead to a long duration for a single EXAFS spectrum. Reducing the time required to move between two successive data points does not help in achieving a good spectrum because it leads to decreased signal to noise ratio because of mechanical instabilities and non-reproducibility of monochromator position. Due to these limitations, there has been extensive work done to

improve the time resolution of XAS technique for last three decades. The excellent work based on energy dispersive method (EDEXAFS) allows the collection of all the data points parallel in energy and has resulted in time resolutions of even 10 ms.[17] There has been significant effort done in this field, which resulted in widening the possibilities of EDEXAFS to make it a well-established tool to time-resolved studies.[18] However, the experimental difficulties with the basic setup and detector system of EDEXAFS and its non-capability of performing fluorescence detection limit its use for diluted samples.

A different approach, known as quick EXAFS (QEXAFS), is to use the standard double crystal monochromator with a stepper motor driven goniometers to achieve the required time resolution.[19] The goniometers continuously move and allow the collection of an EXAFS scan in less than a second. The easy operation and the capability of QEXAFS to use the fluorescence detection make this technique a vulnerable tool for time-resolved studies in catalysis. The improvements in this method have been achieved in the last decade with the use of piezo driven tilt tables for fine tuning the Bragg angle.[20] One typical movement, or oscillation, of monochromator fixed with the goniometer results in measurement of two absorption spectra. The time resolution of QEXAFS can be tuned by changing the frequency of these oscillations of goniometers. In this thesis, the use of QEXAFS allowed the determination of structure of platinum catalysts during the "ignition" process and during oscillating conditions of CO oxidation as described in Chapter 5 and 8 respectively of this thesis. QEXAFS experiments were carried out at the superXAS beamline located at Swiss Light Source (SLS), Villigen, Switzerland. The ring current was approximately 400 mA and operated in top-up mode. The polychromatic radiation from a superbend magnet, with a magnetic field of 2.9 Tesla and critical energy of 11.9 keV, was monochromatized using a channel cut Si(111) crystal in the QEXAFS monochromator.[19] The X-ray beam measured 1 mm horizontal and 0.1 mm vertical at the sample position; the total flux was about $3*10^{12}$ photons/s. The energy scale was calibrated with a platinum foil. Spectra were collected in transmission mode using two ionization chambers filled with air. For absolute energy calibration, the absorption of a platinum foil was always measured simultaneously between the second ionization chamber and a photo diode. The QEXAFS monochromator was oscillating at one Hz, resulting in two spectra per second. Thus, QEXAFS spectra were collected with a time resolution of 0.5 seconds, during ignition and extinction. Fitting of XAS spectra was done as explained in section 2.3.1, after averaging 100 spectra, with k ranging from 2.5 to 13.0 1/Å, and inter-atomic distance

ranging from 1.0 to 3.5 Å, with k^3 weighting for reduced and k^2 weighting for oxidized platinum.

2.4 X-ray emission spectroscopy

Hard X-rays make XES one of the best techniques for studying the electronic structure of catalysts, element specifically, under real reaction conditions. In contrast to XAS, XES provides information about the occupied orbitals, which is beneficial to complete the determination of the electronic structure of the catalysts and to monitor the change in the valence band of the metal during the reaction. In an XES experiment, excitation can be achieved at certain energy and the energy-dispersive X-ray emission can be determined by spectrometers based on perfect crystal Bragg optics.[5,41,21] Depending on the excitation energy, XES spectra are dependent on or independent of the incident energy, i.e. resonant or non-resonant XES, which are discussed below. The general principle of detecting the fluorescence energy of photons, emitted after filling the core hole with valence electrons, is the same for both resonant and non-resonant XES.

2.4.1   Resonant XES and RIXS

After excitation of an electron from a core level such as 1s, in the case of the K edge, and 2p or 2s, in the case of the L edge, a core hole is generated with a specific life-time broadening. This broadening determines the width of the XAS spectra. The electrons from upper levels decay and fill the core hole, resulting in emission of Auger electrons and fluorescence radiation. With XES, the emitted fluorescence energy is recorded by a high-energy resolution spectrometer. The process, during which the fluorescence energy emitted after the filling of the core hole becomes a function of the incident energy, is referred to as resonant XES or RIXS.[41a,22,23] A RIXS plane is obtained when the incident energy is tuned across an absorption edge, the electronic states are resonantly excited and decay, and the fluorescence is detected in a energy-dispersive manner.[41a] The process is described theoretically by the Kramers-Heisenberg scattering formula.[22b,24] Scheme 2.1 illustrates the total energy of the RIXS process and the orbital states. As stated above, the RIXS process is a combination of XAS and XES. After absorption of an X-ray with an incident energy $\Omega = h\nu_1$, the ground state electronic configuration is excited into the intermediate state, representing a configuration where the hole is in the core level. This represents the XAS process. Filling the core hole with an electron from one of the upper orbitals generates the X-ray fluorescence with energy $\omega = h\nu_2$. A final

state is reached with a hole in the upper orbital. The life-time broadening of this state is less than that of the initial XAS process. This phenomenon is used to record spectra with reduced life-time broadening and higher energy resolution, HERFD XAS,[5,41,21] as explained above. The difference in the energy of the incident photon and that of the fluorescence is the energy that is left in the system, the final state energy or energy transfer ($\Omega - \omega$). These energy diagrams are often translated into contour plots (RIXS planes).
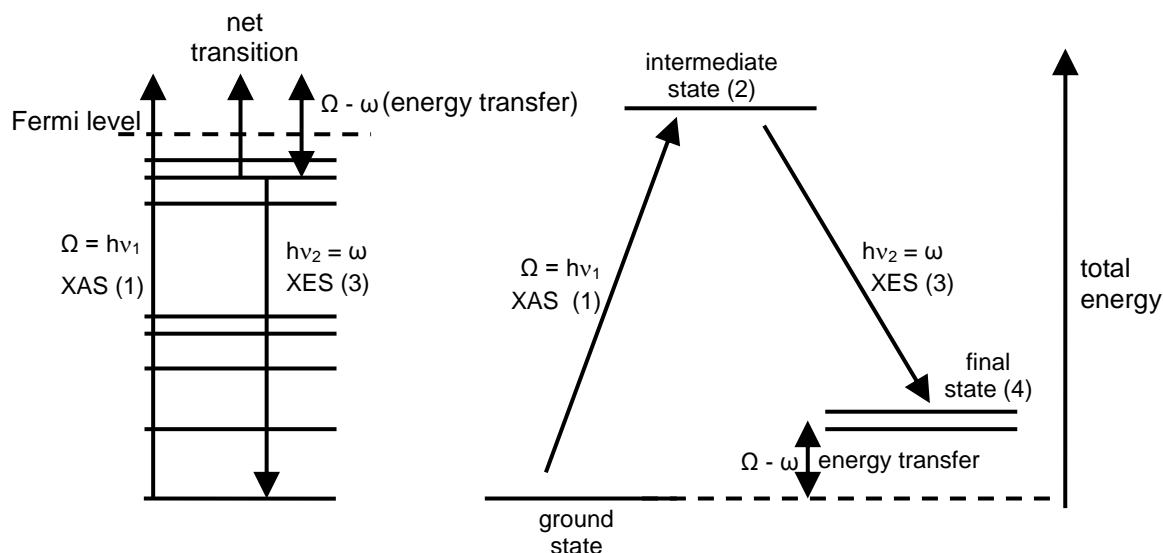
Scheme 2.1: Orbitals (left) and energy levels (right) showing (1) absorption of an X-ray with incident energy (Ω), (2) generation of the intermediate state, and (3) emission of photon with emission energy (ω). The final state (4) results in energy transfer ($\Omega - \omega$).

Figure 2.2 shows the 2p-5d RIXS plane of platinum(IV) chloride (5d transition metal). The RIXS plane clearly shows the two features along the final state energy axis, separated by 3.5 eV. It is noteworthy that RIXS spectra are influenced by the absorption spectral features,[5,25] because the $2p_{3/2}$ life-time broadening extends along the incident energy of the RIXS plane. This broadening is a fundamental physical property and cannot be eliminated or reduced. From the RIXS plane, different line plots can be deduced along the incident energy axis, energy transfer (final state energy) axis, and along the diagonal. RIXS is one of the most powerful tools for studying the electronic structure of the transition metal complexes.[26] RIXS is a bulk-sensitive and charge-neutral process, which can be efficiently used to provide site-selective information.[27]
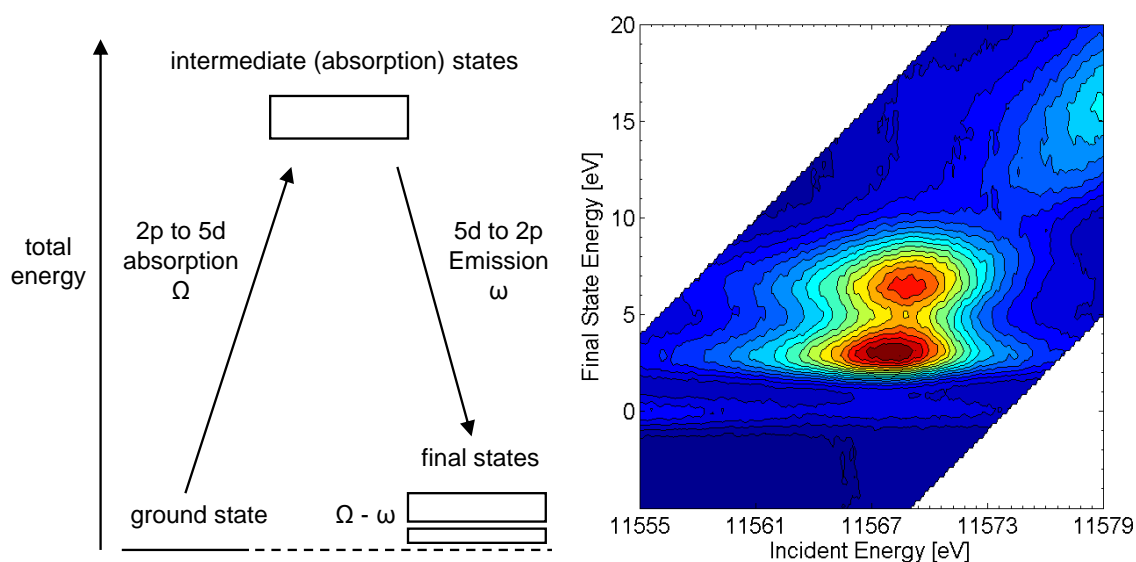
Figure 2.2: Total energy with incident and emitted photons (left) and RIXS plane of platinum chloride (right).

RIXS relies on hard X-rays and thus, does not require vacuum. Therefore, pressure does not restrict the application of this technique, making it the perfect tool for catalysis research.[28] 1s-2p RIXS has been successfully employed by excitation in the K pre-edge region in 3d transition metals to obtain L edge-like spectra5 and provide even more information about the electronic structure than L edge XAS.[23] Thus, RIXS enables the determination of the electronic structure of 3d transition metals with hard X-rays, which has until now been possible only by soft X-ray L edge spectroscopy.[29]

RIXS has been successfully applied to determine the bonding orbitals and change in the d-DOS of the metal after adsorption of reactants, such as CO, in case of 5d elements, such as platinum.[28c] Traditionally, XPS[30] of the valence band and UPS[31] are used to probe the structure of the valence band. However, these methods generally require high vacuum, but generally have better energy resolution than RIXS. In situ RIXS has shown its potential for catalytic studies for real catalysts such as alumina-supported platinum catalysts.[28c] The broadened energy distribution in the RIXS planes and a gap between the elastic peak and the occupied states that form after adsorption of CO clearly show that the electronic structure of platinum changes after adsorption of CO. As the gap opening is related to the shifting of the centre of d band away from the Fermi level, it renders the platinum catalyst to weaker adsorption of reactants.[32] In situ RIXS has been applied to determine the electronic structure of various catalysts used in the research presented in chapter 4.

For the RIXS experiments in this thesis, a total energy bandwidth (incident energy convoluted with emission detection) of 1.5 eV was achieved with the (931) Bragg reflection of one spherically bent Si crystal (bending radius R=1000 mm, crystal diameter d=100 mm). A Canberra silicon photodiode was mounted to measure the total fluorescence simultaneously with the HERFD XAS. The intensity of the elastic peak in RIXS was reduced using a scattering angle of 90 degrees. The elastic peak was used to determine the absolute energy along the charge transfer direction, i.e. the RIXS planes were shifted such that the elastic peak appears at zero charge transfer.

2.4.2 *Non-resonant XES*

When the energy of the incoming X-ray is high enough to excite the electron from the core level, well above the Fermi level, it is specifically referred to as non-resonant XES.[41a,23,33] The nomenclature of the fluorescence line depends on the energy level of the electron, which fills the core hole (Scheme 2.2). The intensity of these fluorescence lines is different from each other. In 3d transition metals, the $K\alpha$ lines are the most intense. Generally, spin-orbit splitting is not strong enough to separate the 3p energy levels. As a result, the $K\beta_1$ and $K\beta_3$ lines merge and are visualized as a single peak,[41a,34] the $K\beta_{1,3}$ fluorescence line, which is symmetric or asymmetric depending on the transition metal and the type of ligand.[35] Furthermore, there is a small feature at the lower side of the fluorescence energy, known as the $K\beta'$ line or feature, which in 3d transition metals is assigned to the exchange interaction between 3p and 3d energy levels.[41b,36] Therefore, this feature is rarely, if at all, seen in the compounds with a small valence spin, which further weakens the 3p and 3d exchange interaction. This explains why the $K\beta'$ feature is not observed in $K_3Fe(CN)_6$ but is observed, with significant intensity, in Fe_2O_3. $K\beta_{1,3}$ and $K\beta'$ are collectively referred to as the $K\beta$ main lines. Because of this 3p and 3d exchange interaction, the $K\beta$ main fluorescence lines are considered to be an indirect probe of the valence electron configuration in the case of 3d transition metals. Different studies have shown the strong potential of measuring the $K\beta_{1,3}$ fluorescence lines to characterize the oxidation state showing an even better correlation with the oxidation state compared to XANES, which is a standard tool for probing the oxidation state.[37] $K\alpha$ fluorescence lines, which are approximately eight times stronger than the $K\beta$ main lines, show strong splitting of the $K\alpha_1$ and $K\alpha_2$ lines due to spin-orbital splitting of the 2p levels. Because the interaction of the 2p levels is weaker than that of 3p with the valence levels, the $K\alpha$ fluorescence lines are a weaker probe of

the valence electron configuration in the case of 3d transition metals compared to the Kβ main fluorescence lines.
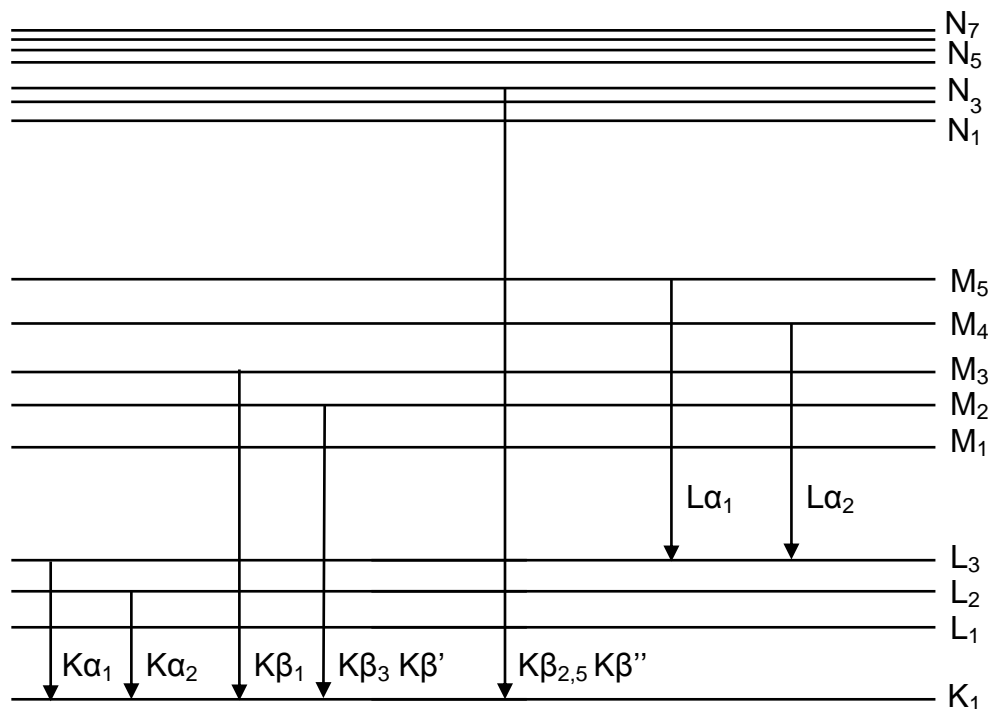
Scheme 2.2. Energy levels and different fluorescence emission lines.[38]

The fluorescence after the decay of an electron from the valence levels of 3d transition metals in order to fill the hole in the core level is $K\beta_{2,5}$ and Kβ'', collectively referred to as Kβ satellite lines.[41a] $K\beta_{2,5}$ indicates the energy of the Fermi level and the Kβ'' feature in transition metal complexes and originates from transitions from the ligand 2s energy levels to the transition metal 1s level.[41,39,40] As these lines are directly influenced by the valence electron configuration, they are particularly useful for determining the valence electron configuration of 3d transition metals. This, however, is at the expense of sensitivity, because the intensity of the Kβ satellite lines is more than 100 times weaker than that of the Kα fluorescence lines. It is the strong sensitivity of these Kβ'' lines, which makes XES superior to EXAFS in discriminating among ligands with a similar atomic number. To measure the weak $K\beta_{2,5}$ and Kβ'' lines, an X-ray source with high flux and brilliance is required. Third-generation synchrotrons now produce such X-rays, and these methods have developed rapidly.

2.4.3 High-energy resolution fluorescence detected X-ray absorption spectroscopy (HERFD XAS)

XAS, as explained above, is employed regularly to study the unfilled electronic states above the Fermi level. In a conventional XAS experiment, one monitors the transmitted photons or the radiative and/or non-radiative decay of the sample, while scanning the incident photons. Fluorescence detection is applied to diluted samples which show too little absorption of incoming photons by the element of interest to enable detection of an absorption edge in the transmission signal. The use of Ge detectors with a higher energy resolution than photo-diodes at third-generation synchrotrons with high flux has revealed the structure of diluted samples. There is a limit to the energy resolution set by the life-time broadening of the core hole in the excited state. To achieve better resolution, it is necessary to circumvent this limitation. This is possible by the selective detection of a fluorescence decay channel, which has a core hole with a longer life-time and, thus, less broadening. This effectively leads to spectra with a higher energy resolution and sharper features.[41,42] Scheme 2.3 illustrates the spectral sharpening of HERFD XAS, showing the life-time broadening of the Pt $2p_{3/2}$ core level at around 5 eV.[43] The same absorption, which represents the unoccupied states above the Fermi level, can be probed by monitoring a selective fluorescence line such as $L\alpha_1$ ($h\nu_2$ in Scheme 2.3) which leaves a core hole with a longer life-time and, thus, less broadening (right hand side of Scheme 2.3). This technique is efficient for the fifth row elements of the periodic table, because the final state effects are almost negligible due to the delocalized character of 5d electrons. Care should be taken in the event that the final state effects in resonant excitations close to the Fermi level are significant, because they may result in features in the HERFD scans that may not be real.[44,45] Therefore, in case of 3d transition metal complexes, special attention should be given to interpreting the spectra, because the interactions in the final state are not always weak in the case of the K fluorescence lines. A full theoretical description provides valuable electronic structural information. An improved theoretical description is required to interpret these data. Theoretical calculations such as multiplet calculations and FEFF, enable the verification of the features in the HERFD spectra, as has been successfully demonstrated.[5,46,47]

Another important advantage of HERFD XAS is that the selective detection of a fluorescence decay channel is element-specific. Thus, HERFD XAS can collect EXAFS spectra with extended an k range, which would be otherwise impossible because of the

undesired edges that arise from another element. One of very few examples is the collection of Mn K edge EXAFS in the multiprotein PS II complex.[48] The Fe K edge arises in the EXAFS region of the Mn K edge and limits the distance resolution of EXAFS. HERFD XAS enables the collection of spectra without the Fe edge, which results in better distance resolution and greater precision in the number of metal-metal scattering pairs.
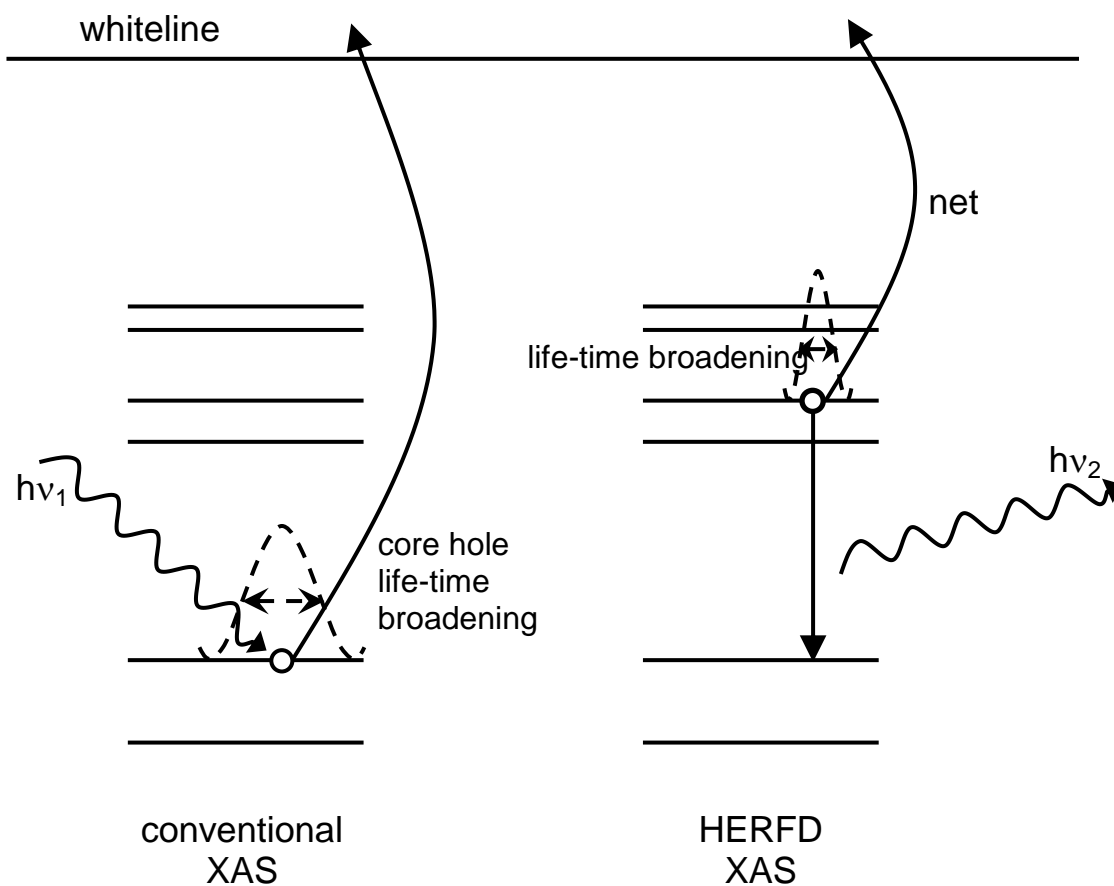
Scheme 2.3: Orbitals showing electronic transitions and life-time broadening.

The studies of the adsorption of CO on the catalyst surface aid in understanding the key steps in CO oxidation catalysis. HERFD XAS has the potential to identify mode of bonding of CO to alumina-supported platinum catalysts.5 The calculations based on the FEFF code[49] aid in interpreting the HERFD XAS spectra and are shown to enable the determination of the dominant CO adsorption configuration on nano-sized platinum and the orbitals involved in the bonding.5 In this thesis, HERFD XAS is combined with infra red (IR) spectroscopy and kinetic measurements during CO oxidation over alumina-supported platinum catalysts to give information about the active species in the reaction.

HERFD XAS experiments conducted for the work presented in this thesis were carried out at beamline ID 26 at the European Synchrotron Radiation Facility (ESRF), Grenoble, France. The electron energy was 6.0 GeV, and the ring current varied from 50 to 90 mA. Two u35 undulators were used to perform the measurements. The x-ray beam measured 0.3 mm horizontal and 1 mm vertical; the total flux was $5 * 10^{12}$ photons/s. The energy was calibrated with a platinum foil. The incident energy was selected by means of a pair of Si(311) crystals with an energy bandwidth of 1.5 eV at the Pt L_3-edge. Higher harmonics were suppressed by using two mirrors, one coated with Pd and the other with Cr, working at 3 mrad in total reflection. High energy resolution emission detection was carried out with a horizontal-plane Rowland circle spectrometer that was tuned to the Pt $L\alpha_1$ (9442 eV) fluorescence line. A total energy bandwidth (incident energy convoluted with emission detection) of 1.8 eV was achieved with the (660) Bragg reflection of one spherically bent Ge wafer (R=1000 mm). This is below the HERFD lifetime broadening of 2.2 eV when based on the Pt $L\alpha_1$ line. The $2p_{3/2}$ core hole lifetime broadening is 5.2 eV. The detector was an avalanche photodiode (APD). A Canberra silicon photodiode was mounted to measure the total fluorescence simultaneously with the HERFD XAS.

2.5 Infra red (IR) spectroscopy

IR spectroscopy is an enormously useful and widespread technique to determine the structure of catalysts and the adsorbed species on catalyst surfaces. The ease of sample preparation, data collection and analysis, and the ability to perform in situ experiments has caused the use of IR spectroscopy in the field of catalysis for more than five decades. The main advantage of performing in situ IR experiments lies in the fact that the species on the catalyst surface can be time- resolved monitored. The gas phase species can also be probed. There are two main ways of performing an IR experiment: collection of light transmitted through the sample, or collection of light diffused by the surface of the sample. The main advantage of using transmission IR spectroscopy over diffusive-reflectance spectroscopy is the quantitative analysis. Also, in diffusive-reflectance spectroscopy, the band intensities are dependent on the grain size and the reaction conditions. Fortunately, most of the commonly used supports in catalysis are transparent over the wide region of infra red.

In this thesis, the IR experiments are performed using transmission mode, where the catalyst is pressed in the form of a self-supporting pellet. This pellet is then placed in front of IR beam as depicted in Figure 2.3. The transmittance, T, of the sample is given as:

$$T = I/I_0 \tag{8}$$

I_0, and I are the intensities of the incident and transmitted light. T can be expressed using Lambert's Beer law as following:

$$T = e^{-\varepsilon cd} \tag{9}$$

ε = extinction co-efficient

c = concentration of the absorber

d = sample thickness

Often, the infra red spectra as expressed in terms of absorbance, A, which is related to transmittance, T, as following:
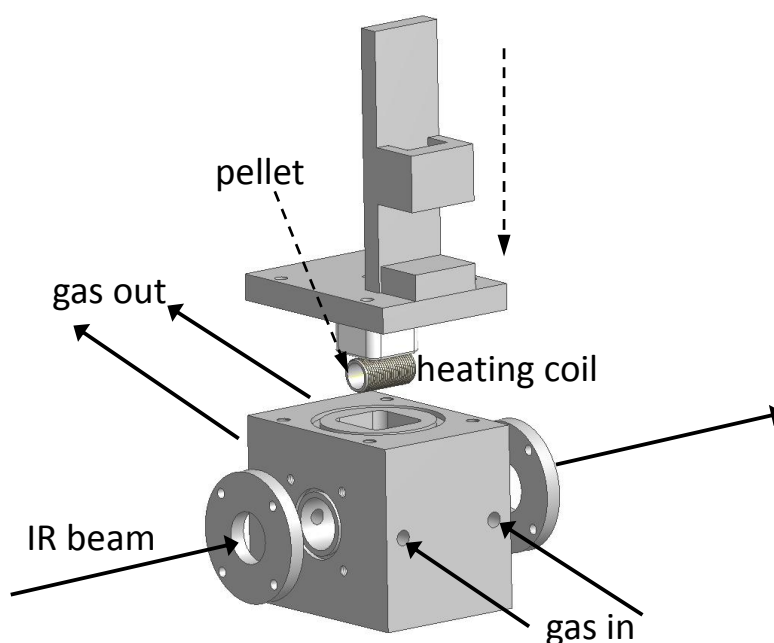
$$A = -\ln(T) = \varepsilon cd \tag{10}$$

Figure 2.3: IR cell used for in situ studies.

The development of Fourier-transform infra red (FT-IR) spectroscopy[50] greatly improved sensitivity. The principle is based on interference of radiation between two IR beams, which are generated by the use of a beam splitter and mirrors, to yield an ''interferogram'', which is a function of the change of the path length between the two beams. To obtain the IR spectrum, the interferogram is subject to Fourier transform. The main advantages of using FT-IR spectroscopy are increased signal to noise ratio and the ability of fast spectra recording.

In situ IR measurements presented in chapter 4, were made using a Bio-Rad spectrometer and using a cell as shown in Figure 2.3. The detector was a cryogenic mercury cadmium telluride (MCT) with a maximum beam divergence of 1.3 milliradians. The measurements were done on a self-supporting catalyst pellet of 15 mg. The IR beam transmitted through the sample. The catalyst was pretreated in 5% hydrogen in helium at 473 K before each experiment and cooled down in a flow of pure helium. The background spectrum was collected with catalyst at 313 K in a flow of 5% O_2 in He. The catalyst was then exposed to the reaction mixture with O_2 to CO ratio of one. The measurements were done at a constant total flux of 30 ml/min through the reactor corresponding to a space velocity of about 64,000 h^{-1}. The pellet was heated at a rate of 2 K/min. The spectra were collected in continuous mode with time resolution of 5 sec. In chapter 8, during the kinetic oscillations of CO oxidation, after taking the background spectrum with catalyst in a flow of pure He at 313K, the catalyst was exposed to the reaction mixture with O_2 to CO ratio of 19:1. The infra red spectra were collected with a time resolution of one second. A heating rate of 2 K/min and a cooling rate of 1 K/min during the CO oxidation were used.

2.6 Kinetic measurements

The experiments were conducted using the flow scheme as shown in Figure 2.4. The setup served as a combined set up for spectroscopic and kinetic measurements. The gas flow rates were controlled using computer controlled mass flow controllers (MFCs). A four-port valve (4 PV) was used to make sure that at no point during the experiment, oxygen and hydrogen were mixed for CO oxidation without presence of H_2. The reactor cell,[51] operating as a plug-flow reactor with a diameter of 1.6 mm, was used as a transmission/fluorescence cell with aluminum windows. The reactor cell is shown in Figure 2.5. The exhaust of the reactor was connected to a mass spectrometer to monitor the outlet gases to calculate carbon monoxide conversion and corresponding rate of

reaction. The catalyst, with a specific mesh size was used for each experiment. The temperature of the reactor was controlled by an embedded thermocouple in the reactor housing.

The traces for CO, O_2, and CO_2, recorded by the mass spectrometer in terms of current, were divided by the helium signal for normalization. They were further processed to conversion curves against time or temperature. Conversion in carbon monoxide, X_{CO}, was defined as:

$$X_{CO} = \frac{\varphi_{v,CO,in} - \varphi_{v,CO,out}}{\varphi_{v,CO,in}} \tag{11}$$

$\varphi_{v,CO,in}$ = the flowrate of CO at the inlet of the reactor

$\varphi_{v,CO,out}$ = the flowrate of CO at the outlet of the reactor

The inlet flowrate was controlled by the mass flow controller. The outlet flowrate was derived from a calibration line assuming that the normalized signal at maximum conversion corresponded to 100% conversion, and that the normalized signal in the absence of conversion was the flowrate set at the inlet. The rate of CO_2 production was calculated from the CO conversion afterwards.

The selectivity toward CO oxidation, S, in case of PROX reaction, was calculated using the following formula:

$$S = \frac{p_{CO_2}}{p_{CO_2} + p_{H_2O}} \tag{12}$$

p_{CO_2} = partial pressure of CO_2

p_{H_2O} = partial pressure of H_2O

For first heating trajectory in Pt/Ce(La)O_x (Figure 9.4 in chapter 9), p_{CO2} was calculated from the mass spectrometer signal of CO assuming that in the start of the reaction, there is no conversion in CO and at 673 K, mass spectrometer signal corresponds to 100% conversion in CO. p_{H2O} was calculated from H_2O signal assuming that H_2O production started around 460 K and at around 550 K, maximum H_2O production occurred from H_2 oxidation. Similarly, selectivity was calculated for first heating trajectory in L-

Pt/Ce(La)O$_x$. For all other heating and cooling trajectories, the selectivity was calculated from the signal of CO$_2$ in the respective trajectory relative to the signal of CO$_2$ in the first heating trajectory.
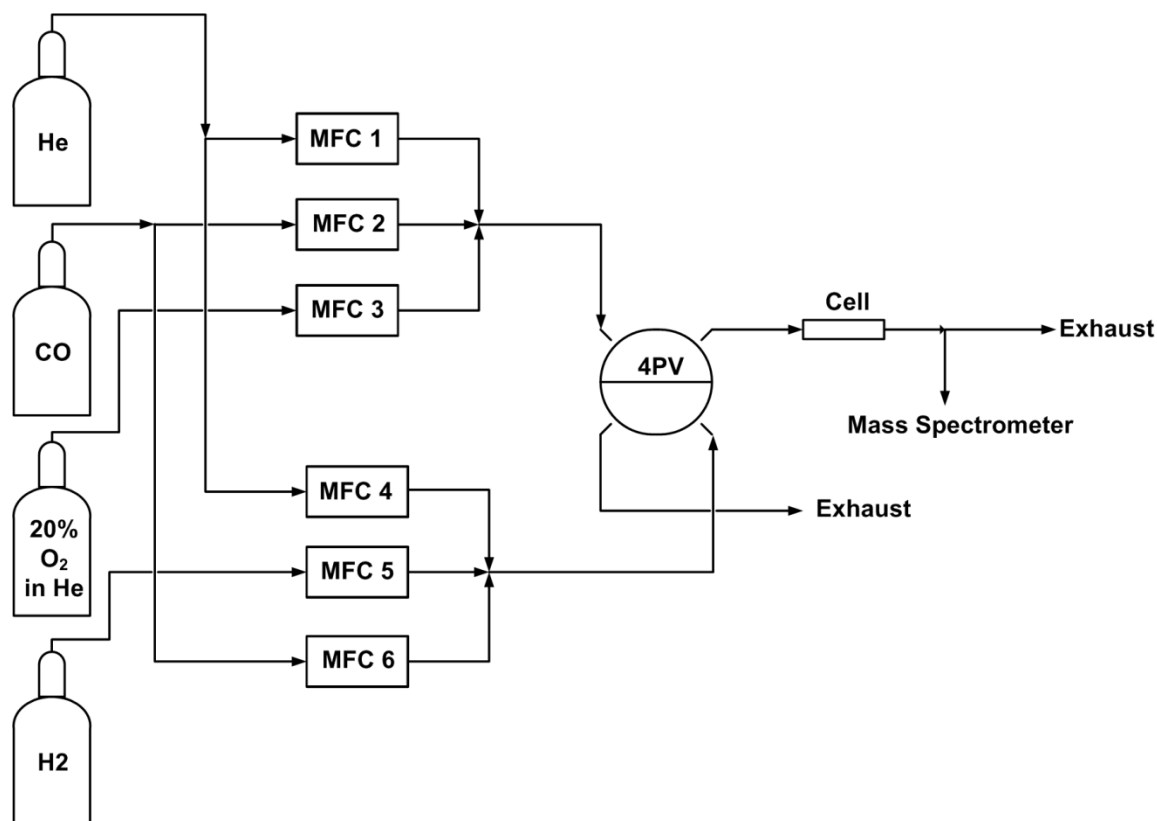

Figure 2.4: Flow scheme of setup used for CO oxidation (MFC: mass flow controller, 4PV: four port valve).
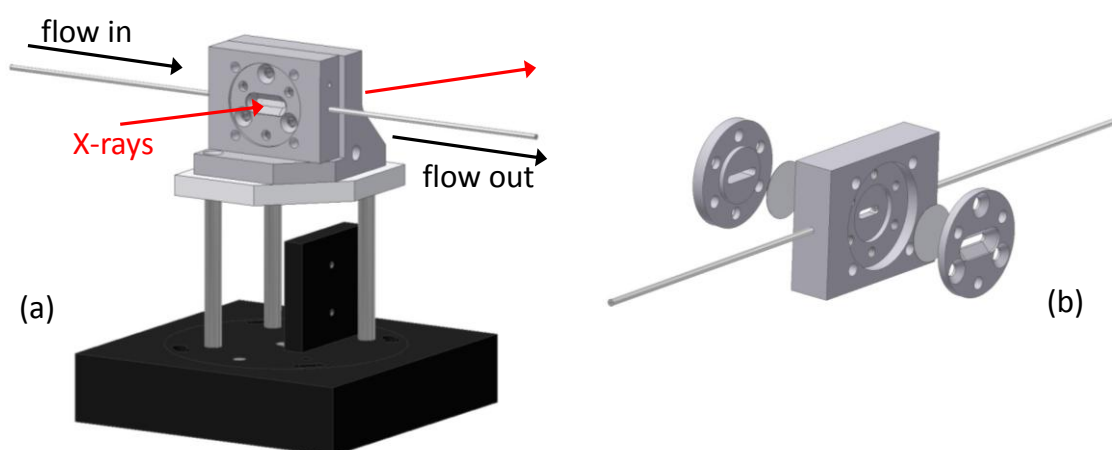

Figure 2.5: (a) Reactor cell with the heating plate at the back, and (b) reactor cell with its different components.

Chapter 2

References

1 G. C. Bond, in Heterogeneous Catalysis: Principles and Applications, Claredon Press, Oxford (1987).

2 F. Krumeich, "Electron Microscopy", http://www.microscopy.ethz.ch.

3 (a) D. E. Ramaker, D. C. Koningsberger, Phys. Rev. Lett., 89 (2002) 139701; (b) A. L. Ankudinov, J. J. Rehr, J. J. Low, A. R. Bare, Phys. Rev. Lett., 89 (2002) 139702.

4 M. Teliska, V. S. Murthi, S. Mukerjee, D. E. Ramaker, J. Phys. Chem. C, 111 (2007) 9267.

5 O. V. Safonova, M. Tromp, J. A. van Bokhoven, F. M. F. de Groot, J. Evans, P. Glatzel, J. Phys. Chem. B, 110 (2006) 16162.

6 E. Bus, D. E. Ramaker, J. A. van Bokhoven, J. Am. Chem. Soc., 129 (2007) 8094.

7 http://leonardo.phys.washington.edu/feff/

8 http://www.aquila.infn.it/gnxas/

9 J. J. Rehr, R. C. albers, Rev. Mod. Phys., 72 (2000) 621.

10 F. de Groot, Coord. Chem. Rev., 249 (2005) 31.

11 G. G. Li, F. Bridges, C. H. Booth, Phys. Rev. B, 52 (1995) 6332.

12 http://ixs.iit.edu/catalog/XAFS_Programs

13 http://www.xsi.nl

14 E. Bus, J. A. van Bokhoven, J. Phys. Chem. C, 111 (2007) 9761.

15 B. Ravel, J. Synch. Rad., 8 (2001) 314.

16 A. L. Ankudinov, B. Ravel, J. J. Rehr, S. D. Conradson, Phys. Rev. B, 58 (1998) 7565.

17 (a) R. P. Phizackerley, Z. U. Rek, G. B. Stephenson, S. D. Conradson, K. O. Hodgson, T. Matsushita, H. Oyangi, J. Appl. Cryst. 16 (1983) 220; (b) E. Dartyge, C. Depautex, J. M. Dubuisson, A. Fontaine, A. Jucha, P. Leboucher, G, Tourillon, Nucl. Instr. And Meth. A246 (1986) 452.

18 (a) S. Pascarelli, T. Neisius, S. de Panfins, J. Synchrotron Rad., 6 (1999) 1044; (b) S. Pascarelli, T. Neisius, S. de Panfins, M. Bonfim, S. Pizzini, K. Mackay, S. David, A. Fontain, A. San Miguel, J. P. Itie, M. Gauthier, A. Polian, J. Synchrotron Rad., 6 (1999) 146.

19 (a) R. Frahm, Nucl. Instrum. Methods Phys. Res. A, 270 (1988) 578; (b) J. Stötzel, D. Lützenkirchen-Hecht, E. Fonda, N. de Oliveira, V. Briois, R. Frahm, Rev. Sci. Instr.,79 (2008) 083107.

20 M. Richwin, R. Zaeper, D. L-hecht, R. Frahm, J. Synchrotron Rad. 8 (2001) 354.

21 K. Hämäläinen, D. P. Siddons, J. B. Hastings, L. E. Berman, Phys. Rev. Lett., 67 (1991) 2850.

22 (a) J. Nordgren and E. Z. Kurmaev, in Soft X-Ray Emission Spectroscopy, J. Electron Spectrosc. Relat. Phenom., 110-111 (2000) 1; (b) A. Kotani, S. Shin, Rev. Mod. Phys., 73 (2001) 203.

23 F. de Groot, Chem. Rev., 101 (2001) 1779.

24 F. Gel'mukhanov, H. Ågren, Phys. Rep. Rev. Soc. Phys. Lett., 312 (1999) 91.

25 P. Carra, M. Fabirizio, B. T. Thole, Phys. Rev. Lett., 74 (1995) 3700.

26 (a) W. A. Caliebe, C. C. Kao, J. B. Hastings, M. Taguchi, T. Uozumi, F. M. F. de Groot, Phys. Rev. B, 58 (1998) 13452; (b) P. Glatzel, U. Bergmann, W. W. Gu, H. X. Wang, S. Stepanov, B. S. Mandimutsira, C. G. Riordan, C. P. Horwitz, T. Collins, S. P. Cramer, J. Am. Chem. Soc., 124 (2002) 9668; (c) P. Glatzel, U. Bergmann, J. Yano, H. Visser, J. H. Robblee, W. Gu, F. M. F. de Groot, G. Christou, V. L. Pecoraro, S. P. Cramer, V. K. Yachandra, J. Am. Chem. Soc., 126 (2004) 9946; (d) F. M. F. de Groot, P. Glatzel, U. Bergmann, P. A. van Aken, R. A. Barrea, S. Klemme, M. Hävecker, A. Knop-Gericke, W. M. Heijboer, B. M. Weckhuysen, J. Phys. Chem. B, 109 (2005) 20751.

27 (a) K. Hämäläinen, C.C. Kao, J. B. Hastings, D. P. Siddons, L. E. Berman, V. Stojanoff, S. P. Cramer, Phys. Rev. B, 46 (1992) 14274; (b) X. Wang, F. M. F. de Groot, S. P. Cramer, Phys. Rev. B, 56 (1997) 4553.

28 (a) J. Singh, R. C. Nelson, B. C. Vicente, S. L. Scott, J. A. van Bokhoven, Phys. Chem. Chem. Phys., 12 (2010) 5668; (b) J. A. van Bokhoven, Phys. Chem. Chem. Phys., 12 (2010) 5502; (c) P. Glatzel, J. Singh, K. O. Kvashnina, J. A. van Bokhoven, J. Am. Chem. Soc., 132 (2010) 2555.

29 (a) G. van der Laan, B. T. Thole, G. A. Sawatzky and M. Verdaguer, *Phys. Rev. B*, 1988, **37**, 6587; (b) J. van Elp, G. Peng, B. G. Searle, S. Mitra-Kirtley, Y. H. Huang, M. K. Johnson, Z. H. Zhou, M. W. W. Adams, M. J. Maroney and S. P. Cramer, *J. Am. Chem. Soc.*, 1994, **116**, 1918; (c) H. X. Wang, C. Y. Ralston, D. S. Patil, R. M. Jones, W. Gu, M. Verhagen, M. Adams, P. Ge, C. Riordan, C. A. Marganian, P. Mascharak, J. Kovacs, C. G. Miller, T. J. Collins, S. Brooker, P. D. Croucher, K. Wang, E. I. Stiefel and S. P. Cramer, *J. Am. Chem. Soc.*, 2000, **122**, 10544.

30 (a) K. Siegbahn, C. Nordling, G. Johansson, J. Hedman, P. F. Heden, K. Hamrin, U. Gelius, T. Bergmark, L. O. Werme, R. Manne, Y. Baer, in ESCA Applied to Free Molecules, North-Holland, Amsterdam (1969); (b) S. Hufner, in Photoelectron Spectroscopy, Springer-Verlag, Berlin (1995); (c) N. Mårtensson, A. Nilsson, in Applications of Synchrotron Radiation: High Resolution Studies of Molecules and Molecular Adsorbates, ed. W. Eberhardt, vol. 35, Springer-Verlag, Berlin (1995).

31 S. D. Kevan, in Angle-Resolved Photoemission, Elsevier, Amsterdam (1992).

32 (a) B. Hammer, J. K. Nørskov, Surf. Sci., 343 (1995) 211; (b) B. Hammer, J. K. Nørskov, Nature, 376 (1999) 238.

33 F. M. F. de Groot, J. Electron Spectrosc., 676 (1994) 529.

34 U. Bergmann, P. Glatzel, F. De Groot, S. P. Cramer, J. Am. Chem. Soc., 121 (1999) 4926.

35 (a) G. Peng, F. M. F. de Groot, K. Hämäläinen, J. A. Moore, X. Wang, M. M. Grush, J. B. Hastings, D. P. Siddons, W. H. Armstrong, O. C. Mullins and S. P. Cramer, J. Am. Chem. Soc., 116 (1994) 2914; (b) P. Glatzel, U. Bergmann, F. M. F. de Groot, S. P. Cramer, Phys. Rev. B, 64 (2001) 045109.

36 K. Tsutsumi, H. Nakamori, K. Ichikawa, Phys. Rev. B: Condens. Matter Mater. Phys., 13 (1976) 929.

37 (a) S. D. Gamblin, D. S. Urch, J. Electron Spectrosc., 113 (2001) 179; (b) H. Visser, E. Anxolabehere-Mallart, U. Bergmann, P. Glatzel, J. H. Robblee, S. P. Cramer, J. J. Girerd, K. sauer, M. P. Klein, V. K. Yachandra, J. Am. Chem. Soc., 123 (2001) 7031; (c) S. A. Pizarro, P. Glatzel, H. Visser, J. H. Robblee, G. Christou, U. Bergmann, V. K. Yachandra, Phys. Chem. Chem. Phys., 6 (2004) 4864.

38 A. C. Thompson, D. T. Attwood, E. M. Gullikson, M. R. Howells, J. F. Kortright, A. L. Robinson, J. H. Underwood, K-Je Kim, J. Kirz, I. Lindau, P. Pianetta, H. Winick, G. P. Williams and J. H. Scofield, in X-ray data booklet, ed. A. C. Thompson and D. Vaughan, (2001).

39 U. Bergmann, C. R. Horne, T. J. Collins, J. M. Workman and S. P. Cramer, Chem. Phys. Lett., 302 (1999) 119

40 D. S. Urch, in Electron Spectroscopy: Theory, Techniques, and Applications, ed. C. R. Brundle and A. D. Baker, Academic Press, New York, vol. 3, pp. 1-39 (1979).

41 (a) P. Glatzel, U. Bergmann, Coord. Chem. Rev., 249 (2005) 65; (b) J. A. van Bokhoven, C. Louis. J. T. Miller, M. Tromp, O. V. Safonova, P. Glatzel, Angew. Chem. Int. Ed., 45 (2006) 4651.

42 F. de Groot, Coord. Chem. Rev., 249 (2005) 31.

43 J. C. Fuggle and J. E. Inglesfield, in Unoccupied Electronic States, Springer-Verlag, Berlin, (1992).

44 P. Carra, M. Fabirizio, B. T. Thole, Phys. Rev. Lett., 74 (1995) 3700.

45 P. Glatzel, M. Sikora, M. Fernandez-Garcia, Eur. Phys. J. Special Topics, 169 (2009) 207.

46 P. Glatzel, J. Singh, K. O. Kvashnina and J. A. van Bokhoven, J. Am. Chem. Soc., 132 (2010) 2555.

47 F. M. F. de Groot, M. H. Krisch, J. Vogel, Phys. Rev. B, 66 (2002) 195112.

48 J. Yano, Y. Pushkar, P. Glatzel, A. Lewis, K. Sauer, J. Messinger, U. Bergmann, V. Yachandra, J. Am. Chem. Soc., 127 (2005) 14974.

49 (a) A. L. Ankudinov, B. Ravel, J. J. Rehr, S. D. Conradson, Phys. Rev. B, 58 (1998) 998; (b) A. L. Ankudinov, C. Bouldin, J. J. Rehr, J. Sims, H. Hung, Phys. Rev. B, 65 (2002) 104107.

50 P.R. Griffiths, J. A. de Haseth, in Fourier Transform Infrared spectroscopy, Wiley, New York, (1986)

51 N. Weiher, E. Bus, B. Gorzolnik, M. Möller, R. Prins, J. A. van Bokhoven, J. Synchr. Rad., 12 (2005) 675.

Chapter 2

Chapter 3

Electronic structure of the valance band of platinum and gold compounds

Abstract

The electronic structure in various platinum and gold compounds was studied by means of hard X-ray absorption and resonant emission spectroscopy (resonant inelastic X-ray scattering (RIXS)) at the L_3-edge. The combination of the different techniques provides a comprehensive map of the occupied and unoccupied 5d density of states. The energy transfer in the RIXS experiments was tuned to only a few electron Volts resulting in the observation of electron excitations within the valence band. The experimental spectra were modeled using multiple scattering theory (FEFF8). In case of small gold particles, the d band was shifted toward lower binding energy in comparison to bulk gold.

Chapter 3

3.1. Introduction

Determining the electronic structure of materials is very important and essential to know their behavior. The physical and chemical properties of bulk materials change drastically when one refers to nano-size materials. When their dimension decreases below a certain size, they lose their metallic character, and / or show new optical, magnetic, and catalytic properties.[1] They are used in a variety of applications, such as sensoring, catalysis, and electronics. To understand structure-property relationships, the geometry and electronic structures of such particles or matter in general must be established.

There are many powerful techniques with their respective advantages and limitations for exploring the structure of matter. X-ray diffraction, which requires extended long-range order in the structure of the matter, is limited to provide information about the nanoparticles due to their small particle size. Altered electronic structures have been observed by X-ray and ultraviolet photoemission spectroscopy (XPS and UPS) by changes in the energy and structure of the bands.[2] The electronic structure of size-selected nanoparticles has been studied using scanning tunneling microscopy (STM).[3] X-ray absorption spectroscopy (XAS) is often used to determine the geometric structure of nano-sized metal particles. Extended X-ray absorption fine structure (EXAFS) spectroscopy provides the coordination geometry such as bond length and distance, which relate to particle size and shape. Analysis of the higher shells and multiple scattering paths provide insights into the three-dimensional structure of the particles.[4] The shape and intensity of the $L_{3,2}$ near-edge spectra of transition metals reflect the empty d density of states (DOS) and provide the electronic structure. The intensity of the white line in $L_{3,2}$ edge spectra varies with the number of holes in the d band.[5] The shape of the near edge provides information about the structure of the adsorption site of reactants on supported metal catalysts.[6] Using high-energy resolution fluorescence detected X-ray absorption spectroscopy (HERFD) near-edge spectra with much higher energy resolution can be obtained,[7] which enabled detection of changes in the d DOS after adsorption of carbon monoxide on an alumina-supported platinum catalyst.[8] Such experiment was performed on a working catalyst,[7c] which identified the structure of the catalytically active phase of a platinum catalyst.[9]

In a traditional XAS experiment, the absorption of X-rays as function of energy is determined. In such an experiment, the core hole is annihilated via Auger or fluorescence decay, which can be measured to detect the absorption signal. Alternatively, one can excite at constant energy and determine the fluorescence. A

chemical dependence may be revealed when the fluorescence emission is detected with an instrumental energy bandwidth that is on the order of the natural line broadening that is determined by the core hole lifetime.[7,8] This is called X-ray emission spectroscopy (XES). Such experiments are possible at X-ray beamline ID26 of the European Synchrotron Radiation Facility (ESRF) Grenoble, France. The chemical dependence in XES in 5d transition metals can be strongly enhanced by tuning the incident X-ray energy to the maximum of the 2p (L) absorption edge. Varying the excitation energy across an absorption edge while measuring the X-ray emission is called resonant inelastic X-ray scattering (RIXS) that can provide detailed electronic information. Variation of incident as well as emitted energy provides a two-dimensional energy distribution, the RIXS plane. XES and RIXS have been often applied to 3d metals.[7a,b,10] Recently, a study on platinum nanoparticles was performed.[11] Because only hard X-rays are involved, this experiment can, like HERFD, be performed under catalytic conditions unlike XPS and UPS, where generally high vacuum is required.
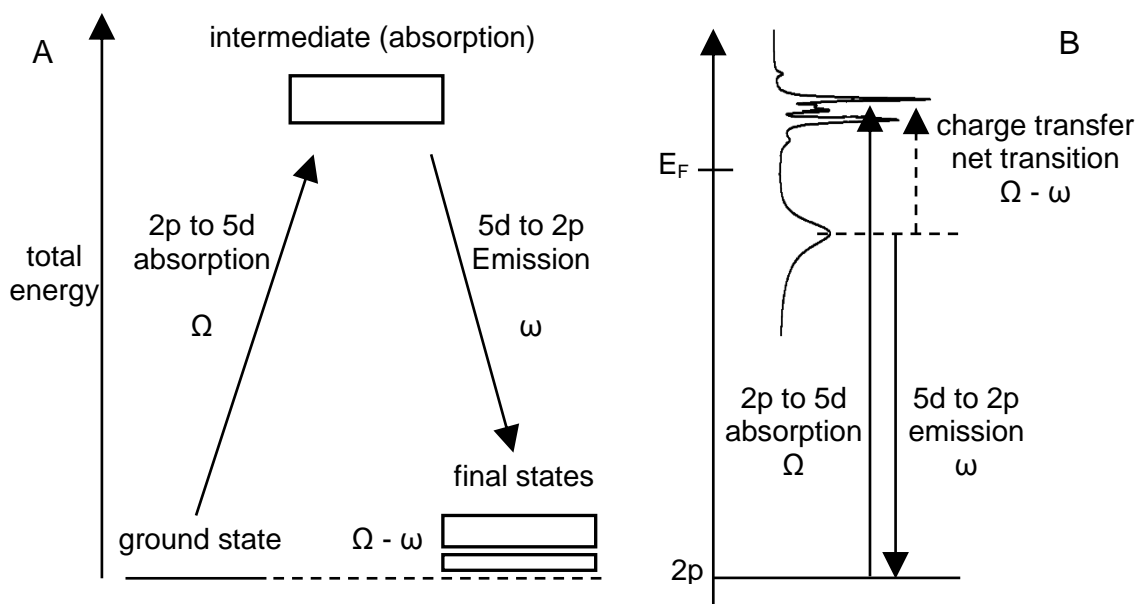

Figure 3.1: Energy schemes for resonant emission spectroscopy. Left: Total energy scheme with incident and emitted photons Ω and ω, respectively. The transferred energy is given by $\Omega - \omega$. Right: Single-electron scheme with transitions to and from the d-density-of-states around the Fermi energy E_F. The dotted line depicts the net transition within the valence shell as a result of the inelastic scattering process.

Figure 3.1 illustrates the electron transitions and energy levels that are relevant in 2p-valence resonant inelastic scattering on 5d elements. A total energy scheme is used in Figure 3.1A where the vertical axis denotes the total energy of the system. The energy Ω of an incident photon is absorbed by elevating a 2p electron into the 5d shell creating a core hole and excited electron. A photon with energy ω is emitted after filling of the 2p core hole by an electron from filled 5d. The energy transfer (final state energy) $\Omega - \omega$ denotes the energy that is deposited in the sample after the X-ray emission process. The net transition that occurs is from the 5d (filled) into the 5d (unfilled) as shown in the right panel of Figure 3.1. The total energy scheme allows for a correct energy balance and thus expresses the energy conservation law. A zero energy transfer is denoted a quasi-elastic transition and a finite energy transfer is called inelastic scattering. The single-electron picture (Figure 3.1B) depicts the electron levels that are mainly involved in the transitions.

Resonant X-ray emission is a charge-neutral process, i.e. no ionized species is created, if the absorption process is resonant into a bound state. The net excitation in the final state is a transition within the valence of a few electron Volts ($\Omega-\omega$). The 5d states are strongly delocalized and the excited electron will only weakly interact with the remaining electrons. Based on this assumption we can compare, with restrictions (*vide supra*), the experimental RIXS data to ionizing techniques such as photoelectron spectroscopy and non-resonant X-ray emission spectroscopy (XES) that also probe the filled 5d density of states.

In this chapter, Pt and Au L_3 edge XAS and resonant valence-to-core XES on platinum and gold compounds are presented and the full RIXS planes are reported. Using full multiple scattering calculations using the FEFF code,[12] the experimental spectra are reproduced. We will illustrate the possibilities and limitations of application of resonant emission spectroscopy to compounds and to nano-sized particles of 5d elements platinum and gold.

3.2 Experimental

Reference compounds, platinum(IV) oxide, platinum(IV) sulfide, platinum(IV) telluride, platinum(IV) chloride, platinum(II) ammonium nitrate, gold(III) hydroxide, and gold(I) sulfide were obtained as pure compounds from Sigma-Aldrich. Gold and platinum foils were obtained from Goodfellow. Gold nano-particles were supported on alumina using

incipient wetness impregnation as explained in section 2.1. X-ray spectroscopy experiments were carried out at beamline ID26 at the ESRF as explained in section 2.3.1. The analyzer crystal of radius of 50 mm was masked down to 30 mm to improve the energy resolution. The full RIXS planes were recorded for platinum foil, platinum(IV) oxide, platinum(IV) sulfide, platinum(IV) telluride, platinum(IV) chloride, platinum(II) ammonium nitrate, gold foil, gold(III) hydroxide, and gold(I) sulfide. The elastic peak extends as a horizontal streak through the plane. The intensity of the elastic peak arises mainly from non-element-specific Thomson scattering in the sample and therefore does not follow the platinum or gold absorption cross section. It serves as an absolute energy calibration because it references the zero energy transfer. Additionally, resonant valence-to-core emission spectra were collected at the excitation energy corresponding to the white line in the L_3 edge absorption spectrum. Such scans are part of the RIXS plane and were recorded to improve statistics in one line scan. X-ray absorption and resonant emission spectra were aligned by overlapping the elastic peak (corresponding to zero energy transfer) at the excitation energy in the valence-to-core emission spectrum with the energy of white line in L_3 edge absorption spectrum. The energy of the elastic peak maximum was then set to absolute zero energy.

Full multiple scattering calculations were performed using FEFF 8 code to interpret the XAS and XES data. The absorption spectra were calculated using the NOHOLE card. For the non-resonant emission spectra we obtained a better agreement between experiment and theory without the NOHOLE card (*vide infra*). The cluster sizes in the calculations for platinum foil, platinum(IV) oxide, platinum(IV) sulfide, platinum(IV) telluride, platinum(IV) chloride, gold foil, gold(III) oxide, and gold(I) sulfide were 135, 175, 80, 54, 64, 131, 161, and 175 respectively. The lifetime broadening in the XES calculations was reduced by 1 eV as compared to the tabulated value by using the EXCHANGE card. In case of platinum(IV) chloride, for calculation of absorption spectra, the Fermi Level was shifted by 3 eV towards lower binding energy. In case of gold(III) hydroxide, the calculations are done for gold(III) oxide.

3.3 Results

3.3.1 Platinum Compounds

Figure 3.2 shows the full RIXS planes for platinum foil, platinum(IV) oxide, platinum(IV) sulfide, platinum(IV) telluride, platinum(IV) chloride, and (f) platinum(II)

ammonium nitrate. The final state energy is plotted as function of the incident energy. The RIXS planes of all the compounds differed, which will be further illustrated by the resonant valence-to-core emission spectra (Figure 3.3). As explained above, the RIXS plane is a two-dimensional energy distribution plane. The resonant valence-to-core emission spectrum is a vertical cut through the RIXS plane at one fixed incident energy, which in this work was set to the white line in the metal L_3 absorption spectra. Figure 3.3 shows the experimental Pt L_3 edge absorption and resonant valence-to-core emission spectra of the platinum compounds. Characteristic features in the spectra are quantified and summarized in Table 3.1. The L_3 edge absorption spectrum of bulk platinum had a medium intense white line, because of the nominal orbital filling of $6s^1 5d^9$ with an almost filled 5d shell. The white line intensity increased with the oxidation state of the platinum and with electro-negativity of the ligand because electron density is removed from the 5d shell. All spectra showed characteristic peaks whose intensity and energy position varied for all compounds. The shape and energy position of the emission spectra also varied for all these compounds, reflecting the filled DOS that depends on the structure and type of ligands. An elastic scatter peak at the excitation energy of varying intensity was observed and should not be confused as an X-ray emission feature arising from electron transitions in platinum. The spectrum of bulk platinum showed a single peak with a steep slope on the low binding energy side. X-ray emission and elastic peak were not separated because the Fermi level cuts through the d band. The width of the spectrum was about 6.80 eV. The valence-to-core emission spectrum of platinum(IV) oxide showed a shoulder at the high binding energy side. The width of the main peak was 3.05 eV, that including the shoulder 5.55 eV. The spectrum of platinum(IV) chloride showed a doublet with widths of 1.45 and 6.15 eV. They were 3.45 eV apart. There was also a small feature towards high binding energy. The spectra of platinum(IV) sulfide and platinum(IV) telluride, and platinum(II) ammonium nitrate had widths of respectively 3.70, 4.55, and 4.70 eV. The spectrum of platinum(IV) sulfide showed a long tail to higher binding energy; those of platinum(IV) telluride, and platinum(II) ammonium nitrate are almost symmetric. An increase of the binding energy in the order platinum foil < platinum(IV) chloride < platinum(IV) sulfide < platinum(II) ammonium nitrate < platinum(IV) telluride < platinum(IV) oxide was found.
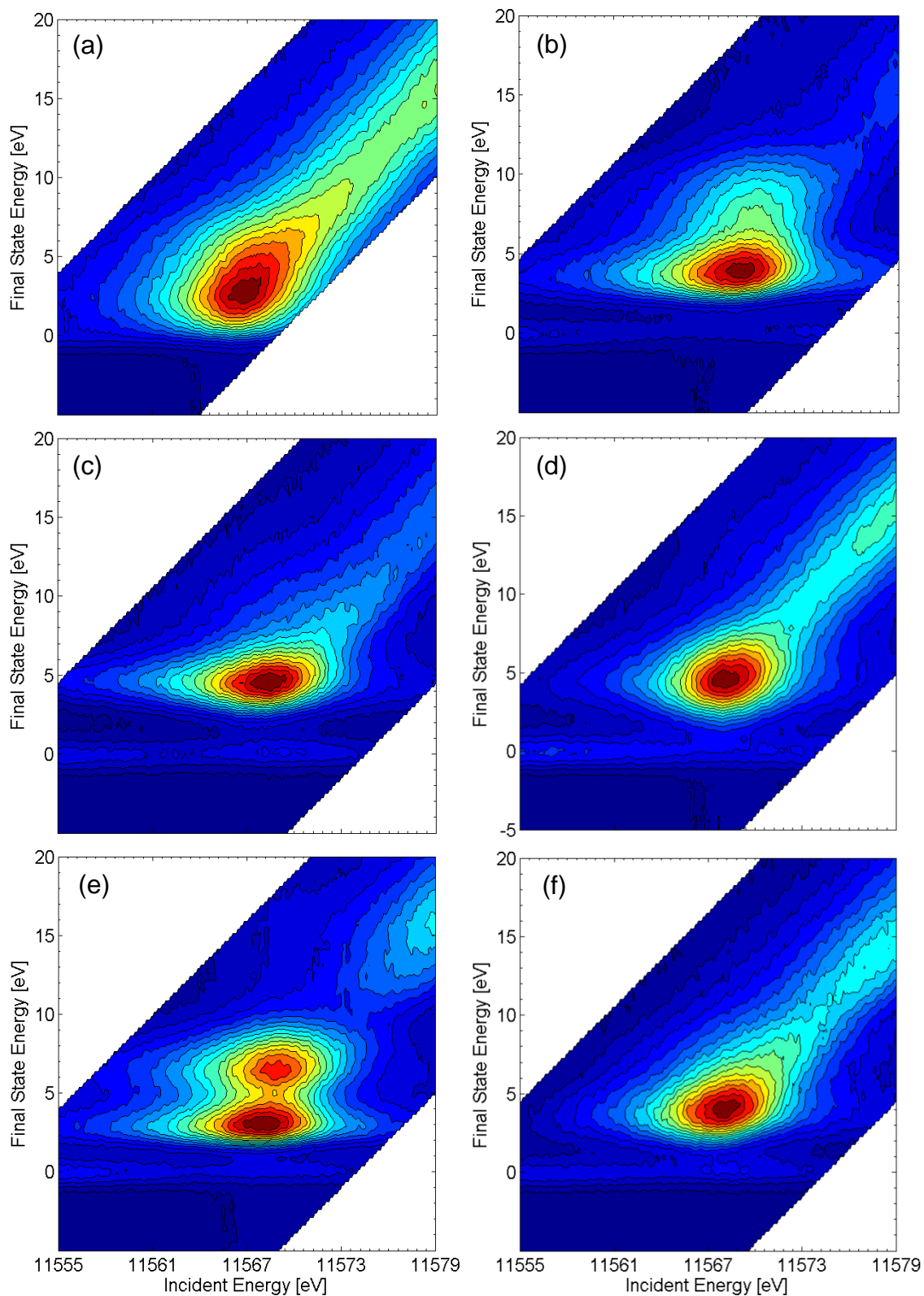
Figure 3.2: RIXS planes of (a) platinum foil, (b) platinum(IV) oxide, (c) platinum(IV) sulfide, (d) platinum(IV) telluride, (e) platinum(IV) chloride, and (f) platinum(II) ammonium nitrate.

Table 3.1: Characteristic values and spectral shape of experimental L$_3$ egde absorption spectra and valence-to-core emission spectra of platinum compounds.

	XAS	XES		
	peak position (eV)	width of spectrum (eV)	Shape of spectrum	charge transfer energy (eV)
Pt-bulk	0.05 14.20 28.20 53.20	6.80	tailing at higher binding energy	-
PtO$_2$	-0.20 14.10 22.40 45.90	5.55	shoulder at high binding energy	2.60
PtS$_2$	-0.30 23.50 45.10	3.70	tailing at high binding energy	3.30
PtTe$_2$	0.15 10.70 20.00 29.30 38.80 48.40	4.55	only slight tail at high binding energy	3.00
PtCl$_4$	-0.10 11.20 31.60 50.20	6.15	two resolved peaks	2.00
Pt(NH$_3$)$_4$(NO$_3$)$_2$	-0.30 9.42 49.15	4.70	tailing at high binding energy	2.55

Figure 3.4 shows calculated Pt L$_3$ edge absorption spectra, valence-to-core emission spectra, and the platinum d DOS for platinum foil, platinum(IV) oxide, platinum(IV) sulfide, platinum(IV) telluride, and platinum(IV) chloride. In all theoretical absorption spectra, the experimental white line intensity and characteristic features were reasonably well reproduced, although their relative intensities deviated somewhat. The calculated emission spectra resembled the experimental valence-to-core emission spectra well for most systems.
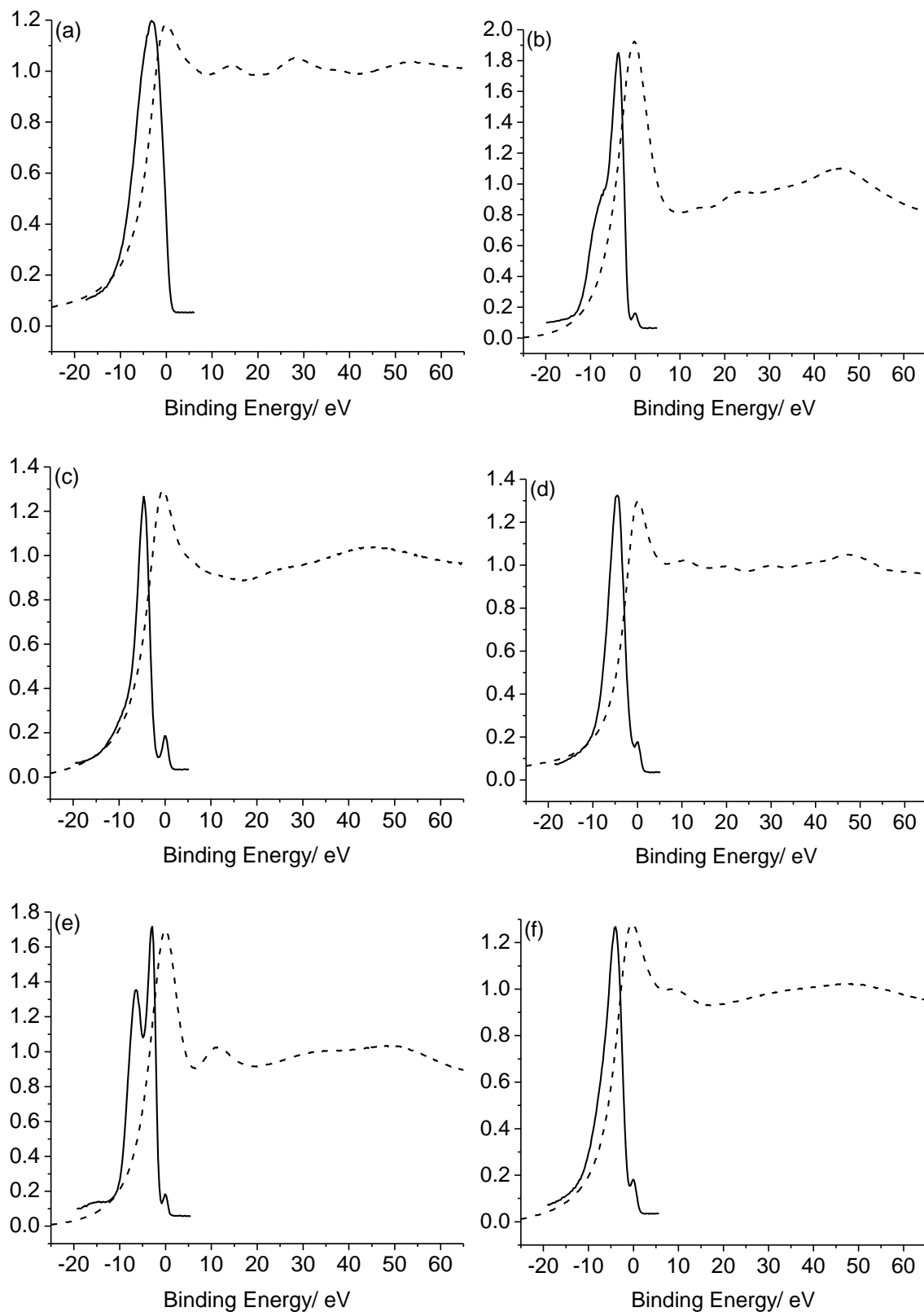
Figure 3.3: Experimental Pt L_3 edge absorption (dash) and valence-to-core emission (solid) spectra of (a) platinum foil, (b) platinum(IV) oxide, (c) platinum(IV) sulfide, (d) platinum(IV) telluride, (e) platinum(IV) chloride, and (f) platinum(II) ammonium nitrate.
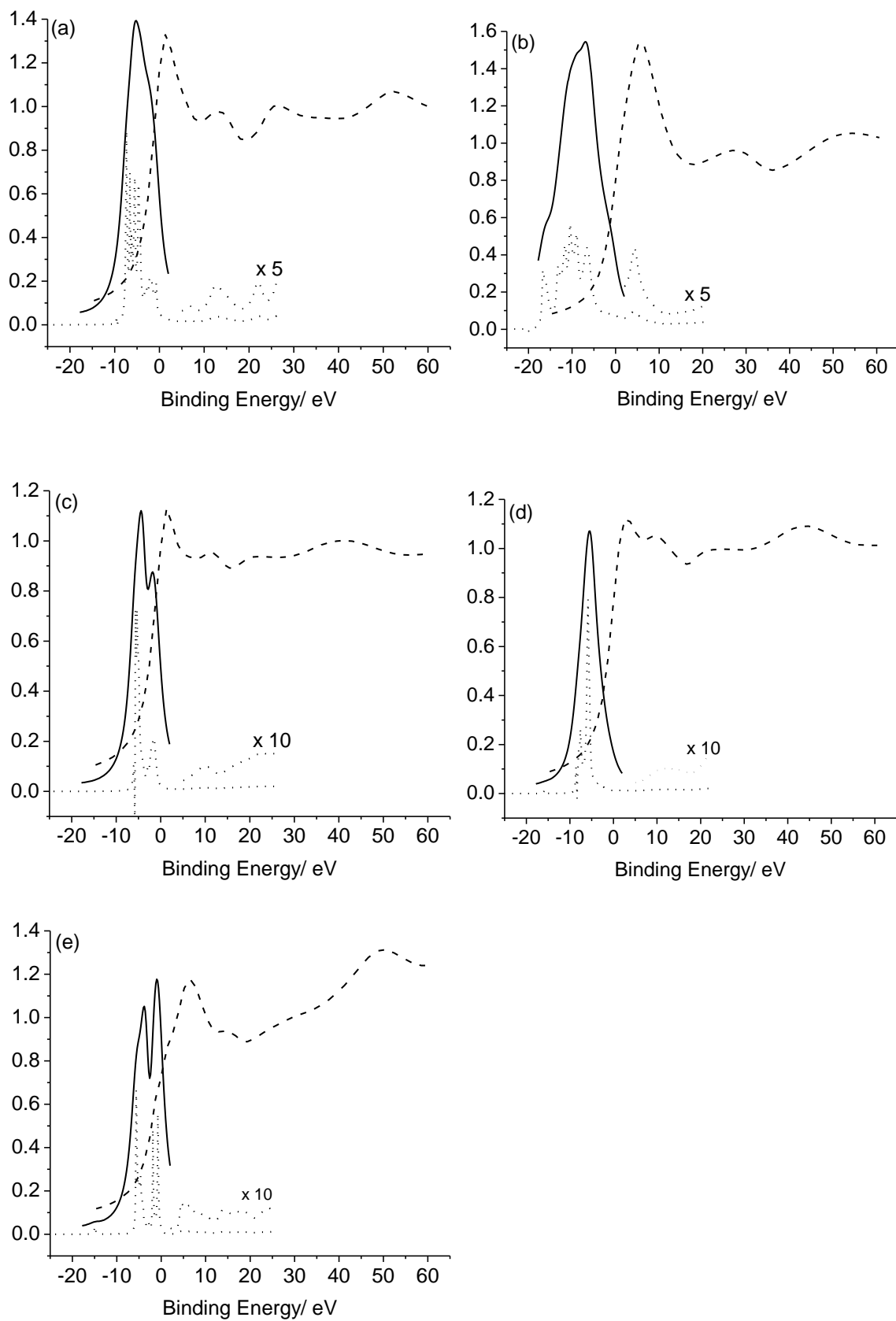
Figure 3.4: Theoretical Pt L_3 edge absorption (dash), valence-to-core emission (solid) spectra, and d DOS (dot) of (a) platinum foil, (b) platinum(IV) oxide, (c) platinum(IV) sulfide, (d) platinum(IV) telluride, and (e) platinum(IV) chloride.

The main features are tabulated in Table 3.2. For example, the double feature in platinum(IV) chloride was clearly reproduced and a small intensity feature at higher binding energy was also observed which was observed in experimental spectrum. The theoretical peak separation of 3.00 eV compares to 3.45 eV in the experimental spectrum. However in case of platinum(IV) sulfide, the calculated emission spectrum shows also a double feature that we do not observe in the experimental spectrum.

Table 3.2: Characteristic values and spectral shape of theoretical Pt L_3 egde absorption spectra and valence-to-core emission spectra of platinum compounds.

	XAS	XES		
	peak position (eV)	width of spectrum (eV)	Shape of spectrum	charge transfer energy (eV)
Pt-bulk	1.30 13.60 25.95 52.25	8.20	small shoulder at low binding energy	0.42
PtO$_2$	5.80 27.85 53.35	11.30	shoulders at high binding energy	2.00
PtS$_2$	1.45 11.60 20.60 41.30	6.75	extra feature with very low intensity at low binding energy	0.50
PtTe$_2$	2.90 9.80 21.05 44.05	5.05	very narrow and symmetrical spectrum	4.40
PtCl$_4$	6.40 15.45 49.60	5.75	two resolved peaks	-0.01

3.3.2 Gold Compounds

The experimental RIXS planes (Figure 3.5) showed for all gold compounds, gold foil, gold(III) hydroxide, and gold(I) sulfide, a symmetric peak, which tailed into the white line for gold(I) sulfide and bulk gold. In case of gold(III) hydroxide, there was minimal tailing. There was a small split along the net transition energy showing features at 4.05 eV and 6.05 eV.
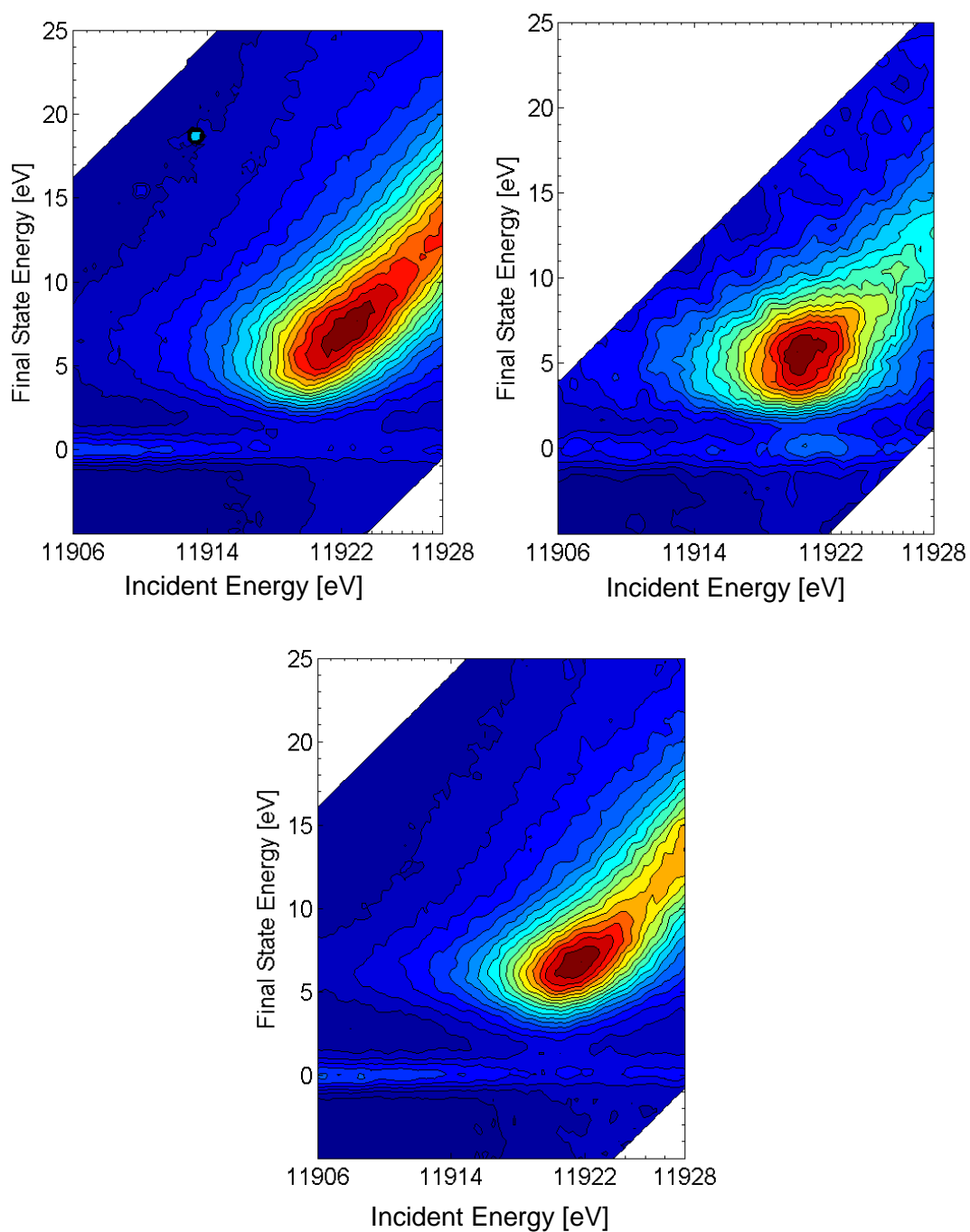

Figure 3.5: RIXS planes of (a) gold foil, (b) gold(III) hydroxide, and (c) gold(I) sulfide.

Figure 3.6 shows the experimental Au L_3 edge absorption and valence-to-core emission spectra of all three gold compounds. The characteristic features in the spectra are summarized in Table 3.3. The white line intensity of bulk gold was very low, because only a minor part of the d band is emptied after hybridization of the s, p, and d orbitals.[13] Gold(I) and gold(III) showed higher white line intensity due to the increased valence of gold in these compounds. The valence-to-core emission spectra showed less structure than those of the platinum compounds. The valence-to-core emission spectrum of bulk gold showed a symmetric peak with a broad tail at the high binding energy side.
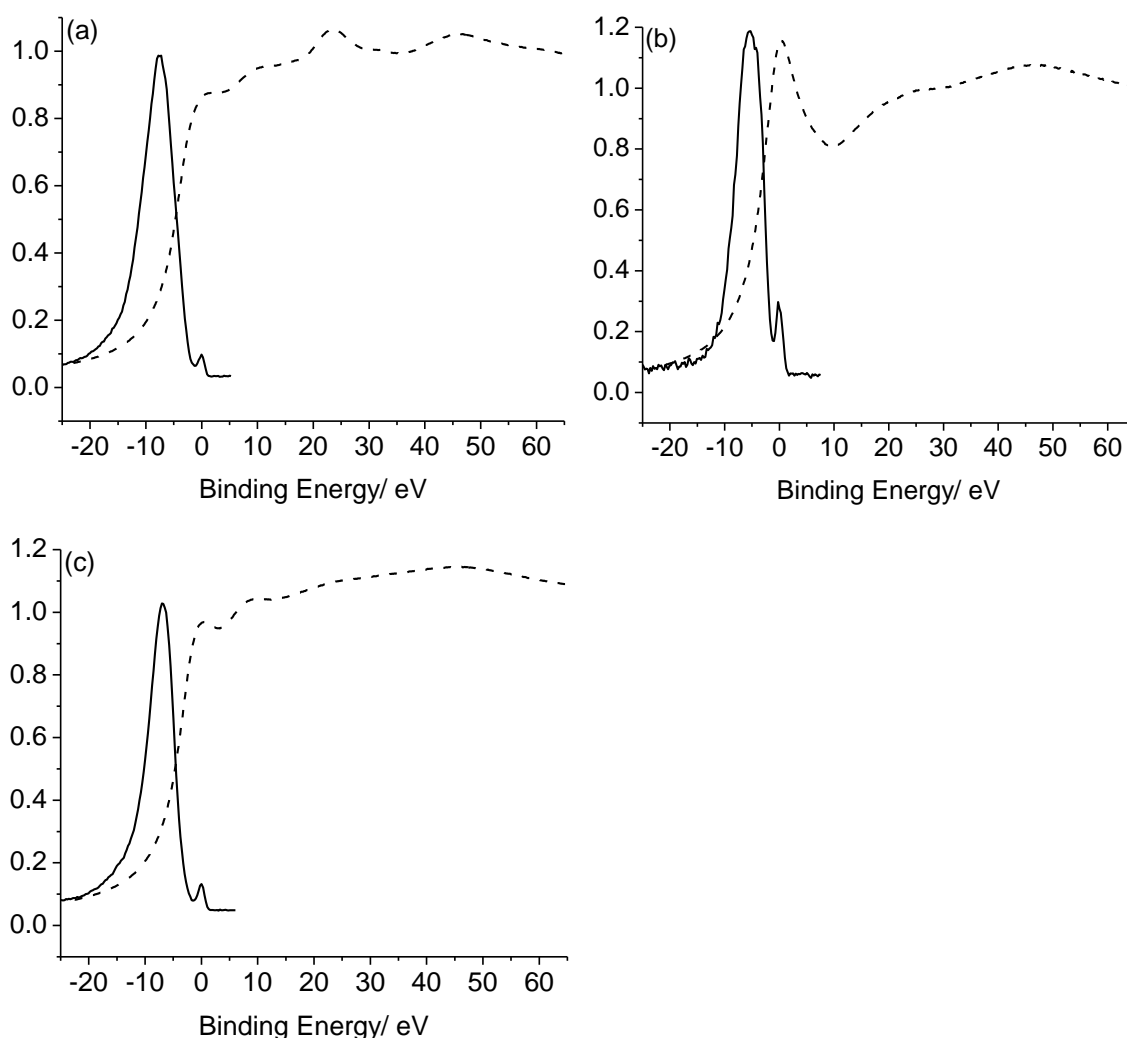
Figure 3.6: Experimental Au L_3 edge absorption (dash) and valence-to-core emission (solid) spectra of (a) gold foil, (b) gold(III) hydroxide, and (c) gold(I) sulfide.

The valence-to-core emission spectrum of gold(III) hydroxide was fairly symmetric; that of gold(I) sulfide was shifted towards the higher binding energy showing tailing at high binding energy side. The final state energy of the maxima of the spectra increased in the

order gold < gold(III) hydroxide < gold(I) sulfide.The width of the band was the largest in bulk gold, that of gold(I) sulfide the narrowest. The theoretical Au L_3 edge absorption and valence-to-core emission spectra are shown in Figure 3.7. They reproduced the experimental absorption spectra well, with some variation in the relative peak intensity. The spectral features are quantified in Table 3.4. The theoretical valence-to-core emission spectrum of bulk gold was characterized by a set of compact bands that form a rather symmetric band. The emission spectrum of gold(I) sulfide showed shoulders at low binding energy that is not observed experimentally. In case of gold(III) hydroxide, the splitting of the d band could be responsible for the small split which was observed in the RIXS plane along the net transition energy.
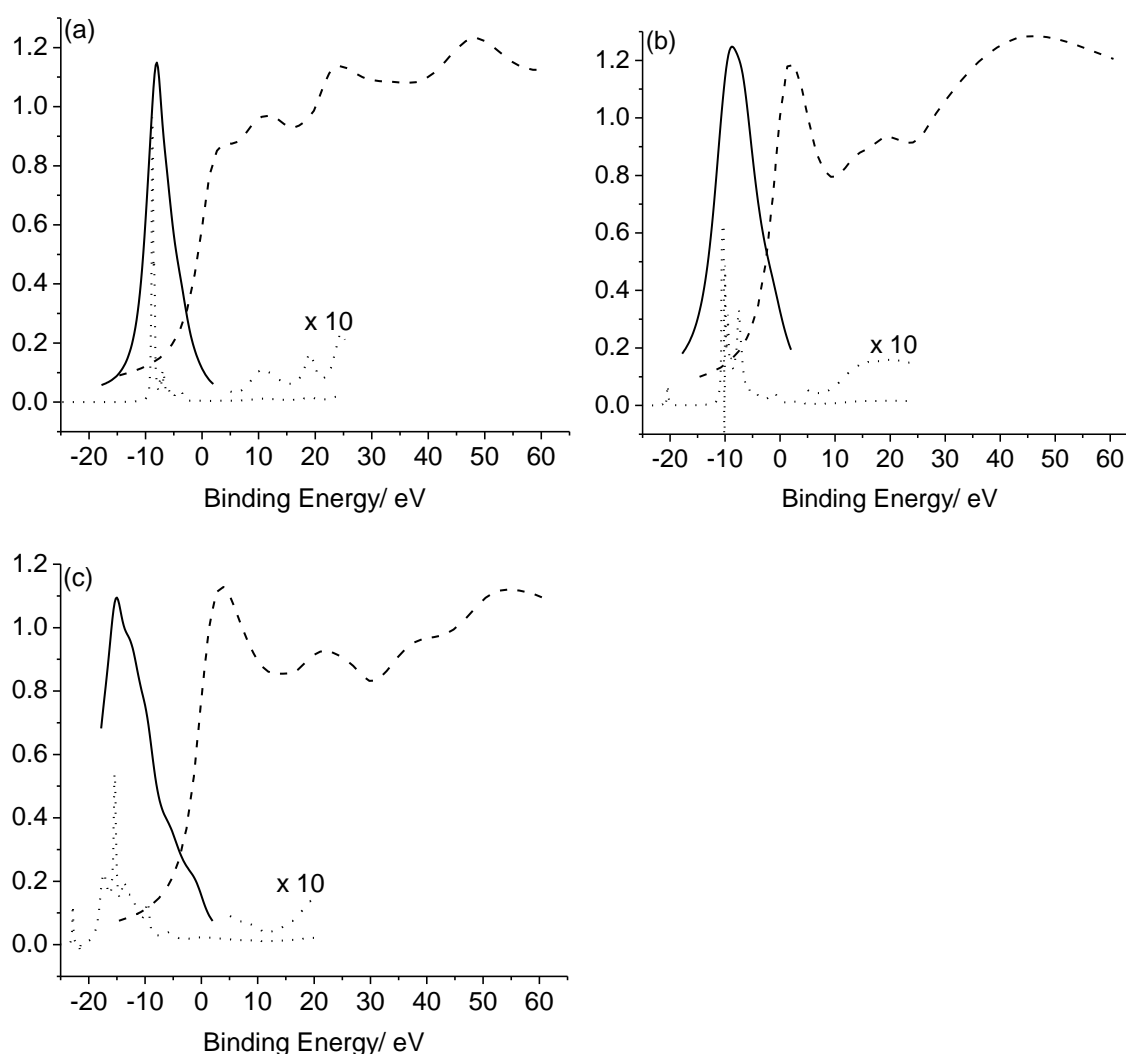

Figure 3.7: Theoretical Au L_3 edge absorption (dash), valence-to-core emission (solid) spectra, and d DOS (dot) of (a) gold foil, (b) gold(III) oxide, and (c) gold(I) sulfide.

Table 3.3: Characteristic values and spectral shape of experimental Au L_3 edge absorption spectra and non-resonant valence-to-core emission of gold compounds.

	XAS	XES		
	peak position (eV)	width of spectrum (eV)	Shape of spectrum	charge transfer energy (eV)
Au-bulk	0.65 9.50 23.40 46.10	5.90	tailing towards high binding energy	3.35
Au(OH)$_3$	0.30 25.45 46.85	5.90	broader spectrum	2.40
Au$_2$S	0.30 8.65 24.25 46.05	4.75	narrow spectrum with tailing at high binding energy	4.60

Table 3.4: Characteristic values and spectral shape of theoretical Au L_3 edge absorption spectra and valence-to-core emission of gold compounds

	XAS	XES		
	peak position (eV)	width of spectrum (eV)	Shape of spectrum	charge transfer energy (eV)
Au-bulk	3.75 11.25 23.95 48.30	5.4	symmetric spectrum with tailing towards high binding energy	7.30
Au(OH)$_3$	1.90 13.70 19.45 45.90	8.1	broader spectrum	5.50
Au$_2$S	3.90 22.30 37.95 53.60	-	shoulders at low binding energy	8.90

Figure 3.8 compares the Au L$_3$ edge absorption and experimental valence-to-core emission spectra of bulk gold to that of a nano-particle of gold. For comparison, the spectrum of bulk platinum has been added. The average size of the gold particles was about 1 nm as determined from electron microscopy.[14] The Au L$_3$ edge absorption spectrum of the nano-sized particle showed a decrease in all features that are characteristic of reduced gold. The white line intensity was lower, which points to an enhanced filling of the d band compared to bulk gold.[5f] The valence-to-core emission spectrum of nano-sized gold particles was shifted to lower binding energy; its width was similar to that of bulk gold.
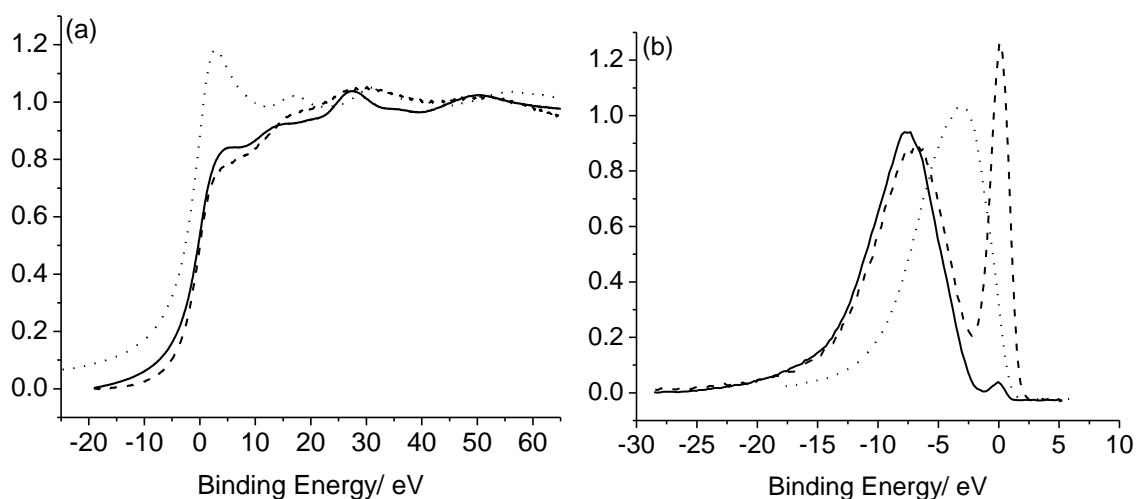

Figure 3.8: Experimental valence-to-core emission (b) and L$_3$ edge absorption (a) spectra of gold foil (solid), platinum foil (dot), and gold nano-particles (dash).

8.4 Discussion

8.4.1 Comparison of XES with other techniques

The physical and chemical properties of matter are dependent on their electronic structure. Slight changes in these properties can strongly affect the behavior of materials, which can further influence the performance of a chemical or a catalytic process in which they are involved. In general, the interaction of two different materials is governed by the electronic structure of both materials. For example, in any catalytic process, bonding of adsorbates on the metal surface depends on the formation of bonding and anti-bonding states between the metal and the adsorbate. When the anti-bonding state is pushed above the Fermi level and the bonding state is filled, the adsorbate bonds to the metal. For d bands that are more than half filled, the closer the

band to the Fermi level, the higher its reactivity.[15] Therefore, to understand the behavior of matter, their electronic structure needs to be explored. Figures 3.2-3.7 show that the d bands of 5d transition metals can be element-specifically probed using resonant hard X-ray emission spectroscopy. The XES is related to the filled DOS, XAS the unfilled, which provides accurate insight into the electronic structures. The valence-to-core emission and experimental L_3 edge absorption spectra can be well reproduced by using full multiple scattering calculations with FEFF 8 code (Figures 3.3, and 3.5). This good agreement between the experimental and theoretical absorption spectra suggests that the core hole in these compounds did not affect the final state DOS to a large extent. It has been suggested that the L edges are best reproduced when assuming a fully screened core hole.[16] The major advantage of technique (RIXS) applied in this work using hard X-rays, compared to XPS and UPS, is that it is a non-ionizing technique where the d DOS is probed element specifically whereas XPS and UPS lack in this regard. However XPS and UPS are ionizing techniques where an electron is removed leaving a positive charge that is screened by itinerant valence electrons. A consequence of the screening is a lower binding energy of the photoelectron. The screening is less efficient in smaller particles resulting in an increased binding energy as compared to bulk metals.[23f,17]

Valence-to-core emission spectra are recorded with the exclusive use of hard X-rays, which have a very large penetration depth. This does not limit the experiment to vacuum or low-pressure conditions, which is of extreme importance in many applications of metal nano-particles in catalysis and sensors. Because of this advantage, RIXS has the potential to probe the structure of the catalysts (e.g. platinum or gold nanoparticles supported on an oxide) under real catalytic conditions for example during oxidation of carbon monoxide, which is a very useful reaction in fuel cells[18] and automobile industry.[19] In contrast, because of the strong interaction of electrons with matter, the maximum pressure in XPS and UPS is limited to high vacuum. Although there are examples of in situ photoemission spectroscopy, where the applied pressure is in the range of few milli bars. The element-specificity and the possibility to perform in situ measurements make XES complementary to other methods that determine the valence shells.

The energy bandwidth in RIXS, applied here, of 1.5 eV is well below the core hole life-time broadening of about 5 eV at the L_{III} edge of platinum.[20] It is important to note that RIXS spectra are indirectly influenced by the absorption spectral features,[7c,21] because

the $2p_{3/2}$ lifetime broadening extends along the incident energy in the RIXS plane. This broadening is a fundamental physical property and cannot be eliminated or reduced. The broadening along the energy transfer axis, however, is considerably smaller because no core hole is present in the final state of the transitions. However, a broad unfilled d-DOS as measured in XAS of metals strongly influences the resonant XES via the lifetime broadening in the $2p_{3/2}$ excited states. In this case, spectral intensity in the resonant XES arises from a range of absorption energies due to the tails of the $2p_{3/2}$ lifetime broadening. Systems with distinct features in the unfilled d-DOS, such as insulators and semi-conductors, thus also render sharper features in the resonant XES data. In contrary, XPS and UPS can have better energy resolution then achieved here. For example, almost three decades back, the achievable resolution with these techniques was in order of 0.5 eV.[2a] However, there are instances of similar or even better energy resolution with XES also.[10a]

8.4.2 Structure of bulk metal compared to nanoparticles

With the features as explained above, RIXS planes have successfully shown the differences in the electronic structures of different compounds, showing that the structure is strongly affected by the ligands around the metal. Also, the RIXS plane reflects the differences in the structure of different metals (platinum and gold). The RIXS plane of bulk platinum shows a virtually symmetric peak. This is a manifestation of the Fermi level passing through the platinum 5d density of states. On the contrary, a gap is observed for bulk gold because the 5d DOS of gold is almost filled and the Fermi level passes through the 6s DOS which has negligible intensity at the L_3 edge. Figure 3.8 compares bulk platinum and bulk gold, which clearly shows the shift of the d DOS towards higher binding energy (to lower energy transfer) in case of bulk gold as compared to bulk platinum. Also the width of the gold X-ray emission spectrum is 5.90 eV versus 6.80 eV in platinum showing the narrower d band in gold compared to platinum.

Particles of gold of about 1 nm have a d band shifted to lower binding energy compared to that of bulk gold (Figure 3.8), which we consider an initial state effect.[22] This compares to shifts in opposite direction for UPS and XPS spectra of the valence band in nano-sized particles. Variations in the electronic structure as function of particle size have been observed and both initial state and final state effects are reported to contribute to the changes in the measured band structures.[23] With decreasing particle size, fewer

atoms contribute to the d band, whose width decreases and which shifts to lower binding energy.

Previously, the intensity of the white line in reduced gold particles was shown to decrease with decreasing particle size,[5f,24] in agreement to our observation in Figure 3.8. Fewer atoms contribute to the s, p, and d bands in nanoparticles as compared to bulk gold. The energy width of these bands becomes narrower decreasing their overlap and hybridization. As a result less d intensity is pushed above the Fermi level and the intensity of the white line at the L edge decreases because fewer states with d symmetry are available. It was proposed that the band narrowing in smaller particles was accompanied by a shift of the d band toward the Fermi level,[5f,25] which is observed in our XES data. Because XES probes the structure of the valence band in 5d metals element specifically, the signal of the substrate in supported metals and that of other metals in alloys need not be subtracted as is the case in XPS and UPS.

8.5 Conclusions

The structure of the 5d valence band in 5d metals is accessible using valence-to-core XES after excitation at the L_3 absorption edge. The electronic structure can be assessed element-specifically under in situ conditions because only hard X-rays are involved. Metal L_3 edge absorption spectra provides the empty DOS, XES the filled DOS, which gives a complete picture of the electronic structure. The experimental L_3 edge absorption could be well reproduced theoretically assuming a fully screened core hole, which suggests that the spectra resemble the initial state structures. The energy of the d valence band in nano-sized gold clusters shifts to lower binding energy. This experiment showed how the intrinsic properties of nano-sized particles vary with size.

Chapter 3

References

1 C. Michel, O. B. Carroll, Adv. Catal. 36 (1989) 55.

2 (a) M. Alnot, A. Cassuto, R. Ducros, J. J. Ehrhardt, B. Weber, Surf. Sci. Lett. 114 (1982) L48; (b) V. Vijayakrishnan, C. N. Rao, Surf. Sci. Lett. 255 (1991) L516; (c) C. Pulgia, A. Nilsson, B. Hernnäs, P. Bennich, N. Martensson, Surf. Sci. 342 (1995) 119; (d) K-D. Schierbaum, S. Fischer, P. Wincott, P. Hardman, V. Dhanak, G. Jones, G. Thornton, Surf. Sci. 391 (1997) 196.

3 A. Naitabdi, L. K. Ono, B. R. Cuenya, Appl. Phys. Lett. 89 (2006) 043102.

4 A. I. Frenkel, C. W. Hills, R. G. Nuzzo, J. Phys. Chem. B 105 (2001) 12689.

5 (a) F. W. Lytle, J. Catal. 43 (1976) 376; (b) F. W. Lytle, P. S. P. Wei, R. B. Greegor, G. H. Via, J. H. Sinfelt, J. Chem. Phys. 70 (1979) 4849; (c) A. N. Mansour, J. W. Cook, D. E. Sayers, J. Phys. Chem. 88 (1984) 2330; (d) R. Manaila, B. R. Orton, D. Macovei, M. Manciu, I. Adil-Smith, Phys. ReV. B 53 (1996) 8164; (e) D. Bazin, D. Sayers, J. J. Rehr, C. J. Mottet, J. Phys. Chem. B 101 (1997) 5332; (f) J. A. van Bokhoven, J. T. Miller, J. Phys. Chem. C 111 (2007) 9245.

6 (a) D. E. Ramaker, B.L. Mojet, M. T. G. Oostenbrink, J.T. Miller, D. C. Koningsberger, Phys. Chem. Chem. Phys. 1 (1999) 2293; (b) A. L. Ankudinov, J. J. Rehr, J. Low, S.R. Bare, Phys. Rev. Lett. 86 (2001) 1642; (c) D. E. Ramaker, D. C. Koningsberger, Phys. Rev. Lett. 89 (2002) 139701; (d) M. K. Oudenhuijzen, J. A. van Bokhoven, J. T. Miller, D. E. Ramaker, D. C. Koningsberger, J. Am. Chem. Soc. 127 (2005) 1530; (e) N. Weiher, E. Bus, L. Delannoy, C. Louis, D. E. Ramaker, J.T. Miller, J. A. van Bokhoven, J. Catal. 240 (2006) 100; (f) E. Bus, D. E. Ramaker, J. A. van Bokhoven, J. Am. Chem. Soc. 129 (26) (2007) 8094.

7 (a) K. Hämäläinen, D. P. Siddons, J. B. Hastings, L. E. Berman, Phys. Rev. Lett. 67 (1991) 2850; (b) P. Glatzel, U. Bergmann, Coord. Chem. Rev. 249 (2005) 65; (c) J. A. van Bokhoven, C. Louis. J. T. Miller, M. Tromp, O. V. Safonova, P. Glatzel, Angew. Chem. Int. Ed. 45 (2006) 4651

8 O. V. Safonova, M. Tromp, J. A. van Bokhoven, F. M. F. de Groot, J. Evans, P. Glatzel, J. Phys. Chem. B 110 (2006) 16162.

9 J. Singh, E. M. C. Alayon, M. Tromp, O. V. Safonova, P. Glatzel, M. Nachtegaal, R. Frahm, J. A. van Bokhoven, Angew. Chem. Int. Ed. 47, (2008) 9260.

10 (a) A. Nilsson, J. Hasselström, A. Föhlisch, O. Karis, L. G. M. Pettersson, M. Nyberg, L. Triguero, J. Elect. Spect. Rel. Phen. 110-111 (2000) 15; (b) T. Strunskus, O.

Fuchs, L. Weinhardt, C. Heske, M. Guraya, M. Muhler, V. Staemmler, Ch. Wöll, J. Elect. Spect. Rel. Phen. 134 (2004) 183; (d) F. M. F. de Groot, Coord. Chem. Rev. 249 (2005) 31.

[11] P. Glatzel, J. Singh, Kristina O. Kvashnina, J.A. van Bokhoven, J. Am. Chem. Soc. 132 (8) (2010) 2555.

12 (a) A. L. Ankudinov, B. Ravel, J. J. Rehr, S. D. Conradson, Phys. Rev. B 58 (1998) 998; (b) A. L. Ankudinov, C. Bouldin, J. J. Rehr, J. Sims, H. Hung, Phys. Rev. B 65 (2002) 104107.

13 (a) L. F. Mattheiss, R. E. Dietz, Phys. Rev. B 22 (1980) 1663; (b) M. G. Mason Phys. Rev. B 27 (1983) 748; (c) H. Häkkinen, M. Moseler, U. Landman, Phys. Rev. Lett. 89 (2002) 033401; (d) P. K. Jain, Struct. Chem. 16 (2005) 421; (c) J. A. van Bokhoven, J. T. Miller, J. Phys. Chem. C 111 (2007) 9245.

14 (a) E. Bus, R. Prins, J. A. van Bokhoven, Catal. Comm. 8 (2007) 1397; (b) E. Bus, R. Prins, J. A. van Bokhoven, Phys. Chem. Chem. Phys. 9 (2007) 3312.

15 B. Hammer, J. K. Norskov, Nature 376 (2002) 38.

16 A. I. Nesvizhskii, J. J. Rehr, J. Synchrotron Rad. 6 (1999) 315.

17 (a) L. Oberli, R. Monot, H. J. Mathieu, D. Landolt, J. Buttet, Surf. Sci. 106 (1981) 301; (b) M. G. Mason, Phys. Rev. B 27 (1983) 748; (c) G. K. Wertheim, S. B. DiCenzo, S.E. Youngquist, Phys. Rev. Lett. 51 (1983) 2310.

18 C. D. Dudfield, R. Chen, P. L. Adock, Int. J. Hydrogen Energy 26 (2001) 763.

19 R. J. Farrauto, R. M. Heck, Catal. Today 51 (1999) 351.

20 J. C. Fuggle, J. E. Inglesfield, in Unoccupied Electronic States, Springer-Verlag: Berlin, (1992).

21 P. Carra, M. Fabirizio, B. T. Thole, Phys. Rev. Lett. 74 (1995) 3700.

22 (a) G.K. Wertheim, S.B. DiCenzo, D.N.E. Buchanan, Phys. Rev. B 33 (1986) 447; (b) G.K. Wertheim, S.B. DiCenzo Phys. Rev. B 37 (1988) 3786; (c) Ch. Kuhrt, M. Harsdorff, Surf. Sci. 245 (1991) 173.

23 (a) P. N. Ross, K. Kinoshita, P. Stonehart, J. Catal. 32 (1974) 163; (b) S.-T. Lee, G. Apai, M. G. Mason, Phys. Rev. B 23 (1981) 505; (c) G. K. Wertheim, S. B. Dicenzo, S.E. Youngquist, Phys. Rev. Lett. 51 (1983) 2310; (d) D.M. Cox, W. Eberhardt, P. Fayet, Z. Fu, B. Kessler, R. D. Sherwood, D. Sondericker, A. Laldor, Z. Phys. D – Atoms, Molecules and Clusters 20 (1991) 385; (e) G. Peto, G. Molnar, G. Bogdanyi, L.

Guczi, Catal. Lett. 26 (1994) 383; (f) H. G. Boyen, Th. Herzog, G. kästle, P. Ziemann, J. P. Spatz, M. Möller, R. Wahrenberg, M. G. Garnier, P. Oelhafen, Phys. Rev. B 65 (2002) 075412.

24 J. T. Miller, A. J. Kropf, Y. Zha, J. R. Regalbuto, L. Delannoy, C. Louis, E. Bus, J. A. van Bokhoven, J. Catal. 240 (2006) 222.

25 (a) B. Hammer, J. K. Norskov Surf. Sci. 343 (1995) 21; (b) B. Hammer, J. K. Norskov Adv. Catal. 45 (2000) 71.

Chapter 4

Electronic structure of alumina-supported monometallic Pt and bimetallic PtSn catalysts

Abstract

The structure of supported platinum and platinum-tin nanoparticles was investigated by Pt L_3 high-energy resolution fluorescence detected X-ray absorption spectroscopy (HERFD XAS) and resonant inelastic X-ray scattering (RIXS). The incorporation of tin decreased the ability of particles to adsorb both hydrogen and carbon monoxide due to tin enrichment on the surface. The platinum d band of platinum-tin particles was narrower and was shifted down relative to the Fermi level in comparison to platinum particles. The difference in electronic structure between pure and alloyed particles persisted after adsorption of hydrogen. The Pt-H anti-bonding state was clearly identified for the pure platinum particles. The strong adsorption of carbon monoxide changed the geometric structure of the PtSn particles. After carbon monoxide adsorption, the geometric structure of both systems was very similar. Room temperature adsorption of carbon monoxide affects the structure of platinum catalysts.

4.1. Introduction

Supported noble metal catalysts are used on a large-scale in petroleum refining, energy conversion, fine chemicals production, and automobile exhaust conversion.[1] To enhance activity, selectivity, and stability, a unique combination of metal, support, and addition of dopants are applied. To understand the origin of the activity and reactivity of these catalysts, an elucidation of the geometric and electronic structure of the ensemble of atoms forming the catalytically active site is essential. An enormous body of work exists aiming to establish structure-activity relationship in heterogeneous catalysis.[2] When an adsorbate is chemically adsorbed on a metal surface, new electronic states are formed. These electronic states consist of bonding and anti-bonding states as shown in Figure 4.1. When the anti-bonding states are pushed above the Fermi level, the adsorbate bonds to the metal.[3] Nørskov and co-workers have developed the adsorbate-metal bonding model based on d band theory.[4] According to this theory, the adsorption energy of the adsorbates, and in parallel the reactivity of the metal surface, depends on the energy position of the d band relative to the Fermi level. Metals that have their d band centre closer to the Fermi level are more active towards the adsorption of adsorbates than those with a d band centre farther from the Fermi level. The d band shape of a metal and thus the d band centre is prone to change after alloying with a different metal.[5] Alloying two different metals is a common practice in heterogeneous catalysis to improve the activity, selectivity, and stability for many reactions. The synergistic effect in bimetallic catalysts has been shown to depend on the precise particle composition, feed composition and operating temperature.[6] The changes in the performance of bimetallic catalysts are often related to their different electronic and geometric structures.[5b] Many experimental[7] and theoretical[8] studies have shown a higher activity for the bimetallic alloys compared to monometallic materials due to electronic modification of the primary metal sites after alloying. However, there are very few experimental studies to quantitatively relate the performance of the catalytic systems to their structure.[5b,9] Here, we determine and compare the differences in electronic structure of alumina-supported platinum particles (monometallic system) and alumina-supported platinum-tin particles (bimetallic system). The addition of tin is a classical way to modify the catalytic performance of platinum catalysts. The filled and unfilled DOS of platinum are probed by high-energy resolution fluorescence detected (HERFD) X-ray absorption spectroscopy[10] and resonant inelastic X-ray scattering (RIXS)[10c,11] respectively (Figure 4.2).
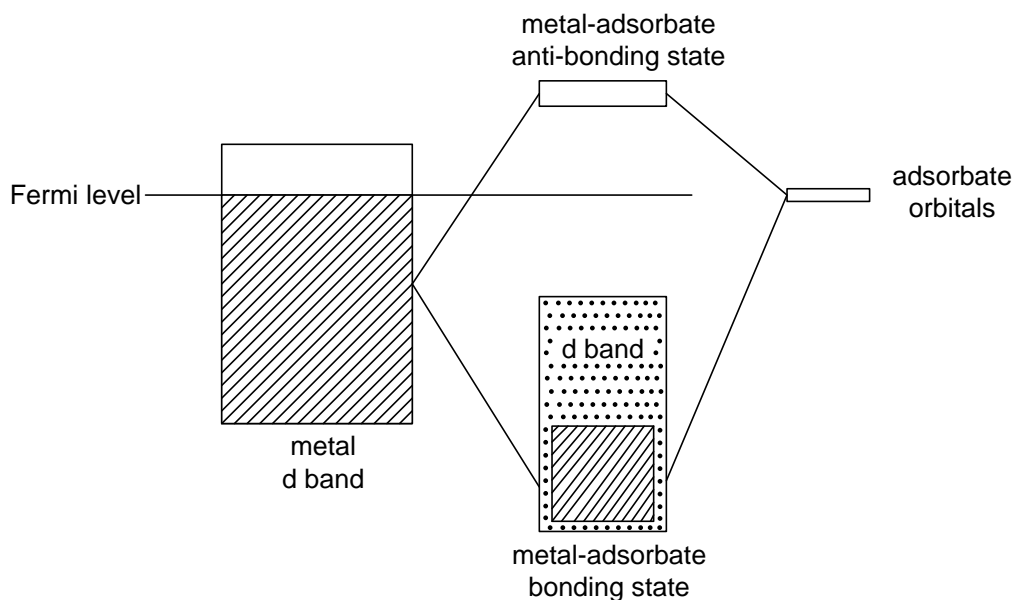
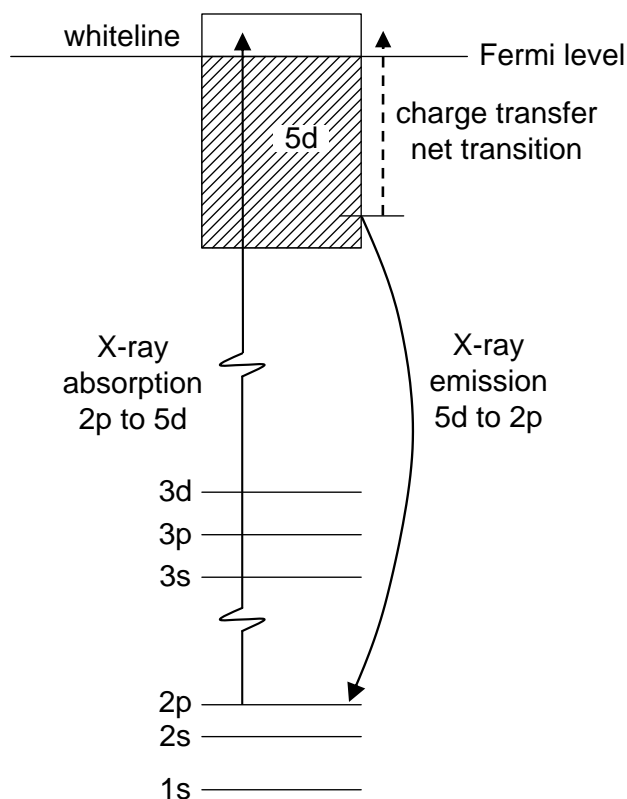Figure 4.1: Simplified scheme describing the interaction of adsorbate orbitals with metal d band.

Figure 4.2: Single-electron energy schemes for resonant emission spectroscopy with electronic transitions to and from the d DOS around the Fermi energy.

HERFD XAS is a technique where X-ray absorption spectra with higher energy-resolution are recorded with an instrumental broadening that is below the core hole lifetime broadening.[10] The selective detection of a fluorescence decay channel, which results in a core hole with a longer lifetime and thus smaller broadening, results in the

sharper features in the spectra. When exciting the L_3 edge, the empty d-DOS are probed. This technique had been successfully employed to explore the electronic structure of supported platinum catalysts under reaction conditions.[2d,10e] The energy-dispersive detection of fluorescence produced by the filling of the core hole (created in the normal absorption process) is the basis of RIXS. RIXS has been applied in many instances to provide the detailed electronic structure of 3d metals.[10b,10c,11,12] When detecting the 5d to 2p decay channel, the filled d-DOS is probed, which we have explored for platinum and gold.[13] Figure 4.2 illustrates the electron transitions that occur. The incident photon energy is used to excite an electron from the 2p energy level into the empty 5d level leaving a core hole behind. This core hole is filled by an electron from the valence 5d, resulting in emission of an X-ray associated with fluorescence energy. The net transition thus occurs from valence 5d to unfilled 5d states, which is called the net charge transfer. This charge transfer is measured by the RIXS process. RIXS, which provides the detailed electronic information, is a process where X-ray emission is measured while varying the excitation energy across an absorption edge. A RIXS plane is a two dimensional energy distribution obtained by varying incident and emitted energy. In this study, the RIXS planes show the charge transfer (incident energy minus emitted energy) distribution along the incident energy across the absorption edge of platinum. Using HERFD and RIXS at the Pt L_3 edge, it is uniquely possible to determine the element-specific electronic structure of the platinum d band, which is especially relevant for the bonding property of the metal. Moreover, because hard X-rays are employed and detected, the experiment does not require vacuum and can be performed under in situ (catalytic) conditions.

In this chapter, the above-described techniques are utilized to probe the filled and unfilled DOS of monometallic (platinum) and bimetallic (platinum-tin) systems and to elucidate the electronic and geometric effect of alloying platinum with tin. The observed changes in the DOS have been related to the adsorption properties of these systems for hydrogen and carbon monoxide.

4.2. Experimental

1.90 wt% Pt/Al_2O_3, hereafter called Pt/Al_2O_3 and 1 wt% Pt 0.25 wt% Sn, on Al_2O_3, hereafter called $PtSn/Al_2O_3$, were synthesized as explained in section 2.1. The size distribution of the catalysts were obtained using electron microscopy as explained in section 2.2. Hydrogen and carbon monoxide chemisorption measurements were done

using a Micromeritics ASAP 2010 apparatus under static volumetric conditions. Catalysts were reduced in pure hydrogen at 473 K for 30 min and then evacuated at 473 K for 30 min before cooling to 303 K under vacuum. The total amount of adsorbed hydrogen or carbon monoxide was obtained by extrapolating the linear part of the adsorption isotherms (10 kPa to 100 kPa). After obtaining the first isotherm, the catalyst was re-evacuated for 60 min prior to obtaining the second adsorption isotherm. This isotherm provided the amount of weakly adsorbed hydrogen or carbon monoxide. The amount of strongly bound (chemisorbed) hydrogen and carbon monoxide was calculated from the difference between the first (total adsorbed) and second (weakly adsorbed) isotherm. Afterward, the total and strong H/Pt and CO/Pt were calculated, which represent the moles of adsorbed atomic hydrogen and carbon monoxide per mole of platinum. The XAS experiments were conducted at beamline ID 26 at the European Synchrotron Radiation Facility (ESRF), Grenoble, France using the flow scheme as described in section 2.4.3. The catalyst was sieved to a fraction of 63-125 μm particles. The amount of catalyst used in the reactor was approximately 40 mg. The catalyst was pre-treated in situ in 5% hydrogen in helium at 473 K, in pure helium at 473 K for 30 min and cooled down in pure helium to 303 K, before switching to the adsorbing gas mixture. The measurements were done at a constant total flow of 30 NmL/min through the reactor, corresponding to a space velocity of about 64,000 h^{-1}. The x-ray beam measured 0.6 mm horizontal and 0.2 mm vertical. HERFD spectra and RIXS planes were collected at 303K under 5% carbon monoxide in helium, at 303 K under 5% hydrogen in helium, and at 473 K under 5% hydrogen in helium, after the system was in steady state as detected by mass spectrometer. The absorption near edge structures measured at increasing temperature had reached a constant stage at about 473 K, so we concluded that the spectrum at 473 K is indicative of bare platinum. The HERFD spectra were collected at a time resolution of 120 s. IR measurements were done as explained in section 2.5.

4.3. Results

4.3.1 Electron microscopy and chemisorption measurements

Figure 4.3 shows the STEM micrographs of Pt/Al$_2$O$_3$ and PtSn/Al$_2$O$_3$. Both catalysts showed well-dispersed particles supported on alumina. The particle size distributions confirmed the average size of particles in both samples of around 0.9 nm. A few particles of around 2.5 nm were observed in case of PtSn/Al$_2$O$_3$. In Table 4.1, H/Pt and

73

CO/Pt values are tabulated for the total and strongly adsorbed hydrogen and carbon monoxide at 303 K. Pt/Al_2O_3 showed total and strong H/Pt values of 1.26 and 0.51 respectively. A previous study has shown that small platinum particles supported on alumina can adsorb more than one hydrogen atom per platinum atom.[14] Total and strong CO/Pt values for Pt/Al_2O_3 were 0.86 and 0.70 respectively. $PtSn/Al_2O_3$ showed significantly lower values for both CO/Pt and H/Pt than Pt/Al_2O_3. the total and strong H/Pt values were 0.75 and 0.25 respectively and the total and strong CO/Pt values were 0.39 and 0.29 respectively. Similar results have been previously reported.[15]

Table 4.1: Chemisorption results for total and strong adsorption of hydrogen and carbon monoxide at 303 K.

	CO/Pt		H/Pt	
	total	strong	total	strong
Pt/Al_2O_3	0.86	0.70	1.26	0.51
$PtSn/Al_2O_3$	0.39	0.29	0.75	0.25

4.3.2 HERFD XAS: Pt/Al_2O_3 and $PtSn/Al_2O_3$

Figure 4.4(a) shows Pt L_3 edge HERFD XANES of Pt/Al_2O_3 under the different environments. The spectrum of bare platinum showed a strong whiteline at 11565.6 eV, which corresponds to the $2p_{3/2}$ to 5d dipole transition. Its intensity is a direct measure of the number of holes in the d band.[16] The features after the whiteline, at 11572.8 eV, 11581.2 eV, and 11594.6 eV, originate from multiple scattering of the photoelectron against the neighbouring platinum atoms. Their relatively low intensity indicated small platinum particles, in agreement with STEM. The spectrum after hydrogen adsorption showed a very similar whiteline intensity to that of bare platinum. There was a positive shift of 0.4 eV in the edge position, suggesting that the Fermi level was pushed up by 0.4 eV. The intensity was enhanced between 11570.2 eV and 11577.6 eV originating from the interaction of platinum with hydrogen atoms resulting in an anti-bonding state. The spectrum of Pt/Al_2O_3 with adsorbed carbon monoxide showed a broadened whiteline consisting of a doublet, which is direct evidence of adsorbed carbon monoxide on platinum surface predominantly in an atop position.[10d] The edge was shifted by 0.8 eV compared to the edge in the spectrum of bare platinum. All the features after the whiteline, at 11572.8 eV, 11581.2 eV, and 11594.6 eV were similar to the spectrum of bare platinum.
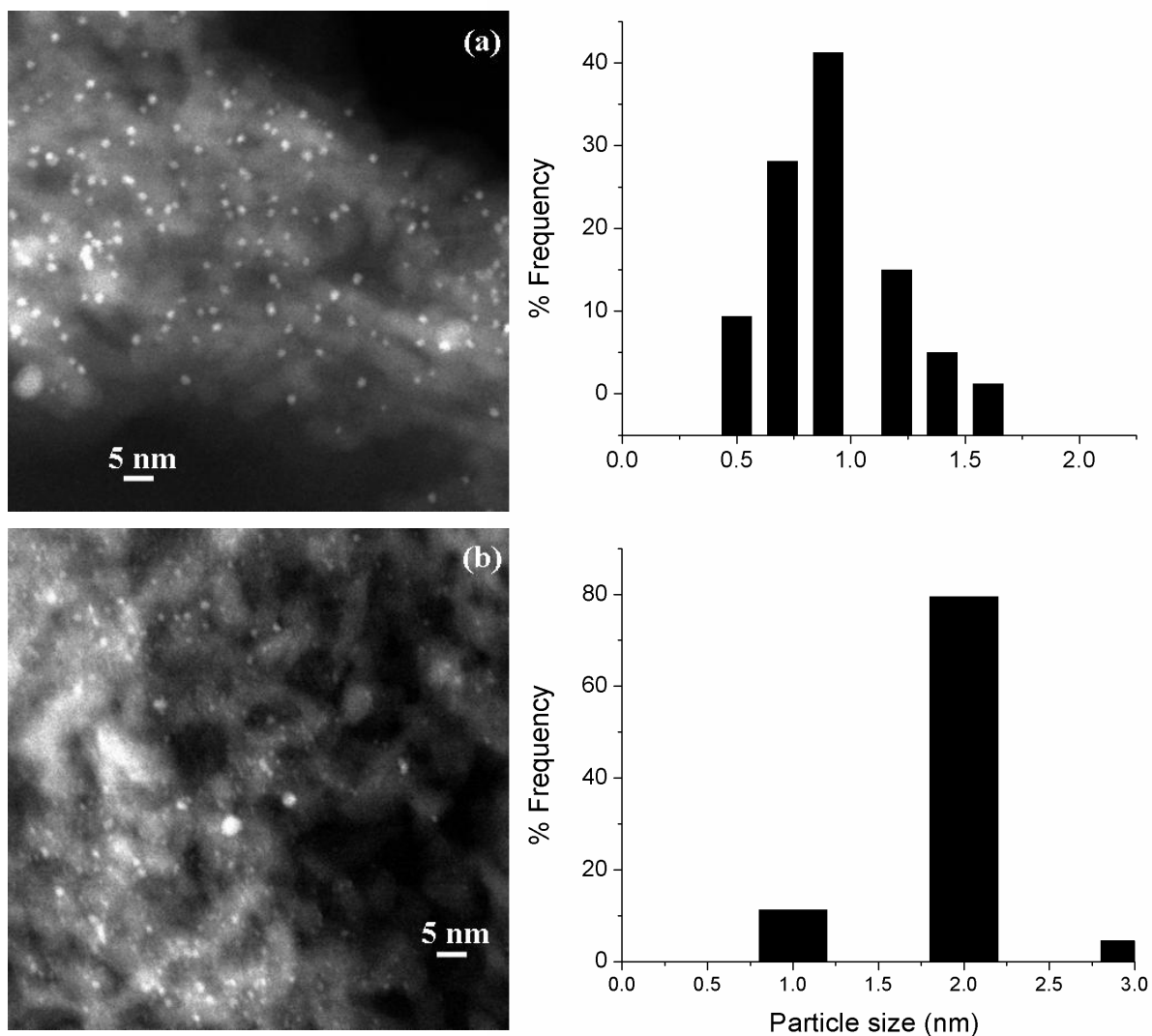
Figure 4.3: STEM micrograph of (a) Pt/Al$_2$O$_3$ and (b) PtSn/Al$_2$O$_3$. The figures on the right side show particle size distribution.
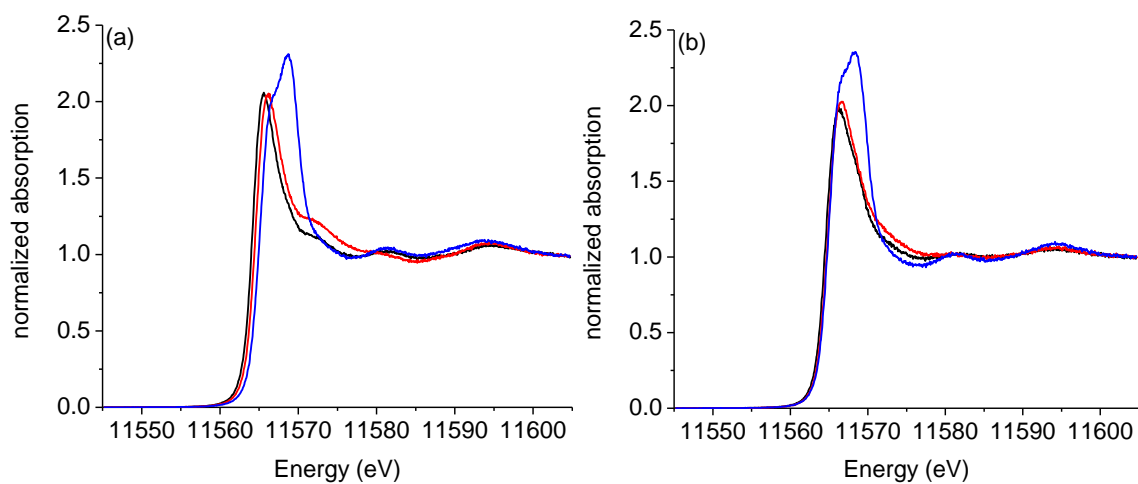

Figure 4.4: Pt L$_3$ edge HERFD XANES of (a) Pt/Al$_2$O$_3$ and (b) PtSn/Al$_2$O$_3$ for bare platinum (black), after hydrogen adsorption (red), and after carbon monoxide adsorption (blue).
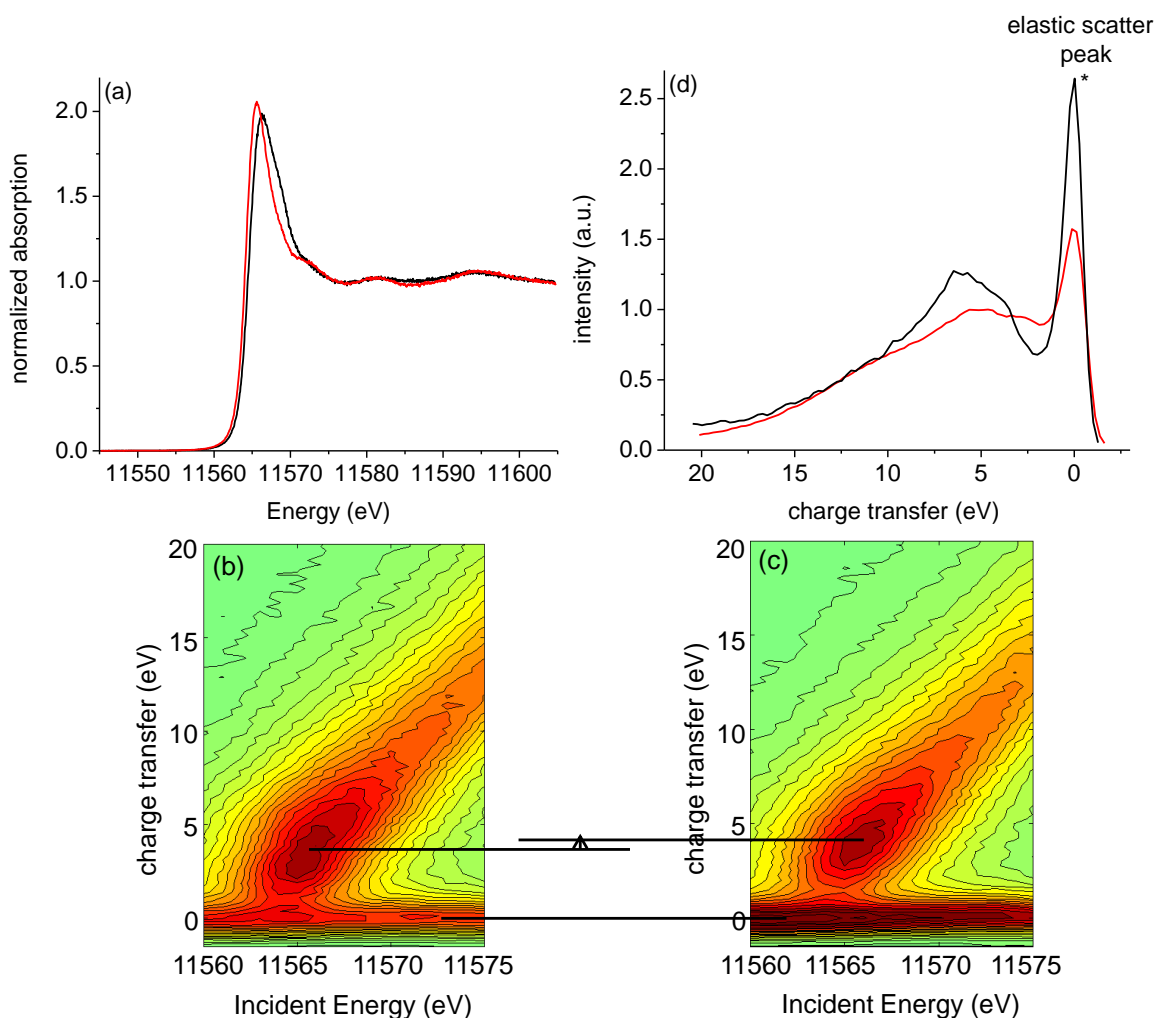
Figure 4.5: (a) Pt L$_3$ edge HERFD XANES of Pt/Al$_2$O$_3$ (red) and PtSn/Al$_2$O$_3$ (black) and $2p_{3/2}$ − 5d RIXS plane of (b) Pt/Al$_2$O$_3$ and (c) PtSn/Al$_2$O$_3$ for bare platinum, (d) integrated line plots along the incident energy of RIXS planes of Pt/Al$_2$O$_3$ (red) and PtSn/Al$_2$O$_3$ (black).

Figure 4.4(b) shows the Pt L$_3$ edge HERFD XANES of PtSn/Al$_2$O$_3$ with different adsorbates. The spectrum of bare platinum showed a whiteline intensity at 11566.3 eV. The features at 11581.2 eV, and 11594.6 eV originated from multiple scattering of the photoelectron against the neighbouring atoms. The spectrum after adsorption of hydrogen showed a shift in the edge position of less than 0.2 eV. There was a slight increase in the whiteline intensity at 11566.7 eV. The hydrogen anti-bonding state was observed between 11569.7 eV and 11578.9 eV and had a small intensity in agreement with the relatively low H/Pt value. The spectrum after adsorption of carbon monoxide showed broadening of the whiteline, consisting of a doublet, which confirmed the predominant atop adsorption of carbon monoxide on the platinum surface. The edge shift was 0.4 eV relative to the spectrum of the bare platinum particles. The features at 11581.2 eV and 11594.6 eV became more pronounced, which might suggest particle

growth or loss of disorder. There was loss of intensity between 11571.8 eV and 11579.6 eV, the origin of which was not immediately clear.

4.3.3 Bare particles

Figure 4.5(a) compares Pt L_3 edge HERFD XANES of Pt/Al_2O_3 and $PtSn/Al_2O_3$ for the bare platinum particles. The whiteline in the spectrum of $PtSn/Al_2O_3$ was slightly less intense and broader compared to that of Pt/Al_2O_3, which indicated a change in the electronic structure after alloying the platinum with tin, as shape of the whiteline is a direct measure of changes in the unfilled platinum d band.[16] The edge of the spectrum of $PtSn/Al_2O_3$ was also shifted by 0.3 eV compared to the one of Pt/Al_2O_3. All the features after the whiteline were similar for monometallic and bimetallic particles, with the exception of the somewhat larger intensity of the features in monometallic platinum, which might result from the mixed Pt-Pt and Pt-Sn contributions in the mixed metal particles. Figures 4.5(b) and (c) show the RIXS planes of Pt/Al_2O_3 and $PtSn/Al_2O_3$, showing the charge transfer distribution that is representative of the filled d-DOS (Figure 4.2). To emphasize the differences in the RIXS planes, Figure 4.5(d) shows the line plots that were obtained from the RIXS planes by integrating the spectral intensity along the incident energy. The feature at 0.0 eV charge transfer is the elastic peak, which occurs when the excited electron decays to fill the core hole without losing energy, implying that the emitted energy is equal to the incident energy. Table 4.2 summarizes the most important characteristic features of the RIXS planes. The shape and position of the filled d-DOS of platinum were different for Pt/Al_2O_3 and $PtSn/Al_2O_3$. The elastic peak at zero charge transfer and the d band of platinum in Pt/Al_2O_3 were merged together, which means that Fermi level lies within the filled d band of platinum. The d band was broad along the incident energy and tailed along the diagonal of the RIXS plane. There was a very small gap opening up between the elastic peak and the d band of platinum in case of $PtSn/Al_2O_3$ (Figure 4.5(c) and (d)). The d band was more symmetrical and tailed along the diagonal of the RIXS plane. The other important difference between the d band of platinum in the two samples was the position of the centre of the d band relative to the Fermi level. The centre of the most intense feature in the RIXS plane for Pt/Al_2O_3 was at charge transfer value of 3.50 eV and for $PtSn/Al_2O_3$ it was at 4.00 eV. These values were large in the line plots, because of the integrated nature of these plots. The trend however was the same. The d band of platinum was narrower in $PtSn/Al_2O_3$ than the one in Pt/Al_2O_3.

Table 4.2. Spectral shape of valence-to-core emission spectra of platinum compounds.

	Pt/Al$_2$O$_3$	PtSn/Al$_2$O$_3$
	shape of spectrum	shape of spectrum
bare	broad spectrum merged with the elastic peak, tailing at higher charge transfer	symmetrical spectrum with a small gap with elastic peak, tailing at higher charge transfer
adsorbed hydrogen	broad symmetrical spectrum with tailing at higher charge transfer	narrower symmetrical spectrum with tailing at higher charge transfer
adsorbed carbon monoxide	symmetrical spectrum with less tailing	symmetrical spectrum with less tailing

4.3.4 Hydrogen adsorption

Figure 4.6(a) shows Pt L$_3$ edge HERFD XANES of Pt/Al$_2$O$_3$ and PtSn/Al$_2$O$_3$ after hydrogen adsorption. The whiteline of the spectrum of PtSn/Al$_2$O$_3$ was slightly broader than the one of Pt/Al$_2$O$_3$. The whiteline intensity was similar. The edge in the spectrum of PtSn/Al$_2$O$_3$ was about 0.2 eV higher than that of Pt/Al$_2$O$_3$. The feature at 11572.8 eV was more intense for Pt/Al$_2$O$_3$. The region between 11579.5 and 11590.7 eV, which originates from multiple scattering showed different fine structure, which is indicative of a different geometry around the platinum atoms. The feature at 11594.6 eV had similar intensity for both samples. Figure 4.6(b) and (c) shows the RIXS planes for Pt/Al$_2$O$_3$ and PtSn/Al$_2$O$_3$ representing the d band of platinum after hydrogen adsorption. The d band of platinum in both the samples was symmetrical and tailed along the diagonal of the RIXS plane (Table 4.2). There was a gap that opened up between the elastic peak and the d band of platinum in both samples, but more so for PtSn/Al$_2$O$_3$. The band in case of Pt/Al$_2$O$_3$ was broader along the incident energy than of PtSn/Al$_2$O$_3$. The centre of the most intense features in the RIXS planes were at 3.65 eV and 4.55 eV for Pt/Al$_2$O$_3$ and PtSn/Al$_2$O$_3$ respectively. Figure 4.6(d) shows the line plots obtained by integrating the spectral intensity along the incident energy of RIXS planes. They confirmed that the d band was broader for PtSn/Al$_2$O$_3$ compared to one of Pt/Al$_2$O$_3$.
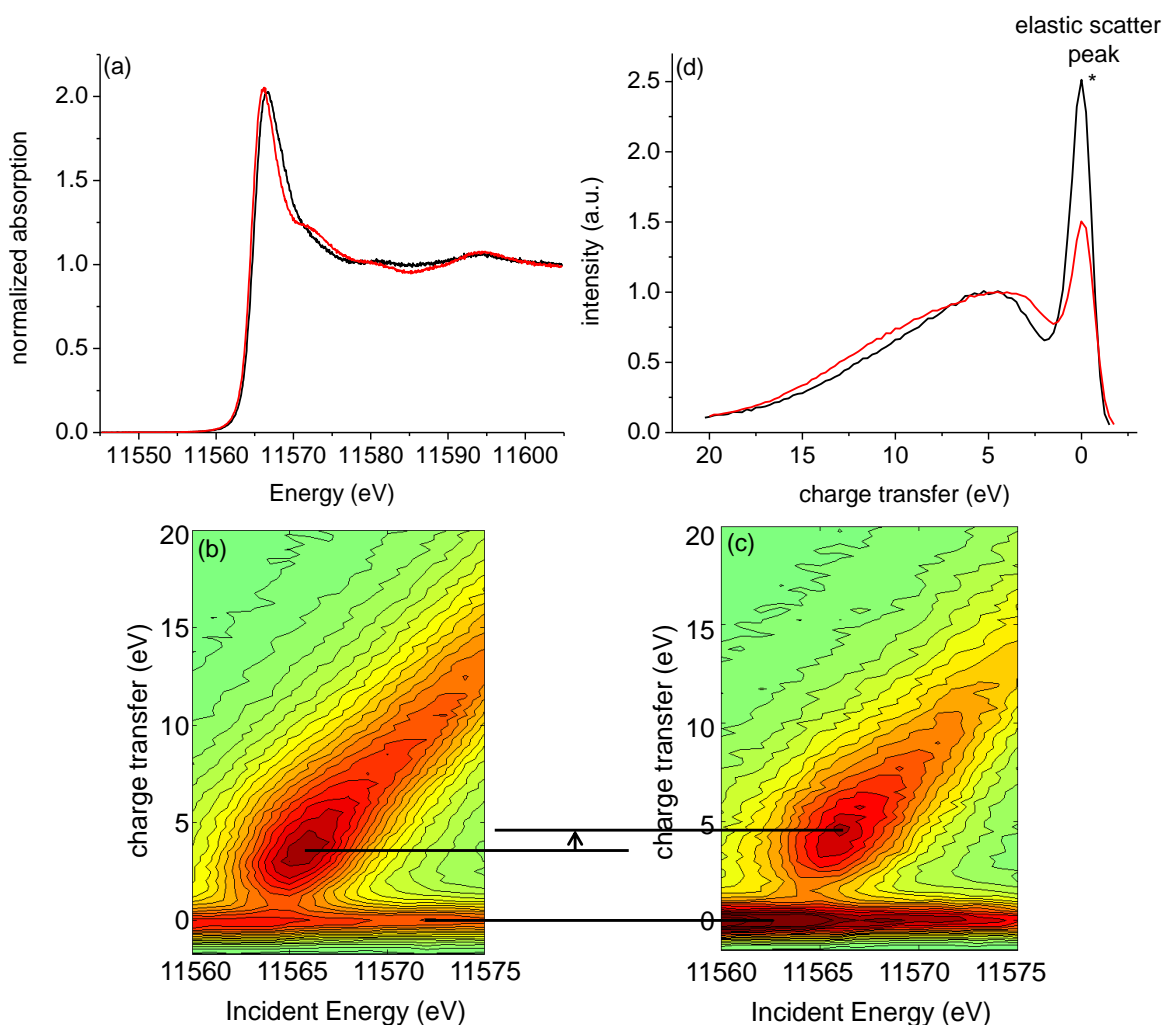
Figure 4.6: (a) Pt L_3 edge HERFD XANES of Pt/Al$_2$O$_3$ (red) and PtSn/Al$_2$O$_3$ (black) and $2p_{3/2} -$ 5d RIXS plane of (b) Pt/Al$_2$O$_3$ and (c) PtSn/Al$_2$O$_3$ after hydrogen adsorption, (d) integrated line plots along the incident energy of RIXS planes of Pt/Al$_2$O$_3$ (red) and PtSn/Al$_2$O$_3$ (black).

4.3.5 Carbon monoxide adsorption

The adsorption of carbon monoxide also resulted in changes in the d band of platinum and the formation of anti-bonding states, which were detected by RIXS and HERFD XAS respectively as shown in Figure 4.7. Figure 4.7(a) shows the comparison of Pt L_3 edge HERFD XANES of Pt/Al$_2$O$_3$ and PtSn/Al$_2$O$_3$ after adsorption of carbon monoxide. The doublet feature in the broad whiteline of the HERFD spectra in both the samples confirmed the predominant atop adsorption of carbon monoxide on the platinum surface. The whiteline intensity of the spectrum of PtSn/Al$_2$O$_3$ was slightly higher than that of Pt/Al$_2$O$_3$. The feature at higher energy in the doublet of the whiteline is formed by the overlapping of orbitals of C and O atoms with platinum d orbitals.[10d]
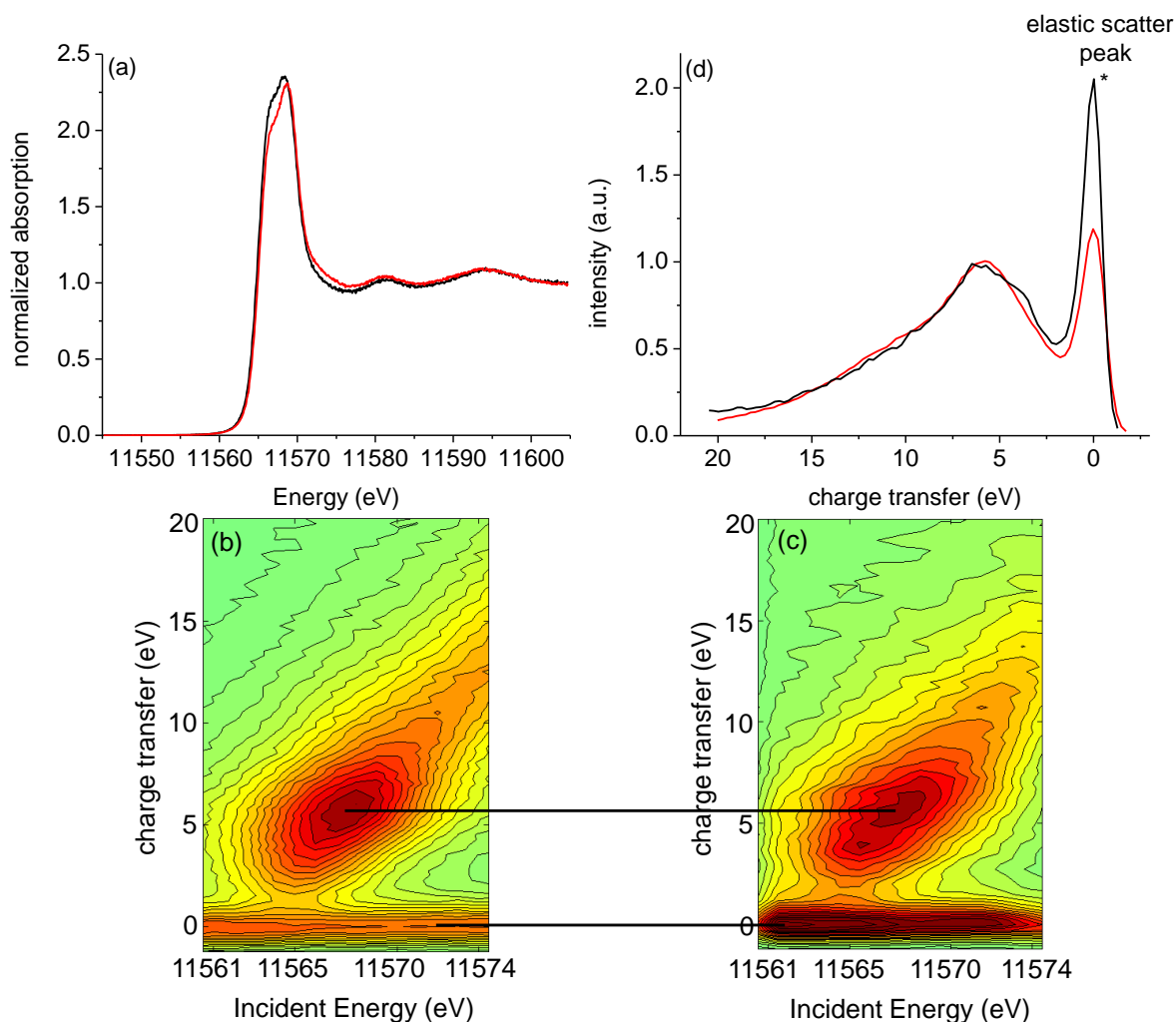
Figure 4.7: (a) Pt L$_3$ edge HERFD XANES of Pt/Al$_2$O$_3$ (red) and PtSn/Al$_2$O$_3$ (black) and $2p_{3/2}$ − 5d RIXS plane of (b) Pt/Al$_2$O$_3$ and (c) PtSn/Al$_2$O$_3$ after carbon monoxide adsorption, (d) integrated line plots along the incident energy of RIXS planes of Pt/Al$_2$O$_3$ (red) and PtSn/Al$_2$O$_3$ (black).

The intensity of the high energy feature of the doublet relative to the low energy feature was lower for PtSn/Al$_2$O$_3$ than for Pt/Al$_2$O$_3$ in agreement to the lower carbon monoxide coverage from the chemisorption measurement. There was loss of intensity after the whiteline, between 11571 and 11578 eV, in PtSn/Al$_2$O$_3$ compared to Pt/Al$_2$O$_3$, the origin of which was not immediately clear. The features at 11581.2 eV, and 11594.6 eV were very similar for both samples, suggesting that after adsorption of carbon monoxide the geometric structure became similar in both samples. Figures 4.7(b) and (c) show the RIXS planes for Pt/Al$_2$O$_3$ and PtSn/Al$_2$O$_3$ respectively. In both planes, there was a large gap between the elastic peak and the most intense feature of the RIXS planes as observed before[13]. A similar gap opening after carbon monoxide adsorption is reported

80

on Pd_4 clusters.[17] The energy distribution in the RIXS planes was quite broad along the incident energy axis in both samples. The centre of the most intense feature in the RIXS planes of both samples was at 5.70 eV charge transfer. Figure 4.7(d) shows the line plots obtained by integrating the spectral intensity along the incident energy of the RIXS planes, which confirmed the gap opening between the band and the elastic scattering peak and the more similar structure of Pt/Al_2O_3 and $PtSn/Al_2O_3$ after CO adsorption than in case of bare particles and after hydrogen absorption.

4.4 Discussion

4.4.1 Alloying

The dispersed monometallic platinum and bimetallic platinum-tin particles supported on alumina showed differences in the adsorption properties for hydrogen and carbon monoxide (Table 4.1). The results showed a decrease in the ability of bimetallic platinum-tin particles to adsorb hydrogen and carbon monoxide, in accordance with many previous studies,[15] which are associated with a decrease in the amount of platinum on the surface.[7c,15 b,15 d,18] These differences between monometallic and bimetallic catalysts are often related to the changes in the electronic[7a,19] and geometric[20] structure of the parent metal upon addition of the second metal. Some studies suggested that both electronic and geometric effects play a vital role in the enhancement of the activity of bimetallic systems.[5,21] These differences in the electronic and/or geometric structures of the bimetallic materials have often been related to their superiority in terms of activity and reactivity for many reactions.[5b,6,6c,15c,15d,22] Preferential oxidation (PROX) of carbon monoxide is one of such reaction that has been studied over monometallic platinum[23] and bimetallic platinum[7c,24] catalysts. There have been reports showing the formation of Sn^{4+}-Pt ensemble sites during the CO oxidation[15c] that activate the CO molecule. The selective adsorption of reactants on these metals also influences the reactivity of these catalysts.[6,25] The atomic ratio of platinum and tin has been shown to be an important factor for the formation of different phases of the platinum-tin alloys, which ultimately effect their catalytic performance for the oxidation reactions.[22a] However, there are reports where no synergism effects have been observed by combining platinum with other metals.[26] The other debated and still ambiguous factor is the electronic structure of tin in these bimetallic catalysts. XPS has been extensively used to decipher the oxidation state of tin in these bimetallic catalysts.[15b,15d,19b,23c] Some studies found mainly cationic

tin as the prevailing species[15d,27] while others observed tin to be mainly in reduced state.[28] Mixed states of tin have also been reported.[15b]

4.4.2. Techniques applied to reveal the effect of alloying

There are many studies using different techniques that try to reveal and interpret the differences in the performance of monometallic and bimetallic catalysts. The change in the C-O stretching frequency of linearly adsorbed carbon monoxide is often used as a measure of structural changes in the bimetallic systems using infra red spectroscopy.[7c,15a,15b,20a,21] The shift of this frequency to lower wave numbers has been explained by the dilution effect of tin in many instances.[7c,29] Alternatively, the decrease in wave numbers has been attributed to changes in the electronic structure of platinum by the addition of a second metal.[30] However, there are reports where no change in the frequency[31] or an upward shift in the frequency[15b,29b] was observed after addition of tin. The XPS binding energy shift of 1 eV in the Pt 4f level towards higher binding energy after alloying platinum with tin has been associated with the electronic transfer from the Pt 4f level to the bond between platinum and tin.[19b] This could be interpreted as rehybridization of d orbitals with s and p orbitals due to the formation of platinum-tin bonds as illustrated by ab initio self-consistent-field calculations.[32] There is a report suggesting that the observed shift of 0.2 eV in case of supported platinum tin catalysts compared to platinum catalysts is too minimal to show any electronic change after the addition of tin.[15a] UPS studies have also shown the change in the electronic structure of platinum after alloying with tin.[7a] XRD studies on contrary[20b] have shown the dominance of geometric effects, where it is shown that the lattice constant of platinum is dilated because of the presence of tin atoms in platinum tin alloys. Using Mössbauer spectroscopy,[33] platinum-rich and tin-rich phases have been observed for platinum tin nanoclusters, which are shown to change in composition during oxidation of carbon monoxide. Theoretical studies have also shown that the interaction of platinum and tin electrons after alloying results in the d band of platinum shifted away from the Fermi level.[19a,c] The results presented here show that using HERFD XAS and RIXS, the electronic structure of platinum can be probed directly in mono and bimetallic supported particles. We have identified changes in the electronic structure of platinum after being alloyed with tin. RIXS showed a downward shift and narrowing of the d band of platinum relative to the Fermi level after alloying with tin (Figure 4.5). The changes in the unfilled d-DOS as measured by the whiteline in the HERFD spectra (Figure 4.5(a))

also suggest that alloying platinum with tin influences the electronic structure of platinum. The modification of the electronic structure affects the reactivity of the metal towards the adsorption of reactants, which ultimately affects their reactivity.[3,5,16d] According to the d band theory[3,4] the closer is the d band centre is to the Fermi level, the stronger will be the bonds. The adsorption energy of carbon monoxide was shown to be lower for supported platinum-tin alloy particles in comparison to supported platinum because of the change in the electronic structure of platinum resulting in downshift of the platinum d DOS relative to the Fermi level.[34] DFT calculations have also shown that adsorption of carbon monoxide is more exothermic for nickel catalysts, which is also a d^9 system like platinum, in comparison to tin-nickel catalysts.[5b] The differences in both electronic and geometric structures have been proposed as the reasons for the difference in the reactivity of bimetallic nickel-tin and monometallic nickel catalysts. However, these lower values have also been associated with the ensemble effect of tin, which acts to dilute the platinum surface resulting in lower amount of adsorbed species.[7c,18] Adsorption on tin itself has been shown to be unfavorable.[35] Although we can not precisely identify the effect of the difference in the geometric structure on the absorption properties, the intense features in the HERFD spectrum of Pt/Al$_2$O$_3$ (Figure 4.5(a)) at 11572.8 eV and 11594.6 eV compared to PtSn/Al$_2$O$_3$ give a clear hint of differences in the geometric structure of platinum after alloying. The geometric difference might result from smaller particle size of platinum in bimetallic platinum-tin catalyst as previously suggested by lower coordination number of the Pt-Pt absorber-scatterer pair.[19b]

4.4.3. Hydrogen and carbon monoxide adsorption

As adsorption of reactants is the first and one of the essential steps for any catalytic process,[36] we have studied the structure of our catalysts after adsorption of hydrogen and carbon monoxide as both these adsorbates constitute the main reactants in many reactions. Our results show that the structure of monometallic and bimetallic systems changes significantly after adsorption of hydrogen and carbon monoxide. As explained above (Figure 4.1), interaction of the d band of a transition metal with adsorbates result in formation of anti-bonding and bonding states and result in the changes in the d band of the metal. After adsorption of hydrogen, Pt/Al$_2$O$_3$ shows a much more pronounced anti-bonding state and shift in the Fermi level than PtSn/Al$_2$O$_3$ (Figure 4.6(a)). Moreover, PtSn/Al$_2$O$_3$ experiences a smaller change in its structure upon adsorption of hydrogen (Figure 4.4(b)). This might be due to the geometric effect of alloying with tin

and to the different electronic structure of the alloy, which does not favour adsorption. This is also confirmed by the lower downward shift of the d band for $PtSn/Al_2O_3$ compared to Pt/Al_2O_3 (Figures 4.6(b) and (c)). Thus, the difference in the electronic structure between the two catalysts affects the bonding of hydrogen, as identified by the difference in the H/Pt values for these catalysts. In contrast, the adsorption of carbon monoxide results in a similar electronic and geometric structure of platinum for both samples (Figure 4.7). The HERFD spectra of both catalysts after adsorption of carbon monoxide are very similar. The resemblance of the whitelines and the intense features at 11581.2 eV, and 11594.6 eV for both the samples suggest that adsorption of carbon monoxide occurs on geometrically similar structures for monometallic and bimetallic systems. A previous study on bimetallic system of platinum gold clusters had shown that these clusters bind carbon monoxide more strongly than hydrogen.[37] The changes in the structure of monometallic platinum, gold, and bimetallic platinum gold clusters after adsorption of hydrogen[38] and ethene[39] have been reported previously. The reconstruction of the bimetallic particles has been proposed upon adsorption of carbon monoxide.[37,40] Our results have shown the big change in the structure of platinum in $PtSn/Al_2O_3$ after adsorption of carbon monoxide (Figure 4.4(b)), which suggests that stronger adsorption of carbon monoxide than hydrogen changes the particle geometry and the platinum-tin distribution.

We have successfully identified the structure of monometallic and bimetallic supported particles using HERFD and RIXS. This study shows the differences in the electronic and, to some extent, the geometric structure of these monometallic and bimetallic systems with d band of platinum shifting down relative to the Fermi level in the bimetallic system. The adsorption of hydrogen and carbon monoxide resulted in changes in the electronic structure of both the systems. However, the adsorption of carbon monoxide resulted in significant changes in the geometric structure of the mixed tin platinum particles.

4.5. Conclusions

The structure of nanometer sized monometallic platinum and bimetallic platinum tin particles was identified utilizing HERFD XAS and RIXS. The d band of platinum after alloying with tin becomes narrow and shows a downward shift relative to the Fermi level. These changes in the structure result in lower adsorption of hydrogen and carbon monoxide over bimetallic system than monometallic system. The electronic and

geometric structure of platinum in monometallic and bimetallic systems is very different after hydrogen adsorption but very similar after carbon monoxide absorption, which suggests that the geometric structure of the particles changes because of the strong adsorption of carbon monoxide.

References

1 (a) J. T. Kummer, J. Phys. Chem., 90 (1986) 4747; (b) R. J. Farrauto, R. M. Heck, Catal. Today, 51 (1999) 351.

2 (a) P. J. Feibelman, D. R. Hamann, Phys. Rev. Lett., 52 (1984) 61; (b) J. Harris, S. Andersson, Phys. Rev. Lett., 55 (1985) 1583; (c) M. H. Cohen, M. V. Gandugliapirovano J. Kudrnovsky, Phys. Rev. Lett., 72 (1994) 3222; (d) J. Singh, E.M, Alayon, M. Tromp, O.V. Safonova, P. Glatzel, M. Nachtegaal, R. Frahm, J.A. van Bokhoven, Angew. Chem. Int. Ed., 47 (2008) 9260.

3 B. Hammer, J. K. Nørskov, Adv. Catal., 45 (2000) 71.

4 (a) B. Hammer, J. K. Nørskov, Surf. Sci., 1995, 343, 211; (b) B. Hammer, J. K. Nørskov, Nature, 376 (1995) 238.

5 (a) J. R. Kitchin, J. K. Nørskov, M. A. Barteau, J. G. Chen, Phys. Rev. Lett., 93 (2004) 156801; (b) E. Nikolla, J. Schwank, S. Linic, J. Am. Chem. Soc., 131 (2009) 2747.

6 Y. Cai, H. G. Stenger, Jr., C. E. Lyman, J. Catal., 161 (1996) 123.

7 (a) M. T. Paffett, S. C. Gebhard, R. G. Windham, B.E. Koel, J. Phys. Chem., 94 (1990) 6831; (b) F. Buatier de Mongeot, M. Scherer, B. Gleich, E. Kopatzki, R.J. Behm, Surf. Sci., 411 (1998) 249; (c) M. M. Schubert, M. J. Kahlich, G. Feldmeyer, M. Hüttner, S. Hackenberg, H. A. Gasteiger, R. J. Behm, Phys. Chem. Chem. Phys., 3 (2001) 1123.

8 (a) R. M. Watwe, R. D. Cortright, M. Mavrikakis, J. K. Nørskov, J. A. Dumesic, J. Chem. Phys., 114 (2001) 4663; (b) C. J. Zhang, R. J. Baxter, P. Hu, A. Alavi, M. H. Lee, J. Chem. Phys., 115 (2001) 5272; (c) M. T. M. Koper, Surf. Sci., 548 (2004) 1.

9 (a) A. Nilsson, L. G. M. Pettersson, B. Hammer, T. Bligaard, C. H. Christensen, J. K. Norskov, Catal. Lett., 100 (2005) 111; (b) V. R. Stamenkovic, B. S. Mun, M. Arenz, K. J. J. Mayrhofer, C. A. Lucas, G. F. Wang, P. N. Ross, N. M. Markovic, Nat. Mater., 6 (2007) 241.

10 (a) K. Hämäläinen, D. P. Siddons, J. B. Hastings, L. E. Berman, Phys. Rev. Lett., 67 (1991) 2850; (b) F. M. F. de Groot, Coord. Chem. Rev., 249 (2005) 31; (c) P. Glatzel, U. Bergmann, Coord. Chem. Rev., 249 (2005) 65; (d) O. V Safonova, M. Tromp, J. A. van Bokhoven, F. M. F. de Groot, J. Evans, P. Glatzel, J. Phys. Chem B., 110 (2006) 16162; (e) J. A. van Bokhoven, C. Louis. J. T. Miller, M. Tromp, O. V. Safonova, P. Glatzel, Angew. Chem. Int. Ed., 45 (2006) 4651.

11 (a) P. Glatzel, U. Bergmann, W. Gu, H. Wang, S. Stepanov, B. S. Mandimutsira, C. G. Riordan, C. P. Horwitz, T. Collins, S. P. Cramer, J. Am. Chem. Soc., 124 (2002)

9668; (b) P. Glatzel, U. Bergmann, J. Yano, H. Visser, J. H. Robblee, W. Gu, F. M. F. de Groot, G. Christou, V. L. Pecoraro, S. P. Cramer, V. K. Yachandra, J. Am. Chem. Soc., 126 (2004) 9946.

12 (a) A. Nilsson, J. Hasselström, A. Föhlisch, O. Karis, L. G. M. Pettersson, M. Nyberg, L. Triguero, J. Elect. Spect. Rel. Phen., 110-111 (2000) 15; (b) T. Strunskus, O. Fuchs, L. Weinhardt, C. Heske, M. Guraya, M. Muhler, V. Staemmler, Ch. Wöll, J. Elect. Spect. Rel. Phen., 134 (2004) 183.

13 P. Glatzel, J. Singh, K. O. Kvashnina, J. A. van Bokhoven, J. Am. Chem. Soc., 132 (2010) 2555.

14 B. J. Kip, F. B. M. Duivenvoorden, D. C. Koningsberger, R. Prins, J. Catal. 105 (1987) 26.

15 (a) P. Meriaudeau, C. Naccache, A. Thangaraj, C. L. Bianchi, R. Carli, V. Vishvanathan, S. Narayanan, J. Catal., 154 (1995) 345; (b) E. Merlen, P. Beccat, J. C. Bertolini, P. Delichère, N. Zanier, B. Didillon, J. Catal., 159 (1996) 178; (c) J. L. Margitfalvi, I. Borbáth, M. Hegedűs, E. Tfirst, S. Gőbölös, K. Lázár, J. Catal., 196 (2000) 200; (d) G. Neri, C, Milone, S. Galvagno, A. P. J. Pijpers, J. Schwank, Appl. Catal. A: Gen., 227 (2002) 105.

16 F. W. Lytle, J. Catal., 43 (1976) 376; (b) A. N. Mansour, J. W. Cook, D. E. Sayers, J. Phys. Chem., 88 (1984) 2330; (c) D. Bazin, D. Sayers, J. J. Rehr, C. J. Mottet, J. Phys. Chem. B, 101 (1997) 5332; (d) J. A. van Bokhoven, J. T. Miller, J. Phys. Chem. C, 111 (2007) 9245.

17 M. C. Valero, P. Raybaud, P. Sautet, J. Catal., 247 (2007) 339.

18 (a) R. Bouwman, L. H. Toneman, A. A. Holscher, Surf. Sci., 35 (1973) 8; (b) D. A. Asbury, G. B. Hoflund, Surf. Sci., 199 (1988) 552.

19 (a) S. Pick, Surf. Sci., 436 (1999) 220; (b) J. M. R-Lopez, G. F. Santori, L. Giovanetti, M. L. Casella, O. A. Ferretti, F. G. Requejo, J. Phys. Chem. B, 107 (2003) 11441; (c) F. Delbecq, P. Sautet, J. Catal., 220 (2003) 115.

20 (a) F. B. Passos, M. Scmal, M. A. Vannice, J. Catal., 160 (1996) 106; (b) L. H. Jiang, G. Q. Sun, S. G. Sun, J. G. Liu, S. H. Tang, H. Q. Li, B. Zhou, Q. Xin, Electrochim. Acta, 50 (2005) 5384.

21 D. A. G. Aranda, M. Schmal, J. Catal., 171 (1997) 398.

22 (a) M. Arenz, V. Stamenkovic, B. B. Blizanac, K. J. Mayrhofer, N. M. Markovic and P. N. Ross, J. Catal., 232 (2005) 402; (b) V. Stamenkovic, M. Arenz, B. B. Blizanac, K. J. J. Mayrhofer, P. N. Ross, N. M. Markovic, Surf. Sci., 576 (2005) 145.

23 (a) S. H. Oh, R. M. Sinkevitch, J. Catal., 142 (1993) 254; (b) M. J. Kahlich, H. A. Gasteiger, R. J. Behm, J. Catal., 171 (1997) 93; (c) M. M. Schubert, M. J. Kahlich, H. A. Gasteiger, R.J. Behm, J. Power Sources, 84 (1999) 175; (d) O. Pozdnyakova, D. Teschner, A. Wootsch, J. Kröhnert, B. Steinhauer, H. Sauer, L. Toth, F. C. Jentoft, A. Knop-Gericke, Z. Paál, R. Schlögl, J. Catal., 237 (2006) 1.

24 S. Özkara, A. E. Aksoylu, Appl. Catal. A, 251 (2003) 75.

25 R. K. Herz, A. Badlani, D. R. Schryer, B. T. Upchurch, J. Catal. 141 (1993) 219.

26 (a) A. G. van den Bosch-Driebergen, M. N. H. Kieboom, A. van Dreumel, R. M. Wolf, F. C. M. J. M. van Delft, B. E. Nieuwenhuys, Catal. Lett., 2 (1989) 73; (b) J. A. Anderson, J. Catal., 142 (1993) 153.

27 S. R. de Miguel, M. C. Roman-Martinez, E. L. Jablonski, J. L. Fierro, D. Cazorla-Amoras, D. A. Scelza, J. Catal., 184 (1999) 514.

28 F. Coloma, A. Sepulveda-Escribano, J. L. G. Fierro, F. Rodriguez-Reinoso, Appl. Catal. A: Gen., 148 (1996) 63.

29 (a) A. G. T. M. Bastein, F. J. C. M. Toolenaar, V. Ponec, J. Catal., 90 (1984) 88; (b) K. Balakrishnan, J. Schwank, J. Catal., 138 (1992) 491.

30 (a) G. Blyholder, J. Phys. Chem., 68 (1964) 2772; (b) A. Palazov, Ch. Bonev, G. Kadinov, D. Shopov, G. Lietz, J. Völter, J. Catal., 71 (1981) 1.

31 G. Leclercq, L. Leclercq, R. Maurel, J. Catal., 50 (1977) 87.

32 J. A. Rodriguez, S. Chaturvedi, T. Jirsak, J. Herbek, J. Chem. Phys., 109 (1998) 4052.

33 J. L. Margitfalvi, I. Borbáth, M. Hegedűs, A. Szegedi, K. Lazar, S. Gőbölös, S. Kristyan, Catal. Today, 73 (2002) 343.

34 P. N. Ross, J. Vac. Sci. Technol. A, 10 (1992) 2546

35 J. Fearon, G. W. Watson, J. Mater. Chem., 16 (2006) 1989.

36 D. Loffreda, F. Delbecq, F. Vigné, P. Sautet, Angew. Chem. Int. Ed., 47 (2009) 8978.

37 B. D. Chandler, A. B. Schabel, L. H. Pignolet, J. Phys. Chem. B, 105 (2001) 149.

38 E. Bus, J. A. van Bokhoven, Phys. Chem. Chem. Phys., 9 (2007) 2894.

39 E. Bus, D. E. Ramaker, J. A. van Bokhoven, J. Am. Chem. Soc., 129 (2007) 8094.

40 R. Bouwman, W. M. H. Sachtler, J. Catal., 19 (1970) 127.

Chapter 5

Generating highly active partially oxidized platinum during oxidation of carbon monoxide over Pt/Al$_2$O$_3$

Abstract

The catalytically active species during the oxidation of carbon monoxide over alumina-supported platinum catalyst have been determined using in situ high-energy resolution fluorescence detection x-ray absorption spectroscopy, quick-EXAFS and kinetic measurements. The catalyst show sudden switches between a regime of low rate and one of high rate, depending on temperature and carbon monoxide and oxygen concentration. The spectroscopic data showed that the changes in reactivity are paralleled by structural changes in the catalyst. At low temperature, the surface is covered by carbon monoxide, which poisons the catalyst; during the switch to the highly active state, oxidized platinum is formed. During the ignition, increasing amount of platinum oxide was observed, which autocatalytically increased the conversion. High temperature and high concentration of oxygen are beneficial to achieving the highly active oxidic platinum.

Chapter 5

5.1. Introduction

The oxidation of carbon monoxide is one of the most intensely studied reactions in heterogeneous catalysis. The preferential oxidation (PROX) of carbon monoxide in a hydrogen-rich mixture is of considerable interest for the technical purification of the hydrogen feed gas.[1] Furthermore, because platinum is an active component of automotive three-way catalysts, the determination of the active structure of platinum for the oxidation of carbon monoxide, nitric oxide, and other hydrocarbons in the exhaust is relevant.[2] Ertl and co-workers showed that on single-crystals under low-pressure conditions, varying reconstruction of the platinum surface, which occurs after the adsorption of carbon monoxide, leads to carbon monoxide-rich and oxygen-rich domains that have different reaction rates.[3] In a low-activity regime over Pt(111), carbon monoxide is bound to the surface and the rate-limiting step is the desorption of this carbon monoxide.[4] The activation energy of the reaction after ignition is lowered from 176 to 59 kJ/mol. Similarly, on supported metal catalysts, little or no adsorbed carbon monoxide was detected under the high-activity conditions.[5]

Most researchers claim that metallic platinum is the active surface species for oxidation of carbon monoxide even in an oxygen-rich environment.[5b,6] Recent surface x-ray diffraction studies on surfaces of platinum single crystals[7] on the other hand, indicate that the rate of oxidation of carbon monoxide is higher when the surface is oxidized. Finally, it has been suggested that the active structure is a combination of metallic and oxidic phases on the supported metal catalysts.[8,9] Theoretical calculations have shown the important role played by partially oxidized metal surfaces in generating high catalytic activity over metal surfaces.[10] Furthermore scanning tunnelling microscopy revealed the high reactivity of an oxygen-rich ruthenium surface in the oxidation of carbon monoxide.[11]

In this chapter, the structure of a working supported metal catalyst is studied in a plug-flow reactor, combining in situ, time-resolved, and high-energy resolution fluorescence x-ray spectroscopy (HERFD XAS) with kinetic measurements by means of mass spectrometry, thus bridging the materials and pressure gaps. We demonstrate a highly dynamic behaviour of the reactivity and structure of the catalyst under changing conditions. XAS provides the local electronic and geometric structure of the platinum species. The intensity of the whiteline of an L_3 edge XAS spectrum reveals the unfilled d band and is sensitive to the metal oxidation state and the presence of adsorbates on the surface.[12d,13] The use of HERFD XAS improves the resolution of the spectra.[12b-e] The

sharper features in these spectra originate from the decreased final state core-hole lifetime broadening of one particular fluorescence channel, as detected by a secondary energy-selective spectrometer.[12a,c,e] Therefore, HERFD XAS provides more insight into the geometric and electronic structures of the active metal. We have established the influence of temperature and the ratio between carbon monoxide and oxygen on the rate of oxidation of carbon monoxide and on the structure of platinum under those conditions.

5.2. Experimental

The catalyst was prepared by incipient-wetness impregnation as explained in section 2.1. The particle size was determined by scanning transmission electron microscopy as explained in section 2.2. For the HERFD XAS experiments, all gases were ultra-pure and mixed to give the desired ratio of oxygen and carbon monoxide by means of six mass-flow controllers (MFCs), all of which were computer-controlled. The exhaust of the reactor, explained in section 2.6, was connected to a QIC-20 mass spectrometer (Hiden Analytical) to monitor the outlet gases. The amount of catalyst in the reactor was approximately 18 mg. The catalyst was treated in situ in 2% hydrogen in helium at 473 K before each experiment. Subsequently, the catalyst was exposed to an atmosphere of carbon monoxide and oxygen in varying mixtures. The partial pressure of carbon monoxide in all the experiments was kept constant at 0.04 bar. The measurements were done at a constant total flux of 25 ml/min through the reactor corresponding to a space velocity of about 54,000 h^{-1}. HERFD experiments were carried out at beamline ID 26 at the European Synchrotron Radiation Facility (ESRF), Grenoble, France. The electron energy was 6.0 GeV, and the ring current varied from 50 to 90 mA. The x-ray beam measured 0.3 mm horizontal and 1 mm vertical; the total flux was about $5*10^{12}$ photons/s. Spectra were collected before and during heating of the sample at 5 K/min to the temperature of maximum conversion; the ratio of oxygen to carbon monoxide was increased from one to five in an oxygen-rich environment. Furthermore, at constant temperature, spectra were collected at various ratios of oxygen to carbon monoxide; starting with a pre-oxidized sample and then decreasing the ratio respectively starting with a catalyst pre-reduced in carbon monoxide and then increasing the ratio of the two gases. Each HERFD XANES scan took one minute, after which a one minute EXAFS scan was recorded to allow normalisation of the data. QEXAFS experiments were carried out at the new superXAS beamline located at Swiss Light Source (SLS),

Villigen, Switzerland. The ring current was approximately 400 mA and operated in top-up mode. The polychromatic radiation from a superbend magnet, with a magnetic field of 2.9 Tesla and critical energy of 11.9 keV, was monochromatized using a channel cut Si(111) crystal in the QEXAFS monochromator.[15] The x-ray beam measured 0.1 mm horizontal and 0.1 mm vertical at the sample position; the total flux was about $3*10^{12}$ photons/s. Spectra were collected in transmission mode using two ionization chambers filled with air. For absolute energy calibration, the absorption of a platinum foil was always measured simultaneously between the second ionization chamber and a photo diode. The QEXAFS monochromator was oscillating at one Hz for the QEXAFS mode data collection, resulting in two spectra per second. Thus, QEXAFS spectra were collected with a time resolution of 0.5 seconds, during ignition and extinction while heating and cooling the sample at 2 K/min using a ratio of one between oxygen and carbon monoxide.

5.3. Results

5.3.1. Particle size

Figure 5.1a shows the STEM micrograph of 2 wt% Pt/Al_2O_3 after being reduced at 673 K in hydrogen for two hours. The bright spots represent the platinum particles. The darker area represents alumina and the dark area the copper grid. The average cluster size was about 0.9 nm with a narrow size distribution (Figure 5.1b).
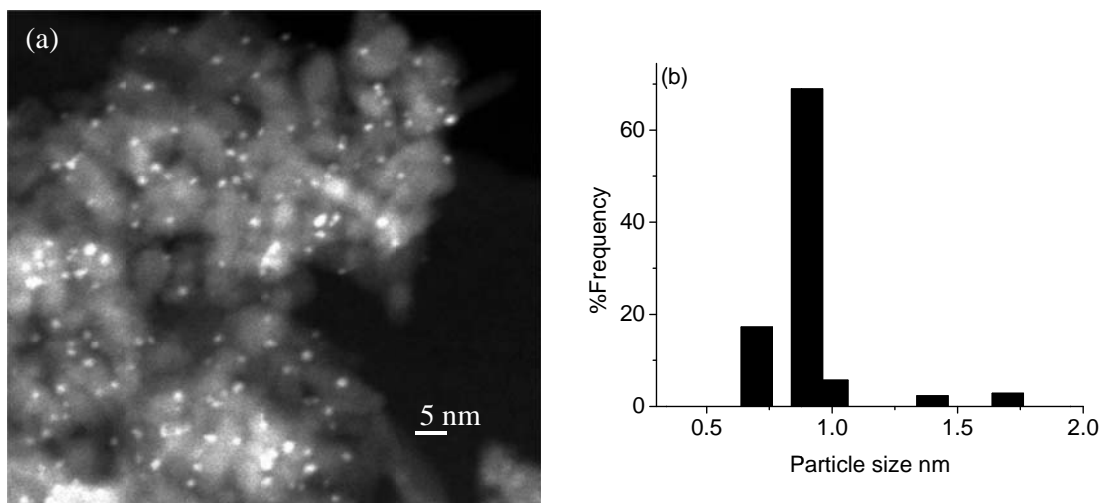

Figure 5.1: (a) STEM micrograph of 2 wt% Pt/Al_2O_3 prepared by incipient wetness impregnation and (b) particle size distribution of platinum particles.

5.3.2. Reaction regimes

Figure 5.2 shows the rate of oxidation of carbon monoxide as a function of temperature (5 K/min) at various oxygen to carbon monoxide ratios. At any particular temperature, higher oxygen concentrations always showed higher conversion, indicating a positive effect of the oxygen pressure on the conversion of carbon monoxide.[4,14] When ramping up the temperature, at a particular temperature there was a sudden increase in activity to the high-activity regime. This "ignition" occurred at lower temperature with increasing oxygen concentration (Table 5.1), which is in agreement with previous findings.[3b,4,5b,14d,14a] Heating was continued until the rate of oxidation of carbon monoxide was constant and the conversion of carbon monoxide was complete. As the temperature decreased, the rate of oxidation of carbon monoxide also decreased until, at a specific temperature, the reaction rate decreased suddenly, which is the so-called extinction. At all carbon monoxide to oxygen ratios, hysteresis occurred between ignition and extinction temperatures (Table 5.1). Table 5.1 also shows the temperature at the onset of carbon monoxide conversion.

Table 5.1: Results of kinetic measurements of oxidation of carbon monoxide over a 2 wt% Pt/Al$_2$O$_3$ catalyst.

O$_2$/CO ratio	ignition or extinction temperature (K)		hysteresis	temperature at onset of conversion (K)
	heating	cooling		
1	472	456	yes	340
2	445	440	yes	338
5	433	421	yes	329

5.3.3. HERFD XAS

Figure 5.3 shows the in situ Pt L$_3$ edge HERFD XAS spectra of Pt/Al$_2$O$_3$ as a function of temperature and thus conversion at oxygen to carbon monoxide ratios of one. Spectra were obtained every two minutes. Large changes occurred between spectra taken below and above the ignition temperature. Below ignition, a whiteline of low intensity was observed at 11569 eV. Moreover, it displayed a double feature, which is characteristic of adsorbed carbon monoxide on the platinum particles.[12d] With increasing temperature, the intensity of the shoulder decreased, which indicates desorption of carbon monoxide. Under a stream of carbon monoxide to oxygen ratio of one at 407 K (Figure 5.3a), at a

higher temperature than the ignition temperature, the spectra showed a strong increase in the intensity of the whiteline while the edge energy shifted to lower energy, which is characteristic of oxidized platinum.[12d] At this point the conversion of carbon monoxide was almost complete (Figure 5.2). The XAS spectra showed no further changes at higher temperatures. The spectra above ignition show very little structure above the whiteline, which suggests an amorphous structure of the oxide.
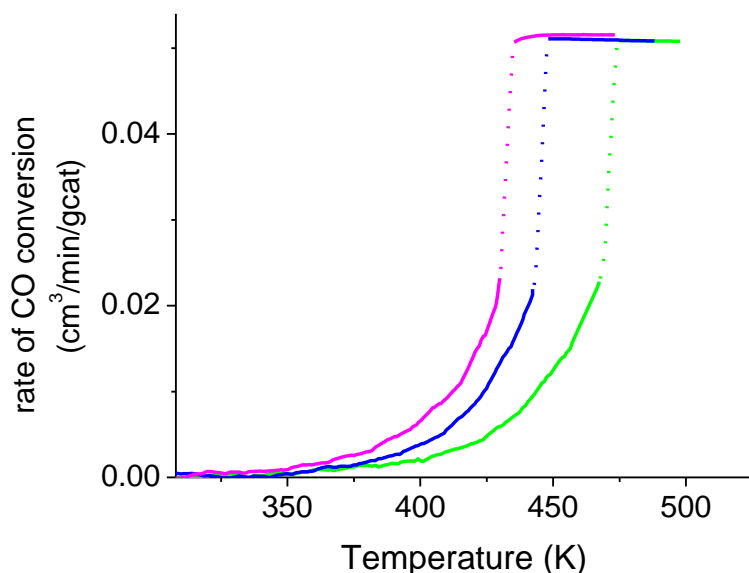

Figure 5.2: Rate of oxidation of carbon monoxide over 2 wt% Pt/Al_2O_3 during heating (5 K/min) at oxygen to carbon monoxide ratios of 1 (green), 2 (blue), and 5 (pink).
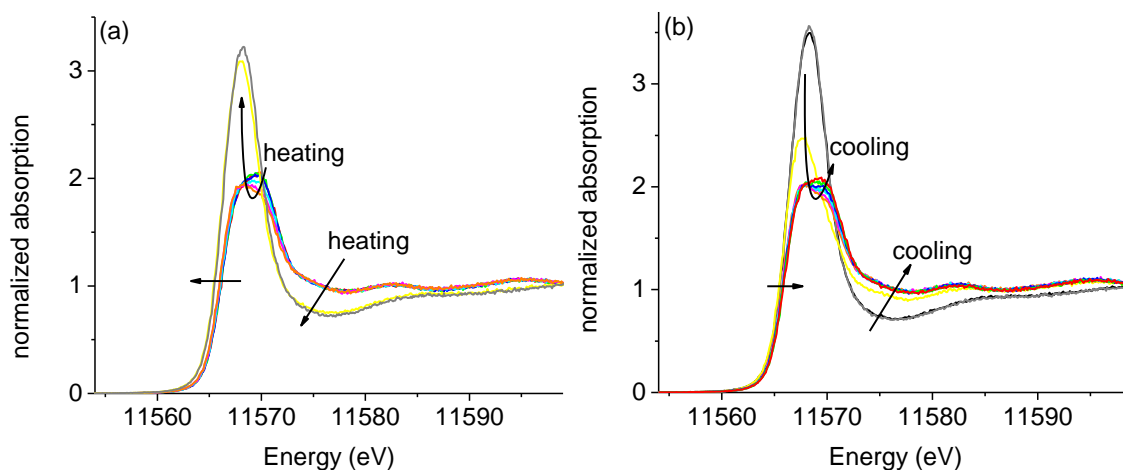

Figure 5.3: Pt L_3 edge HERFD XANES of 2 wt% Pt/Al_2O_3 during oxidation of carbon monoxide at an oxygen to carbon monoxide ratio of one (a) measured during heating at 308 K (red), 328 K (green), 361 K (blue) 394 K (cyan), 425 K (pink), 443 K (orange), 475 K (yellow), and 491 K (grey) and (b) during cooling at 503 K (black), 487 K (grey), 471 K (yellow), 453 K (orange), 421 K (pink), 387 K (cyan), 359 K (blue), 331 K (green), and 313 K (red). The ignition and extinction temperature were 472 and 456 K respectively. The arrows indicate the trends.

Under streams of oxygen to carbon monoxide ratios of two and five, the ignition temperature occurred at lower temperatures with increasing oxygen concentration, but identical spectral changes were observed below and above ignition (Figures 5.4a and 5.5a). Figure 5.3b shows the spectra as the catalyst cooled to 313 K under a stream of carbon monoxide to oxygen of one. At the extinction temperature, the intensity of the whiteline decreased and the doublet corresponding to adsorbed carbon monoxide re-appeared. As expected, its intensity increased further with decreasing temperature, because of the re-adsorption of carbon monoxide. Again, identical behaviour was observed for carbon monoxide to oxygen ratios of two and five, which showed different extinction temperatures, but identical changes occurred in the spectra above and below extinction temperature (Figures 5.4b and 5.5b).

5.3.4. Different gas environments

To determine the structure of the platinum catalyst in various gas environments, the catalyst was exposed to streams of oxygen and carbon monoxide in different ratios, either starting from pure oxygen, and increasing the carbon monoxide concentration or starting from pure carbon monoxide, and increasing the oxygen content. This experiment was performed below the ignition temperature. Figure 5.6 shows the Pt L$_3$ edge HERFD XAS spectra of Pt/Al$_2$O$_3$ at 398 K under these conditions.

5.3.5. Ignition

Insights into the structural changes that occurred during ignition were obtained with Quick Extended X-ray Absorption Fine structure (QEXAFS) measurements.[15,16] Figure 5.7 shows the spectra that were recorded with a time resolution of 0.5 s. For clarity, not all recorded spectra are shown. As soon as the ignition started, the whiteline increased in intensity. After only 9 s the changes in the spectra were complete. In this time period, the conversion of carbon monoxide increased from 53 to 89% (Figure 5.7b). The isobestic points in Figure 5.7a indicate that there is a direct conversion of reduced platinum to partial oxidized platinum.
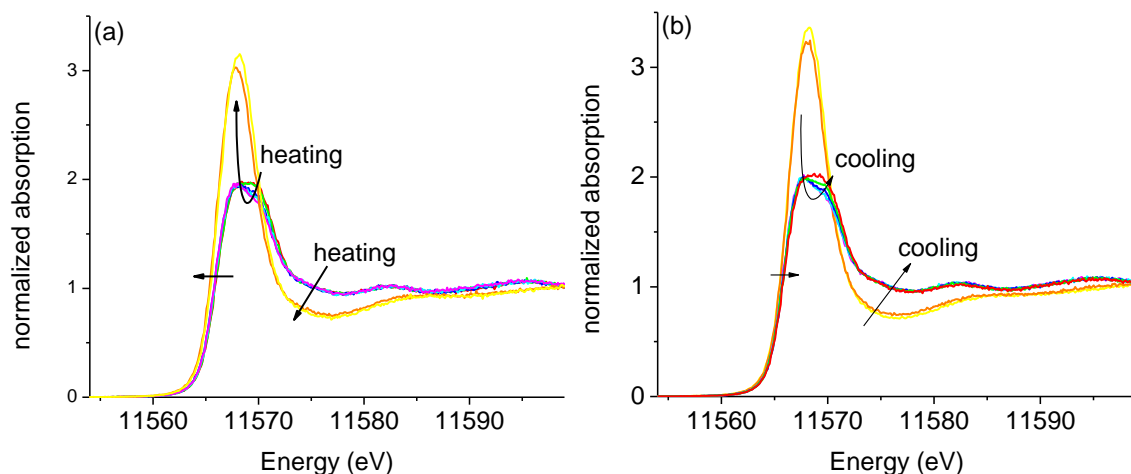
Figure 5.4: Pt L_3 edge HERFD XANES of 2 wt% Pt/Al_2O_3 during oxidation of carbon monoxide at an oxygen to carbon monoxide ratio of two measured (a) during heating at 308 K (red), 340 K (green), 386 K (blue) 422 K (cyan), 439 K (pink), 455 K (orange), and 472 K (yellow) and (b) during cooling at 488 K (yellow), 456 K (orange), 439 K (pink), 423 K (cyan), 396 K (blue), 339 K (green), and 311 K (red). The arrows indicate the trends.
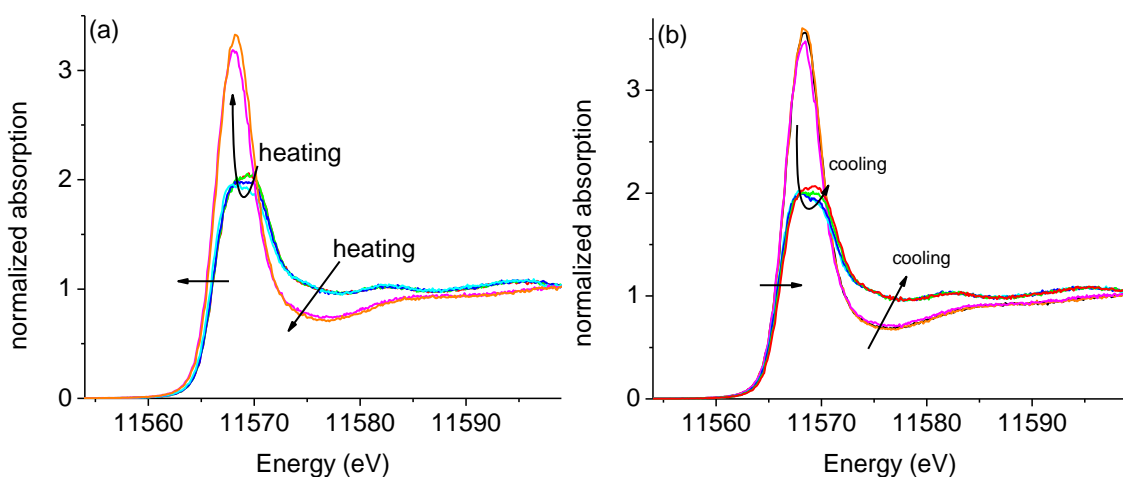

Figure 5.5: Pt L_3 edge HERFD XANES of 2 wt% Pt/Al_2O_3 during oxidation of carbon monoxide at an oxygen to carbon monoxide ratio of five measured (a) during heating at 308 K (red), 340 K (green), 385 K (blue) 422 K (cyan), 438 K (pink), 454 K (orange), and 472 K (yellow) and (b) during cooling at 473 K (black), 456 K (orange), 441 K (pink), 424 K (cyan), 397 K (blue), 340 K (green), and 314 K (red). The arrows indicate the trends.

All spectra show the characteristic doublet in the whiteline, which identifies carbon monoxide adsorbed on the surface except the spectrum that was measured under a stream of pure oxygen, which showed the high-intensity whiteline of oxidized platinum. The spectra indicate that traces of carbon monoxide are sufficient to reduce a pre-oxidized catalyst.
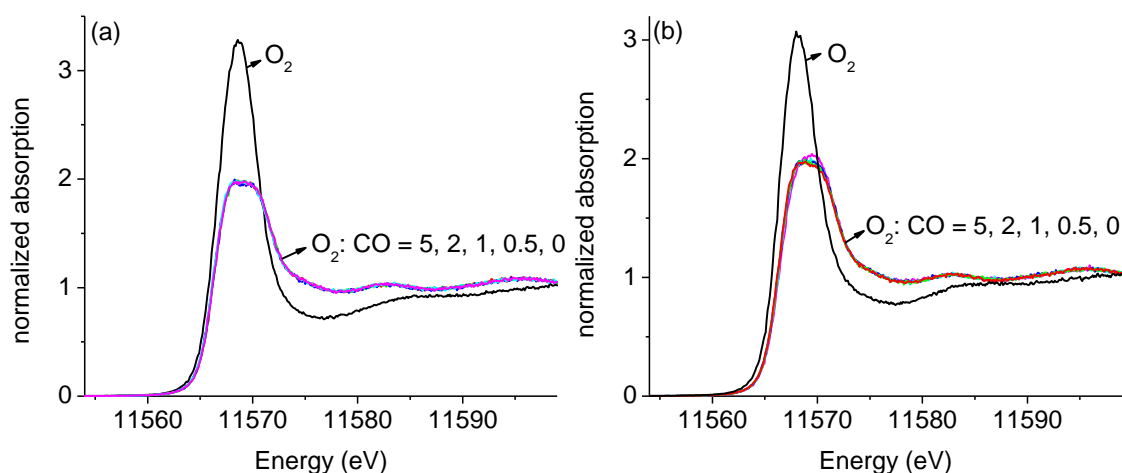
Figure 5.6: Pt L$_3$ edge HERFD XANES of 2 wt% Pt/Al$_2$O$_3$ during oxidation of carbon monoxide at 398 K starting (a) with an oxygen-rich environment and (b) with a carbon monoxide-rich environment at ratios of oxygen to carbon monoxide of ∞ (black), 5 (red), 2 (green), 1 (blue), 0.5 (cyan), and 0 (pink).
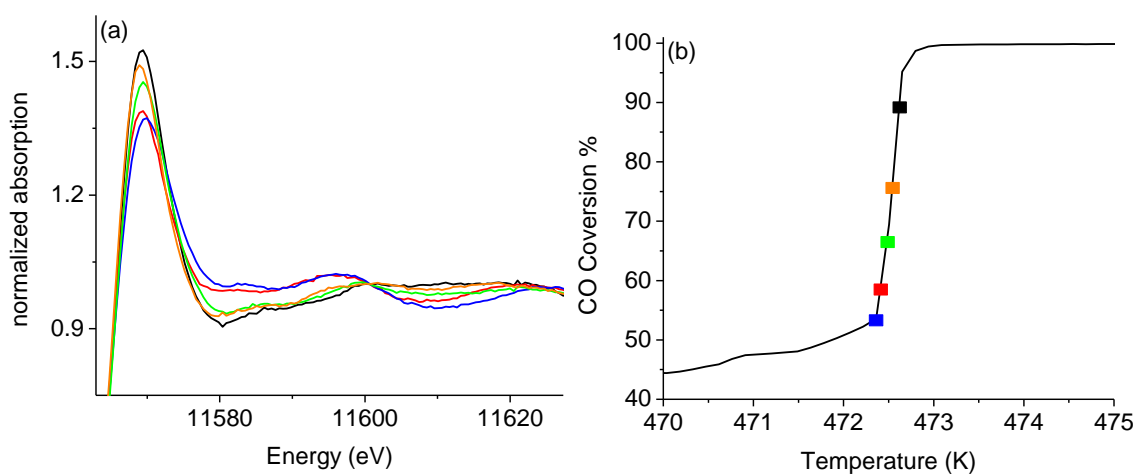

Figure 5.7: Pt L$_3$ edge XANES of 2 wt% Pt/Al$_2$O$_3$ recorded in QEXAFS mode (a) taken at start of ignition (blue), after 1.5 seconds (red), 4 seconds (green), 6.5 seconds (orange), and 9 seconds (black) after start of ignition; (b) percentage conversion of carbon monoxide during ignition, color coding of the squares correlate to the spectra in (a).

5.4. Discussion

5.4.1. Activity of catalyst

The two reaction regimes,[3b,4,5,14d] as seen in Figure 5.2 are characterized by different structures of the platinum particles. At low activity, adsorbed carbon monoxide on reduced platinum was observed (Figure 5.3), in general agreement with infra-red data [5b,6a,14b,14d] and at high activity, a large fraction of oxidized platinum was observed. High activity is found only at elevated temperature (Figure 5.1).[6a] Based on our in situ HERFD XAS data, the high-activity regime is characterized by the presence of large amounts of oxidic platinum. Earlier, infra-red studies showed that there is a minimal amount or no carbon monoxide on the surface of the catalyst at high temperature,[4,5b,5d] which agrees with the surface of the catalyst that is largely oxidic. There is a very sudden change in catalyst performance, which is paralleled by structural changes.

The in situ HERFD XAS and QEXAFS data suggest that oxidized platinum plays an active role in generating high activity. As soon as the surface is sufficiently depleted of carbon monoxide, oxygen reacts with the platinum surface, with a simultaneous increase of rate of oxidation of carbon monoxide. This decreases the concentration of carbon monoxide in the gas phase and further depletes the surface of carbon monoxide and subsequently increases the extent of surface oxidation, which additionally enhances the rate of reaction. The result is the autocatalytic enhancement in conversion.

5.4.2. Proposed model for oxidation of carbon monoxide

Figure 5.8 shows a diagram that gives an overview of the oxidation of carbon monoxide over supported platinum nano-particles. Below ignition temperature, the surface is covered with carbon monoxide and the reaction rate is low and determined by the desorption of carbon monoxide. At these temperatures, the platinum particles are reduced with adsorbed carbon monoxide, even in an oxygen-rich environment. As the temperature increases, some of the carbon monoxide is converted and increasingly desorbs from the platinum surface. At the ignition temperature, oxidic platinum forms and the rate suddenly increases. At high activity and temperatures above the ignition temperature, the particles are largely oxidic, which is proposed to be required to generate the highly active state of the catalyst.
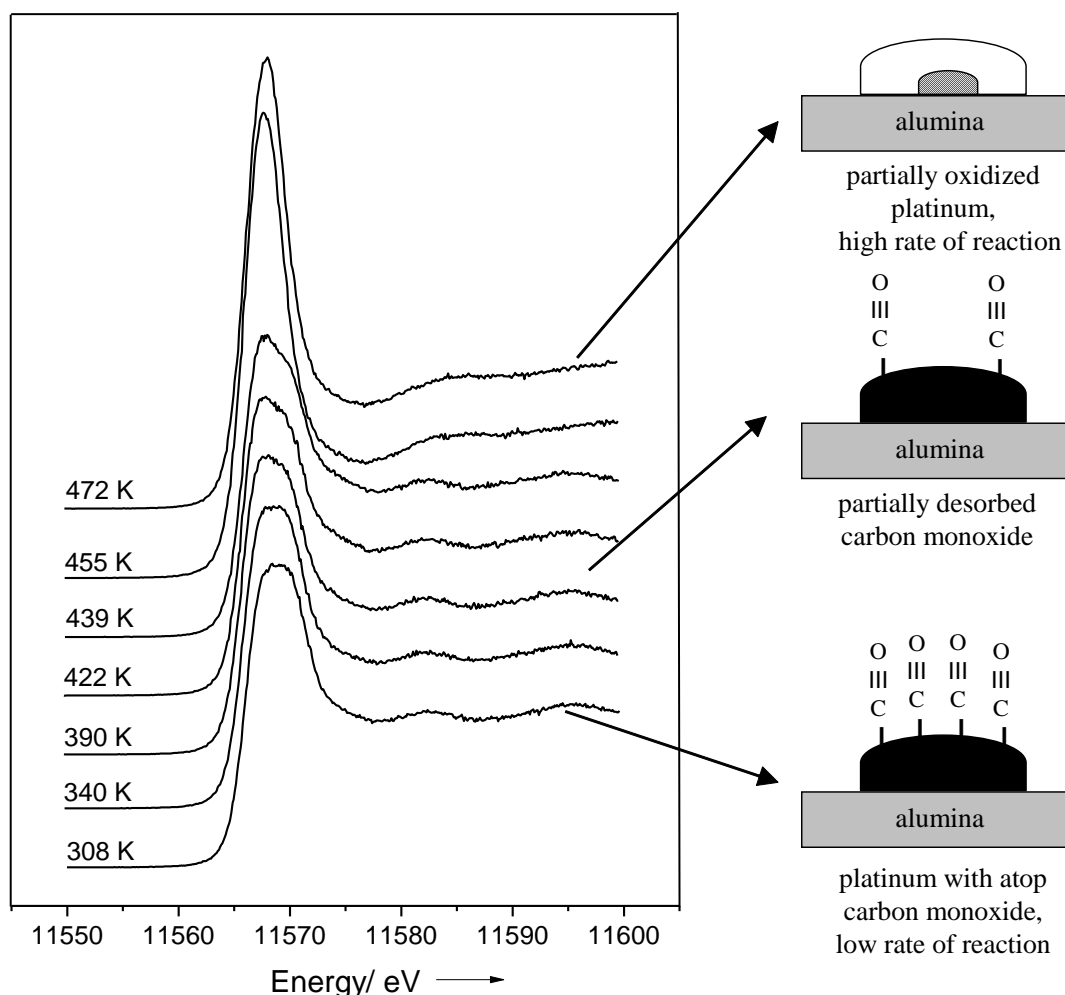
Figure 5.8: Diagram of oxidation of carbon monoxide over 2 wt% Pt/Al$_2$O$_3$.

5.5 Conclusions

The oxidation of carbon monoxide over alumina supported platinum nano-particles is sensitive to both the gas composition and the temperature. In situ HERFD XAS spectroscopy distinguished the active phases in the low- and the high-activity regimes: platinum adsorbed with carbon monoxide in the low-activity regime and oxidic platinum in the high-activity regime. Kinetics studies by mass spectroscopy identified the rapid change in the activity, which is paralleled by rapid change in catalyst structure as identified by QEXAFS. The ignition and extinction occur sudden, because the formation and disappearance of the more active phase are autocatalytic. High temperature and a high oxygen concentration are required to obtain the more active oxidic platinum catalyst.

References

1 C. D. Dudfield, R. Chen, P. L. Adcock, Int. J. Hydrogen Energy, 26 (2001) 763.

2 R. J. Farrauto, R. M. Heck, Catal. Today, 51, (1999) 351.

3 (a) G. Ertl, P. R. Norton, J. Ruestig, Phys. Rev. Lett., 49 (1982) 177; (b) G. Ertl, Surf. Sci., 287-288 (1993) 1; c) G. Ertl, Adv. Catal., 37 (1990) 213.

4 X. Su, P. S. Cremer, Y. R. Shen, G. A. Somorjai, J. Am. Chem. Soc., 119 (1997) 3994.

5 (a) F. J. Gracia, L. Bollmann, E. E. Wolf, J. T. Miller, A. J. Kropf, J. Catal., 220 (2003) 382; (b) P.-A. Carlsson, L. Oesterlund, P. Thormählen, A. Palmqvist, E. Fridell, J. Jansson, M. Skoglundh, J. Catal., 226 (2004) 422; (c) F. J. Gracia, S. Guerrero, E. E. Wolf, J. T. Miller, A. J. Kropf, J. Catal., 233 (2005) 372; (d) P.-A. Carlsson, V. P. Zhdanov, M. Skoglundh, Phys. Chem. Chem. Phys., 8 (2006) 2703.

6 (a) T. H. Lindstrom, T. T. Tsotsis, Surf. Sci., 150 (1985) 487; (b) J. A. Anderson, J. Chem. Soc. Faraday Trans., 88 (1992) 1197; (c) T. Visser, T. A. Nijhuis, A. M. J. van der Eerden, K. Jenken, Y. Ji, W. Bras, S. Nikitenko, Y. Ikeda, M. Lepage, B. M. Weckhuysen, J. Phys. Chem. B, 109 (2005) 3822.

7 M. D. Ackermann et al., Phys. Rev. Lett., 95(25) (2005) 255505.

8 R. Burch, P. K. Loader, Appl. Catal. B, 5 (1994) 149.

9 S. Yang, A. Maroto-Valiente, M. Benito-Gonzalez, I. Rodriguez-Ramos, A. Guerrero-Ruiz, Appl. Catal. B, 28 (2000) 223.

10 (a) C. Stampfl, M. Scheffler, Phys. Rev. Lett., 78 (1997) 1500; (b) X.-G. Wang, A. Chaka, M. Scheffler, Phys. Rev. Lett., 84 (2000) 3650; (c) K. Reuter, M. Scheffler, Phys. Rev. B, 65 (2001) 035406 d) K. Reuter, M. Scheffler, Phys. Rev. B, 68 (2003) 045407.

11 H. Over, Y. D. Kim, A. P. Seitsonen, S. Wendt, E. Lundgren, M. Schmid, P. Varga, A. Morgante, G. Ertl, Science, 287 (2000) 1474.

12 (a) K. Hämäläinen, D. P. Siddons, J. B. Hastings, L. E. Berman, Phys. Rev. Lett., 67 (1991) 2850; (b) F. M. F. de Groot, Coord. Chem. Rev., 249 (2005) 31; (c) P. Glatzel, U. Bergmann, Coord. Chem. Rev., 249 (2005) 65; (d) O. V. Safonova, M. Tromp, J. A. van Bokhoven, F. M. F. de Groot, J. Evans, P. Glatzel, J. Phys. Chem. B, 110 (2006) 16162; (e) J. A. van Bokhoven, C. Louis. J. T. Miller, M. Tromp, O. V. Safonova, P. Glatzel, Angew. Chem. Int. Ed., 45 (2006) 4651.

13 (a) D. E. Ramaker, D. C. Koningsberger, Phys. Rev. Lett., 89 (2002) 139701; (b) A. L. Ankudinov, J. J. Rehr, J. J. Low, S. R. Bare, Phys. Rev. Lett., 89 (2002) 139702; (c)

M. K. Oudenhuijzen, J. A. van Bokhoven, J. T. Miller, D. E. Ramaker, D. C. Koningsberger, J. Am. Chem. Soc., 127 (2005) 1530.

14 (a) N. W. Cant, P. C. Hicks, B. S. Lennon, J. Catal., 54 (1978) 372; (b) D. M. Haaland, F. L. Williams, J. Catal., 76 (1982) 450; (c) Y.-E. Li, D. Boeker, R.D. Gonzalez, J. Catal., 110 (1988) 319; d) P. T. Fanson, W. N. Delgass, J. Lauterbach, J. Catal., 204 (2001) 35.

15 (a) R. Frahm, Nucl. Instrum. Methods A, 270 (1988) 578; (b) R. Frahm, Rev. Sci. Instrum., 60 (1989) 2515; (c) R. Frahm, B. Griesebock, M. Richwin, D. Lützenkirchen-Hecht, Proc. 8th Int. Conf. Synchrotron Radiation Instumentation (San Francisco, USA) 2004, pp. 1411; (d) R. Frahm, B. Griesebock, D. Luetzenkirchen-Hecht, Phys. Scrip., T115 (2005) 974.

16 A. J. Dent, Top. Catal., 18 (2002) 27.

Chapter 5

Chapter 6

CO oxidation over supported platinum catalysts with different supports

Abstract

In situ x-ray absorption spectroscopy identified the role of oxidized platinum species, in generating a high-activity state in the oxidation of carbon monoxide over Pt/Al_2O_3, Pt/TiO_2 and Pt/SiO_2. The disordered oxide formed has platinum with low coordination in oxygen, suggesting a strongly defected platinum oxide with a lower coordination than octahedral and possibly square planar. Two activity regimes were identified: low-activity at high carbon monoxide concentration and low temperature, and high activity at low carbon monoxide concentration and high temperature. The change between the two regimes occurred suddenly; there was ignition when going from low to high activity, and extinction from high to low activity. Ignition only occurred when the concentration of oxygen was higher than that of carbon monoxide. The catalyst was metallic and covered with carbon monoxide at low activity and partially oxidic at high activity. Carbon monoxide poisoned the catalyst at low activity. The partially oxidized platinum catalysts showed high activity. The catalyst structure showed a dynamic behavior and the amount of oxide depended on the concentration of reactants in the gas phase. Smaller particles of Pt/Al_2O_3 reached high activity at lower temperature than the larger particles. Pt/TiO_2 reached high activity at the lowest temperature while Pt/SiO_2 required the highest temperature. Parallel with the temperature of ignition, Pt/SiO_2 was the most oxidized while Pt/TiO_2 was the least oxidized.

Chapter 6

6.1. Introduction

The catalytic properties of platinum remain one of the most fascinating subjects of study. While it belongs to the family of noble metals because of its rarity in the earth's crust and its resistance to corrosion, it has a different chemical behavior than the other noble metals copper, silver, and gold. Its extended d-orbitals enable chemisorption of adsorbates that subsequently react and desorb to complete the catalytic cycle. In spite of the wide importance platinum has gained in industry, and the extensive research performed on its catalytic behavior, the fundamental aspects of adsorption, reaction, and desorption that occur at its surface continue to be debated. Understanding what is happening at the catalyst surface and what the structure of the catalytically active phase is, are important for controlling the kinetics of the reaction in terms of activity, selectivity, and stability. Structural characterization is most relevant when performed under reaction conditions, which is generally at high pressure and temperature.[1] X-ray absorption spectroscopy (XAS) is an element-specific technique that enables structural analysis under catalytically relevant conditions.[2,3] The Pt L_3 whiteline, which is the first intense feature in the spectrum, is sensitive to the oxidation state of the catalyst as it reflects the empty d-density of states. The Pt L_3 x-ray absorption near-edge structure (XANES) is also sensitive to the local geometry and to the presence of adsorbates on the surface of the nanoparticles and the shape of the whiteline reveals the mode of adsorption.[4-6] The extended x-ray absorption fine structure (EXAFS) function is dependent on the local structure of the absorbing platinum atom. It provides coordination number, inter-atomic distance, and Debye-Waller factor.[2]

The catalytic oxidation of carbon monoxide is the key reaction during the preferential oxidation of carbon monoxide in a hydrogen feed gas mixture in fuel cells, where it is crucial to decrease the carbon monoxide concentration below 50 ppmv.[7] It is also one of the reactions occurring in a three-way catalytic converter, where the pollutant gases are transformed into less harmful ones. Despite the seeming simplicity of carbon monoxide oxidation, the structure of the catalyst and the mechanism at high activity are still debated. Structural transformation of the platinum catalyst during carbon monoxide oxidation, both on single crystals and supported particles, has been reported. On a single crystal of Pt(100),[8,9] a transformation occurs from a hexagonal phase to a (1x1) phase with islands of c(2x2) when going from a low to a high carbon monoxide surface concentration. This surface phase transition[8] has been identified to be the driving force for the kinetic oscillations in catalytic carbon monoxide oxidation because the adsorption

properties of the surface switch with the transition. The experiments were carried out on clean single crystals under ultra-high vacuum in a system equipped with LEED, AES, and work function measurement facilities. A possible formation of an oxide was linked to the presence of surface impurities, thus the surface of the catalyst was repeatedly cleaned to suppress oxide formation. Later experiments performed with scanning tunneling microscopy[10] and surface x-ray diffraction[11] on a single crystal of Pt(110) surface near atmospheric pressure showed a roughening of the surface coinciding with a sudden increase in catalytic activity for carbon monoxide oxidation. This switching of surfaces was attributed to a change in the surface composition. When the carbon monoxide concentration dropped below a particular value, the surface oxidized. This oxidized surface showed higher catalytic activity than the metallic surface.[10,11] To mimic industrial supported catalysts, nano-meter sized metal particles of platinum were deposited on silica, titania and alumina in ordered arrays by electron beam lithography. Carbon monoxide oxidation was performed at a few hundred Torr in various carbon monoxide and oxygen ratios and the total pressure brought to atmospheric pressure with helium. The reaction became sustainable above an ignition temperature, at which new carbon monoxide species, which were active for oxidation, were identified.[12] However, because the oxidic species has less affinity for carbon monoxide adsorption and the enhancement of conversion occurred at high temperature, metallic platinum was identified as the active surface for carbon monoxide oxidation.[13,14] Oxidation was also associated to catalyst deactivation during rate oscillations corresponding to periodic oxidation and reduction of the silica-supported platinum catalyst.[15] From previous results the low surface concentration of carbon monoxide at high temperature enabled oxygen to react with the platinum surface, which switched the reaction from being limited by desorption of the carbon monoxide to a regime with a different rate limiting step. The result was a higher rate of reaction and a partially oxidized catalyst. The enhanced conversion of carbon monoxide depleted the gas phase carbon monoxide concentration further, which decreased the surface concentration of carbon monoxide. This increased the extent of surface oxidation and caused an autocatalytic ignition of the reaction.[16]

The size of supported platinum particles strongly affects their catalytic performance.[13,17,18] Moreover, the type of support and the interface between particles and support influence the catalytic turnover.[19-25] Thus, the important factors controlling catalytic activity over platinum are particle size, support, and the active phase. It is our goal to determine the structure of the active catalyst under reaction conditions, and to

determine the effect of particle size and that of the support. In this chapter, the behavior of nano-sized platinum on Al_2O_3, TiO_2 and SiO_2 is compared during CO oxidation and their structure under catalytic conditions using in situ Pt L_3 XAS is determined. The influence of particle size in Pt/Al_2O_3 is determined.

6.2. Experimental

2 wt% Pt/Al_2O_3 was prepared by incipient-wetness impregnation as explained in section 2.1. Two sets of this catalyst were synthesized. 3 wt% Pt/TiO_2, and 2 wt% Pt/SiO_2 were prepared as explained in section 2.1. The size and shape of the platinum nanoparticles were observed by transmission electron microscopy (TEM) with a Tecani F30 microscope operating at 300 kV as explained in section 2.2.

Each of the catalysts was sieved to 63-125 μm, before loading in a plug flow (tubular packed bed) reactor, which was 1.6 mm in internal diameter, and which could accommodate 18 to 21 mg of the supported platinum catalysts depending on their density. The reactor also functioned as a transmission and/or fluorescence cell for x-ray absorption spectroscopy as explained in section 2.6. In addition, 2 wt% Pt/Al_2O_3 catalyst was loaded in a thin bed reactor, which accommodated 150 mg of the catalyst. This cell also functioned as a transmission cell for XAS. Table 6.1 summarizes the catalyst loadings. Before a reaction, the catalyst was reduced in a sequence shown in Table 6.2. The total gas flowrate was always 30 mL/min corresponding to a space velocity of 0.06 s through the catalyst bed or a weight hourly space velocity (WHSV) of 15 to 26 g_{gas} h^{-1} g_{cat}^{-1} depending on the gas mixture and catalyst loading in the plug flow reactor. After the pretreatment, a reactant gas mixture consisting of 10 mL/min of 10% oxygen in helium, 1 mL/min of carbon monoxide, and 19 mL/min of helium was fed to the reactor. This corresponds to a three percent carbon monoxide feed and an oxygen/carbon monoxide ratio of one. Temperature was ramped up using 2°C/min until a 100% conversion in carbon monoxide was observed from the mass spectrometer traces of carbon monoxide, oxygen, and carbon dioxide. At two to five degrees higher than the temperature of maximum conversion, the carbon monoxide flow was increased to 1.25 mL/min, yielding a four percent carbon monoxide in the feed, while maintaining the total flowrate at 30 mL/min. This resulted in a conversion in carbon monoxide of less than 100%. Flow rates were always returned to their initial values before the temperature was ramped down at 2°C/min to room temperature.

Table 6.1: Summary of catalytic properties of supported platinum catalysts in the oxidation of carbon monoxide

catalyst	particle size (nm)	wt % platinum	amount of catalyst (mg)	platinum loading (mg)	ignition temperature (°C)	extinction temperature (°C)	hysteresis (°C)
s-Pt/Al$_2$O$_3$	0.9	2	18.4	0.4	204	195	9
b-Pt/Al$_2$O$_3$	2.0	2	18.0	0.4	226	191	35
b-Pt/Al$_2$O$_3$[a]	2.0	2	150.0	3.0	169	115	40
Pt/TiO$_2$	1.3	3	21.2	0.6	188	145	43
Pt/SiO$_2$	1.9	2	18.0	0.4	299	281	18

[a] measured in thin bed reactor

Table 6.2: Gas treatment and reaction conditions

step	gas	flow (mL/min)	temperature ramp (°C/min)	temperature (°C)
Reduction sequence				
1	He	30.0	-	35
2	10% H$_2$/He	30.0	5	-
3	10% H$_2$/He	30.0	-	200
4	He	30.0	-	200
5	He	30.0	5	-
6	He	30.0	-	35
Heating to maximum CO conversion				
7	10% O$_2$/He	10.0	2	ramp
	CO	1.0		
	He	19.0		
Increasing CO flow				
8	10% O$_2$/He	10.0	0	-
	CO	1.25		
	He	18.75		
Cooling to room temperature				
9	10% O$_2$/He	10.0	2	ramp
	CO	1.0		
	He	19.0		

XAS measurements were performed at the X10DA (superXAS) beamline at the Swiss Light Source, Villigen, Switzerland. Beam size was approximately 100 μm by 115 μm. Spectra were collected either in fluorescence or transmission geometry depending on the

support. During ramping up and down the temperature, XANES spectra were recorded from 11.545 to 11.600 keV. One XANES scan took four minutes, which corresponds to an eight degree span from start to finish using a ramp of two degrees per minute. Under stable temperature and flow conditions, EXAFS scans were recorded from 11.350 to 12.200 keV. It took about 30 minutes to complete one EXAFS scan. Multiple scans were averaged to improve the signal to noise ratio. Data reduction for the XAS spectra was done using standard procedures,[2,3] as explained in section 2.3.1. Multiple shell fitting was performed in R-space (1.5 < R < 3.5) after Fourier transformation (2.5 < k < 12), and using a k-weighting of three for platinum-platinum scatterer pairs and two for the spectra that contained a mixture of platinum-oxygen and platinum-platinum pairs.

6.3. Results

6.3.1 Particle size

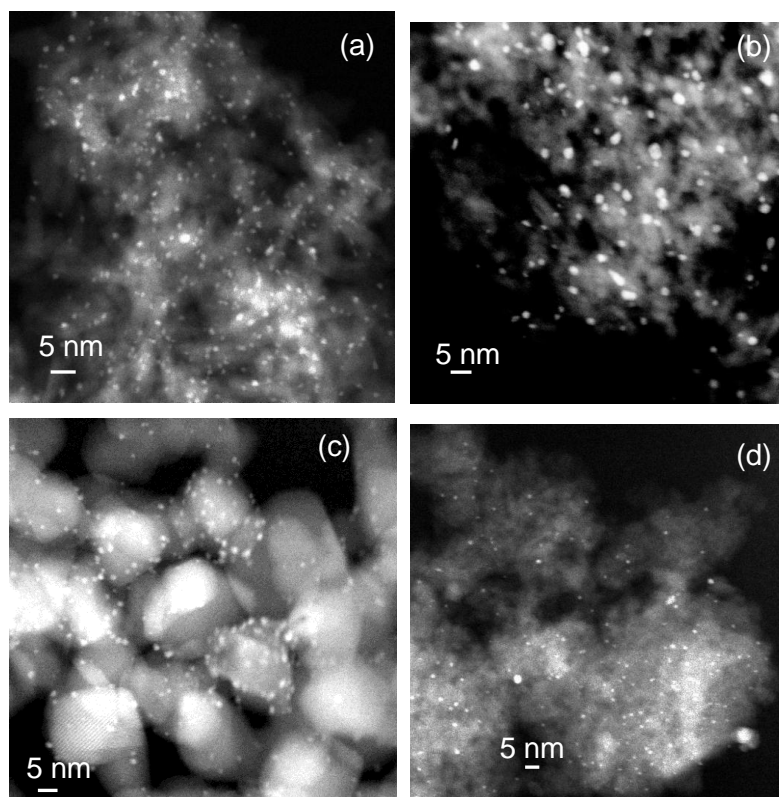Figure 6.1 shows TEM micrographs of the supported platinum catalysts.

Figure 6.1: TEM images of the supported platinum catalysts (a) Pt/Al_2O_3 small particles, (b) Pt/Al_2O_3 big particles, (c) Pt/TiO_2, and (d) Pt/SiO_2.

The little bright dots are the platinum particles and the larger light gray areas are the metal oxide supports. The small platinum on alumina particles (referred to as $s-Pt/Al_2O_3$)

were mainly 0.9 nm; the bigger platinum on alumina (b-Pt/Al$_2$O$_3$) particles 2.0 nm; the platinum on titania particles 1.3 nm, and the platinum on silica particles 1.9 nm. The particles on the latter support showed a significant fraction of larger particles.

6.3.2 Kinetic data

Table 6.1 summarizes the results of the kinetic measurements. Figure 6.2 shows the normalized intensity signals from the mass spectrometer traces of carbon monoxide, oxygen, and carbon dioxide coming out of the reactor during carbon monoxide oxidation over s-Pt/Al$_2$O$_3$, and the temperature of the reactor. Figure 6.3 displays the corresponding carbon monoxide conversion curve as function of temperature. The points marked with letters A to E in Figure 6.2 correspond to those in Figure 6.3. Starting at room temperature, the conversion of carbon monoxide increased exponentially with temperature. At 204°C (B), a sudden jump in carbon monoxide conversion was observed and the catalyst reached a high activity state, at which the conversion in carbon monoxide was about 54 mL/min/g$_{cat}$ or 1.3 x 10^{21} molecules/min/g$_{cat}$. This jump is called ignition. At 21200 seconds (C), the carbon monoxide flow was increased to 1.25 mL/min and the flow of helium was decreased to maintain the total flow at 30 mL/min. The resulting conversion was about 97%. At 28800 seconds (D), the carbon monoxide and helium flows were returned to 1 and 18 mL/min respectively and the conversion returned to 100%. Upon decreasing temperature, a sudden jump to 42% conversion was observed at 195°C (E). This reverse jump is called extinction and the catalyst returned to the low activity state. Hysteresis of 9°C between the two activity regimes was observed. Ignition curves for carbon monoxide oxidation over a polycrystalline platinum wire were previously reported,[26] but emphasis was more on the evolution of catalyst temperature with time. More recently, ignition and extinction during carbon monoxide oxidation over platinum were also identified,[27] however these terms were used to identify the temperature at which 50% of carbon monoxide converted. This 50% conversion point is referred to as light-off temperature in literature. Carbon monoxide conversion curves with temperature, including a similar oxygen/carbon monoxide ratio were presented earlier[18] but only light-off conditions were identified and not jumps in conversion. Ignition and extinction were indicated in the carbon monoxide conversion plots[28] where the relationships among the kinetic parameters under conditions of catalyst surface ignition during selective carbon monoxide oxidation on Pt/Ru/ceramic support were investigated.
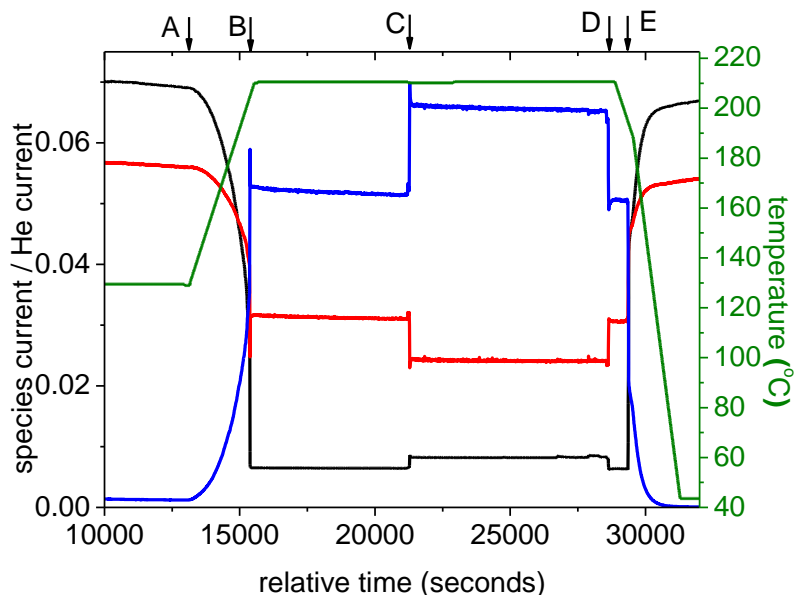
Figure 6.2: Mass spectrometer traces of carbon monoxide (black), oxygen (red), and carbon dioxide (blue) normalized to the helium signal and the temperature profile (green) during carbon monoxide oxidation over s-Pt/Al$_2$O$_3$.
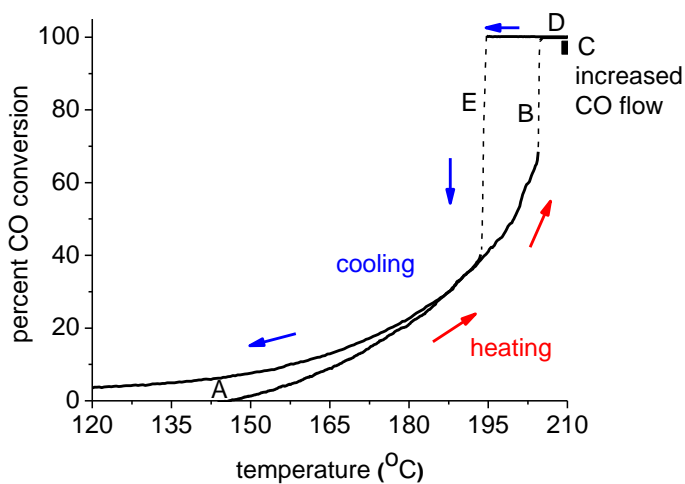

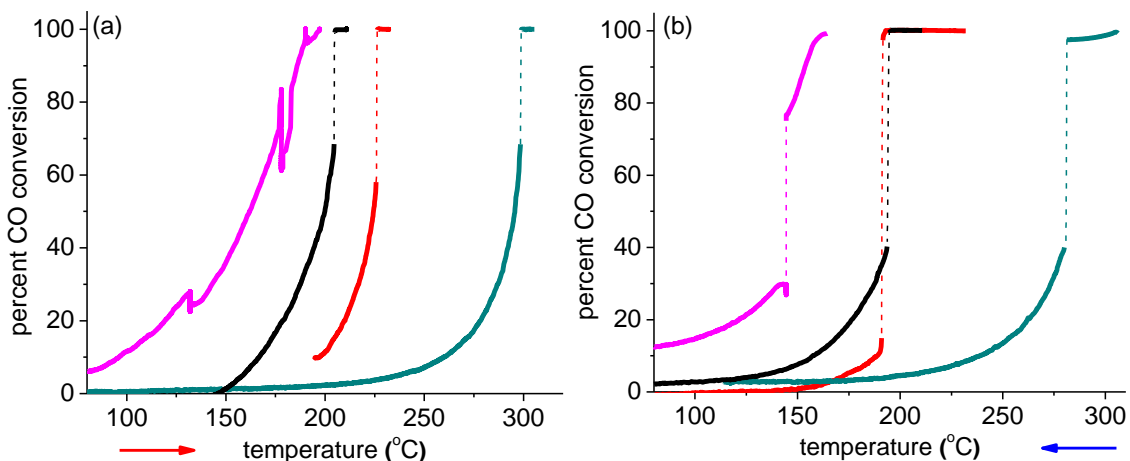Figure 6.3: Conversion plot of carbon monoxide with temperature over s-Pt/Al$_2$O$_3$.

Figure 6.4: Comparison of the heating (a) and cooling (b) curves for the different supported platinum catalysts: Pt/TiO$_2$ (pink), s-Pt/Al$_2$O$_3$ (black), b-Pt/Al$_2$O$_3$ (red), and Pt/SiO$_2$ (green).

For all catalysts reported in this chapter, the trend is similar to that observed for the s-Pt/Al$_2$O$_3$ particles, however with distinctly different ignition and extinction temperatures. Figure 6.4 shows the conversion plot against temperature during heating and cooling over the b-Pt/Al$_2$O$_3$, Pt/TiO$_2$, and Pt/SiO$_2$. During heating, the platinum catalyst supported on TiO$_2$ reached the high activity region at the lowest temperature. Ignition was at 188°C, which was already near to maximum conversion. The first two breaks in the conversion curve for Pt/TiO$_2$ correspond to the points where temperatures were held constant for about 1.5 hours for taking EXAFS scans. Pt/TiO$_2$ switched to low conversion at 145°C, which is the lowest extinction temperature of all catalysts measured here. Pt/SiO$_2$ required the highest temperature, 299°C, to switch to the high activity region. Pt/SiO$_2$ jumped back to low activity also at the highest temperature, 281°C. The b-Pt/Al$_2$O$_3$ and s-Pt/Al$_2$O$_3$ catalysts were intermediate between Pt/TiO$_2$ and Pt/SiO$_2$ in terms of activity and the temperatures required for ignition and extinction. The temperatures of ignition and extinction showed some variation upon varying the amount of catalyst, flowrates, and temperature ramps. This indicates that ignition and extinction occur in an unstable reaction regime. The conversion of carbon monoxide was also determined with b-Pt/Al$_2$O$_3$ mounted in a thin bed reactor. The switch from low to high activity and the inverse switch from high to low activity occurred at lower temperatures than when the same catalyst was mounted in the plug flow reactor (Table 6.1). After ignition, the conversion reached only about 70% probably because of unfavorable flow conditions. The total flowrate was double that of the plug flow by increased helium flow. The different observations cannot be attributed solely to the different flows and flow scheme in the two types of reactors, since the thin bed reactor contained much more catalyst than the plug flow reactor, 150 mg versus 18.0 mg.

3.3. XANES spectra

Figure 6.5 shows the Pt L$_3$ XANES spectra of platinum in the metallic and in the Pt^{4+} oxidized state. In the metallic state, the whiteline showed a maximum absorption of 1.25, less compared to that in the oxidic state of 2.25. The metallic spectrum showed two bands at 11.580 and 11.596 keV immediately after the whiteline region. The oxidic spectrum showed a characteristic dip after the whiteline, and showed fine structure at 11.582 and 11.590 keV.
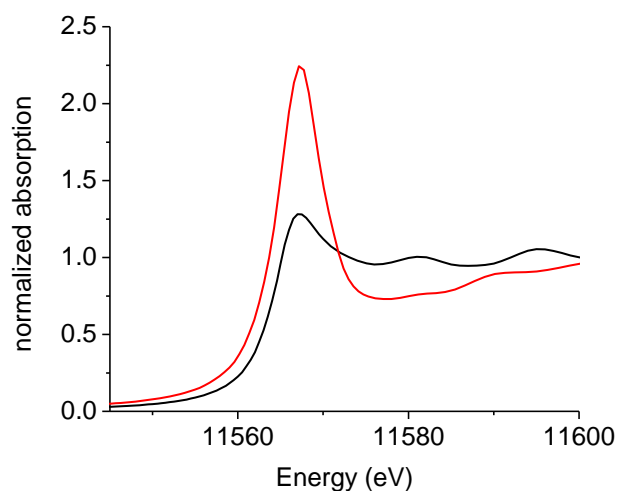
Figure 6.5: Pt L$_3$ XANES of references: α-PtO$_2$ (red), and platinum foil (black).
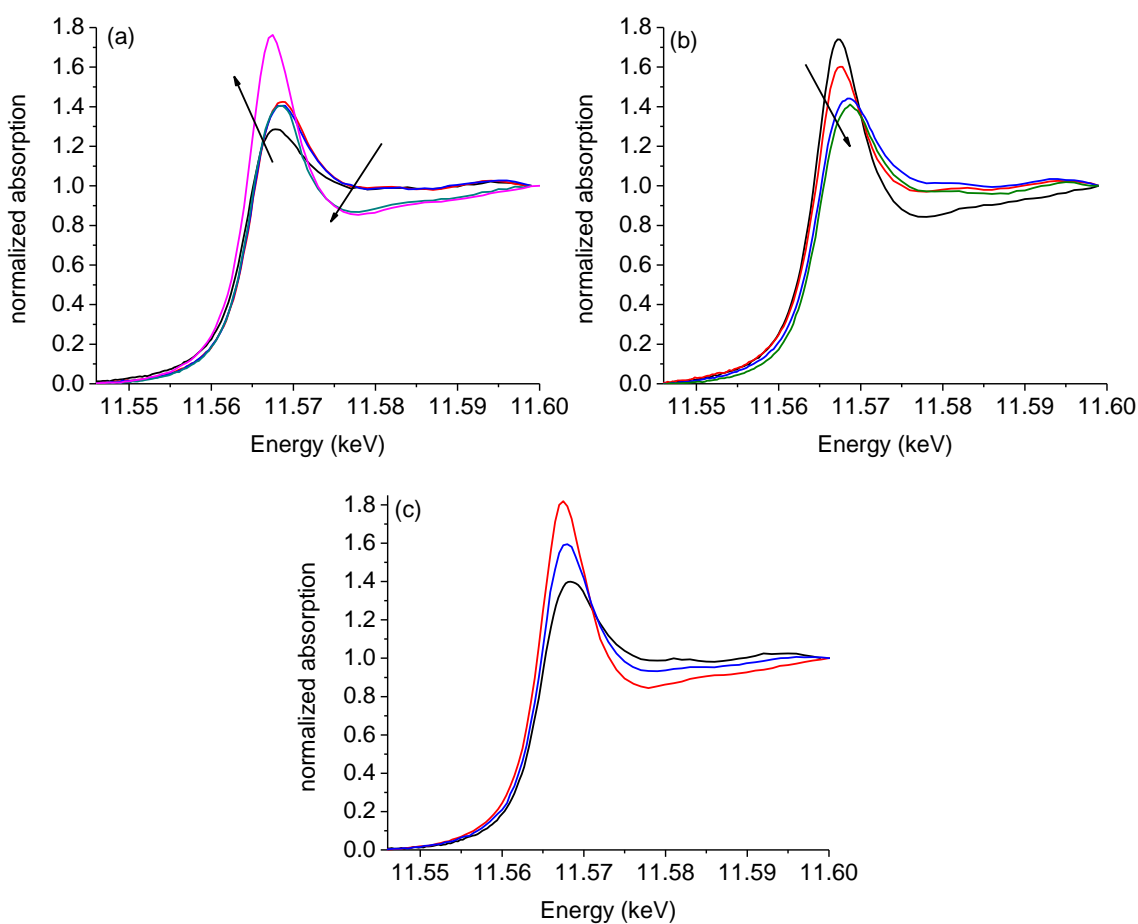
Figure 6.6: Pt L$_3$ XANES spectra recorded during heating (a) at 145°C in helium (black), 150°C in oxygen and carbon monoxide (red), 174°C (blue), 198°C (green), and 211°C (pink), during cooling (b) at 207°C (black), 199°C (red), 183°C (blue), and 83°C (green), and at the region of high activity (c) below ignition at 190°C (black), above ignition at 211°C and 100% conversion (red), and above ignition at 210°C and 97% conversion (blue) of s-Pt/Al$_2$O$_3$; ignition occurred at 204°C, extinction at 195°C.

Figures 6.6a and 6.6b compare the Pt L_3 XANES spectra measured while heating and cooling s-Pt/Al$_2$O$_3$ under the flow of oxygen/carbon monoxide with a ratio of one at various temperatures. The indicated temperatures refer to the beginning of each scan. The spectrum at 145°C was taken in an atmosphere of helium after reduction and removal of hydrogen. The spectrum showed a whiteline intensity similar to that of the platinum foil in Figure 6.5. The bands at energies above the whiteline were subdued compared to that of the platinum foil spectrum but the characteristic feature of the wiggles was the same. This spectrum shows that the small platinum particles were in a reduced state after reduction and removal of hydrogen.

The spectrum at 150°C was obtained in a mixed carbon monoxide and oxygen atmosphere. Compared to the one recorded in helium, there was an increase in intensity and broadening of the whiteline to the high energy side, which is indicative of platinum with carbon monoxide adsorbed on the surface.[6,16] The features after the absorption edge overlapped those of the spectrum in helium, indicating the metallic character of the catalyst under these conditions. The spectrum measured at 174°C shared the same features as the one at 150°C but with a slightly decreased broadening of the whiteline indicating that part of the carbon monoxide was desorbed from the surface. The spectrum taken at 198°C, which was at 46% conversion, started with a shape that resembled that of metallic platinum with carbon monoxide adsorbed on the surface, however, at 11.571 keV, it suddenly changed to that of an oxide. This corresponds to the temperature of ignition of 204°C, which correlates to point B in Figures 6.2 and 6.3. The rapid change in rate of reaction is paralleled by fast structural changes of the platinum, as observed with time resolved XAS.[16] The spectrum taken at 211°C, which is above ignition, had characteristic features of the spectrum of oxidized platinum in Figure 6.5. The maximum intensity of the whiteline was 1.8, which is less than that of the Pt^{4+} spectrum, which indicates that either the oxidation state is less than +4 or that there are still metallic platinum species left in the catalyst under these conditions. During cooling, the shape of the spectrum taken at 207°C and above extinction showed an intense whiteline and the characteristic dip after the absorption edge. The scan taken at 199°C with a conversion of 100% started with the intense whiteline feature of an oxide and at 11.573 keV shifted to the wiggles of the metallic spectrum after the edge, which again corresponds to the point of extinction at 195°C, when the conversion jumped down to 41%, which is point E in Figures 6.2 and 6.3. The other two scans recorded at lower temperatures 183°C (26% conversion) and 83°C (2% conversion) showed low whiteline

intensity and small features above the edge. They also showed the broadened whiteline region characteristic of carbon monoxide adsorbed on the surface.

Figure 6.6c shows the XANES spectrum taken above ignition at 97% conversion. The whiteline intensity is lower than that of the spectrum at above ignition at 100% conversion, yet higher than that at below ignition. The post-edge line is lower than the one at below ignition, with features similar to the post-edge dip and subtle curves of that at 100% conversion. The overall features of this spectrum show a shape similar to the oxidic spectrum with a reduced whiteline intensity, which suggests a reduced extent of oxidation.

In summary, the changes in the shapes of the spectra during cooling were opposite to those observed during heating. Above the temperature of ignition, the spectra showed elements of oxidized platinum, even after increasing the carbon monoxide concentration, such that no full conversion was reached. Below the ignition and extinction temperatures the spectra resembled those of carbon monoxide adsorbed platinum nanoparticles.

Figure 6.7 shows the XANES spectra taken at increasing and decreasing temperature over b-Pt/Al$_2$O$_3$, Pt/TiO$_2$, and Pt/SiO$_2$. The same trends are observed. All spectra below ignition temperature showed the less intense and broadened whiteline of metallic platinum with carbon monoxide adsorbed on the surface, the amount of which decreases with temperature. Above ignition, the whiteline increased intensity similar to that of an oxidic species. The spectra were of metallic character at low activity and then switched to having oxidic features at high activity. The change to the oxidic features was a function of the temperature of ignition. The increase in the whiteline intensity was most pronounced for Pt/SiO$_2$, which ignited at the highest temperature, and the lowest increase was observed for Pt/TiO$_2$, which ignited at the lowest temperature. Upon decreasing the temperature, just above extinction, the conversion decreased for b-PtAl$_2$O$_3$ and Pt/TiO$_2$, which was paralleled by a decrease in intensity of the spectral whiteline and thus lower extent of oxidation.
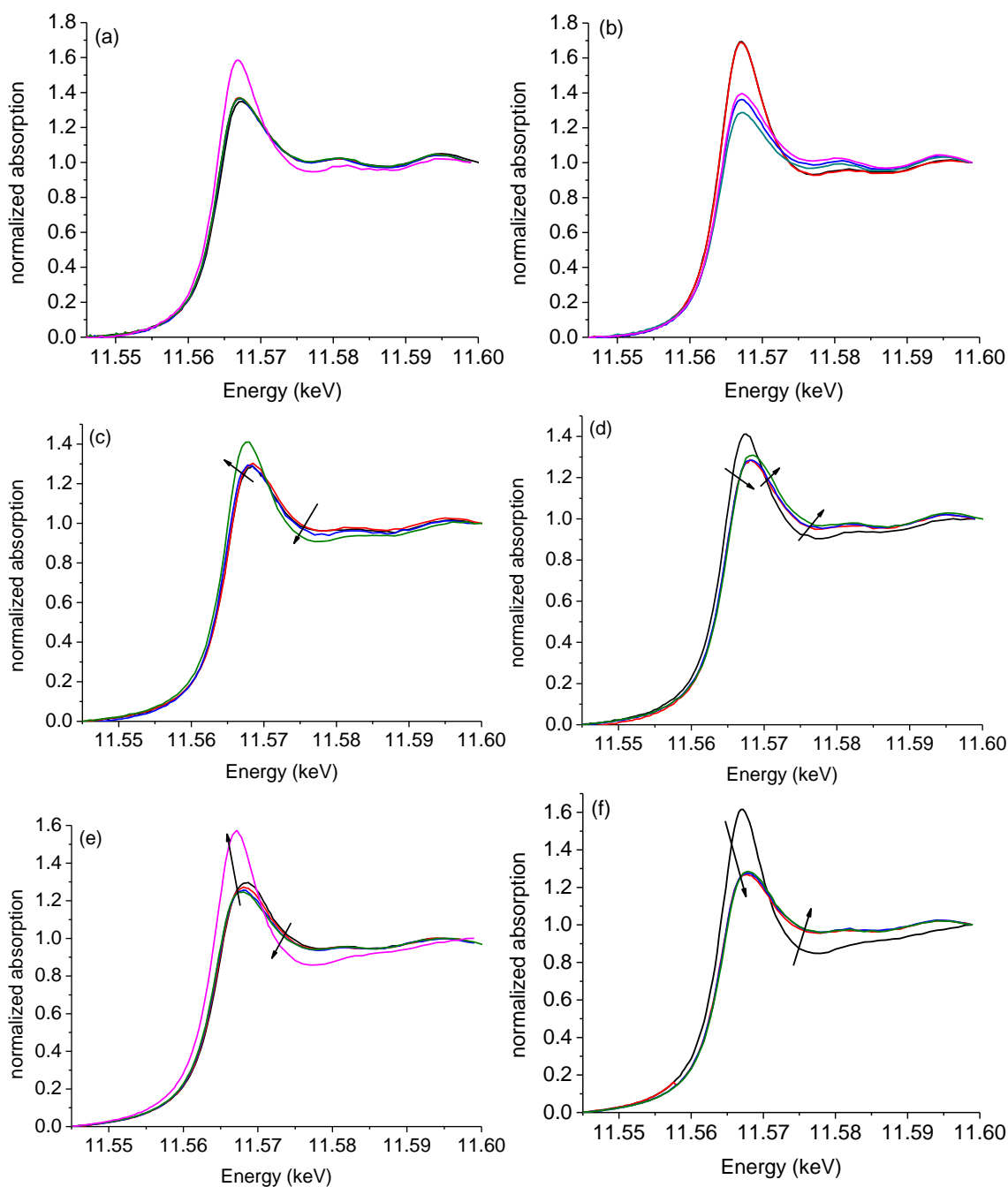
Figure 6.7: Pt L$_3$ XANES spectra recorded during heating (a) at 125°C (black), 194°C (red), 210°C (blue), 218°C (green), and 231°C (pink), and cooling (b) at 232°C (black), 213°C (red), 185°C (blue), 156°C (green), and 111°C (pink) of b-Pt/Al$_2$O$_3$; ignition occurred at 226°C, extinction occurred at 191°C; Pt L$_3$ XANES spectra recorded during heating (c) at 68°C (black), 134°C (red), 180°C (blue), and 190°C (green), and cooling (d) at 177°C (black), 145°C (red), 114°C (blue), and 36°C (green) of Pt/TiO$_2$; ignition occurred at 188°C, extinction occurred at 145°C; Pt L$_3$ XANES spectra recorded during heating (e) at 40°C (black), 140°C (red), 240°C (blue), 294°C (green), and 306°C (pink), and cooling (f) at 296°C (black), 286°C (red), 236°C (blue), and 106°C (green) of Pt/SiO$_2$; ignition occurred at 299°C, extinction occurred at 281°C.

Chapter 6

6.3.4. EXAFS fitting results

Figure 6.8 shows the averaged and k^3-weighted EXAFS function and corresponding Fourier transform of the EXAFS spectra taken at room temperature under a flow of helium for b-Pt/Al$_2$O$_3$ big particles after reduction and removal of hydrogen. The fits (dotted lines) of these functions provided coordination number (7.5), Debye-Waller factor (0.0040 Å^2), inter-atomic Pt-Pt distance (2.72 Å), and edge shift (1.7 eV) (Table 6.3).
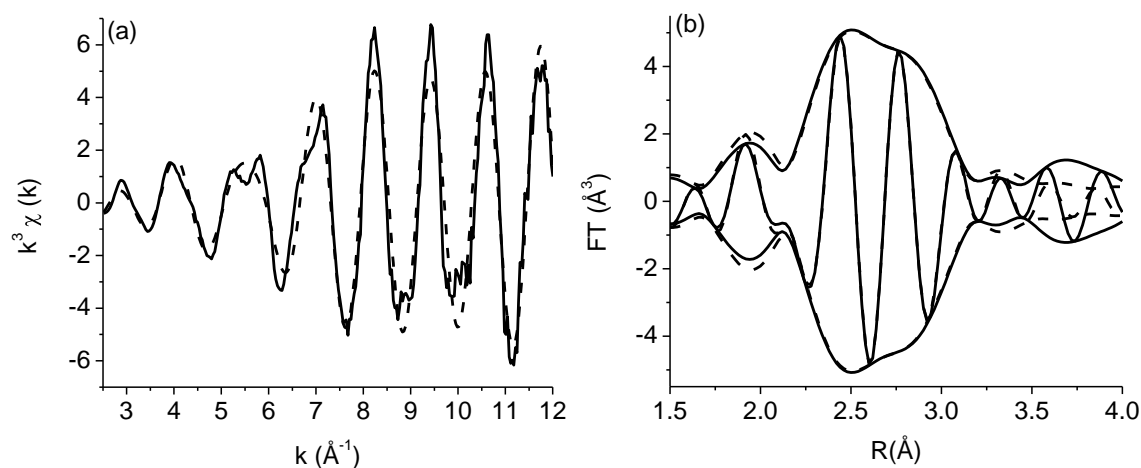

Figure 6.8: (a) k^3-weighted chi function and (b) corresponding Fourier transform (k^3 weighted, 2.5 < k < 12 Å^{-1}) of b-Pt/Al$_2$O$_3$ experimental data (solid line) and fit (dashed line) in flowing helium at room temperature.

The structural parameters for the fits of all the EXAFS spectra taken during the stages of the carbon monoxide oxidation runs are presented in Table 6.3. The spectrum taken at room temperature and in flowing helium for s-Pt/Al$_2$O$_3$ showed a first shell dominated by a Pt-Pt backscattering pair, with coordination number of 5.5. This correlates to metallic platinum particles with an average size of about 1 nm.[29] The Pt-Pt distance was 2.72 Å, smaller than the 2.76 Å of bulk platinum, indicating that the platinum cluster contracts when the particle size is very small.[29-32] The EXAFS spectrum taken at slightly higher temperature in the presence of oxygen and carbon monoxide shows an increased Pt-Pt distance to 2.77 Å and equal coordination number within the margin of error. Bond length relaxation occurred after the adsorption of carbon monoxide as supported by the XANES similar to what occurs after adsorption of hydrogen[30,32,33] Above ignition, an additional Pt-O scatterer with a Pt-O distance of 1.99 Å was observed that agree well with the Pt-O distances of the platinum oxides.[34] This is also in agreement with the XANES spectra in Figure 6.6 that showed characteristic

116

oxidic features of platinum above ignition. The Pt-Pt coordination number decreased to 2.0 and the Pt-Pt distance decreased to 2.71 Å. This Pt-Pt contribution appeared to be a combination of more than one Pt-Pt contributions that are difficult to fit separately., At increased carbon monoxide flow and 97% conversion, the fit still showed the Pt-Pt and Pt-O contributions with a slight increase in the Pt-Pt coordination to 3.0 and a slight decrease in the Pt-O coordination to 1.2 in agreement with features in the XANES (Figure 6.6c). The EXAFS fit of the spectrum that was recorded at room temperature again was dominated by Pt-Pt scattering. The coordination number of 5.6 was similar to the starting value of 5.5 when it was in helium. The distance was 2.76 Å compared to 2.72 Å when measured in helium, which is again attributed to the presence of adsorbed carbon monoxide that slightly expands the cluster. The Debye-Waller factor showed higher values at higher temperature and returned to almost its original value when cooled down to room temperature.

The b-Pt/Al$_2$O$_3$ catalyst, measured in the plug flow reactor at 35°C in flowing helium, had a Pt-Pt coordination number of 7.5. This translates to a size of about 2 nm. The Pt-Pt distance increased slightly from 2.74 Å to 2.75 Å after introducing oxygen and carbon monoxide at 125°C. The increase in bond length is less pronounced for the big particles than for the small particles. Fits of spectra recorded above ignition showed the presence of a Pt-O scatterer and decreased Pt-Pt contribution. Cooling down to 42°C, the spectrum returned to the Pt-Pt dominated fit. In comparison to the values at 35°C and in helium, the coordination number is the same, 7.5, but the Pt-Pt distance stayed at 2.75 Å because of the influence of adsorbed carbon monoxide. For the same catalyst but mounted in a different reactor, the fit parameters above and below ignition were similar to that in the plug flow reactor, in agreement with the XANES spectra.

Fits of the Pt/TiO$_2$ EXAFS recorded at 35°C in helium atmosphere showed a coordination number of 7.0, which corresponds to a size of about 1.3 nm. The 2.71 Å Pt-Pt distance was smaller than the bulk value of 2.76 Å, again indicative of contraction when decreasing particle size. Heating to 132°C and 178°C, in an oxygen and carbon monoxide environment, the Pt-Pt distance increased to 2.75 Å, the Debye-Waller factor increased, and the Pt-Pt coordination number remained 7.0.

Table 6.3: EXAFS fitting results

Conditions		Ab-Sc Pair	N	DW(Å^2)	R (Å)	ΔE_o (eV)	Goodness of Fit
Temp, °C	Gas CO Conversion, %						
s-Pt/Al$_2$O$_3$ (0.9 nm)							
35	He	Pt-Pt	5.5	0.0040	2.7	1.7	5.0
129	O$_2$/CO	Pt-Pt	5.7	0.0047	2.7	0.5	14.9
211	O$_2$/CO	Pt-O	2.4	0.0025	1.9	3.2	104.3
		Pt-Pt	2.0	0.0050	2.7	-1.4	
210	O$_2$/CO	Pt-O	1.2	0.0025	1.9	1.7	51.3
		Pt-Pt	3.0	0.0050	2.7	2.6	
38	O$_2$/CO	Pt-Pt	5.6	0.0038	2.7	1.9	11.2
b-Pt/Al$_2$O$_3$ (2.0 nm) in plug flow reactor							
35	He	Pt-Pt	7.5	0.0004	2.7	0.3	18.0
125	O$_2$/CO	Pt-Pt	7.8	0.0010	2.7	0.7	32.3
231	O$_2$/CO	Pt-O	1.3	0.0025	1.9	3.6	36.7
		Pt-Pt	6.7	0.0047	2.7	1.6	
232	O$_2$/CO	Pt-O	1.4	0.0025	1.9	3.9	33.5
		Pt-Pt	6.7	0.0047	2.7	1.9	
42	O$_2$/CO	Pt-Pt	7.5	0.0004	2.7	0.4	17.6
Pt/TiO$_2$							
35	He	Pt-Pt	7.0	0.0018	2.7	1.6	13.4
132	O$_2$/CO	Pt-Pt	7.0	0.0037	2.7	1.1	21.0
178	O$_2$/CO	Pt-Pt	7.0	0.0040	2.7	1.1	20.0
190	O$_2$/CO	Pt-O	0.7	0.0026	1.9	3.6	22.9
		Pt-Pt	6.1	0.0050	2.7	1.7	
36	O$_2$/CO	Pt-Pt	6.9	0.0018	2.7	1.8	26.8
Pt/SiO$_2$							
35	O$_2$/CO	Pt-Pt	7.6	0.0035	2.7	0.2	23.0
305	O$_2$/CO	Pt-O	3.1	0.0032	1.9	2.1	320.2
		Pt-Pt	2.3	0.0070	2.7	-1.8	
305	O$_2$/CO	Pt-O	3.7	0.0032	1.9	2.9	310.4
		Pt-Pt	2.0	0.0070	2.6	-1.1	

Above ignition, the Pt-Pt coordination number decreased to 6.1 along with a decrease in the Pt-Pt distance to 2.72 Å. A small Pt-O contribution with coordination number of 0.7 at 1.97 Å was observed. After cooling to room temperature, the Pt-Pt dominated

spectrum returned: the coordination number became 6.9, which is similar to the values below ignition at various temperatures. The Pt-Pt distance also returned to 2.75 Å.

For Pt/SiO_2 at 35°C in helium, coordination number was 7.6 and the Pt-Pt distance was 2.77 Å, which were quite similar to those of $b-Pt/Al_2O_3$ (2.0 nm) under the same conditions. Above ignition, the Pt-Pt coordination decreased to 2.3 and the Pt-Pt distance likewise decreased to 2.70. The Pt-O contribution appeared with a coordination number of 3.1 at 1.98 Å.

In summary, all catalysts showed an increase in Pt-Pt distance after switching from a flow of helium to one containing carbon monoxide. The platinum particles were in the metallic state at low conversion values as seen by only a Pt-Pt backscattering pair dominating the EXAFS functions and Fourier transforms. Above ignition, a Pt-O contribution appeared at a distance characteristic to that of a Pt-O pair in a platinum oxide. A Pt-Pt contribution remained, but with a shorter Pt-Pt distance than in a typical platinum oxide; it resembled the Pt-Pt distance of metallic platinum. Thus the catalyst at above ignition consists of mixed oxide-metal phases, the oxide most likely at the surface. The higher the temperature of ignition, the larger was the fraction of oxidic platinum. Upon cooling to below the temperature of extinction, the structure of all catalysts returned to their original structure.

6.4 Discussion

6.4.1 Generating high activity

In the oxidation of carbon monoxide over supported platinum catalysts, two activity regimes are observed: a low-activity regime and a high-activity regime (Figures 6.3 and 6.4). The low activity region occurs at low temperature and low carbon monoxide conversion. The high activity regime occurs at high temperature and high carbon monoxide conversion. Similar results had been reported during carbon monoxide oxidation on various forms of platinum-based catalysts.[10-12,27,35-38] Some studies on carbon monoxide oxidation have been made by varying the oxygen and carbon monoxide partial pressures at fixed temperatures.[10,11,38] The changes in conversion in our study have been achieved by changing temperature at fixed inlet oxygen and carbon monoxide partial pressures.

The switch between high and low activity regimes is characterized by discontinuous changes in carbon monoxide conversion. The jump to high activity is called ignition, the reverse extinction. These switches are reversible but show hysteresis. The temperature of

ignition is higher than the temperature of extinction. One reason may be the local heating of the platinum particles because of the exothermicity of the reaction. During the oxidation of methane over Pt/Al_2O_3, a comparison of the calculated and observed conversions had been made[39] and it appeared that platinum particles could be between 75 and 100°C hotter than the average temperature detected by the thermocouple in the catalyst bed. A similar effect likely occurs in the carbon monoxide oxidation (Figures 6.3 and 6.4). Another reason can be attributed to different states of the surface of the catalyst at high and low activity.

The jump in conversion indicates that there is a change in the mechanism of the reaction. This is also shown by varying activation energy below and above ignition of 176 kJ/mol and 59 kJ/mol respectively.[12] At low activity, the conversion of carbon monoxide increases exponentially with temperature. The reaction proceeds via the Langmuir-Hinshelwood mechanism,[36,40] where both carbon monoxide and oxygen adsorb on the surface of the catalyst to react to form carbon dioxide. The presence of carbon monoxide at the surface of platinum was reflected in the XANES spectra and EXAFS analysis and is generally observed by infra red spectroscopy.[13,41,42] Desorption of carbon monoxide is required to enable oxygen to adsorb and dissociate on the surface. The partial reaction order in carbon monoxide is close to -1 and for oxygen close to +1 for the carbon monoxide covered surface, which reflects the inhibiting effect of carbon monoxide on the rate of reaction.[18,43] With increasing temperature, there is enhanced production of carbon dioxide and decreasing concentration of carbon monoxide. The decrease in the coverage of carbon monoxide with temperature was reflected in the XANES spectra and is also well known in literature based on infra red spectroscopy.[13,41,42]

The sudden switch in activity was paralleled by a change in the structure of the catalyst. The XANES spectra and EXAFS analysis showed a switch from the metallic to the partially oxidic state upon ignition and the reverse upon extinction. The low activity in the original state of the catalyst originates from the poisoning of the surface by carbon monoxide.[12,41] The high activity is a result of the exposure of surface sites of the catalyst after depletion of surface carbon monoxide. The low carbon monoxide concentration on the surface enabled oxygen to react to it forming an oxide layer. The result is a more active catalyst compared to the carbon monoxide poisoned catalyst. During ignition, the enhancement in conversion is paralleled by the formation of the oxide,[16] a process, which proceeds auto-catalytically. The structural transformation of the nano particles is,

however, different from the surface reconstruction of the Pt(100) surface from a carbon monoxide-covered 1x1 phase to a hex phase saturated with adsorbed oxygen [8,9], which occurs under UHV conditions. Both these surfaces are still metallic. Our EXAFS analysis showed breaking of platinum-platinum bonds. SXRD measurements performed during carbon monoxide oxidation on a Pt(110) crystal[11] reported that the surface became covered with a distorted α-PtO$_2$; a commensurate and an incommensurate type, with the two types of oxides having a significantly higher reaction rate than the metallic surface. Recently, a monolayer of surface oxygen on rhodium, palladium, and platinum showed a hyperactivity, about two to three orders of magnitude greater than the surfaces that were poisoned by carbon monoxide.[44] However, our data do not suggest the presence of the α-PtO$_2$ phase or a chemisorbed layer of oxygen on our nano particles (vide infra).

In general, no or very little carbon monoxide adsorbed on a platinum catalyst in the high activity state is observed using infra red spectroscopy,[13] which correlates to the partially oxidic state of platinum. The reactivity towards carbon monoxide may be so high that the concentration of carbon monoxide on either reduced or oxidized surface is too low to be detected. In contrast to the low activity regime, the reaction order is half in carbon monoxide and oxygen and the activation energy decreased to 59 kJ/mol.[12] This has also been attributed to a diffusion-limited surface reaction between adsorbed carbon monoxide and oxygen.[37] The change in the reaction order and activation energy indicates that the rate is not anymore limited by carbon monoxide desorption and subsequent oxygen activation. A high reactivity of a ruthenium surface oxide has often been described, and Mars van Krevelen[45] and Langmuir-Hinshelwood mechanisms[46] have been proposed.

6.4.2 Structure of the active oxide

Both XANES and EXAFS showed that the extent of oxidation, upon ignition, strongly depended on particle size[23,47] and support[24,25] as shown in Figures 6.6 and 6.7. The higher the temperature of ignition was, the higher the extent of oxidation of the platinum particles. Thus Pt/TiO$_2$ was the least and Pt/SiO$_2$ the most oxidized. Pt/Al$_2$O$_3$ showed the opposite trend. With increasing temperature the solubility of oxygen in the metal increases.[48] With oxidation likely on the surface, our EXAFS analysis consistently showed that there was still a metal core left in all the oxidized catalysts. A larger metallic platinum core was left in the bigger particles. Based on the coordination

numbers correlated to particle size,[29] the extent of oxidation on s-Pt/Al$_2$O$_3$ was sufficient to completely cover its surface with an oxide layer, but it was just enough for b-Pt/Al$_2$O$_3$, which could therefore have metal sites exposed. The particles of s-Pt/Al$_2$O$_3$ deeply oxidized as did those of Pt/SiO$_2$. The amount of oxide on Pt/TiO$_2$ is insufficient to cover its surface completely. When increasing the amount of carbon monoxide at 207°C over s-Pt/Al$_2$O$_3$, resulting in about 97% conversion, the XANES and EXAFS showed that there was a slight decrease in amount of oxide, but that the system did not switch to the low-activity regime. This shows that the structure of the catalyst is very dynamic and depends on the exact gas composition.

Using core level spectroscopy and density functional theory calculations,[49] it was proposed that platinum ridges undergo 1-dimensional oxidation. The 1-D oxide stripes were found to be highly reactive in carbon monoxide oxidation due to the favorable transition states at the phase boundary. Because platinum nanoparticles have more edges, they are likewise expected to undergo 1-D oxidation as precursor to platinum oxidation. When a monolayer of oxygen adsorbs on the catalyst, it cannot desorb from the surface and platinum begins to oxidize.[38] Theory suggested that the surface of Pt (111) cannot be fully covered by oxygen,[34,50] and that the highest coverage attainable with an O$_2$ oxidant is 0.5 monolayer.[51] The extent of oxidation strongly depends on the oxygen partial pressure.[10] The dependence of the heat of oxide formation to particle size has been studied[47] by calorimetric measurements. The evolved heat of oxide formation increased with decreasing particles size and the stoichiometry of the oxide approached that of PtO$_2$. These studies indicate that smaller particles tend to show more oxidation than single crystals. From SXRD[11] the surface oxide structure over Pt(110) during reaction conditions was found to be a thin distorted α-PtO$_2$, exhibiting a compressive and tensile strain relative to the bulk α-PtO$_2$ lattice . Bulk PtO$_2$ however displays low catalytic activity. The most oxidized spectrum at high activity (Pt/SiO$_2$) obtained here, had hints of post-edge features of β-PtO$_2$[52] but with a whiteline intensity intermediate between the α-PtO$_2$ and β-PtO$_2$. These post-edge features were absent for the less oxidized spectra of Pt/Al$_2$O$_3$ and Pt/TiO$_2$. These suggest that the platinum oxide lacked long-range order, is distorted,and has a different structure than either of the bulk α or β-PtO$_2$. The oxidized s-Pt/Al$_2$O$_3$ fit for Pt-Pt appeared to be a combination of more than one Pt-Pt contributions that are difficult to fit separately. It would have come from the Pt-Pt contributions of the remaining metal core and of the oxide, and the longer Pt-Pt distance for the typical oxide would have been underestimated. The short Pt-O distance and low

Pt-O coordination also suggests that this could belong to a lower coordination than octahedral configuration such as the square-planar configuration in Pt_3O_4. The Pt_3O_4 structure has an interesting metallic character as a consequence of its undercoordinated structure and the fractional oxidation state of the platinum atom.[53] Calculations predicted that Pt_3O_4 is active for oxidation, as carbon monoxide binds strongly to the undercoordinated oxygen at the surface.[51] Likewise, in-situ XRD showed that oxygen covered particles during carbon monoxide oxidation were composed of combined metallic, PtO, and Pt_3O_4 clusters.[15] However, the likelihood of the oxide structure to a PtO_2 that is defected in oxygen could not be ruled out. Our oxide structure does not resemble a surface that is partially covered with oxygen that showed hyperactivity,[44] nor does it resemble bulk PtO_2 that showed low activity.[54] Under-coordination at the surface of the nanoparticles, strain, and partial oxidation are the key phenomena responsible for the high catalytic activity.

6.5 Conclusions

Carbon monoxide oxidation on supported platinum catalysts exhibits two activity regimes: low activity at high carbon monoxide concentration and low temperature and high activity at low carbon monoxide concentration and high temperature. There is ignition when going from low to high activity and there is extinction when going from high to low activity. The catalyst at low activity is metallic covered with carbon monoxide, which hampers oxygen from reacting. At high activity, the particles are partially oxidic. The data suggest that a disordered surface oxide is formed in which platinum has low coordination to oxygen. This points to a strongly defected platinum oxide with lower coordination than octahedral, possibly square planar. The depletion of carbon monoxide at high activity enables oxygen to interact with the surface, and enhances the catalytic activity by changing the rate-limiting step. The thickness of the disordered oxide layer strongly depends on particle size and the support and could be partially related to the temperature at which it formed. Among the supported catalysts, Pt/TiO_2 reached high activity at the lowest temperature and Pt/SiO_2 needed the highest temperature to reach high activity. Pt/Al_2O_3 showed an intermediate temperature.

Chapter 6

References

1 B. M. Weckhuysen, Phys. Chem. Chem. Phys. 5 (2003) 4351.

2 J. A. van Bokhoven, T. Ressler, F. M. F. de Groot, G. Knopp-Gericke, B. M. Weckhuysen (Ed.), in In-situ spectroscopy of catalysts, American Scientific Publishers, California, (2004) p. 123.

3 D. C. Koningsberger, B. L. Mojet, G.E. van Dorssen, D. E. Ramaker, Top. Catal. 10 (2000) 143.

4 D. E Ramaker, D. C. Koningsberger, Phys. Rev. Lett. 89 (2002) 139701.

5 A. L. Ankudinov, J. J. Rehr, J. J. Low, S. R. Bare, Phys. Rev. Lett. 89 (2002) 139702.

6 O. V. Safonova, M. Tromp, J. A. van Bokhoven, F. M. F. de Groot, J. Evans, P. Glatzel, J. Phys. Chem. B 110 (2006) 16162.

7 J. M. Zalc, D. G. Löffler, J. Power Sources 111 (2002) 58.

8 G. Ertl, P. R. Norton, J. Rüstig, Phys. Rev. Lett. 49 (1982) 177.

9 R. Imbihl, M. P. Cox, G. Ertl, J. Chem. Phys. 84 (1986) 3519.

10 B. L. M. Hendriksen, J. W. M. Frenken, Phys. Rev. Lett. 89 (2002) 046101.

11 M. D. Ackermann, T. M. Pedersen, B. L. M. Hendriksen, O. Robach, S. C. Bobaru, I. Popa, C. Quiros, H. Kim, B. Hammer, S. Ferrer, J. W. M. Frenken, Phys. Rev. Lett. 95 (2005) 255505.

12 G. A. Somorjai. Appl. Surf. Sci. 121/122 (1997) 1.

13 F. J. Gracia, L. Bollmann, E. E. Wolf, J. T. Miller , A. J. Kropf, J. Catal. 220 (2003) 382.

14 B. C. Sales, J. E. Turner, M. B. Maple, Surf. Sci. 114 (1982) 381.

15 N. Hartmann, R. Imbihl, W. Vogel, Cat. Lett., 28 (1994) 373.

16 J. Singh, E. M. Alayon, M. Tromp, O. Safonova, P. Glatzel, M. Nachtegaal, R. Frahm, J. A. van Bokhoven, Angew. Chem. Int. Ed., 47 (2008) 9260.

17 B. Atalik, D. Uner, J. Catal. 241 (2006) 268.

18 J. Yang, V. Tschamber, D. Habermacher, F. Garin, P. Gilot, Appl. Catal. B 83 (2008) 229.

19 D. E. Ramaker, G. E. van Dorssen, B. L. Mojet, D.C. Koningsberger, Top. Catal. 10 (2000) 157.

20 M. Vaarkamp, J. T. Miller, F. S. Modica, D. C. Koningsberger, J. Catal. 163 (1996) 294.

21 T. Visser, T. A. Nijhuis, A. M. J. van der Eerden, K. Jenken, Y. Ji, W. Bras, S. Nikitenko, Y. Ikeda, M. Lepage, B. M. Weckhuysen, J. Phys. Chem. B 109 (2005) 3822.

22 A. Saramat, P. Thormählen, M. Skoglundh, G. S. Attard , A. E. C. Palmqvist, J. Catal. 253 (2008) 253.

23 Y. Yazawa, H. Yoshida, T. Hattori, Appl. Catal. A 237 (2002) 139.

24 M. Kobayashi, A. Morita, M. Ikeda, Appl. Catal. B 71 (2007) 94.

25 A. Y. Stakheev, L. M. Kustov, Appl. Catal. A 188 (1999) 3.

26 M. Rinnemo, D. Kulginov, S. Johansson, V. P. Zhdanov, B. Kasemo. Surf. Sci. 376 (1997) 297.

27 S. Salomons, R. E. Hayes, M. Votsmeier, A. Drochner, H. Vogel, S. Malmberg, J. Gieshoff, Appl. Catal. B 70 (2007) 305.

28 A. Y. Rozovskii, M. A. Kipnis, E. A. Volnina, G. I. Lin, P. V. Samokhin, Kinet. Catal. 48 (2007) 701.

29 A. I. Frenkel, C. W. Hills, R. G. Nuzzo, J. Phys. Chem. B 105 (2001) 12689.

30 M. K. Oudenhuijzen, J. H. Bitter, D. C. Koningsberger, J. Phys. Chem. B 105 (2001) 4616.

31 E. Bus, J. T. Miller, A. J. Kropf, R. Prins, J. A. van Bokhoven, Phys. Chem. Chem. Phys. 8 (2006) 3248.

32 J. T. Miller, A. J. Kropf, Y. Zha, J. R. Regalbuto, L. Delannoy, C. Louis, E. Bus, J. A. van Bokhoven, J. Catal. 240 (2006) 222.

33 L. L. Wang, D. D. Johnson, J. Am. Chem. Soc. 129 (2007) 3658.

34 N. Seriani, W. Pompe, L. C. Ciacchi, J. Phys. Chem. B 110 (2006) 14860.

35 A. Urakawa, T. Burgi, H. P. Schläpfer, A. Baiker, J. Chem. Phys. 124 (2006) 054717.

36 T. H. Lindstrom, T. T. Tsotsis. Surf. Sci. 150 (1985) 487.

37 X. Su, P.S. Cremer, Y. R. Shen, G. A. Somorjai, J. Am. Chem. Soc. 119 (1997) 3994.

38 F. van Neer, A. Bliek, Chem. Eng. Sci. 54 (1999) 4483.

39 R. Burch, P. K. Loader, Appl. Catal. B 5 (1994) 149.

40 T. A. Nijhuis, M. Makkee, A. D. van Langeveld, J. A. Moulijn, Appl. Catal. A 164 (1997) 237.

41 P. T. Fanson, W. N. Delgass, J. Lauterbach. J. Catal. 204 (2001) 35.

42 D. M. Haaland, F. L. Williams. J. Catal. 76 (1982) 450.

43 R. H. Nibbelke, M. A. J. Campman, J. H. B. J. Hoebink, G. B. Marin., J. Catal. 171 (1997) 358.

44 M. S. Chen, Y. Cai, Z. Yan, K. K. Gath, S. Axnanda, D. W. Goodman, Surf. Sci. 601 (2007) 5326.

45 H. Over, Y. D. Kim, A. P. Seitsonen, S. Wendt, E. Lundgren, M. Schmid, P. Varga, A. Morgante, G. Ertl, Science 287 (2000) 1474.

46 C. Stampfl, M. Scheffler, Phys. Rev. Lett. 78 (1997) 1500.

47 C. B. Wang, H. K. Lin, S. N. Hsu, T. H. Huang, H. C. Chiu, J. Mol. Catal. A 188 (2002) 201.

48 M. Salmeron, L. Brewer, G. Somorjai, Surf. Sci. 112 (1981) 207.

49 J. G. Wang, W. X. Li, M. Borg, J. Gustafon, A. Mikkelsen, T. M. Pedersen, E. Lundgren, J. Weissenrieder, J. Klikovits, M. Schmid, B. Hammer, J. N. Andersen, Phys. Rev. Lett. 95 (2005) 256102.

50 A. D. Smeltz, R. B. Getman, W. F. Schneider, F. H. Ribeiro, Catal. Today 136 (2008) 84.

51 R. B. Getman, Y. Xu, W. Schneider, J. Phys. Chem. C 112 (2008) 9559.

52 A. N. Mansour, D. E. Sayers, J. W. Cook, Jr., D. R. Short, R. D. Shannon, J. R. Katzer, J. Phys. Chem. 88 (1984) 1778.

53 N. Seriani, J. Zin, W. Pompe, L.C. Ciacchi, Phys. Rev. B, 76 (2007) 155421.

54 L. Olsson, E. Fridell, J. Catal. 210 (2002) 340.

Chapter 7

CO oxidation over alumina supported platinum catalysts with different particle size

Abstract

The structure of alumina supported platinum catalysts has been studied using in situ time resolved high-energy resolution fluorescence x-ray spectroscopy (HERFD XAS), in situ infra red (IR) spectroscopy, and kinetic measurements during CO oxidation at O_2 to CO ratio of one. Regardless of the particle size, the CO oxidation occurred in two distinctive regimes, a high-activity regime and a low-activity regime, which have high and low rates of reaction respectively, as observed in previous studies. The size of the particles slightly affects the rate in the low-activity regime, which was more difficult to assess in the high-activity regime. The catalyst surface is poisoned by adsorbed CO in the low-activity regime, as probed by HERFD and IR, and in the high-activity regime, the catalyst exhibits higher activity paralleled with the formation of a surface oxide.

Chapter 7

7.1. Introduction

The CO oxidation over platinum is one of the most studied catalytic reactions in the field of heterogeneous catalysis. One of the main aims in these studies of heterogeneous catalysis is to understand and relate the observed catalytic behaviour of the metal particles to the structure and geometry of the particles on their respective supports. This allows optimizing the synthesis of better catalysts. The electronic properties of the metal, which varies drastically with cluster size and shape,[1-6] play a vital role in many industrial processes such as preferential oxidation (PROX) of CO in a hydrogen-rich mixture for the technical purification of the hydrogen feed gas[7] and in automotive applications.[8] The observed particle size effect[9-18] during CO oxidation has been well documented and related to the reaction rate and experimental conditions. The structure sensitivity of the CO oxidation has been well established for platinum single crystals under high vacuum conditions, and for catalysts with varying platinum nanoparticle sizes,[19-23] which amongst others has been related to the higher reaction rate on terrace sites in comparison to the defect sites (steps and kinks). Adsorbed CO on plane surfaces is shown to be more reactive than adsorbed on low coordination sites.[12] Reaction turnover frequencies increase with increasing particle size.[24,28]

The knowledge of the atomic-level structure of catalytic active sites is important to determine the activity of these noble metal catalysts. The active species on supported catalysts are still uncertain. There have been many studies claiming that metallic platinum is the active surface species for CO oxidation even in an O_2-rich environment.[25-28] Recent surface diffraction studies on surfaces of platinum single crystals[29] on the other hand, indicate that the rate of CO oxidation is higher when the surface is oxidized. It has also been suggested that the active structure is a combination of metallic and oxidic phases on the supported metal catalysts.[30,31] Theoretical calculations have shown the role played by partially oxidized surfaces in generating high catalytic activity.[32-35] Scanning tunneling microscopy revealed the high reactivity of an O_2-rich ruthenium surface in the oxidation of carbon monoxide.[36]

The CO oxidation on single crystals[26,29,37] and supported platinum catalysts[38-42] occurs in two reaction regimes respectively with low and high reaction rates at O_2 to CO ratios greater than stoichiometric. The low activity state is characterized by the adsorbed CO that poisons the active surface.[25,38,43,44] The high activity state is characterized by the presence of a surface oxide.[29,41,42] Most of the studies had applied IR spectroscopy to probe the active sites during the reaction. Despite these extensive studies,[25,43,45-47] there

is little agreement concerning the role of carbonyl species in the CO oxidation. There are reports where linear and bridged adsorbed CO are shown to be active[25] and reports where bridged adsorbed carbonyl species are more active for CO oxidation.[48] The co-adsorbed CO with oxygen atom is also shown to be responsible for the formation of carbon dioxide.[45] Also, the existence of islands on the catalyst surface has been shown [44,49] to be relevant for CO oxidation, the formation of which is dependent on the particle morphology and size.[50]

In this chapter, the structure of working supported platinum catalysts of different particle sizes is studied in a plug-flow reactor, combining time-resolved x-ray absorption spectroscopy (XAS), infra red (IR) spectroscopy, and kinetic measurements by means of mass spectrometry. In situ IR spectroscopy provides the information of the adsorbed species on the metal surfaces during the reaction conditions. As the adsorption of reactants and intermediates on the surface of transition metals involves the interaction of the atomic or molecular orbitals of the adsorbate with the bands on the metal, it is important and relevant to study the state of the metal itself during the reaction and detect the orbitals that are involved in bonding reactants. In situ XAS provides the local electronic and geometric structure of the platinum species during CO oxidation. The intensity of the whiteline of an L_3 edge XAS spectrum reveals the unfilled d band and is sensitive to the metal oxidation state and presence of adsorbates on the surface. The shape of the spectrum reveals the mode of adsorption.[51-54] The use of high-energy resolution fluorescence x-ray spectroscopy (HERFD XAS) improves the resolution of the spectra[54-57] The sharper features in these spectra originate from the broadening of a smaller final state core-hole lifetime of a particular fluorescence channel, as detected by a secondary energy-selective spectrometer.[55,57] Therefore, HERFD XAS provides more insight into the geometric and electronic structures of the active metal and IR spectroscopy provides the insight into the surface species present on the active sites. We have established the influence of particle size on the rate of CO oxidation and on the structure of platinum under the reaction conditions.

7.2 Experimental

1.90 wt% Pt/Al_2O_3 was synthesized using the incipient-wetness impregnation method as explained in section 2.1. One batch of the catalyst was calcined at 623 K and another batch at 773 K, both in the presence of static air. The catalysts calcined at 623 K and 773

K will be mentioned, further in this chapter, as Pt-623 and Pt-773 respectively. Catalysts were characterized using electron microscopy as explained in section 2.2. The experiments were conducted at beamline ID 26 at the European Synchrotron Radiation Facility (ESRF), Grenoble, France using the flow scheme as described in section 2.3. The catalysts were pre-treated in situ in 5% hydrogen in helium at 473 K before each experiment and cooled down in a flow of pure helium. After pre-treatment, the oxidation reaction was carried out in an atmosphere of CO and O_2 with O_2 to CO ratio of one. The measurements were done at a constant total flux of 30 Nml/min through the reactor corresponding to a space velocity of about 64,000 h^{-1}. For calculating rate of CO_2 production, the traces for CO, O_2, and CO_2, recorded by the mass spectrometer in terms of current, were divided by He signal for normalization. Assuming a linear correlation between CO conversion and normalized signal of CO_2, with boundary conditions of no CO conversion at the start of reaction and 100% CO conversion after ignition temperature, CO conversion was calculated from the mass spectrometer signals. The rate of CO_2 production was calculated from the CO conversion afterwards. HERFD XAS spectra were collected before and during heating of the sample at 2 K/min to the temperature of maximum conversion; the ratio of O_2 to CO was one corresponding to an O_2-rich environment. The spectra were collected with a time resolution of 90 s. In situ IR measurements were made using a Bio-Rad spectrometer. The measurements were done on a self-supporting catalyst pellet of 15 mg. The catalyst was pretreated prior to each experiment as explained above. The background spectrum was collected with catalyst at 313 K in a flow of 5% O_2 in He. The catalyst was then exposed to the reaction mixture with O_2 to CO ratio of one. The measurements were done, similar to XAS measurements, at a constant total flux of 30 ml/min through the reactor corresponding to a space velocity of about 64,000 h^{-1}. The pellet was heated at a rate of 2 K/min. The spectra were collected in continuous mode with time resolution of 5 sec.

7.3 Results

7.3.1 Particle size

The synthesis of catalysts resulted in well dispersed nanoparticles on alumina. Figure 7.1 shows STEM micrographs of Pt-623, and Pt-773 catalysts. For Pt-773 the particle size ranged from 1 nm to 4 nm with maximum particles of about 2.3 nm in size. Pt-623 has a narrow size distribution of the platinum nanoparticles around 0.7 nm. The small bright

spots were confirmed, by EDX, to be platinum particles supported on alumina, which was reflected as less bright texture in the STEM micrographs.
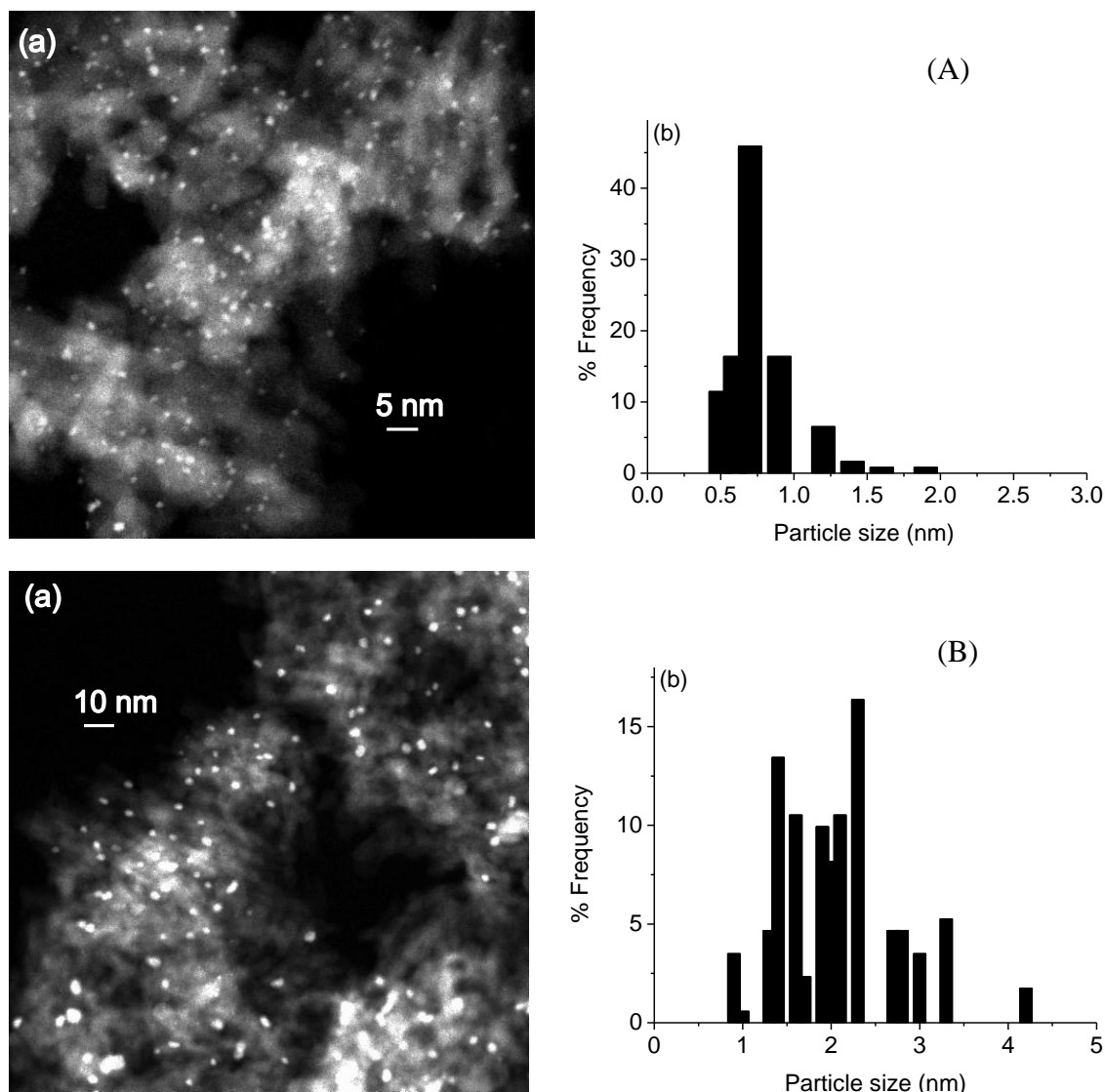

Figure 7.1: (a) STEM micrograph of 2 wt% Pt/Al_2O_3 prepared by incipient wetness impregnation and (b) particle size distribution of platinum particles for (A) Pt-623 and (B) Pt-773.

7.3.2 Kinetic data

These supported platinum nanoparticles after being exposed to the reaction mixture of CO and O_2 showed the conversion curves in CO when the catalyst bed was heated at 2 K/min. The runs were done in an O_2-rich environment, with O_2 to CO ratio of one. Figure 7.2 shows the rate of CO_2 production for Pt-623 (black) and Pt-773 (red) that had been calculated from mass spectrometer traces of CO_2. From the figure, it is clear that both catalysts show two different reaction regimes namely high activity regime and a

low-activity regime. These regimes had been observed before also for single crystals[26,29,37] and supported platinum catalysts[38-42] under UHV and atmospheric pressure. The two regimes are separated by a sudden increase in the activity of the catalyst that results in the increase in rate of CO_2 production. This sudden jump in the activity is referred as "ignition". After the ignition, the catalyst does not show any increase in the rate of CO_2 production owing to 100% conversion of CO. Just after the ignition, before the catalyst goes in the regime of constant rate of reaction with high activity, there is an extra positive spike in CO_2 production, which is explained later. Noticeable is that intensity of this spike is higher in case of Pt-623 compared to Pt-773. After the onset of CO_2 production, around 380 K, Pt-623 always showed higher rate of reaction in comparison to Pt-773 for any particular temperature. The TOF was calculated using the dispersion, which was calculated from the particle size using an established correlation in the literature.[69] TOF for Pt-623 at 440 K was 0.02 s^{-1}, which was approximately 1.5 times that of Pt-773.
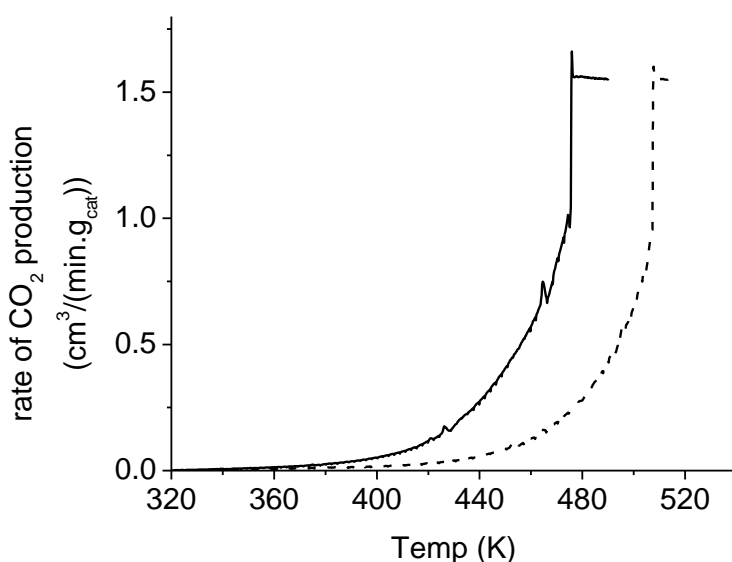

Figure 7.2: Rate of CO oxidation during heating at O_2 to CO ratio of one over Pt-623 (solid) and Pt-773 (dash).

7.3.3 Infra red data

The catalysts showed different adsorption of CO in the two reaction regimes. Figure 7.3(a) shows IR spectra that had been collected during the CO oxidation in O_2 to CO ratio of one. For clarity reasons, not all the spectra are shown which were collected at a time resolution of 5 sec. At the start of the reaction, at about 330 K, the spectrum showed a pronounced peak at 2079 cm^{-1}, corresponding to stretching frequency of

linearly absorbed CO on platinum[28,44,58] and a broad shoulder at 1838 cm^{-1}, which is assigned to stretching frequency of bridge-bonded CO on platinum particles.[44,58] The double peak between 2100 and 2200 cm^{-1} is due to the gaseous CO.
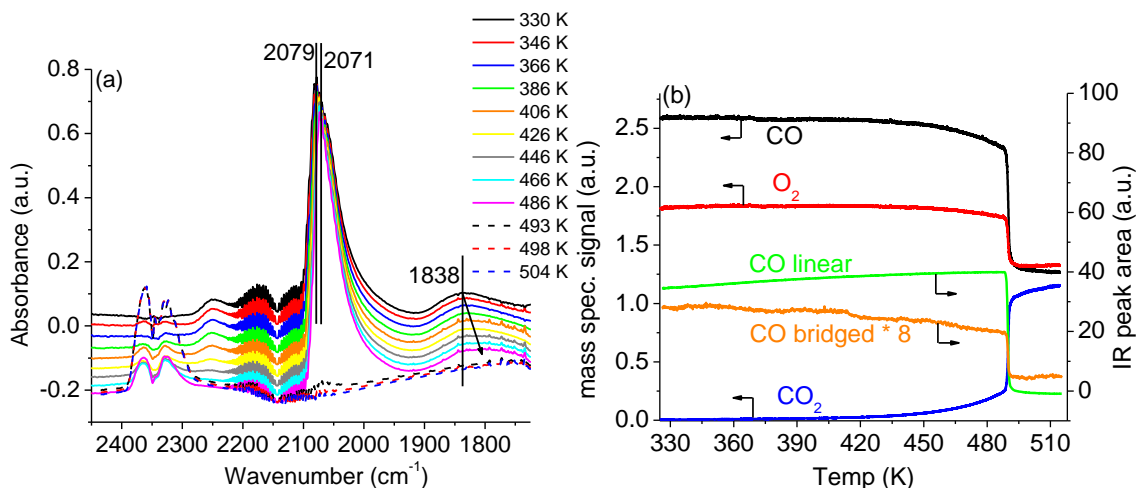

Figure 7.3: (a) IR spectra of Pt-773 in a pellet reactor at O_2 to CO ratio of one at 330 K (solid black), 346 K (solid red), 366 K (solid blue), 386 K (solid green), 406 K (solid orange), 426 K (solid yellow), 446 K (solid grey), 466 K (solid cyan), 486 K (solid pink), 493 K (dash black), 498 K (dash red), and 504 K (dash blue); ignition occurred at 490 K; (b) mass spectrometer traces of CO, O_2, and CO_2, and peak areas of linearly adsorbed and bridged CO.
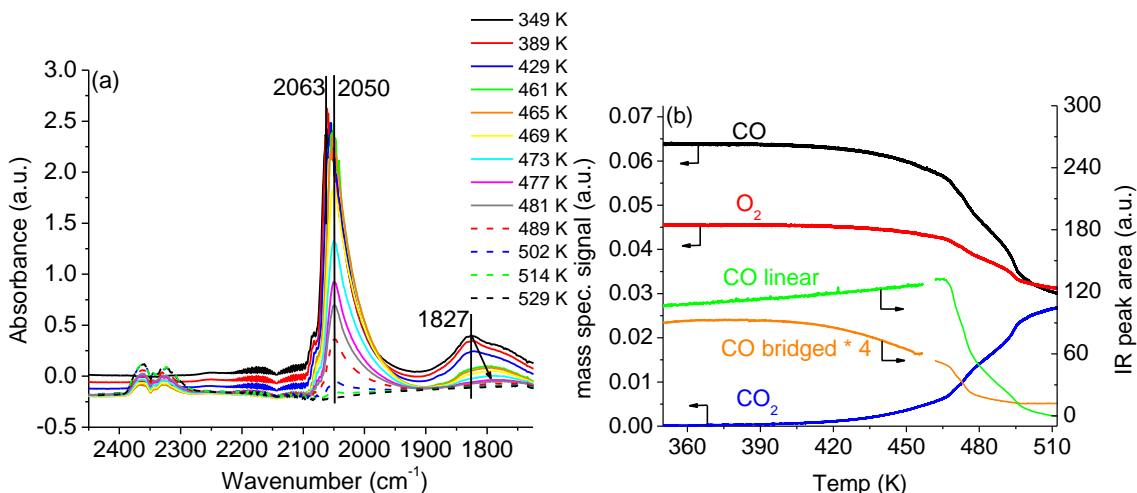

Figure 7.4: IR spectra of Pt-623 in pellet reactor at O_2 to CO ratio of one at 349 K (solid black), 389 K (solid red), 429 K (solid blue), 461 K (solid green), 465 K (solid orange), 469 K (solid yellow), 473 K (solid cyan), 477 K (solid pink), 481 K (solid grey), 489 K (dash red), 502 K (dash blue), 514 K (dash green), and 529 K (dash black); (b) mass spectrometer traces of CO, O_2, and CO_2, and peak areas of linearly adsorbed and bridged CO.

The peak at 2250 cm^{-1} may be assigned to carbon monoxide multiply bonded to oxidized platinum sites.[37] As the temperature was increased, the spectrum changed. The peak at

2079 cm^{-1}, assigned to linearly adsorbed CO was shifted to lower wavenumber. However, the intensity of the peak decreased slightly until 486 K. The peak at 2350 cm^{-1}, assigned to gaseous CO_2 species appeared at 406 K. The intensity of this peak increased with increase in temperature upto 486 K. The spectrum at 493 K showed a sudden increase in intensity at 2350 cm^{-1} and a large drop in the intensities of 2079 cm^{-1} and 1838 cm^{-1}. This sudden "ignition" as explained above, occured at 490 K. Figure 7.3(b) shows the changes in the mass spectrometer traces collected at the end of the reactor with increase in temperature. Also, the peak areas of linearly adsorbed and bridged CO, calculated from the spectra shown in Figure 7.3(a), are plotted. Mass spectrometer signals of CO and O_2 started to decrease with increase in temperature resulting in CO_2 production as shown by increase in CO_2 signal. The peak area of linearly adsorbed CO shows a slight increase with increase in temperature. This increase may originate either from the discrepancy in calculation of peak areas at different temperatures as only one background was collected at 313 K or from the fluctuations in the baseline at higher temperatures as observed for supported platinum catalysts, resulting in broadening of the peak around 2000 cm^{-1} [44] or from the changes in the extinction coefficient with temperature. The peak area of bridged CO decreases with increase in temperature suggesting the desorption of CO from the surface. The changes in the peak areas of adsorbed CO paralleled mass spectrometer signals with increase in temperature. Just after ignition, CO and O_2 signals dropped and CO_2 signal increased suddenly and became constant in the high-activity region. This sudden change was in parallel with the drop in the peak areas of linearly adsorbed and bridged CO on the platinum surface.

Similar results were obtained for the Pt-623 catalyst. Figure 7.4(a) shows the IR spectra at various temperatures acquired during heating the catalyst in an environment of O_2 to CO ratio of one. Although, no clear ignition was observed, as shown in Figure 7.4(b), for Pt-623 sample in the IR cell with catalyst as a self-supporting pellet, the trend of loss in the intensity of CO peaks is very similar to that of Pt-773 sample. In the low-activity region, up to approximately 470 K, platinum surface was covered by CO. With increase in temperature, the peaks at 2063 cm^{-1} and 1827 cm^{-1} were blue shifted (Figure 7.4(a)). After about 470 K, the mass spectrometer signals of CO and O_2 showed a decrease which is sharper than the decrease below 470 K. Parallel to this there was an increase in CO_2 signal. The peak areas of CO adsorbed both linearly and bridged followed exactly the trend of the mass spectrometer signals.
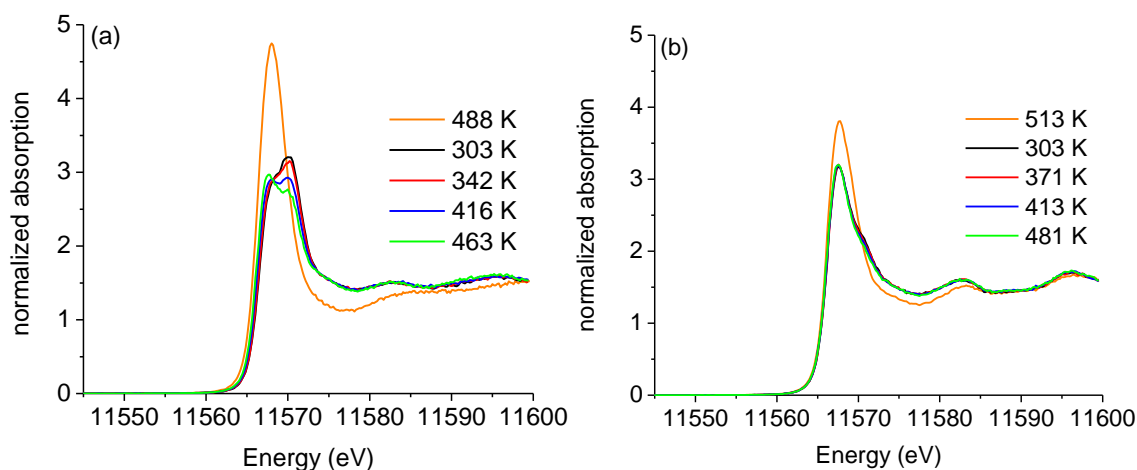
Figure 7.5: Pt L_3 edge HERFD XANES of (a) Pt-623 and (b) Pt-773 during CO oxidation at O_2 to CO ratio of one measured during heating in plug flow reactor.

7.3.4 HERFD XAS data

Figure 7.5(a) shows the Pt L_3 edge HERFD XAS spectra of Pt-623 measured between 300 K and 490 K in an atmosphere of O_2 and CO at a ratio of one. The spectra were recorded while measuring the conversion plot of Figure 7.2. Below 470 K, the spectra shows a pronounced doublet in the whiteline, which is characteristic of adsorbed CO.[54] As the temperature increased, the intensity of the doublet decreased and the edge shifted to lower energy. At 487 K, a higher temperature than the ignition temperature, the spectra showed a strong increase in the intensity of the whiteline while the edge energy shifted, which is characteristic of partially oxidized platinum.[54] At this point, the conversion of CO was complete (Figure 7.2). The XAS spectra showed no further changes at higher temperatures. Figure 7.5(b) shows the Pt L_3 edge HERFD XAS spectra of Pt-773 measured between 300 K and 515 K in an atmosphere of O_2 and CO at a ratio of one. The spectra in the low-activity region, below 500 K, are very different from Pt-623. The doublet feature in the whiteline, characteristic of atop adsorbed CO is not observed. However there is a small shoulder in the whiteline at around 11570 eV. This shoulder is assigned as the same signature of atop CO on the platinum surface. The intensity of this shoulder decreased with increase in temperature.

7.4 Discussion

7.4.1 Reaction regimes

The two distinct reaction regimes were observed during CO oxidation. These regimes had been observed before also for single crystals[26,29,37] and supported platinum catalysts[38-42] under UHV and atmospheric pressure. Under O_2-rich conditions, in the low activity region, the CO oxidation is sensitive to the structure of the catalyst.[10,11,15,16] The ignition temperature also strongly depended on the size of the platinum particles. Pt-623 showed ignition temperature of 476 K compared to 507 K in case of Pt-773. This implies that under similar reaction conditions, 0.7 nm platinum particles require lower temperature to ignite and go to the high-activity regime compared to 2.3 nm platinum particles supported on alumina. IR spectroscopy probed the adsorbed species on the catalyst surface during CO oxidation. Increasing the temperature resulted in a peak shift for linearly bonded CO on both catalysts (Figure 7.3(a) and 4(a)). This peak shift is well known and had been observed before on supported platinum catalysts and single crystals.[44,49,59-61] This shift emerges from two contributions; dipole-dipole interaction and temperature. The dipole-dipole interaction of adjacent CO molecules on the platinum surface affects the frequency of vibration. The vibrational frequency increases with increase in the density of CO dipoles on the surface. The similar explanation holds for the blue shift of bridged CO frequency on platinum with increase in temperature. Figure 7.3(b) clearly shows that in the low-activity region adsorbed CO poisons the active surface and does not allow the catalyst to exhibit high activity.[38,41,42,44] The desorption of this adsorbed CO is the rate-determining step in this low-activity region.[26,43,44,47] Once the catalyst surface is free of CO, after ignition, the catalyst has the ability to display a higher activity.[29,41,62]

7.4.2 Particle size effect

Comparing the IR spectrum of Pt-623 in the low-activity region, at about 350 K, with Pt-773 sample, the peak of linearly adsorbed CO is blue shifted to 2063 cm^{-1}. Such differences have been observed,[63] depending on the dispersion of platinum particles. With decrease in particle size, average number of platinum-platinum bonds per platinum atom decreases,[64] resulting in different hybridization between s, p, and d orbitals. This may result in weakening of the C-O bond due to more back bonding into the $2\pi^*$ orbital of adsorbed CO that further results in lower stretching frequency of adsorbed CO. Also, a change in dipole-dipole interaction because of different island sizes may contribute to

this shift. The results also agreed with the explanation of lower CO stretching frequency with lower coordination sites (corners and edges) of platinum atoms.[65,66] The blue shift of bridged CO results in the peak at 1827 cm^{-1} in comparison to 1838 cm^{-1} in case of Pt-773 sample. The lower intensity of the surface adsorbed CO doublet signature in case of Pt-773 compared to that of Pt-623 can also be explained due to the much lower fraction of the surface atoms. The higher fraction of these lower coordination sites (surface atoms) of platinum atoms in case of Pt-623 may explain the higher spike in CO_2 production (Figure 7.2) just after ignition for 0.7 nm particles (Pt-623) in comparison to 2.3 nm particles (Pt-773). Because 0.7 nm particles have a higher surface area, more CO is adsorbed on the catalyst with small particle compared to the one with 2.3 nm particles, and is reacted away to form the additional CO_2. Also, because ignition occured at lower temperature in case of Pt-623 compared to Pt-773, less CO is desorbed from the surface. As there was no sudden ignition observed in this case, the surface was never free totally from CO. This can be observed from the observed peak of linearly adsorbed CO in Figure 7.4(a). As the intensity of the peak of adsorbed CO goes down, during ignition there is no shift in the peak position which might suggest a constant island size and that particles are freed from CO one by one. Ultimately in the high-activity region, some CO remained adsorbed to poison the catalyst, however, a high activity part of the catalyst coexisted. The evolution of CO_2 peaks also confirms the formation of more active surface at these prevailing conditions.

7.4.3 Structure of catalysts

To probe the structure sensitivity and to determine the structure of the catalyst in the low- and high-activity regimes, in situ HERFD XAS was applied. The HERFD XAS technique provides complementary information to that obtained from the vibrational techniques; i.e. gives the geometric and electronic structures of the catalytic metal site during reaction. Therefore, with this technique the electronic structure of platinum was determined and is explained under different reaction conditions for the two samples with different particle sizes. Similar to IR results, adsorbed CO was observed in the low-activity regime as indicated by the doublet feature in the HERFD spectrum corresponds to the atop adsorbed CO on platinum and it emerges due to the formation of anti-bonding state above the Fermi level through overlap of platinum d-orbitals and $2\pi^*$ of the C and O atoms.[54] This observation of adsorbed CO on reduced platinum is in agreement with

our and others' IR data.[25, 28,43,44] At temperatures below the ignition point, traces of CO are sufficient to completely reduce a pre-oxidized platinum catalyst even in the presence of an excess of O_2.[28,44,65] CO thus poisons the catalyst surface and prevents it from oxidation even under an overdose of O_2 at sufficiently low temperature. The decreased intensity of doublet with temperature indicated desorption of CO at elevated temperatures,[41] similar to IR results. In our previous study,[42] above the ignition temperature, the EXAFS analysis had shown that there is a loss of Pt-Pt contribution and appearance of Pt-O and a Pt-Pt contribution had a bond length that is characteristic of an oxide. Also, we observed that a platinum core remained. Above ignition, intense whiteline suggested the presence of a fraction of oxidized platinum which paralleled the high rate of reaction. The whiteline intensity of oxidized platinum in case of Pt-773 is less than in Pt-623, which suggests that 2.3 nm particles are not oxidized as deeply as 0.7 nm particles, which correlates to the surface oxidation of particles.[42] The intense features after the whiteline, at 11585 and 11595eV, compared to Pt-623 also suggested that even in the high-activity region the spectra still had contributions from the relatively large platinum core. There is evidence of these results using full EXAFS analysis for particle size effects on the extent of oxidation in the high-activity region.[42]

Therefore, regardless of the particle size, as studied here, in the low-activity region, below ignition temperatures, the surface is covered with CO and the reaction rate is low and determined by the desorption of CO. At these temperatures, the platinum particles are reduced with adsorbed CO, even in an O_2-rich environment. As the temperature increases, some of the CO desorbs from the platinum surface, which is reflected in the lower intensity of whiteline doublet in the HERFD spectra and in the blue shift of the stretching frequency of adsorbed CO in the IR data. At the ignition temperature, the rate increases suddenly and oxidic platinum forms. HERFD XAS is very sensitive to the particle size, as the doublet in the whiteline is pronounced only when the particle size is below or equal to 1 nm.

7.5 Conclusions

Platinum nanoparticles of different particle sizes, supported on alumina, and prepared by incipient-wetness impregnation, show different activities in the CO oxidation. In situ HERFD XAS and infra studies have distinguished the active phases in the low- and the high-activity regimes: platinum adsorbed with CO in the low-activity regime. In the low-activity region, the catalyst is poisoned by CO, thus limiting the reaction of CO. These

results are consistent for different particle size. Also, the particle size effects the temperature of ignition, which in turn effects the activity of the catalyst towards CO oxidation. The higher conversion over the catalyst with the smaller particles is responsible for a lower coverage of CO enabling O_2 to react with the surface and start ignition at a lower temperature.

Chapter 7

References

1 L. F. Mattheiss, R. E. Dietz, Phys. Rev. B 22 (1980) 1663.

2 B. Delley, D. E. Ellis, A.J. Freeman, E. J. Baerends, D. Post, Phys. Rev. B 27 (1983) 2132.

3 M. G. Mason, Phys. Rev. B 27 (1983) 748.

4 M. Kuhn, J. A. Rodriguez, J. Hrbek, A. Bzowski, T. K. Sham, Surf. Sci. 341 (1995) L1011.

5 G. C. Bond, D. T. Thompson, Catal. Rev. Sci. Eng. 41 (1999) 319.

6 N. Lopez, J. K. Nørskov, J. Am. Chem. Soc. 124 (2002) 11262.

7 C. D. Dudfield, R. Chen, P. L. Adock, Int. J. Hydrogen Energy 26 (2001) 763.

8 R. J. Farrauto, R. M. Heck, Catal. Today 51 (1999) 351.

9 H. Hopster, H. Ibach, G. Comsa, J. Catal. 46 (1977) 37.

10 E. C. Akubuiro, X. E. Verykios, L. Lesnick, Appl. Catal. 14 (1985) 215.

11 D. N. Belton, S. J. Schmieg, Surf. Sci. 202 (1988) 238.

12 A. Szabó, M. A. Henderson, J. T. Yates, J. Chem. Phys. 96 (8) (1992) 6191.

13 G. S. Zafiris, R. J. Gorte, Surf. Sci. 276 (1992) 86.

14 I. Stará, V. Nehasil, V. Matolín, Surf. Sci. 331–333 (1995) 173.

15 V. Nehasil, I. Stará, V. Matolín, Surf. Sci. 352–354 (1996) 305.

16 U. Heiz, A. Sanchez, S. Abbet, W.D. Schneider, J. Am. Chem. Soc. 121 (1999) 3214.

17 I. Meusel, J. Hoffmann, J. Hartmann, J. Libuda, H. J. Freund, J. Chem. Phys. B 105 (2001) 3567.

18 A. K. Santra, D. W. Goodman, Electrochim. Acta 47 (2002) 3595.

19 J. L. Gland, M. R. McClellan, F. R. McFeely, J. Chem. Phys. 79 (1983) 6349.

20 A. Szabo, M. A. Henderson, J. T. Yates, J. Chem. Phys. 96 (1992) 6191.

21 D. W. Goodman, C. H. F. Peden, G. B. Fisher, S.H. Oh, Catal. Lett. 22 (1993) 271.

22 M. Bowker, Q. Guo, Y. Li, R. W. Joyner, Catal. Lett. 22 (1993) 275.

23 J. Z. Xu, J. T. Yates, J. Chem. Phys. 99 (1993) 725.

24 G. S. Zafiris, R. J. Gorte, J. Catal. 140 (1993) 418.

25 T. H. Lindstrom, T. T. Tsotsis, Surf. Sci. 150 (1985) 487.

26 J. A. Anderson, J. Chem. Soc. Faraday Trans. 88 (8) (1992) 1197.

27 R. Burch, P. K. Loader, Appl. Catal. A 122 (1995) 169.

28 F. J. Gracia, L. Bollmann, E. E. Wolf, J. T. Miller, A. J. Kropf, J. Catal. 220 (2003) 382.

29 M.D. Ackermann, T. M. Pedersen, B. L. M. Hendriksen, O. Robach, S. C. Bobaru, I. Popa, C. Quiros, H. Kim, B. Hammer, S. Ferrer, J. W. M. Frenken, Phys. Rev. Lett. 95 (2005) 255505.

30 R. Burch, P. K. Loader, Appl. Catal. B 5 (1994), 149.

31 S. Yang, A.M. Valiente, M. B. Gonzalez, I. R. Ramos, A. G. Ruiz, Appl. Catal. B 28 (2000) 223.

32 C. Stampfl, M. Scheffler, Phys. Rev. Lett. 78 (1997) 1500.

33 X.-G. Wang, A. Chaka, M. Scheffler, Phys. Rev. Lett. 84 (2000) 3650.

34 K. Reuter, M. Scheffler, Phys. Rev. B. 65 (2002) 035406.

35 K. Reuter, M. Scheffler, Phys. Rev. B. 68 (2003) 045407.

36 H. Over, Y. D. Kim, A. P. Seitsonen, S. Wendt, E. Lundgren, M. Schmid, P. Varga, A. Morgante, G. Ertl, Science 287 (2000) 1474.

37 X. Su, P. S. Cremer, Y.R. Shen, G. A. Somorjai, J. Am. Chem. Soc. 119 (1997) 3994.

38 P.-A. Carlsson, L. Oesterlund, P. Thormaehlen, A. Palmqvist, E. Fridell, J. Jansson, M. Skoglundh, J. Catal. 226 (2004) 422.

39 F.J. Gracia, S. Guerrero, E.E. Wolf, J.T. Miller, A.J. Kropf, J. Catal. 233 (2005) 372.

40 P.-A. Carlsson, V. P. Zhdanov, M. Skoglundh, Phys. Chem. Chem. Phys. 8 (2006) 2703.

41 J. Singh, E. M. Alayon, M. Tromp, O. Safonova, P. Glatzel, M. Nachtegaal, R. Frahm, J. A. van Bokhoven, Angew. Chem. Int. Ed. 47 (2008) 9260.

42 E. M. Alayon, J. Singh, M. Nachtegaal, M. Harfouche, J. A. van Bokhoven, J. Catal. 263 (2009) 228.

43 D. M. Haaland, F. L. Williams, J. Catal. 76 (1982) 450.

44 P. T. Fanson, W. N. Delgass, J. Lauterbach, J. Catal. 204 (2001) 35.

45 Y. Barshad, X. Zhou, E. Gulari, J . Catal. 94 (1985) 128.

46 N. W. Cant, D. E. Angove, J. Catal. 97 (1986) 36.

47 Y-E. Li, D. Boecker, R. D. Gonzalez, J. Catal. 110 (1988) 319.

48 J. Sarkany, R. D. Gonzalez, Appl. Catal. 5 (1983) 85.

49 J. Sarkany, M. Bartok, R. D. Gonzalez, J . Catal. 81 (1983) 347.

50 J. A. Anderson, Catal. Lett. 13 (1992) 363.

51 D. E. Ramaker, D. C. Koningsberger, Phys. Rev. Lett. 89 (2002) 139701.

52 A. L. Ankudinov, J. J. Rehr, J. J. Low, A. R. Bare, Phys. Rev. Lett. 89 (2002) 89, 139702.

53 M. K. Oudenhuijzen, J. A. van Bokhoven, J. T. Miller, D. E. Ramaker, D. C. Koningsberger, J. Am. Chem. Soc. 127 (2005) 1530.

54 O. V Safonova, M. Tromp, J. A. van Bokhoven, F. M. F. de Groot, J. Evans, P. Glatzel, J. Phys. Chem B. 110 (2006) 16162.

55 P. Glatzel, U. Bergmann, Coord. Chem. Rev. 249 (2005) 65.

56 F. M. F. de Groot, Coord. Chem. Rev. 249 (2005) 31.

57 J. A. van Bokhoven, C. Louis. J. T. Miller, M. Tromp, O. V. Safonova, P. Glatzel, Angew. Chem. Int. Ed. 45 (2006) 4651.

58 N. Sheppard, T. T. Nguyen, *in* "The Vibrational Spectra of CO Chemisorbed on the Surfaces of Metal Catalysts - A Suggested Scheme of Interpretation" (R. J. H. Clark and R. E. Hester, Eds.), Vol. 5, p. 67. Heyden, London, 1978.

59 A. Crossley, D. A. King, Surf. Sci. 68 (1977) 528.

60 P. Hollins, J. Pritchard, Prog. Surf. Sci. 19(4) (1985) 275.

61 P. Araya, W. Porod, E.E. Wolf, Surf. Sci. 230 (1990) 245.

62 M. S. Chen, Y. Chai, Z. yan, K. K. Gath, S. Axnanda, D. W. Goodman, Surf. Sci. 601 (2007) 5326.

63 L.-C. deM´enorval, A. Chaqroune, B. Coq, F. Figueras, J. Chem. Soc., Faraday Trans. 93 (1997) 3715.

64 G. Blyholder, J. Phys. Chem. 68 (1964) 2773.

65 R. K. Brandt, M. R. Hughes, L. P. Bourget, K. Truszkowska, R. G. Greenler, Surf. Sci. 286 (1993) 15.

66 M. J. Kappers, J. H. van der Maas, Catal. Lett. 10 (1991) 365.

69 T. Lear, R. Marshall, J. A. L. -Sanchez, S. D. Jackson, T. M. Klapötke, M. Bäumer, G. Rupprechter, H.-J. Freund, D. Lennona, J. Chem. Phys. 123 (2005) 174706.

Chapter 8

Structure changes during kinetic oscillations in CO oxidation

Abstract

The oxidation of CO over alumina-supported nano-meter sized platinum catalysts in a plug-flow reactor showed oscillations in the conversion. A strong dependence of the catalyst structure and thus reactivity of the catalyst on reaction conditions and on position within the plug-flow reactor was observed. Oscillations occurred because of local changes in the catalyst structure inside the reactor. During the oscillations, a decrease in CO_2 production was paralleled by reduction of a disordered surface platinum oxide, which was identified as the catalytically active structure. The surface got re-activated with a sudden spike in carbon dioxide production which coincided with re-oxidation of the surface. The kinetic oscillations during CO oxidation were paralleled with the reduction and re-oxidation of the surface.

8.1. Introduction

The rational design and synthesis of tailored catalysts and catalytic processes require understanding of the structure-performance relationship under reaction conditions involving high temperature and pressure. The catalytic oxidation of CO is one of the best studied reactions in catalysis.[1] This reaction occurs in automotive catalysts and is important in removal of CO from streams of hydrogen in fuel cell applications.[2,3] Surface sensitive techniques, such as low energy electron diffraction (LEED), scanning tunneling microscopy (STM) and X-ray photoelectron and Auger electron spectroscopy (XPS, AES), have greatly contributed to the understanding of the oxidation of CO taking place on well defined single crystal surfaces.[1,4] During CO oxidation, two or more reaction regimes with distinct CO oxidation rates have been identified on model single crystal catalysts and technical catalysts.[5,6] There is consensus that a CO-covered metallic surface shows low activity because of poisoning by the CO.[7] The surface structure of a highly active state can be either a surface oxide[8-12] or an oxygen-covered surface.[13] Surface science studies showed that under specific conditions the oxidation of CO will oscillate on well-defined single crystal surfaces such as the Pt(110) surface.[14,15] Oscillations are not limited to vacuum conditions and also occur on technical catalysts under actual catalytic conditions.[16,17] Most of the above stated techniques are limited to low pressure environments, and are thus far away from industrial relevant conditions. Furthermore, the structure of single crystal model catalyst surfaces deviates from that of technical catalysts, especially when the particles are nanometer in size and supported on an (active) support to increase their reactivity. Deriving a fundamental understanding of the correlation between structure and performance of a technical catalyst inside a reactor under operating conditions is thus at the frontier of contemporary catalytic research.[18-21]

Thanks to the penetration depth of hard X-rays, synchrotron-based X-ray techniques allow for the study of the catalyst structure in a reactor under operating conditions. X-ray absorption spectroscopy (XAS) is particularly powerful for in situ studies of nano particles, since it probes the average local geometric (up to about 5 Å) and electronic bonding environment of the element of interest. As a result, XAS has been increasingly applied over the last three decades to uncover the structure of catalysts under operating conditions. Recent developments in beamline optics allow for the study of the kinetics of structural changes of the catalyst in the reactor with a sub-second time resolution[22-27] and for investigating the catalyst structure with a (sub) micro-meter resolution.[14]

In this chapter, work done has combined in situ time- and space- resolved X-ray absorption spectroscopy with mass spectrometry and infrared (IR) spectroscopy to derive at a spatially resolved understanding of dynamic structure-performance relationships in a reactor during a famous oscillating reaction: the oxidation of carbon monoxide (CO). XAS at the Pt L_3 edge enables determining the oxidation state and local structure of the platinum under actual reaction conditions. The white line in the L_3 edge XAS spectra is sensitive to the structure of the metal and to the number of holes in the d band. Complimentary in situ infrared spectroscopy detects adsorbates on the surface of the catalyst.

8.2 Experimental

1.9 wt% Pt/Al_2O_3 was prepared by the incipient wetness impregnation method as explained in section 2.1. The platinum particle size was between one and two nm based on the EXAFS data analysis in agreement to electron microscopic data. The XAS measurements were done in down-flow in a plugflow (tubular packed bed) reactor, which was 1.6 mm in internal diameter, enclosing about 20 mg catalyst. The reactor (explained in detail in section 2.6) functioned as transmission cell for XAS. All gases used were from Messer and were of high purity (>99.995 vol%). The infra red measurements were done in an in situ cell (explained in detail in section 2.5), in which the gas flowed through a self-supporting pellet. 15 mg of catalyst was pressed into the pellet, which was about 7 mm in diameter, and placed in the reactor. In both reactors, the exhaust was connected to a mass spectrometer from Pfeiffer Vacuum (GSD 300 O_2, OmniStar) for product gas analysis. The mass spectrometric data were aligned to the infrared and XAS spectra by correcting for the time delay of the gasses to reach the mass spectrometer. Before any measurement, the catalyst was treated in situ in 2% hydrogen in helium at 473 K. Subsequently, the catalyst was exposed to an atmosphere of O_2 and CO in a ratio of 19:1. The total gas flow rate was always 30 mL/min corresponding to a space velocity of 64000 h^{-1} in the XAS measurements. Pt L_3 edge spectra were measured with a time resolution of 0.5 seconds. The infrared spectra were collected with a time resolution of one second. A heating rate of 2 K/min and a cooling rate of 1 K/min during the oxidation of carbon monoxide were used.

XAS measurements were performed at the SuperXAS beam line of the Swiss Light Source in Villigen, Switzerland, as explained in section 2.32. An X-ray beam of ~1000 * 100 μm^2 (H x V) transmitting the plug-flow reactor at various heights of the catalyst bed

145

was used. Spectra were collected in transmission mode using two ionization chambers filled with air. For absolute energy calibration, the absorption of a platinum foil was always measured simultaneously between the second ionization chamber and a photodiode. For each measurement, a new fraction of sieved (63-125 μm) catalyst was loaded into the reactor. The infrared measurements were done using a Bio-Rad spectrometer, as explained in section 2.5. The background spectrum was collected with catalyst at 313 K under a flow of pure helium. Fitting of XAS spectra was done, after averaging 100 spectra, with k ranging from 2.5 to 13.0 1/Å, and inter-atomic distance ranging from 1.0 to 3.5 Å, with k^3 weighting for reduced and k^2 weighting for oxidized platinum. Estimated error margins, except for Pt-Pt of the oxide, which showed a large error because of its intensity, were 20% in coordination number, ±0.02 in inter-atomic distance, 10% in Debye-Waller factor, and ±2.5 in edge shift energy.

8.3 Results

8.3.1 Infra red data

Figure 8.1 shows the pellet-bed reactor used to study the oscillations in CO conversion over supported platinum nano-particles with IR spectroscopy. The reactor was coupled to a mass spectrometer to follow the integrated activity of the catalyst at the end of the reactor. CO conversion was achieved by heating reduced platinum particles in a flow of O_2 and CO at a molar ratio of 19:1 to 382 K. At this temperature the catalyst showed high activity and full conversion of CO. Then, cooling of the reactor was started. Figures 8.2a show the traces of CO_2, CO, and O_2 as detected in the mass spectrometer upon cooling in the infra red experiment. The oscillations in the signal of CO_2 were observed with increasing intensity over time. One oscillation (Figure 8.2a) was characterized by a slow decrease in amount of CO_2 followed by a sharp increase of the signal to a level higher than characteristic of full CO conversion. With decreasing CO_2, an enhanced CO signal was observed. The CO signal showed a maximum, and thus the catalyst its lowest activity, a few seconds past the minimum in the CO_2 signal. The CO signal returned to its base level at the same time as the CO_2 signal came back to its base level. Within an oscillation, the decrease in CO_2 production was larger than its excess during the spike. This indicates that the integral activity of the catalyst decreased in the first part of the oscillation, which was also indicated by the enhanced CO signal. The decrease of the CO_2 and increase of CO signal at the exhaust were paralleled by an increase in the infrared signals of linearly (atop) bonded CO and bridged CO, indicated by the infrared

bands at 2063 and 1828 cm^{-1}, respectively. No other bands in the spectra showed variation over time during the oscillations as observed earlier.[28]
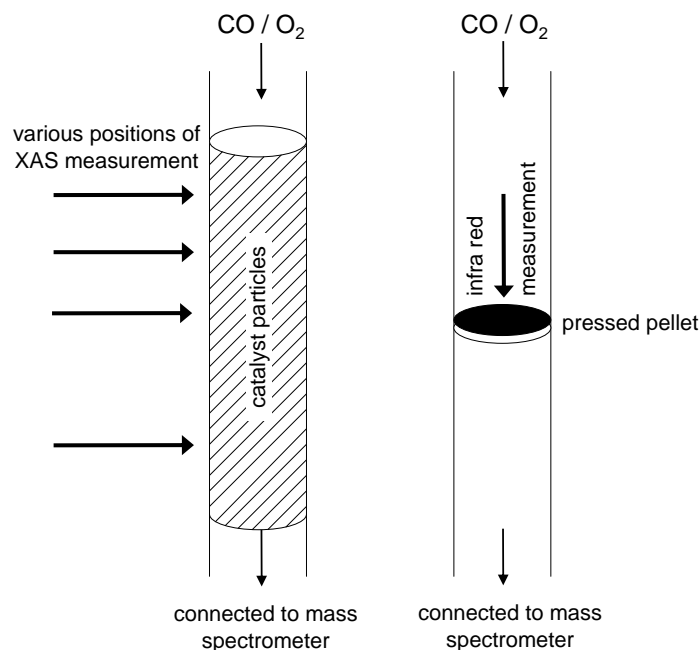
Figure 8.1: In situ measurement cells for XAS (left) and infrared spectroscopy (right). The XAS was measured with the X-rays penetrating packed-bed reactor from the side at various heights of the catalyst bed. The transmission infrared measurements were performed on a pellet with the infrared beam penetrating through the pellet from the top.

8.3.2 QEXAFS data

Oscillations were also observed in the mass spectrometer traces of CO_2 at the end of the packed-bed reactor (Figure 8.1), which was used for the quick XAS studies (Figure 8.2b). The conditions for achieving the oscillations were similar to those in infra red experiment. There are some notable differences compared to the pellet reactor. At conditions that showed full conversion, the signal of CO showed no clear variation during the oscillations. This changed the moment that the conversion decreased to below 100% when a small increase in CO was observed with decreasing CO_2, similar to the observations in the infrared experiment. Figures 8.2b and c show the amount of oxidized platinum as determined by the maximum intensity of the white line in the XAS spectra and linear combination fitting with spectra of oxidized and reduced platinum, as function of temperature. High intensity in Figure 8.2b reflects a high percentage of oxidized platinum.[29] At 395 K, a maximum amount of oxidized platinum was observed. In the cooling trajectory until 377 K, the white line intensity was constant and was not affected by the oscillations as shown by the mass spectrometer.
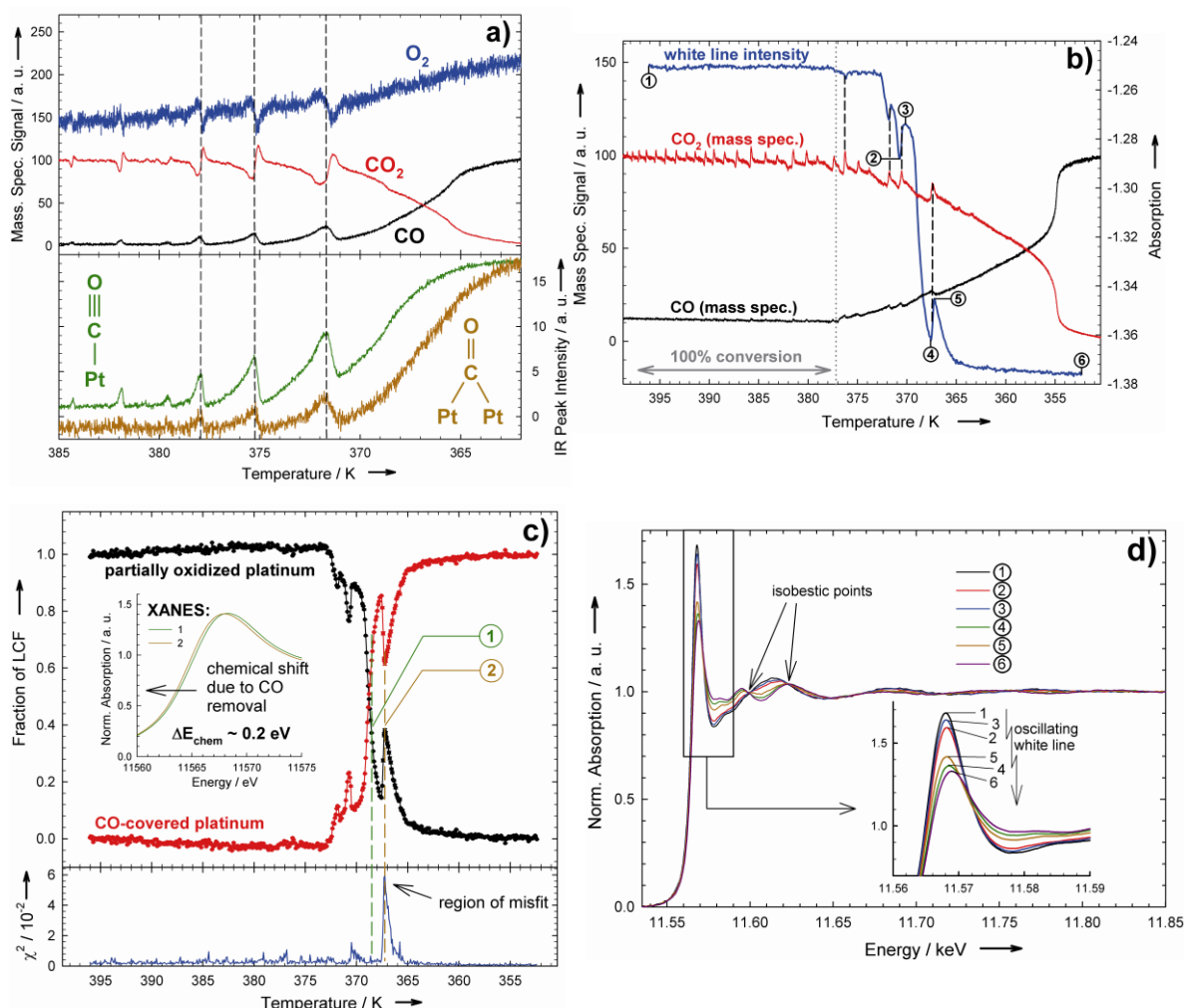
Figure 8.2: Mass spectrometer traces of CO (black), O_2 (blue), and CO_2 (red) compared to a) the intensities of the infra red bands of linearly and bridged CO, measured in a pellet reactor and b) the white line intensity of the Pt L_3 edge spectra measured one mm below the top of a plug-flow reactor during the oscillations of CO oxidation as a function of temperature over 2 wt% Pt/Al$_2$O$_3$. c) Linear combination fitting (LCF) of the XANES spectra in b). d) Selected Pt L_3 edge XAS spectra measured at the positions mentioned in b).

When the conversion in CO decreased to below 100%, a gradual decrease in amount of oxidized platinum, as reflected by decreasing white line, was observed until the white line intensity reached its minimum and became constant. On top of this decreasing whiteline, an oscillation in the maximum of the white line intensity was observed which paralleled the oscillations in the CO_2 concentration in the mass spectrometer, except for the sudden spike in CO_2 production. Within an oscillation, the decreased amount of CO_2 at the exhaust was paralleled by decreased intensity of the whiteline.

The detailed analysis of QEXAFS spectra were done and are summarized in Table 8.1 and Figure 8.3.

Table 8.1: Structural parameters derived from the best fitting of Pt L_3 edge EXAFS spectra.

Condition	Absorber-Scatterer	Coordin-ation Number	Debye-Waller factor ($\mathring{A}^2$)	Inter-atomic disctance ($\mathring{A}$)	Edge-shift E_0 (eV)	GOF[a]
CO-covered	Pt-Pt	8.9	0.0064	2.75	1.8	12.9
Surface oxidized	Pt-Pt	5.4	0.0091	2.60	7.6	76.4
	Pt-O	2.9	0.0014	2.00	3.4	
	Pt-Pt	3.1	0.0150	3.10	-1.6	

[a]goodness of fit GOF, indication of fit quality with regard to the amplitude and imaginary part of the Fourier transform[30]
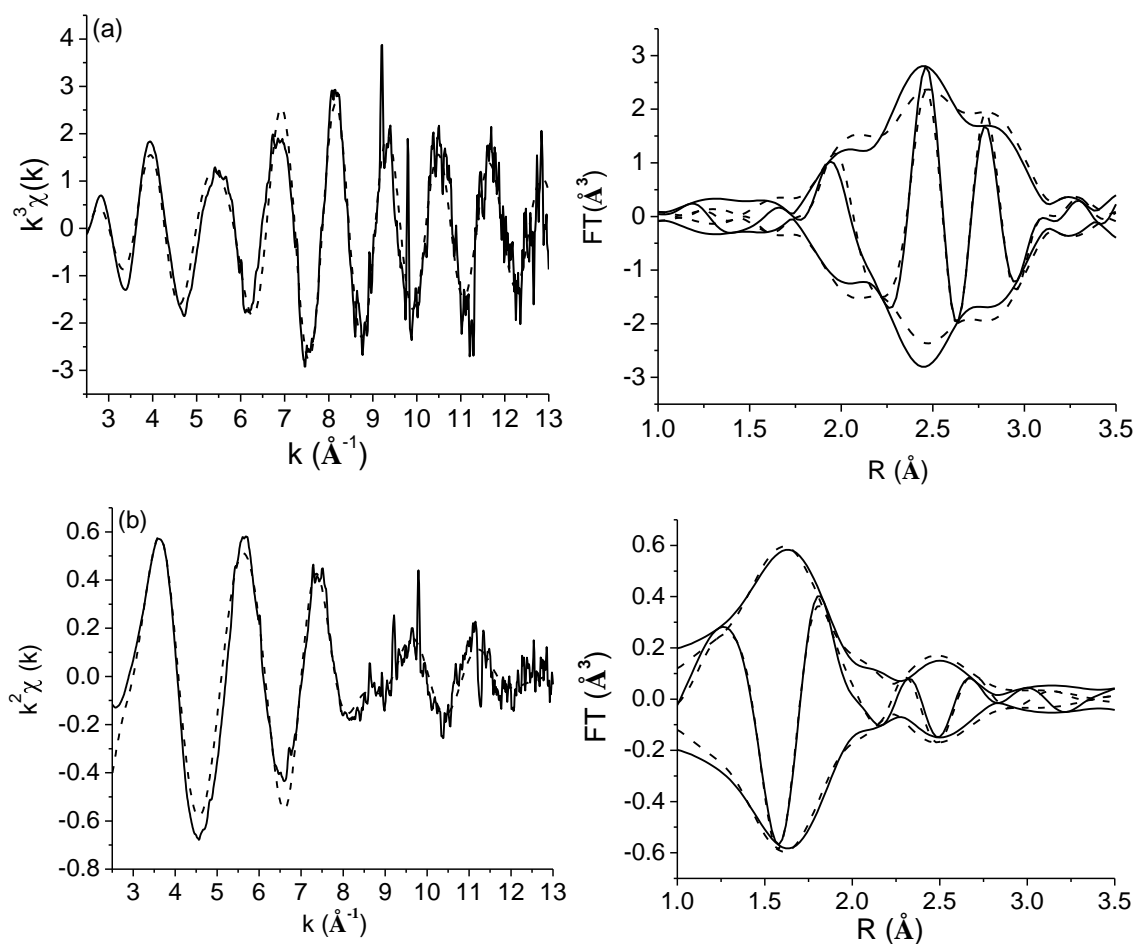

Figure 8.3: EXAFS function and corresponding Fourier transform of spectrum taken for Pt/Al$_2$O$_3$ at (a) low activity and (b) high activity, experimental data (solid line) and best fit (dashed line).

Fitting of XAS spectra was done, after averaging 100 spectra. Figure 8.4 shows the comparison of a 0.5 sec QEXAFS spectrum with the one obtained after averaging 100 such spectra. The spectral features were similar in both spectra with high signal to noise ratio in the averaged signal.
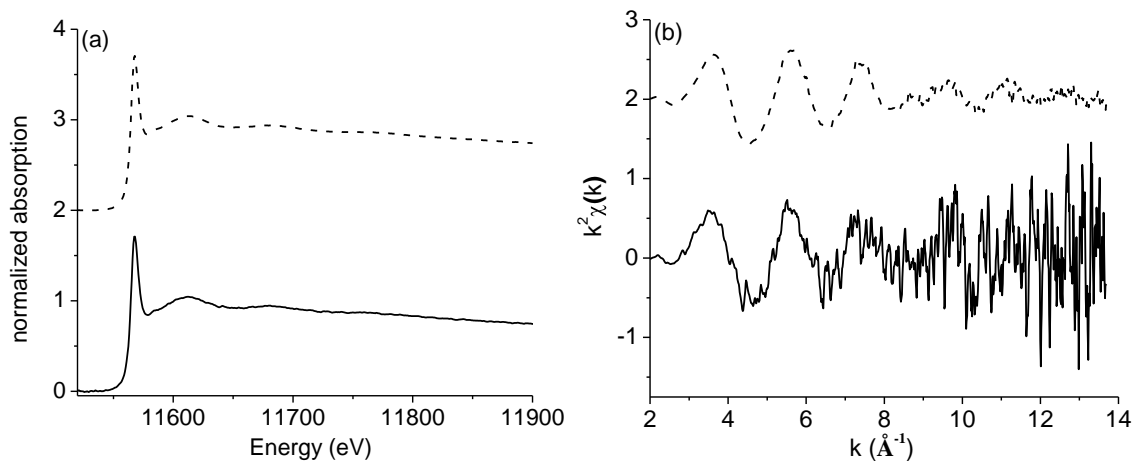

Figure 8.4: (a) Pt L$_3$ edge XAS and (b) EXAFS function of Pt/Al$_2$O$_3$ at high activity. Solid line corresponds to 0.5 sec spectrum and dashed line to spectrum obtained after averaging 100 such 0.5 sec spectra.

Therefore, it allowed better fitting of the spectra. At 100% conversion, there were contributions of Pt-O and Pt-Pt coordination shells located at distances of 1.99 and 3.09 Å, that match those of an oxide.There was an additional metal contribution, characterized by a Pt-Pt coordination shell located at 2.6 Å. The data were consistent with a metallic core and a shell of platinum oxide.[31] The Pt-Pt scattering at 3.09 Å of the oxide had a high Debye-Waller factor. This is attributed to the combined effects of temperature and the strongly disordered structure of the surface oxide. The oxidic contribution disappeared after extinction, as seen by the disappearance of the characteristic oxide coordination shells. Only a metallic Pt-Pt contribution remained. The catalyst at low activity has a Pt-Pt distance of 2.75 Å.

8.3.3 Spatially resolved measurements inside the reactor

The reduction of the platinum oxide, as indicated by the minimum white line intensity (Figure 8.2b), measured one mm below the top by XAS was complete at about 75% conversion of CO measured at the reactor exhaust. The reduction of the oxide was related to the enhanced local concentration of CO, in agreement with the infrared data and with earlier observations.[8,31,32] Measuring various positions, summarized in Table

8.2, in the catalyst bed showed that the lower the position in the catalyst bed, the lower the conversion at the exhaust was at the moment at which the white line intensity reached its minimum, reflecting the reduction of (Figure 8.5). Because of conversion of CO, catalyst at lower positions in the catalyst bed experiences a lower CO to O_2 ratio than at higher positions. Thus, the concentration of CO needed to reduce the oxide is reached at a lower conversion level.

Table 8.2: Conversion level at the reactor exhaust at the moment that the catalyst was fully reduced at the position in the reactor bed (total length of 6mm) where the XAS was measured.

Position in reactor bed (mm)[1]	Conversion (%)[2]
Top	94
1.0	74[3]
2.5	36[3]
4.5	30

[1] from top   [2] estimated error ±5%   [3] average of two measurements
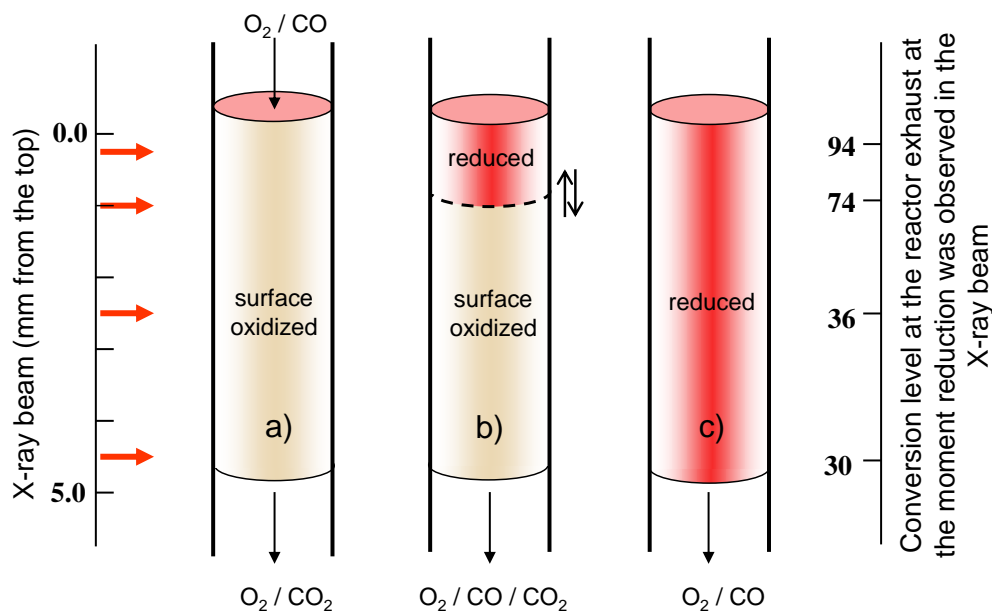

Figure 8.5: Schematic of the structure of the Pt catalyst in a packed-bed catalyst. a) Surface oxidized Pt catalyst was identified as the active phase in CO conversion. b) During extinction of the reaction, CO-poisoned surface forms at the top of the reactor and gradually moves downward. On top of the reduction front that moves down the reactor bed, the border between reduced and surface-oxidized metal oscillates in position causing the oscillations in CO_2 signal and in amounts of reduced respectively oxidized catalyst (Figure 8.2). Only when the oscillations occur at a position where the XAS is measured, it is detected in the spectra. c) At low activity, reduced Pt was found. The reduced surface is poisoned by CO as identified by infrared spectroscopy.

151

8.4 Discussion

8.4.1 Combination of in situ time- and space- resolved XAS and IR spectroscopy

As the kinetic oscillations occur at high frequencies with small amplitudes, it requires a fast response technique with capabilities of revealing the catalyst structure under in situ conditions. QEXAFS promises such requirement. The combination of information acquired from IR spectroscopy is advantageous for gaining the complimentary insight into the adsorbed species on the catalysts surface.

During one oscillation (Figure 8.2a and b) the slow decrease in CO_2 production is paralleled by the increasing amount of CO on the catalyst surface as indicated by the infra red signals of linearly bonded CO and bridged CO. These bands indicated the formation of islands of absorbed CO. The frequency of vibration was constant and independent of the intensity of the vibration.[33,34] These inactive islands of CO replaced the active surface during deactivation and leaded to the low activity of the catalyst. The catalyst at low activity had a Pt-Pt distance of 2.75 Å (Table 8.1), which was indicative of bond relaxation of the small platinum particles in the presence of adsorbed CO.[31] The sudden spike in CO_2 production in an oscillation (Figure 8.2a and b) can be explained by storage of CO on the catalyst during the decrease of CO_2 production, which is suddenly released during the sharp rise in CO_2. This sharp rise in CO_2 is caused by fast reaction of chemisorbed CO with oxygen. This frees the surface of the poisoning CO, which enables the catalyst to generate a more active surface by freeing sites to dissociate oxygen. This dissociated oxygen can react to CO very fast or it can further react to the surface and oxidize it. This surface oxide formed was disordered[31] as also indicated by the high Debye-Waller factor (Table 8.1). The overall result is a more active surface, which causes the CO signal to fall. Storage of CO on the catalyst surface leads to a lower production of CO_2 and to increased CO in the gas phase. The spike in CO_2 production is observed because of the reaction of the surface CO in addition to the gas phase CO being converted into CO_2.

The advantage of measuring the structure of catalyst at different positions in the reactor as shown in Figure 8.5 is that it allows to spatially characterize the structure of catalyst in the reactor and leads to understand how the front of reducing metal moves along the reactor as explained in Figure 8.5. At first, the oscillations in the conversion and the corresponding reduction and oxidation of the metal occur near the top of the catalyst bed, above the point where the XAS of Figure 8.2b was measured. This also

explains why in the temperature range 398 to 388 K the CO signal is rather insensitive to oscillations as the bottom part of the reactor is able to convert CO.

8.4.2 Linear combination fitting

Figure 8.2c shows that most of the spectra collected during the few oscillations can be well described by a combination of spectra of surface oxidized platinum and CO covered reduced platinum. Within an oscillation, the initial loss of activity was paralleled by increased amount of CO-covered surface at the expense of surface-oxidized platinum. During the sharp rise and excess formation of CO_2, the linear combination fit showed misfits, which suggests that surface oxidized and CO-covered surface are not the only components during this part of the oscillation. Comparing two spectra with identical white line intensity (inset Figure 8.2c) showed a small shift in energy, which is characteristic of the difference between bare surface and surface with adsorbed CO.[29] These linear combination fits provide further evidence that after freeing the surface of CO there exist sites for dissociative O_2 absorption.

8.4.3 Mechanism of kinetic oscillations

Based on the QEXAFS, IR results and kinetic measurements the following mechanism is proposed to account for the oscillations during CO oxidation on technical catalysts and under atmospheric pressure. Reduction of the surface oxide enables storage of CO on its surface, which is shown by the infrared data. This stored CO is released in the sudden ignition, which enables re-oxidation of the surface and the spike in CO_2. The reduced surface with chemisorbed CO (Figures 8.2a-c) shows lower activity. This indicates that the amount of surface oxide matches the catalytic activity of the catalyst and is thus responsible for the catalytic conversion.[8-10] Because bulk oxides are near inactive, the presence of coordinatively unsaturated metal sites for adsorption of CO and possibly oxygen are required to reach high activity over a surface oxidized particle. These may be exposed platinum atoms in the oxide similar to the coordinative unsaturated sites proposed on ruthenium oxides[35-37] and on palladium oxides.[38] Alternatively, the boundary region between the surface oxide and reduced metal sites has been proposed to display high activity,[39] though this has been shown to be a minor component[6] in agreement with our observation of the loss of activity with decreased amount of oxide, and increased amount of CO poisoned surface. The oscillations are also shown to occur due to changes in the size of islands of CO on the platinum surface,[6] accounting for

changes in the platinum surface with chemisorbed oxygen. However, we have found no evidence of an oxygen covered surface, which has been proposed as the active phase.[6,40,41]

The results presented in this work identify that lattice oxygen of the surface oxide reacts with CO within an oscillation and that it is replenished by gas phase O_2 in the latter part of the oscillation. This is characteristic of the Mars van Krevelen mechanism.[42] When an oxygen atom from the surface oxide reacts with CO, a defect site is formed, which can be replenished by oxygen or, alternatively, by CO. The adsorbed CO may further react with oxygen from the surface oxide, thus further reducing the surface. The reduced surface builds slowly, as indicated by XAS, and CO is stored on the surface that was detected by infrared spectroscopy and XAS. CO-covered surfaces show low activity, which causes a decrease in conversion, and thereby a local increase in the CO concentration and possibly a decrease in the local temperature, which would further decrease conversion. Because the particles in our catalyst are between one and two nano-meter in size (Table 1), many particles are simultaneously reduced and re-oxidized in the process, which can only occur when they are mediated and act in parallel.[43] The individual particles switch from partially oxidized to reduced with adsorbed CO. The higher local CO concentration can mediate reduction of surface oxides of nearby particles. The infrared and XAS measurements indicate that a higher local CO concentration leads to higher degree of reduction. Local fluctuations may cause a CO-covered surface to ignite, which occurs very sudden.[44] During this ignition, carbon monoxide disappears from the surface, which is paralleled by oxidation of the platinum surface. We assign this to dissociative adsorption of oxygen that could react either with adsorbed CO or with the platinum surface. The surface oxide that is formed is more active than the CO-poisoned one.

8.5 Conclusions

The time and space resolved XAS, to measure the dynamic structure of the catalyst, in combination with mass spectrometry, to determine the performance of the catalyst, and infrared spectroscopy, to establish the surface adsorbates, allowed to identify the mechanism of oscillations in CO oxidation in a packed-bed reactor. A surface oxide was identified that is highly disordered and possibly rich in oxygen defects as the catalytically more active species under technologically relevant conditions. The structure of platinum varied as function of time and position within the catalytic reactor.

References

1   G. Ertl, Angew. Chem. Int. Ed. 47 (2008) 3524.

2   M. J. Kahlich, H. A. Gasteiger, R. J. Behm, J. Catal. 1997, 171, 93-105.

3   R. J. Farrauto, R. M. Heck, Catal. Today 1999, 51, 351-360.

4   G. Ertl, H. Knötzinger, F. Schüth, J. Weitkamp, in   Handbook of Heterogeneous Catalysis, Wiley-VCH, Weinheim, (2008).

5   X. Su, P. S. Cremer, Y. R. Shen, G. A. Somorjai, J. Am. Chem. Soc. 119 (1997) 3994.

6   P. T. Fanson, W. N. Delgass, J. Lauterbach, J. Catal. 204 (2001) 35.

7   J.Wintterlin, S. Volkening, T. V. W. Janssens, T. Zambelli, G. Ertl, Science 278 (1997) 1931.

8   B. L. M. Hendriksen, J. W. M. Frenken, Phys. Rev. Lett. 89 (2002) 046101.

9   M. D. Ackermann et al., Phys. Rev. Lett. 95 (2005) 255505.

10 B. L. M. Hendriksen, S. C. Bobaru, J. W. M. Frenken, Catal. Today 105 (2005) 234.

11 M. E. Grass, Y. W. Zhang, D. R. Butcher, J. Y. Park, Y. M. Li, H. Bluhm, K. M. Bratlie, T. F. Zhang, G. A. Somorjai, Angew. Chem. Int. Ed. 47 (2008) 8893.

12 J. Singh, E. M. Alayon, M. Tromp, O. V. Safonova, P. Glatzel, M. Nachtegaal, R. Frahm, J. A. van Bokhoven, Angew. Chem. Int. Ed. 47 (2008) 9260.

13 M. S. Chen, Y. Cal, Z. Yan, K. K. Gath, S. Axnanda, D. W. Goodman, Surf. Sci. 601 (2007) 5326.

14 M. Eiswirth, R. Schwankner, G. Ertl, Z. Phys. Chem. 144 (1985) 59.

15 M. Eiswirth, G. Ertl, Surf. Sci. 177 (1986) 90.

16 P. Hugo, Ber. Bunsen-Ges. 74 (1970) 121.

17 H. Beusch, D. Fieguth, E. Wicke, Chem. Ing. Tech. 15 (1972) 445.

18 P. Nolte, A. Stierle, N. Y. Jin-Phillipp, N. Kasper, T. U. Schulli, and H. Dosch, Science 321 (2008) 1654.

19 M. A. Newton, C. Belver-Coldeira, A. Martinez-Arias, M. Fernandez-Garcia, Nature Mater. 6 (2007) 528.

20 J. A. van Bokhoven, T. Ressler, F. M.F. de Groot, G. Knopp-Gericke, in In-situ spectroscopy of catalysts, (Ed. B. M. Weckhuysen), American Scientific Publishers, California, (2004).

21 B. M. Weckhuysen, Angew. Chem. Int. Ed. 2009, 48, 4910-4943.

22 (a) R. Frahm, Nucl. Instrum. Methods Phys. Res. A 270 (1988) 578; (b) J. Stötzel, D. Lützenkirchen-Hecht, E. Fonda, N. de Oliveira, V. Briois, R. Frahm, Rev. Sci. Instr. 79 (2008) 083107.

23 S. G. Fiddy, M. A. Newton, J. M. Corker, S. Turin, T. Campbell, J. Evans, A. J. Dent, G, Salvini, Chem. Commun. 9 (1999) 851.

24 M. A. Newton, S. G. Fiddy, G. Guilera, B. Jyoti, J. Evans, Chem. Commun. 1 (2005) 118.

25 M. A. Newton, A. J. Dent, S. D- Moreno, Steven G. Fiddy, B. Jyoti, J. Evans, Chem. Eur. J. 12 (2006) 1975.

26 R. Bal, M. Tada, T. Sasaki, Y. Iwasawa, Angew. Chem. Int. Ed. 45 (2006) 448.

27 J-D. Grunwaldt, B. Kimmerle, A. Baiker, P. Boye, C. G. Schroer, P. Glatzel, C. N. Borca, F. Beckmann, Catal. Today 145 (2009) 267.

28 The frequency of the atop- and bridged-bonded CO was independent of the intensity of the band, which shows that CO experienced a constant dipolar interaction with neighboring CO molecules. This indicates that CO is present as islands, not as isolated CO on the surface[14]

29 O. V. Safonova, M. Tromp, J. A. van Bokhoven, F. M. F. de Groot, J. Evans, P. Glatzel, J. Phys. Chem. B 110 (2006) 16162.

30 D. C. Koningsberger, B. L. Mojet, G. E. van Dorssen, D. E. Ramaker, Top. Catal. 10 (2000) 143.

31 E. M. Alayon, J. Singh, M. Nachtegaal, M. Harfouche, J. A. van Bokhoven, J. Catal. 263 (2009) 228.

32 P.-A. Carlsson, L. Oesterlund, P. Thormählen, A. Palmqvist, E. Fridell, J. Jansson, M. Skoglundh, J. Catal. 226 (2004) 422.

33 J. A. Anderson, J. Chem. Soc. Faraday Trans. 1992, 88(8), 1197-1201.

34 J. A. Anderson, Catal. Lett. 1992, 13, 363-369.

35 H. Over, Y. D. Kim, A. P. Seitsonen, S. Wendt, E. Lundgren, M. Schmid, P. Varga, A. Morgante, G. Ertl, Science 2000, 287, 1474-1476.

36 J. Wang, C. Y. Fan, K. Jacobi, G. Ertl Surf. Sci. 2001, 481, 113-118

37 C. Y. Fan, J. Wang, K. Jacobi, G. Ertl, J. Chem. Phys. 2001, 114, 10058-10062.

38 J. Rogal, K. Reuter, M. Scheffler, Phys. Rev. B 2008, 77, 155410.

39 W. X. Li, B. Hammer, Chem. Phys. Lett. 2005, 409, 1-7.

40 D. M. Haaland, F. L. Williams, J. Catal. 1982, 76, 450-465.

41 T. H. Lindstrom, T. T. Tsotsis, Surf. Sci. 1985, 150, 487-502.

42 This does not necessarily mean that the steady state conversion follows a Mars van Krevelen mechanism.

43 M. M. Slinko, N. Jaeger, in Oscillating Heterogeneous Catalytic Systems, Elsevier, Dordrecht, 1994.

44 Y. Suchorski, J. Beben, E. W. James, J. W. Evans, R. Imbihl, Phys. Rev. Lett. 1999, 82, 1907-1910.

Chapter 8

Chapter 9

Preferential oxidation (PROX) of CO over platinum catalysts

Abstract

In situ time resolved high-energy resolution fluorescence x-ray spectroscopy (HERFD XAS) has been used to determine the structure of ceria-supported platinum nano-clusters and platinum-doped ceria in a reaction mixture of 75% H_2, 1% CO, and 1% O_2 in He. Cyanide leaching of ceria-supported platinum catalyst resulted in platinum-doped ceria that consisted of platinum mostly in cationic form. Preferential oxidation of CO (PROX), water gas shift (WGS) reaction, and methanation occurred on metallic platinum nanoparticles supported on alumina and ceria. Ceria-supported platinum nano-clusters showed superiority in terms of activity during oxidation of both H_2 and CO. In situ HERFD spectra collected at the Pt L_3 edge showed the reduction of cationic platinum under the reaction conditions of high temperature and 100% conversion in O_2. The support and platinum loading had an influence on the structure of the catalyst.

9.1. Introduction

The removal of CO from a stream of hydrogen has attracted significant attention, because proton-exchange membrane fuel cells require CO-free hydrogen.[1] Selective removal of CO is required to decrease the CO content to below 1-100 ppm, which can be achieved by various methods. These are the preferential oxidation of CO (PROX),[2] the water gas shift (WGS) reaction,[3] and methanation.[1,4] The WGS reaction is generally the first reaction applied to lower the CO content from the stream of hydrogen that may be formed via steam or auto thermal reforming or via partial natural gas oxidation. The CO concentration is lowered to about 1 vol % by WGS and further decrease is required, which is achieved by PROX and / or methanation depending on the specific application. Many catalytic systems have been proposed for each of these reactions. Materials like ceria have received much attention, because of their capacity to store oxygen.[5] The addition of a metal is required to provide highly active catalysts for PROX, WGS, and methanation. Many different metals, such as Pt, Rh, Au, and multi-metallic systems,[6] have been proposed for such purpose. The oxidation state of these metals is highly debated. Nonmetallic cationic Au and Pt on or in ceria have been proposed to be active in the WGS reaction and CO oxidation.[6c,7] Catalysts, after cyanide leaching, were still effective or even showed higher catalytic activity compared to the catalyst before leaching. Recent theoretical results have suggested that in doped ceria, the bond between the oxygen atoms and the oxide is weakened in the presence of the dopant.[8] The ceria doped with metal cations was thus proposed to be an active catalyst in the oxidation of CO. Cationic metals have been proposed to be active in PROX, WGS, oxidation, and even hydrogenation reactions.[9] On the other hand, reduced particles were proposed to be the catalytically active species, with the reaction taking place either on the particle or at the metal-support interface.[10] The role of metallic gold in WGS reaction has been established using various techniques like in situ X-ray absorption spectroscopy, infra red spectroscopy, and X-ray photoelectron spectroscopy.[11] In many of the studies, the structure of the catalyst has not been determined under in situ conditions and authors have relied on ex situ measurements. However, there is another issue in addition to the oxidation state of the metal, which makes an analysis more complex. The catalytic performance of supported metals often shows a strong particle size effect.[10b,12] A metal that is deposited as very large particles does not exhibit the same catalytic performance as a (sub) nanometer-sized particle. Gold, for example, shows in many reactions no or very low catalytic activity unless finely dispersed on a support into the nano-meter or

even sub-nano-meter range.[10b] Thus, relating catalytic activity to reduced or oxidic species is not straight forward. The presence of (sub) nanometer-sized particles or clusters may be responsible for most of the catalytic activity.[13]

It is well known that the structure of a supported metal strongly varies with temperature and composition of the gas phase.[14] Moreover, within a single reactor the structure of the catalyst differs.[14a,15] Because often both oxidizing and reducing gases are present in the reacting gas mixtures and their relative concentration varies with conversion, experimental detection of the active phases under reaction conditions is absolutely essential to determine the catalytically relevant structure. In this chapter, the structure of platinum supported on alumina and ceria is determined under PROX conditions at varying temperature, during which WGS and methanation also occur. High-energy resolution fluorescence detected X-ray absorption spectroscopy (HERFD XAS) at the Pt L_3 edge was used,[16] which is a very sensitive technique to determine the local platinum structure, oxidation state, and the presence of adsorbates on the metal surface.[17] It has been well-established that adsorbates on the surface of a metal particle can be detected and even the adsorption mode (atop, bridged or three-fold sites) can be distinguished.[17] XAS also enables to estimate the size of metal particles on a support.[18] Because of its ability to measure the metal structure of a functioning catalyst within a catalytic reactor, it is one of the most suitable methods to determine the relation between electronic and geometric structure and performance.

9.2 Experimental

1.90 wt% Pt/Al_2O_3 was synthesized using the incipient-wetness impregnation method as explained in section 2.1. La doped ceria was synthesized using co-precipitation method as described in section 2.1. 4.4 wt% Pt/Ce(La)O_x, hereafter called Pt/Ce(La)O_x in this chapter, was synthesized using an incipient-wetness impregnation method as explained in section 2.1. Afterward, the leaching of Pt/Ce(La)O_x was done using 2% aqueous solution of NaCN at room temperature for 24 h. The leaching resulted in 2 wt% Pt/Ce(La)O_x, where the platinum content was approximated from energy-dispersive X-ray spectroscopy (EDX). The sample will be called hereafter as L-Pt/Ce(La)O_x in this chapter. The catalysts were later characterized by scanning transmission electron microscopy (STEM) as explained in section 2.2.

The experiments were conducted using the flow scheme described in section 2.6, at beamline ID 26 at the European Synchrotron Radiation Facility (ESRF), Grenoble, France. The reactor, as explained in section 2.6, was operated in down flow and simultaneous fluorescence XAS experimentation was done with the aid of aluminum windows. Pt/Al_2O_3 was pre-treated in situ in 5% H_2 in He at 473 K before switching to the PROX reaction mixture of 1% CO, 1% O_2, and 75% H_2 in He. For $Pt/Ce(La)O_x$ and L-$Pt/Ce(La)O_x$ catalysts, no pretreatment was done before the PROX reaction. The measurements were done at a constant total flow of 30 NmL/min through the reactor, corresponding to a space velocity of about 64,000 h^{-1}. The selectivity toward CO oxidation was calculated as explained in section 2.6.

The X-ray beam measured 0.3 mm horizontal and 1 mm vertical, and traversed the reactor 1 mm from the top of the catalyst bed. The incident energy was selected by means of a pair of Si(111) crystals with an energy bandwidth of 1.5 eV at the Pt L_3-edge. An X-ray emission spectrometer based on perfect crystal Bragg optics was employed for recording high-energy resolution fluorescence detected X-ray absorption scans with an avalanche photodiode (APD) as photon counting detector. The instrumental bandwidth was 1.5 eV, which is smaller than the core hole lifetime broadenings. A Canberra silicon photodiode was mounted to measure the total fluorescence simultaneously with the HERFD XAS. The spectra were taken with a time resolution of 125 sec during the heating and cooling trajectories of PROX varying the temperature between 323 K to 673 K at 2 K/min.

9.3 Results

9.3.1 Pt/Al_2O_3 and $Pt/Ce(La)O_x$

Figure 9.1 shows STEM micrographs of Pt/Al_2O_3, $Pt/Ce(La)O_x$, and L-$Pt/Ce(La)O_x$. catalysts. Pt/Al_2O_3 (Figure 9.1a) has a narrow size distribution of the platinum nanoparticles around 1 nm. The small bright spots were confirmed, by EDX, to be platinum particles supported on alumina, which was reflected as the less bright texture in the STEM micrographs. For lanthanum-doped cerium oxide, the characterization was more challenging due to rather small difference in the scattering potential of platinum and the support. EDX confirmed the presence of platinum in the form of very small entities on roughly spherical ceria support.
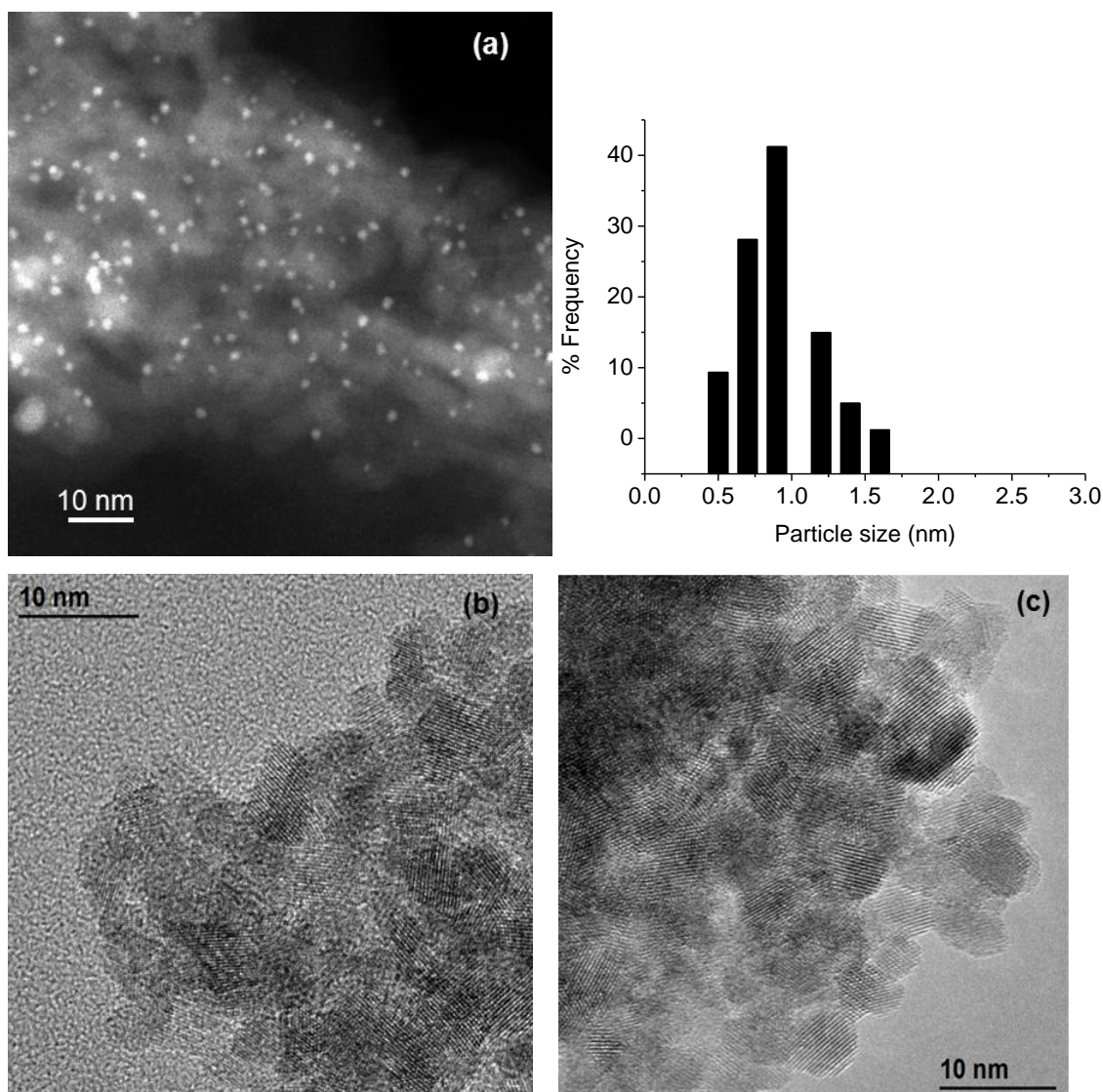
Figure 9.1: STEM micrographs of (a) Pt/Al$_2$O$_3$, (b) Pt/Ce(La)O$_x$, and (c) L-Pt/Ce(La)O$_x$. Particle size distribution of platinum particles for Pt/Al$_2$O$_3$ is also shown.

Figure 9.2 shows the mass spectrometer traces of CO, O$_2$, CO$_2$, H$_2$O in the efflux of gas from the reactor, which was packed with Pt/Al$_2$O$_3$, as function of temperature of the reactor. The catalyst was pre-reduced at 473 K prior to PROX in a flowing mixture of 5% H$_2$ in He. Figure 9.2a and b shows the heating respectively cooling trajectories in a mixture of 1% CO, 1% O$_2$, 75% H$_2$ and rest He. In the heating trajectory, at about 315 K, the O$_2$ and CO signals started to decrease indicating conversion to CO$_2$. At around 420 K, all O$_2$ was consumed, and at approximately the same temperature the H$_2$O signal reached a maximum. At higher temperature, the WGS started. At around 500 K, CO and H$_2$O reached their minimal concentration and CO$_2$ its maximum. Methanation started at around 550 K and propagated until all CO was converted into methane. These data

163

strongly resemble those previously reported,[6a] which indicated that CO is preferentially adsorbed on the metal surface and is thus oxidized preferentially. Increasing the temperature up to 400 K lowered the CO coverage and thus the selectivity to CO_2. The cooling trajectory was essentially the same as the heating one.
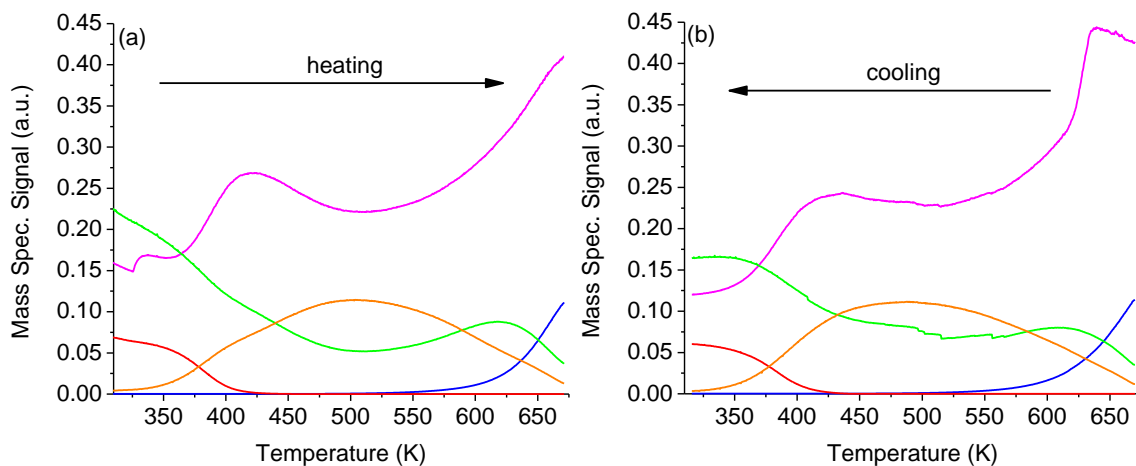

Figure 9.2: Mass spectrometer traces of CO (green), O_2 (red), CO_2 (orange), H_2O (pink), and CH_4 (blue) during (a) heating and (b) cooling trajectory of PROX over 1.9 wt% Pt/Al_2O_3.
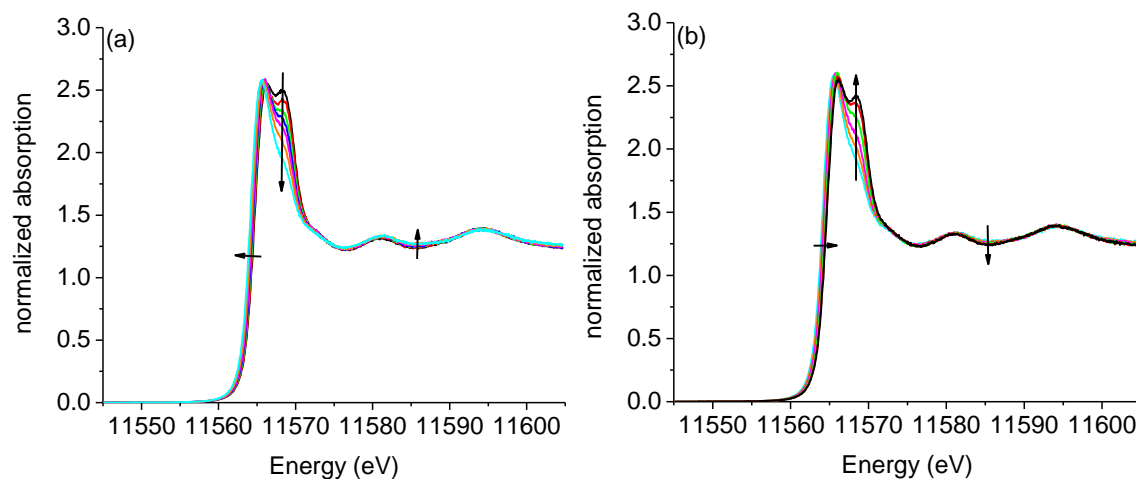

Figure 3: Pt L_3 edge HERFD XANES of 1.9 wt% Pt/Al_2O_3 during PROX (a) measured during heating at 305 K (black), 347 K (red), 426 K (green), 476 K (blue), 538 K (pink), 622 K (orange), and 671 K (cyan), and (b) during cooling at 316 K (black), 374 K (red), 449 K (green), 524 K (pink), 635 K (orange), and 670 K (cyan).

Figure 9.3a and b shows the HERFD XAS spectra that were recorded while measuring the catalytic data in Figure 9.2. The arrows indicate the direction of the changes with increasing (Figure 9.3a), respectively decreasing (Figure 9.3b) temperature. The spectrum measured at the lowest temperature of 305 K showed a doublet in the whiteline

at 11566.3 and 11568.3 eV, which is characteristic of adsorbed CO on the surface of a nano-sized platinum particle.[14c,d,17] With increasing temperature, the high-energy peak decreased in intensity because of the desorption of CO. The peaks at 11581.1 and 11594.2 eV are characteristic of reduced metal. They are caused by the scattering of the photo-electron against the neighboring atoms, and unambiguously point to the presence of a reduced metal particle. Their intensity is a measure of the metal particle size, which is estimated to be about 1 nm, based on comparison to the intensity of these features to previously published data.[14c] This agrees with the particle size of 1 nm determined from TEM (Figure 9.1a). Their intensity decreased with temperature, because of the larger Debye-Waller factor. It can be said with certainty that less than 0.5% of the platinum atoms were present, if any, in an oxidic oxidation state. Like the catalytic data, the changes were completely reversible during the cooling trajectory: the appearance of the doublet, because of the re-adsorption of CO and the increase of intensity at 11581.1 and 11594.2 eV.

In agreement to previous reports,[19] the catalytic behavior of $Pt/Ce(La)O_x$ without any pretreatment was very different from that of Pt/Al_2O_3. Figure 9.4a and b shows the mass spectrometer traces during heating respectively cooling trajectories in a PROX mixture of 1% CO, 1% O_2, 75% H_2, and rest He for $Pt/Ce(La)O_x$. The catalyst showed a very low activity below about 420 K, at which temperature the CO began to be very preferentially oxidized. At about 100 K higher temperature than in case of Pt/Al_2O_3, also water began to be formed to significant extend. At a temperature of about 510 K, when the conversion of CO was almost complete and the selectivity to CO_2 was 68%, a sharp change in selectivity occurred and the selectivity switched from being preferentially to CO_2 to H_2O. This sudden change in selectivity occurred at a temperature at which the conversion of oxygen was complete. Upon further heating, the water peak showed a surplus in intensity until about 525 K, which probably originated from reduction of the catalyst (vide infra). A temporal decrease in CO and CO_2 was observed, which suggests that carbon is retained on the surface. Further increasing the temperature let to decreased formation of CO_2 and the onset of methanation as shown by the intensities of masses 15 and 16 and the enhanced water. At about 610 K all CO was ultimately converted into methane. Unlike Pt/Al_2O_3, the cooling trajectory of $Pt/Ce(La)O_x$ showed large differences compared to the heating one. The cooling trajectory was the reverse of the heating one from 671 to about 525 K, at which temperature the heating trajectory

showed the sudden shift in selectivity. No such shift was observed in the cooling trajectory, indicating that permanent changes to the catalyst had occurred. Below 525 K, the CO_2 concentration decreased with decreasing temperature, indicative of the occurrence of the WGS reaction, which is known to take place over $Pt/Ce(La)O_x$ at such temperature.[6c] At 423 K, the concentration of CO_2 reached a minimum and further cooling slowly increased it to until about 330 K. In this interval, a sharp decrease in H_2O signal was observed, which showed a minimum at 330 K. At that temperature, oxygen reappeared at the exhaust of the reactor and the selectivity to CO_2 was intermediate.
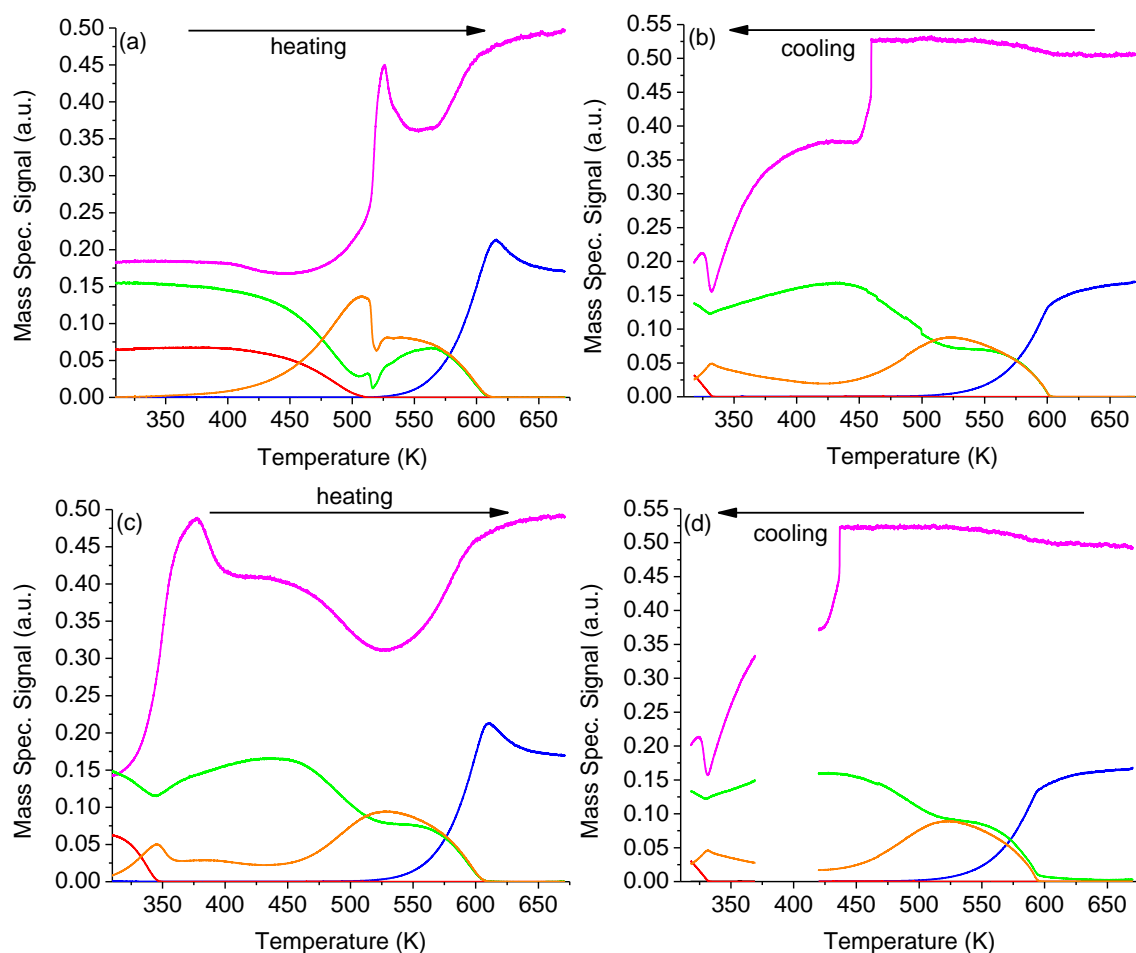

Figure 9.4: Mass spectrometer traces of CO (green), O_2 (red), CO_2 (orange), H_2O (pink), and CH_4 (blue) during (a) first heating, (b) first cooling, (c) second heating, and (d) second cooling trajectory of PROX over $Pt/Ce(La)O_x$.

Further cooling decreased CO_2, because of incomplete oxygen conversion. The catalyst showed a much higher activity during the cooling trajectory than during the heating one. Because of the large changes between the heating and the cooling trajectories, the cycle was repeated. The second heating and cooling trajectories (Figure 9.4c and d) showed

essentially the same behavior as the first cooling trajectory (Figure 9.4b), with the exception of the presence of a peak in the H_2O signal in second heating trajectory at about 375 K, which probably originated from water desorption that was built up on the catalyst. This indicated that the catalyst during these cooling and heating trajectories had very similar structure at about similar temperature and that it strongly differed in the first heating trajectory.
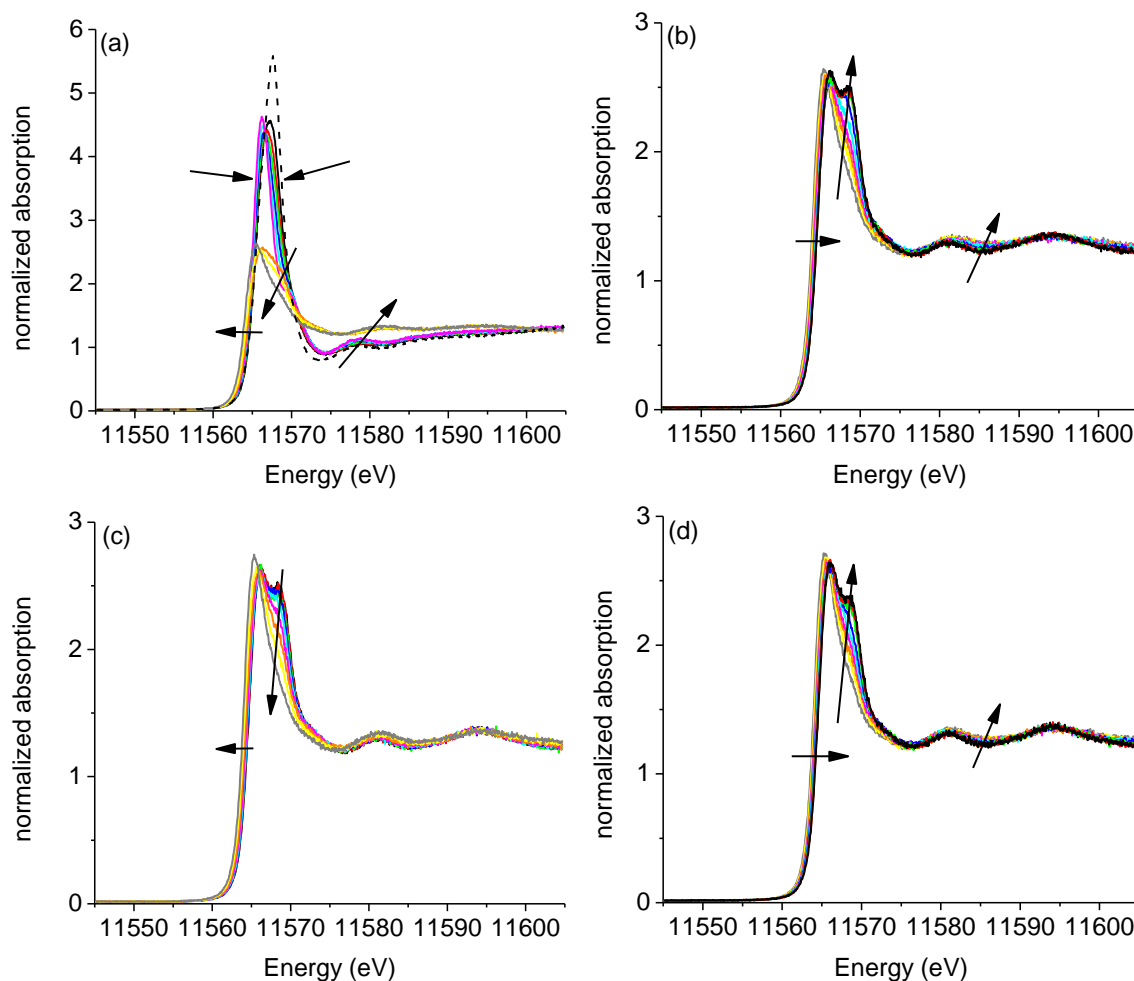

Figure 9.5: Pt L_3 edge HERFD XANES of Pt/Ce(La)O_x during PROX (a) measured during first heating trajectory at 304 K (black), 326 K (red), 373 K (green), 423 K (blue), 473 K (cyan), 523 K (pink), 578 K (orange), 623 K (yellow), and 671 K (grey); the spectrum in He before the start of reaction is also shown (black dash), (b) during first cooling trajectory at 303 K (black), 322 K (red), 373 K (green), 423 K (blue), 473 K (cyan), 530 K (pink), 573 K (orange), 623 K (yellow), and 670 K (grey), (c) during second heating trajectory at 305 K (black), 323 K (red), 373 K (green), 423 K (blue), 473 K (cyan), 523 K (pink), 573 K (orange), 623 K (yellow), and 671 K (grey), and (d) during second cooling at 304 K (black), 326 K (red), 373 K (green), 423 K (blue), 473 K (cyan), 523 K (pink), 578 K (orange), 623 K (yellow), and 671 K (grey).

The strong differences between the first and second heating and cooling trajectory were reflected in the HERFD spectra (Figure 9.5), which were also measured one mm below the top of the catalyst bed. The spectrum of the as-synthesized sample was characterized by large whiteline intensity, which is indicative of platinum in a high valence state (Figure 9.5a). The whiteline intensity slightly dropped after introducing the PROX reaction mixture into reactor. Also, the feature at about 11578.4 eV is characteristic of oxidized platinum. During heating, the shape of the whiteline changed, decreasing in its area, however, its maximum remained constant. The decreased area under the whiteline indicated reduction of part of the platinum oxide. The peak at 11578.4 eV shifted slightly in this temperature range. This indicated that the structure of the platinum oxide changed. A strong and sudden change of the spectral shape occurred in spectra that were measured above 520 K, the temperature at which oxygen was depleted and the selectivity of the reaction had switched (Figure 9.4a). The spectral shape resembled that of the Pt/Al_2O_3 catalysts that were measured at high temperature; a doublet of which the high-energy component decreased in intensity with temperature and small features at 11581.1 and 11594.2 eV were observed. The intensity of these features was markedly lower than for the Pt/Al_2O_3 catalyst. They unambiguously point to the presence of reduced platinum particles, which are however smaller in size compared to those in the Pt/Al_2O_3 catalyst. The first cooling trajectory resulted in the formation of a more pronounced doublet until the lowest temperature measured (Figure 9.5b). With certainty, more than 99.5% of the platinum atoms were in the reduced state. The platinum particles were covered by CO, the more so the lower the temperature. The series of spectra measured during the second heating and cooling trajectories (Figures 9.4c and d) were very similar to that of the first cooling trajectory, which confirms that the structure of the catalyst had stabilized.

9.3.2. Leaching

In analogy to previous reports,[6c,11] leaching of the metallic platinum particles was done using NaCN to generate $L-Pt/Ce(La)O_x$. Its catalytic performance and structure was determined. Figure 9.6 shows the mass spectrometer traces of CO, O_2, O_2, H_2O in the efflux of gas from the reactor, as function of temperature of the reactor. A very low conversion of CO, H_2, and O_2 was observed below 375 K (Figure 9.6a).
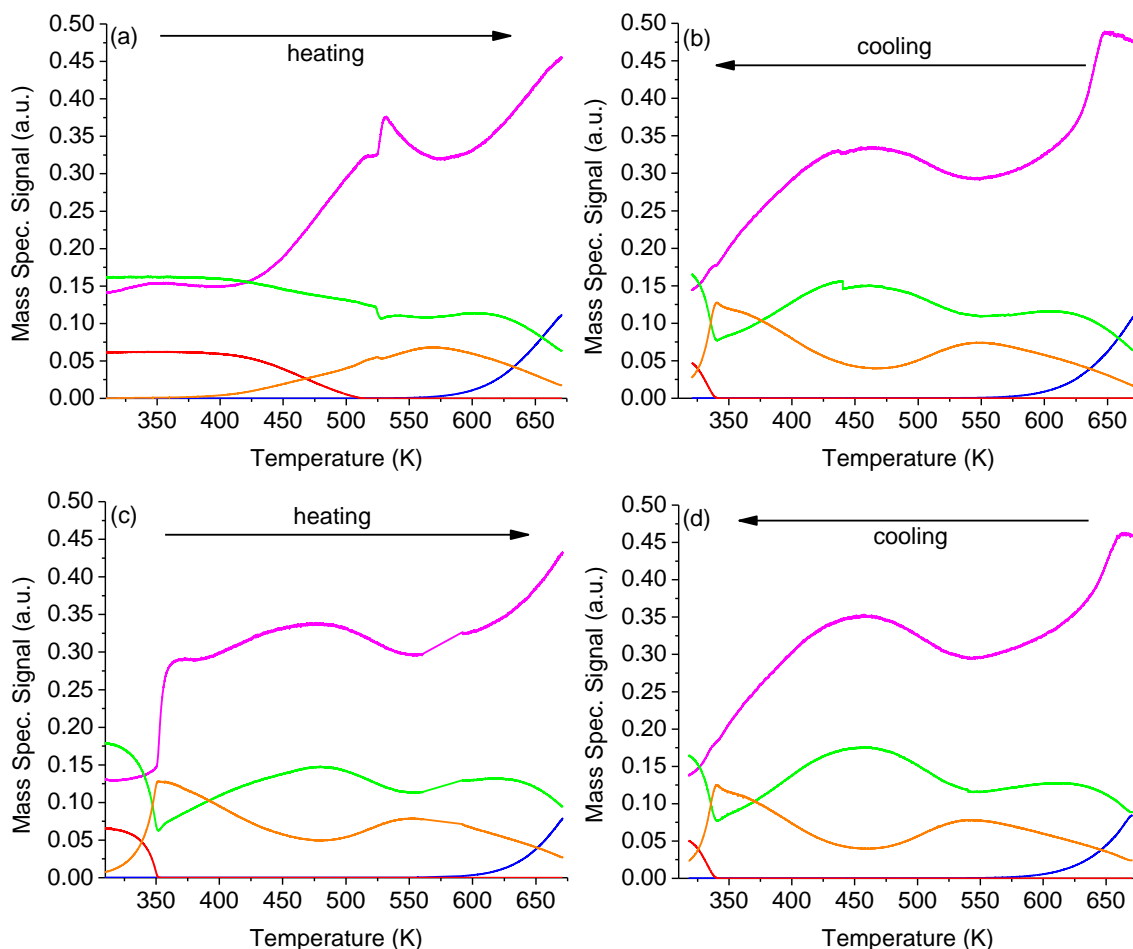
Figure 9.6: Mass spectrometer traces of CO (green), O_2 (red), CO_2 (orange), H_2O (pink), and CH_4 (blue) during (a) first heating, (b) first cooling, (c) second heating, and (d) second cooling trajectory of PROX over L-Pt/Ce(La)O_x.

At about 385 K, the conversion started, however, in contrast to the non-leached sample, Pt/Ce(La)O_x, with a high selectivity to H_2O. At about 520 K, the oxygen conversion was complete and a small discontinuity occurred in the mass spectrometer traces of H_2O, CO_2 and CO. The signal of H_2O showed a surplus and there was a small loss of selectivity to CO_2. Upon further increasing the temperature, the conversion to CO_2 increased until about 570 K, at which temperature the methanation reaction started. This was at about 50 K higher temperature than for Pt/Ce(La)O_x. The reactor was heated until 671 K, at which conversion of CO was still incomplete.

The first cooling trajectory (Figure 9.6b) of L-Pt/Ce(La)O_x was remarkably different from the heating one, but resembled both the cooling trajectories and the second heating trajectory of Pt/Ce(La)O_x (Figure 4). Unlike the heating trajectory, no discontinuity in the CO_2 signal was observed around 520 K and the CO, H_2, and O_2 were

169

converted at a much lower temperature. Full conversion of oxygen occurred until about 335 K with relatively high selectivity to CO_2. This was approximately same temperature at which O_2 reappeared in the first cooling trajectory in case of $Pt/Ce(La)O_x$ (Figure 4b). The second heating and cooling trajectories strongly resembled the first cooling trajectory, with the exception of a surplus in H_2O in the second heating trajectory at about 350 K. Although the general trend of PROX reaction was the same for both leached and non-leached samples, there were small differences between the first and second cooling and second heating trajectories of the leached and non-leached samples: the leached sample was less active for methanation and showed lower selectivity to CO_2 in the PROX reaction. At the onset of methanation, the conversion to CO_2 was lower for the leached sample.

The differences and similarities between the various heating and cooling trajectories of $L\text{-}Pt/Ce(La)O_x$ were reflected in the HERFD XAS spectra (Figure 9.7). The spectrum of the as-synthesized catalyst showed a very strong whiteline, which is indicative of platinum almost completely in an oxidic state (Figure 9.7a). Very little fine structure was observed at energy higher than the whiteline, which suggested a lack of long-range order. This agrees to previous reports that have shown that after leaching the metal particles and by exposing ceria-supported platinum to an oxidative atmosphere metal-doped ceria (either in bulk or on surface) was obtained.[6c,d,e,f,g,11] In contrast to non-leached sample $Pt/Ce(La)O_x$, the spectrum measured at 303 K, during first heating trajectory, showed a very similar spectrum compared to as-synthesized catalyst, $L\text{-}Pt/Ce(La)O_x$. Increasing the temperature caused a gradual decrease in white line intensity, which indicated reduction of part of the platinum atoms. Above 520 K, the temperature at which a sudden change in conversion and selectivity occurred (Figure 9.6a), the whiteline intensity was reduced strongly without any appearance of doublet in the whiteline. This suggested the reduction of the platinum oxide and the appearance of reduced platinum with minimal amount of CO on the surface. The intensity of the scattering features at 11581.1 and 11594.2 eV was very low, which indicated that the reduced metal clusters were smaller than 1 nm. The cooling trajectory showed that the changes were partially reversible. Spectra that were measured below 323 K, at which the conversion in oxygen was incomplete, showed enhanced white line intensity, which indicated the formation of a fraction of cationic platinum. This did not happen for $Pt/Ce(La)O_x$ and Pt/Al_2O_3. The second heating and cooling trajectories (Figures 9.6c and d) showed spectra that resembled those of the first cooling trajectory at similar

temperature. Again, the largest change in structure that had occurred during the first heating trajectory was irreversible. However, unlike Pt/Al_2O_3 and $Pt/Ce(La)O_x$, changes in oxidation state occurred during the subsequent cooling and heating trajectories.
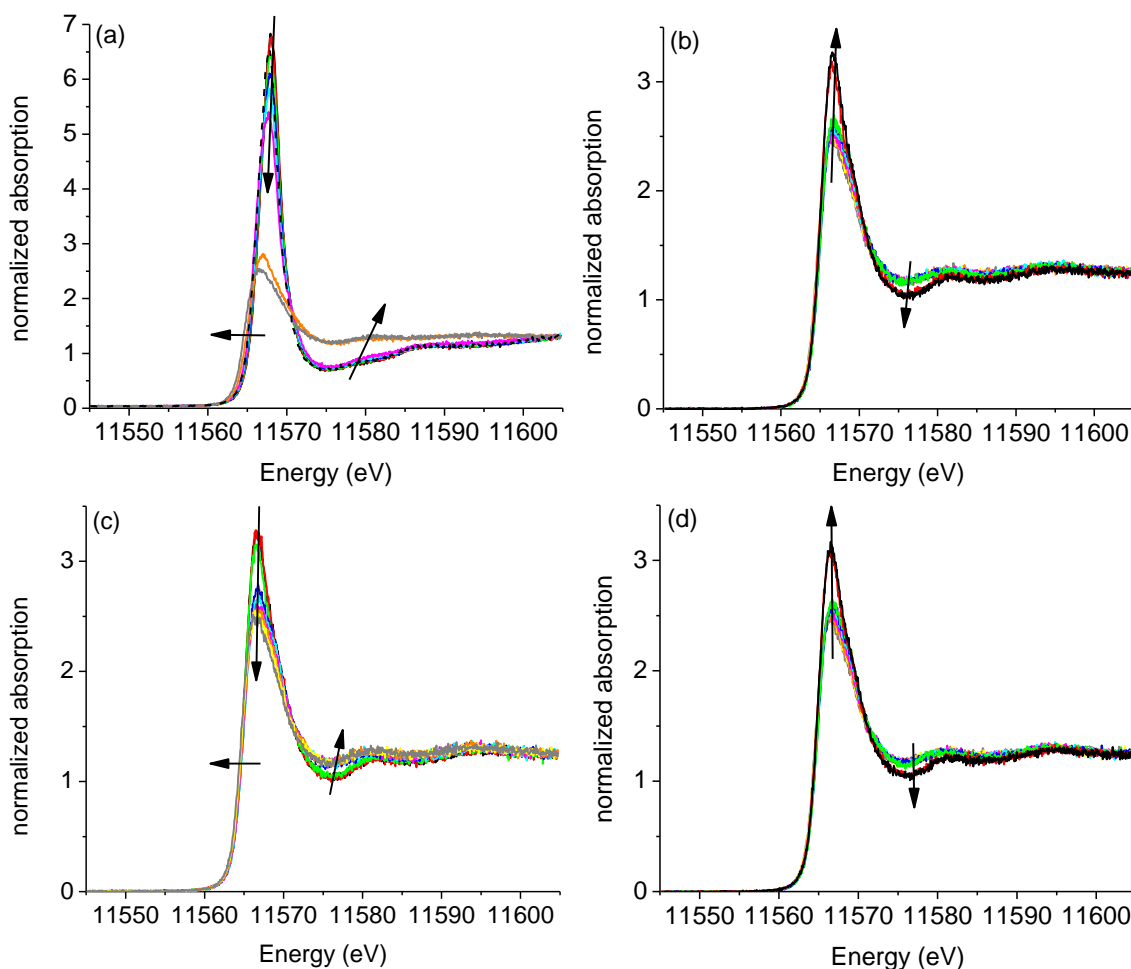

Figure 9.7: Pt L_3 edge HERFD XANES of L-Pt/Ce(La)O_x during PROX (a) measured during first heating trajectory at 303 K (black), 323 K (red), 373 K (green), 423 K (blue), 473 K (cyan), 523 K (pink), 573 K (orange), and 671 K (grey); the spectrum in He before the start of reaction is also shown (black dash), (b) during first cooling trajectory at 303 K (black), 323 K (red), 373 K (green), 423 K (blue), 473 K (cyan), 523 K (pink), 573 K (orange), 616 K (yellow), and 671 K (grey), (c) during second heating trajectory at 303 K (black), 323 K (red), 373 K (green), 423 K (blue), 473 K (cyan), 523 K (pink), 573 K (orange), 626 K (yellow), and 671 K (grey), and (d) during second cooling at 303 K (black), 326 K (red), 371 K (green), 423 K (blue), 467 K (cyan), 522 K (pink), 572 K (orange), 613 K (yellow), and 669 K (grey).

9.4 Discussion

9.4.1 Formation and stability of platinum-doped oxide

It has been established that under an oxidizing atmosphere the surface of ceria stabilizes cationic platinum[6c,20] and that a doped oxide may form. Ceria-supported metal particles of one to two nm re-disperse upon exposure to oxygen and enhanced temperature.[20c,d,e,21] The metal thus reversibly changes its structure between reduced metal particle and platinum-doped ceria depending on the oxidizing and reducing nature of the atmosphere. Doped oxides have been proposed to be catalytically active in oxidation, WGS, and hydrogenation reactions.[6d,e,f,g] The presence of gas phase oxygen is required to stabilize these doped oxides and a reductive atmosphere that is free of oxygen favors the formation and stabilization of a supported metal catalyst.[8,21,22] Likewise, it has been shown that the addition of oxygen to the reactants of WGS stabilizes the cationic structure of the metal to maintain its unique catalytic performance.[23] Our results also indicate that the oxidizing and reducing nature of the atmosphere strongly influence the structure of the platinum, which affect the catalytic performance. Our data also confirmed that leaching by cyanide completely removes the metal particles from the catalyst, resulting in an almost complete cationic state of the metal. Most likely, a doped ceria was obtained. In L-Pt/Ce(La)O$_x$, as more oxygen got converted when increasing the temperature (Figure 9.6a), gradual reduction of cationic platinum occurred until platinum was suddenly completely reduced (Figure 9.7a). This occured at the point where oxygen was completely absent at the exhaust of the reactor. A small amount of oxygen in the gas phase is able to stabilize the cationic platinum, even in an overdose of the strong reducing environment of H$_2$ and CO. After reduction, the spectra were reminiscent of very small fully reduced platinum particles. Reduction of the platinum in the doped oxide most likely starts at the bottom of the reactor where the oxygen is depleted first. A front of reduced metal then propagates towards the inlet of the reactor, because of the higher activity of the metal compared to the doped catalyst. This structural change is mostly irreversible during our subsequent cooling and heating trajectories (Figures 9.7b, c and d). Upon cooling and increase of the oxygen concentration, only a small fraction of platinum reoxidizes (Figure 9.7b). As the particles are covered by CO, they are not easily reacted to oxygen and are thus prevented from re-dispersion, which occurs for reduced particles supported on ceria in the presence of oxygen and in the absence of hydrogen and CO.[20e,21,22]

The non-leached sample $Pt/Ce(La)O_x$ also initially showed a very large fraction of cationic platinum. Like in the leached catalyst, the cationic platinum completely reduced in the absence of gas phase oxygen. In this case, however, reoxidation was never observed, probably because of the larger size of the particles compared to the doped platinum. Furthermore, alumina-supported platinum, which had particles in the range of 1-2 nm did not show any reoxidation under reaction conditions. The extend of reoxidation thus depends on the presence of oxidizing and reducing molecules in the gas phase and on particle size and support. Our data unambiguously show that the oxidation state and structure of platinum changes with reaction conditions and that the structural changes are irreversible, to large extend, when they remain exposed to reactants and products.

9.4.2 Catalytic activity of doped oxide versus supported metal: PROX

Our data provide insight into the catalytic performance of platinum-doped ceria and that of ceria-supported platinum and their relation to catalyst structure. A very selective catalyst for PROX, with highest selectivity to CO_2 as high as 68%, was obtained after depositing platinum on lanthanum-doped ceria. This catalyst consisted of platinum-doped ceria and ceria-supported platinum particles. A likely reaction mechanism is that the metal particles are covered with CO, which spillover to the support to react with the weakly bonded oxygen in the Pt-O-Ce bond that exists in platinum-doped ceria.[8,20e] In the absence of reduced metal or when present in a small concentration, like in case of the leached catalyst $L-Pt/Ce(La)O_x$, the catalyst showed a much higher selectivity to hydrogen, while the activity expressed by the conversion of oxygen was roughly the same. The reaction channel via CO adsorption on the metal and spillover to the support is absent, decreasing the selectivity to CO_2 formation (Table 1).

After full reduction of the metal, which occurs in the absence of oxygen in the gas phase, the high selectivity to CO_2 was irreversibly lost for the non-leached sample $Pt/Ce(La)O_x$. One may speculate that the reactive oxygen in Pt-O-Ce is absent, under reducing conditions. It has been shown that reduction of ceria occurs in parallel with the metal.[19c,24b]

One way of interpreting our results is that the presence of cationic platinum is reminiscent of the presence of oxidized ceria, likewise the presence of fully reduced platinum of partially reduced ceria (in the absence of oxygen).[19c,24b] After the complete

conversion of O_2, and thus when platinum is completely reduced, hydrogen atoms that may form by dissociation of gas phase H_2 on this reduced platinum, could spillover to the ceria, thereby partially reducing it and forming hydroxyl groups.[19c,24] These hydroxyl groups on the surface of reduced ceria play an important role in the formation of formates and carbonates, which accumulated on the surface.[25] They have been suggested to be reactive intermediates, spectator species, and catalyst poison in the WGS reaction.[19c,24a,25,26,27]

9.4.3 Catalytic activity: WGS

Reaction regimes, during which the WGS reaction is operative over the platinum-ceria system, have been determined. The catalyst $Pt/Ce(La)O_x$ showed conversion above 450 K (Figure 4b), and the leached one at about 25 K higher temperature (Figure 6b). In any case, the presence of cationic platinum or platinum doped-oxide could not be established. Reduced platinum particles or clusters, which were covered with a variable amount of CO, depending on temperature and CO concentration, were detected (Figures 5b and 7b). Neglecting a particle size effect for the moment, the lower activity of L-$Pt/Ce(La)O_x$ compared to $Pt/Ce(La)O_x$ is most likely explained by the lower metal loading after leaching. Alumina-supported platinum also showed activity in the WGS reaction between 425 and 500 K (Figure 2a), which also contained CO-covered platinum particles (Figure 3a). Because no evidence of the presence of cationic platinum was found, it is concluded that supported metal particles are able to catalyze WGS reaction under the reaction conditions of this study. Previous in situ studies on ceria-supported catalysts[11,28] have also identified reduction of cationic metal under reaction conditions.

9.4.4 Catalytic activity: Methanation

Methanation of CO requires breaking the carbon oxygen bond. This occurs at relatively high temperature. Pt/Al_2O_3 showed methanation above 550 K (Figure 2), $Pt/Ce(La)O_x$ above 525 K (Figure 4), and L-$Pt/Ce(La)O_x$ above 580 K (Figure 6). The low loading after leaching is probably responsible for its relatively low activity. Reaction at the support-interface on the ceria support could be the cause of the higher activity on the ceria support compared to alumina, however, no experimental evidence is present in this work to support this. In all cases, the reaction occurred over reduced platinum particles that were covered by CO for as long CO was present (Figures 3, 5, and 7). There was no evidence of the formation of a carbidic phase.

9.5 Conclusions

The highest selectivity to CO_2 in PROX was achieved on a catalyst that contained ceria-supported platinum nanoparticles and platinum-doped ceria. The ceria is most likely fully oxidized under these conditions. Platinum-doped ceria is much less reactive in the oxidation of H_2 and CO compared to ceria-supported platinum particles. PROX, WGS, and methanation can all occur over fully reduced platinum nanoparticles and clusters that are supported on alumina and ceria. The kind of support, the particle size and its loading, and the gas composition strongly affect the structure of the catalyst. In the presence of oxygen, cationic platinum is stabilized by ceria even when hydrogen and CO are present. In the presence of CO and hydrogen, supported metal particles are protected from oxidation. Redispersion of reduced particles only occurs over very small ceria-supported platinum clusters and to a small extend.

References

1 R. F. Mann, J.C. Amphlett, B. A. Peppley, Frontiers Sci. Ser. 7 (1993) 613.

2 (a) A. J. Appleby, F.R. Foulkes, in Fuel Cell Handbook, Van Nostrand Reinhold, New York, (1989); (b) C. D. Dudfield, R. Chen, P.L. Adock, Int. J. Hydrogen Energy 26 (2001) 763).

3 (a) J. N. Armor, Appl. Catal. 176 (1999) 159; (b) J. M. Zalc, D. G. Löffler, J. Power Sources 111 (2002) 58.

4 (a) R. A. Demmin, R. J. Gorte, J. Catal. 105 (1987) 373; (b) R. A. Lemons, J. Power Sources 29 (1990) 251.

5 (a) A. Trovarelli, Catal. Rev. Sci. Eng. 38 (1996) 439; (b) H. C. Yao, Y.F.Y. Yao, J. Catal. 86 (1984) 254; (c) P. Fornasiero, G. Balducci, R. Di Monte, J. Kaspar, J. Sergo, G. Gubitosa, A. Ferrero, M. Graziani, J. Catal. 164 (1996) 173.

6 (a) M. J. Kahlich, H. A. Gasteeiger, R. J. Behm, J. Catal. 171 (1997) 93; (b) Y.-F. Han, M. J. Kahlich, M. Kinne, R. J. Behm, Phys. Chem. Chem. Phys. 4 (2002) 389; (c) Q. Fu, H. Saltsburg, M. Flytzani-Stephanopoulos, Science 301 (2003) 935; (d) P. Bera, K. R. Priolkar, A. Gayen, P.R. Sarode, M. S. Hegde, S. Emura, R. Kumashiro, V. Jayaram, G. N. Subbanna, Chem. Mater. 15 (2003) 2049; (e) P. Bera, S. Malwadkarb, A. Gayena, C. V. V. Satyanarayanab, B. S. Raob, M. S. Hegde, Catal. Lett. 96 (2004) 213; (f) A. Gayen, K. R. Priolkar, R. Sarode, V. Jayaram, M. S. Hegde, G. N. Subbanna, S. Emura, Chem. Mater. 16 (2004) 2317; (g) T. Baidya, A. Gayen, M. S. Hedge, N. Ravishankar, L. Dupont, J. Phys. Chem. B 110 (2006) 5262.

7 (a) S. Carrettin, P. Concepcion, A. Corma, J. M. Lopez Nieto, V. F. Puntes, Angew. Chem. Int. Ed. 43 (2004) 2538; (b) W. Deng, J. D. Jesus, H. Saltsburg, M. Flytzani-Stephanopoulos, Appl. Catal. A 291 (2005) 126; (c) J. Guzman, S. Carrettin, A. Corma, J. Am. Chem. Soc. 127 (2005) 3286; (d) A. M. Venezia, G. Pantaleo, A. Longo, G. Di Carlo, M. P. Casaletto, F.L. Liotta, G. Deganello, J. Phys. Chem. B 109 (2005) 2821; (e) W. L. Deng, M. Flytzani-Stephanopoulos, Angew. Chem. Int. Ed. 45 (2006) 2285.

8 V. Shapovalov, H. Metiu, J. Catal. 245 (2007) 205.

9 X. Zhang, H. Shi, B.-Q. Xu, Angew. Chem. Int. Ed. 44 (2005) 7132.

10 (a) F. Boccuzzi, A. Chiorino, M. Manzoli, P. Lu, T. Akita, S. Ichikawa, M. Haruta, J. Catal. 202 (2001) 256; (b) M. Haruta, Cattech 6 (2002) 102.

11 (a) D. Tibiletti, A. Amieiro-Fonseca, R. Burch, Y. Chen, J.M. Fisher, A. Goguet, C. Hardacre, P. Hu, D. Thompsett, J. Phys. Chem. B 109 (2005) 22553; (b) A. Karpenko,

R. Leppelt, V. Plzak, R.J. Behm, J. Catal. 252 (2007) 231; (c) N. Guo, B.R. Fingland, W. D. Williams, V. F. Kispersky, J. Jelic, W. N. Delgass, F.H. Ribeiro, R. J. Meyer, J. T. Miller, Phys. Chem. Chem. Phys., 2010 DOI: 10.1039/c000240m

12 D. W. Goodman, C. H. F. Peden, G.B. Fisher, S. H. Oh, Catal. Lett. 22 (1993) 271.

13 A. A. Herzing, C. J. Kiely, A.F. Carley, P. Landon, G. J. Hutchings, Science 321 (2008) 1331.

14 (a) J. D. Grunwaldt , S. Hannemann, C. G. Schroer, A. Baiker, J. Phys. Chem. B 110 (2006) 8674; (b) M. A. Newton, C. Belver-Coldeira, A. Martinez-Arias, M. Fernandez-Garcia, Nature Mater. 6 (2007) 528; (c) J. Singh, E. M, Alayon, M. Tromp, O. V. Safonova, P. Glatzel, M. Nachtegaal, R. Frahm and J. A. van Bokhoven, Angew. Chem. Int. Ed. 47 (2008) 9260.

15 J. Singh, M. Nachtegaal, E.M.C. Alayon, J. Stötzel, J. A. van Bokhoven, ChemCatChem 2 (2010) 653.

16 (a) P. Glatzel, U. Bergmann, Coord. Chem. Rev. 249 (2005) 65; (b) F. M. F. de Groot, Coord. Chem. Rev. 249 (2005) 31; (c) J. A. van Bokhoven, C. Louis. J. T. Miller, M. Tromp, O. V. Safonova, P. Glatzel, Angew. Chem. Int. Ed. 45 (2006) 4651.

17 O. V Safonova, M. Tromp, J. A. van Bokhoven, F. M. F. de Groot, J. Evans, P. Glatzel, J. Phys. Chem B. 110 (2006) 16162.

18 D. C. Koningsberger, R. Prins, in X-ray Absorption: Principles, applications, techniques of EXAFS, SEXAFS and XANES, John Wiley and Sons, New York, (1988).

19 (a) A. Holmgren, B. Andersson, D. Duprez, Appl. Catal. B 22 (1999) 215; (b) A. Wootsch, C. Descorme, D. Duprez, J. Catal. 225 (2004) 259; (c) O. Pozdnyakova, D. Teschner, A. Wootsch, J. Kröhnert, B. Steinhauer, H. Sauer, L. Toth, F.C. Jentoft, A. Knop-Gericke, Z. Paál, R. Schlögl, J. Catal. 237 (2006) 1.

20 (a) A. F. Diwell, R. R. Rajaram, H. A. Shaw, T. J. Truex, Stud. Surf. Sci. Catal. 71 (1991) 139; (b) L. L. Murrell, S. J. Tauster, D. R. Anderson, Stud. Surf. Sci. Catal. 71 (1991) 275; (c) Y. Nagai, N. Takagi, Y. Ikeda, K. Dohmae, T. Tanabe, G. Guilera, S. Pascarelli, M. Newton, H. Shinjoh, S. Matsumoto, Stud. Surf. Sci. Catal. 172 (2007) 623; (d) Y. Nagai, K. Dohmae, Y. Ikeda, N. I. Takagi, T. Tanabe, N. Hara, G. Guilera, S. Pascarelli, M. A. Newton, O. Kuno, H. Jiang, H. Shinjoh, S. Matsumoto, Angew. Chem. Int. Ed. 47 (2008) 9303; (e) M. Hatanaka, N. Takahashi, N. Takahashi, T. Tanabe, Y. Nagai, A. Suda, H. Shinjoh, J. Catal. 266 (2009) 182.

21 Y. Nagai, T. Hirabayashi, K. Dohmae, N. Takagi, T. Minami, H. Shinjoh, S. Matsumoto, J. Catal. 242 (2006) 103.

22 Y. Nagai, K. Dohmae, K. Teramura, T. Tanaka, G. Guilera, K. Kato, M. Nomura, H. Shinjoh, S. Matsumoto, Catal. Today 145 (2009) 279.

23 (a) Q. Fu, W. Deng, H. Saltsburg, M. Flytzani-Stephanopoulos, Appl. Catal. B 56 (2005) 57; (b) W. L. Deng, M. Flytzani-Stephanopoulos, Angew. Chem. Int. Ed. 45 (2006) 2285.

24 (a) T. Schido , Y. Iwasawa, J. Catal. 141 (1993) 71; (b) G. Jacobs, U. M. Graham, E. Chenu, P. M. Patterson, A. Dozier, B.H. Davis, J. Catal. 229 (2005) 499.

25 R. Burch, Phys. Chem. Chem. Phys. 8 (2006) 5483.

26 M. M. Schubert, A. Venugopal, M. J. Kahlich, V. Plzak, R. J. Behm, J. Catal. 222 (2004) 32.

27 R. Leppelt, B. Schumacher, V. Plzak, M. Kinne, R. J. Behm, J. Catal. 244 (2006) 137.

28 (a) P. Bera, K. R. Priolkar, P. R. Sarode, M. S. Hegde, S. Emura, R. Kumashiro, N.P. Lalla, Chem. Mater. 14 (2002) 3591; (b) X. Wang, J. A. Rodríguez, J. C. Hanson, D. Gamarra, A. Martínez-Arias, M. Fernández-García, J. Phys. Chem. B 109 (2005) 19595; (c) X. Wang, J.A. Rodriguez, J.C. Hanson, M. Perez, J. Evans, J. Chem. Phys. 123 (2005) 221101.

Chapter 10

Overall conclusion and outlook

The aim of this research was to establish the structure-performance relationship during CO oxidation over supported platinum catalysts using newly developed techniques of X-ray absorption and emission spectroscopy at third generation synchrotrons. The electronic and geometric properties of various platinum catalysts were determined under the influence of different gas environment and temperature that were relevant to CO oxidation. HERFD XAS allowed the structural determination of the catalyst with better energy resolution than can be obtained by conventional XAS and thus aided in better understanding the dynamic changes occurring at the catalyst surface. RIXS, with its in situ ability, gave insight into the altered electronic structure of catalysts, which contained platinum respectively platinum-tin nano-particles, upon adsorption of various reactants. HERFD XAS along with RIXS gave an overall picture of the bonding and anti-bonding orbitals that were formed after the adsorption of reactants on the catalyst surface. The combination of XAS with IR spectroscopy revealed the adsorbing species on the catalyst surface and the structure of the catalyst itself.

To explore the application of the relatively novel technique of RIXS for platinum, which belongs to the 5d transition metals reference compounds were first investigated. Thus, the electronic structure of various platinum and gold compounds was determined. The full multiple scattering calculations done using FEFF8 showed a good agreement between the experimental and theoretical spectra. Although the spectral resolution of RIXS achieved in this research was lower compared to XPS and UPS, the exclusive use of hard X-rays, which have a very large penetration depth, proved RIXS as the better technique to probe the structure of the catalysts under real catalytic conditions. Taking this approach, the structure of bulk gold was compared to that of gold nano-particles. As fewer atoms contributed to the d band in the nano-sized gold, the width of the d band decreased and it shifted to lower binding energy compared to that of bulk gold.

The alloying of two metals, such as platinum and tin, is common practice in heterogeneous catalysis to improve the activity, selectivity, and stability of the catalyst. The platinum-tin alloy catalyst is one of the most studied catalysts due to its superiority over a monometallic platinum catalyst in many reactions. RIXS and HERFD XAS were utilized to determine and compare the differences in electronic structure of alumina-supported platinum particles and alumina-supported platinum-tin particles. The d band of platinum narrowered and showed a downward shift relative to the Fermi level after alloying with tin. These changes in the d band of platinum rendered the bimetallic

system to behave different from that of monometallic system towards the adsorption of reactants. Because according to the d band theory, developed by Nørskov and co-workers, the reactivity of the metal surface depends on the energy position of the d band relative to the Fermi level. Metals that have their d band centre closer to the Fermi level are more active towards the adsorption of reactants and intermediates than those with a d band centre farther from the Fermi level. The adsorption of hydrogen induced significant changes in the electronic and geometric structure of platinum in monometallic system compared to the bimetallic one, with monometallic platinum showing a much more pronounced anti-bonding state and shift in the Fermi level than bimetallic platinum-tin. However, the adsorption of CO resulted in a similar electronic and geometric structure of platinum for both catalysts. Therefore, the strong adsorption of CO could have resulted in significant changes in the geometric structure of the bimetallic platinum-tin system.

Knowledge of the structure of the catalytically active sites in supported metal catalysts is essential to understand the functioning of these catalysts and chemical processes and thus, establish structure-performance relationships. The combination of HERFD XAS, QEXAFS, and IR spectroscopy with kinetic measurements made it possible to determine the structure of supported platinum catalysts under real conditions during CO oxidation. Performing the in situ experiments helped bridging the pressure and material gaps and translating results from single crystal studies to understand catalytic process of CO oxidation under real catalytic conditions. Two reaction regimes were identified for CO oxidation: a regime with low-activity and one with high-activity. These two regimes were only observed at ratios of O_2 to CO greater than stoichiometric. When heating, at a particular temperature there was a sudden increase in activity and the catalyst reached the high-activity regime. This so-called "ignition" occurred at lower temperature with increasing oxygen concentration. Below ignition, HERFD spectra collected at Pt L_3-edge showed a whiteline of low intensity with a double feature, which is characteristic of the platinum particles with adsorbed CO on an atop site. At a higher temperature than the ignition temperature, the spectra showed a strong increase in the intensity of the whiteline while the edge energy shifted to lower energy, which is characteristic of partially oxidized platinum. The catalyst above ignition consisted of mixed oxide-metal phases, the oxide most likely at the surface. The higher the temperature of ignition, the larger was the fraction of oxidic platinum. Therefore, below the ignition temperature, CO was bound atop to the surface, and the reaction rate was

low due to poisoning of the active surface by CO and above ignition, the high activity state was characterized by the presence of a surface oxide. The structure of the oxide was highly defective and platinum was under-coordinated to oxygen. Determining the structure of the catalyst during the ignition process was important to bridge the gap between structure of catalyst in the low- and the high-activity regime. This ignition, which occurs generally within a few seconds, was rather a challenging process to characterize as it required a fast response technique with capabilities of revealing the catalyst structure under in situ conditions. During the ignition, the whiteline intensity of the Pt L_3 spectra recorded with a time resolution of 0.5 sec using QEXAFS technique increased with the increasing conversion of CO. This confirmed the increasing amount of oxidized platinum. These results were confirmed using IR spectroscopy, which revealed the surface species on the active sites during CO oxidation. In the low-activity regime, linearly- and, to smaller extend, bridged-bonded CO was observed that poisoned the active surface and did not allow the catalyst to exhibit high activity. With increasing temperature, CO desorbed, which allowed oxygen to interact with the sites previously occupied by CO and increased the reaction rate. The surface of the catalyst became abruptly free from adsorbed CO during and after ignition. The depletion of CO from the surface during ignition enabled oxygen to react, which increased conversion and caused the surface to oxidize. The IR experiments were conducted separately from the XAS experiments using self-supporting pellets of catalysts. Although, these data were in full agreement, a simultaneous measurement on the identical catalysts would be preferred and definitely be more elegant.

CO oxidation occurred in a similar way over supported platinum catalysts of different particle sizes. Regardless of the particle size, the CO oxidation occurred in two distinctive regimes, a high-activity regime and a low-activity regime, which had high and low rates of reaction respectively. The size of the particles slightly affected the rate in the low-activity regime, which was related to higher fraction of the lower coordination sites (corners and edges) of platinum atoms in smaller particles compared to bigger particles. This size effect was more difficult to assess in the high-activity regime. The platinum nano-particles supported on alumina, silica and titania, all showed similar behavior during CO oxidation. The thickness of the disordered oxide layer that was formed in the high-activity regime strongly depended on particle size, the support, and the temperature of formation.

The combination of QEXAFS, IR spectroscopy and kinetic measurements elucidated the structural changes that occur during the kinetic oscillations of CO oxidation over supported platinum catalyst. The kinetic oscillations were observed under conditions that showed near full conversion of carbon monoxide. The catalyst structure and the reactivity were strongly related and both changed with position in the reactor bed. During the oscillations, a decrease in carbon dioxide production was paralleled by partial reduction of the surface and subsequent surface poisoning. The surface was re-activated with a sudden spike in carbon dioxide production, which coincided with re-oxidation of the surface. Therefore, the kinetic oscillations during oxidation of carbon monoxide were paralleled with the reduction and re-oxidation of the surface.

Preferential oxidation of CO (PROX) is one of the important reactions that is practiced in fuel cell industry to meet the requirement of a near CO-free hydrogen feed stock. We used ceria-supported platinum catalyst, because of the oxygen-storage capacity of ceria. Two different catalysts were synthesized, one with supported platinum particles on ceria and the other where platinum was leached and a platinum-doped ceria was supposed to be formed. The structure and catalytic performance of both catalysts strongly differed during the PROX as probed by HERFD XAS. The non-leached catalyst was very selective to CO oxidation and it consisted of platinum-doped ceria and ceria-supported platinum particles. Platinum nano-particles adsorbed CO, which then reacted with the weakly bonded oxygen from platinum-doped ceria. The absence of the reaction channel via CO adsorption on platinum in the leached sample made it less selective towards PROX. During the heating and cooling cycles, the regimes of WGS and methanation were also observed and characterized by means of HERFD XAS. HERFD showed the presence of cationic platinum (only) in the presence of oxygen, which was stabilized by ceria even when hydrogen and CO were present. In the presence of CO and hydrogen, supported metal particles existed that were protected from re-oxidation, because of the adsorbed layer. Taking this work further, the electronic structure of ceria needs to be determined to complete the knowledge of the catalyst structure during PROX on these systems. IR spectroscopy will yield the adsorbing species during the reaction and would help in establishing structure-performance relationship.

The use of hard X-rays employed in newly developed techniques of XES enabled in situ measurements to establish structure-performance relationships of real catalysts and to translate the results from surface-science experiments, which are often done with single crystals under vacuum conditions and by means of soft X-rays or electrons.

HERFD XAS and RIXS are powerful tools for studying the electronic structure in an element–specific manner. The high-energy resolution achieved by selective detection of a fluorescence channel aided significantly in understanding the behaviour of supported platinum catalysts under catalytic conditions of high temperature and various gas environments during total and preferential CO oxidation. Such measurements play a vital role in following a reaction over a catalyst surface as the structure of the surface sites can be probed efficiently with better resolution compared to conventional XAS. In situ RIXS studies determined the valence band of platinum catalysts particles under various gas environments. The knowledge gained from the RIXS planes provided complimentary information to XAS and thus assisted in gaining the overall picture about the states involved in the bonding process.

The use of XES for performing site selective EXAFS is beneficial in probing the structure of specific catalyst elements present in certain sites. The combination of XES and XAS to provide complimentary information, the involvement of theory to comprehend the experimental data, and the combination of other techniques such IR and Raman spectroscopy will continue to attract the interest of researchers active in various scientific fields. The continued development of setups that combine complimentary methods and fast X-ray sources will open up a new era for the study of catalytic reactions.

Publications

Papers

1. "Generating Highly Active Partially Oxidized Platinum during Oxidation of Carbon Monoxide over Pt/Al2O3; In situ, Time-Resolved, and High Energy-resolution X-ray Absorption Spectroscopy", **Jagdeep Singh**, Evalyn M. C. Alayon, Moniek Tromp, Olga V. Safonova, Pieter Glatzel, Maarten Nachtegaal, Ronald Frahm, and Jeroen A. van Bokhoven, *Angew. Chem. Int. Ed.*, **2008**, 47, 9260-9264.

2. "Exploring the dynamic platinum structure during CO oxidation", **Jagdeep Singh**, Evalyn M.C. Alayon, Moniek Tromp, Olga V. Safonova, Pieter Glatzel, Maarten Nachtegaal, Ronald Frahm, Jeroen A. van Bokhoven, *ESRF Highlights*, **2008**, 15-16.

3. "In situ XAS with high-energy resolution: the changing structure of platinum during oxidation of carbon monoxide", **Jagdeep Singh**, Moniek Tromp, Olga V. Safonova, Pieter Glatzel, Jeroen A. van Bokhoven, *Catal. Today*, **2009**, 145, 300-306.

4. "Time resolved X-ray absorption spectroscopy applied during ignition of oxidation of carbon monoxide", **Jagdeep Singh**, Evalyn M.C. Alayon, Maarten Nachtegaal, Jeroen A. van Bokhoven, *J. Phys.: Conf. Ser.*, **2009**, 012159.

5. "Structure of alumina supported platinum catalysts of different particle size during CO oxidation using in situ IR and HERFD XAS", **Jagdeep Singh**, Jeroen A. van Bokhoven, *Catal. Today*, **2010**, 155, 199-205.

6. "Electronic structure of alumina-supported monometallic Pt and bimetallic PtSn catalysts under hydrogen and carbon monoxide environment", **Jagdeep Singh**, Ryan C. Nelson, Brian C. Vicente, Susannah L. Scott, Jeroen A. van Bokhoven, *Phys. Chem. Chem. Phys.*, **2010**, 12, 5668-5677.

7. "Dynamic structure changes of a heterogeneous catalyst within a reactor: oscillations in CO oxidation over a supported platinum catalyst" **Jagdeep Singh**, Maarten Nachtegaal, Evalyn M.C. Alayon, Jan Stötzel, Jeroen A. van Bokhoven, *ChemCatChem*, **2010**, 2, 653-657.

8. "Advanced X-ray absorption and emission spectroscopy: in situ catalytic studies" **Jagdeep Singh**, Carlo Lamberti, Jeroen A. van Bokhoven, *Chem. Soc. Rev.*, **2010**, 39, 4754-4766.

9. "On highly active partially oxidized platinum in carbon monoxide oxidation over supported platinum catalysts", Evalyn M. Alayon, **Jagdeep Singh**, Maarten Nachtegaal, Messaoud Harfouche, Jeroen A. van Bokhoven, *J. Catal.,* **2009**, 263, 228-238.

10. "In situ XAS probes partially oxidized platinum generating high activity for CO oxidation", Evalyn M.C. Alayon, **Jagdeep Singh**, Maarten Nachtegaal, Messaoud Harfouche, Jeroen A. van Bokhoven, *J. Phys.: Conf. Ser.*, **2009**, 12152.

11. "In Situ Characterization of the 5d Density of States of Pt Nanoparticles upon Adsorption of CO", Pieter Glatzel, **Jagdeep Singh**, Kristina O. Kvashnina, Jeroen A. van Bokhoven, *J. Am. Chem. Soc.*, **2010**, 132 (8), 2555-2557.

12. "Electronic structures of supported Pt and PtSn nanoparticles in the presence of adsorbates and during CO oxidation", Brian C. Vicente, Ryan C. Nelson, **Jagdeep Singh**, Susannah L. Scott, Jeroen A. van Bokhoven, *Catal. Today,* **2010**, *in press, available online.*

13. "PROX, water-gas shift, and methanation over platinum-doped ceria and ceria-supported platinum, dynamic structure of the catalyst" Jeroen A. van Bokhoven, **Jagdeep Singh**, *to be submitted.*

Publications

Presentations

Oral

1. "Generating highly active sites during oxidation of carbon monoxide", SCS Fall Meeting, **2008**, 11th September, Zurich, Switzerland.
2. "Generating highly active sites during oxidation of carbon monoxide", XAS Workshop, **2008**, 8th October, PSI Villigen, Switzerland.
3. "Dynamic structure of supported platinum catalysts during oxidation of carbon monoxide", Operando III, International Congress on Operando Spectroscopy, **2009**, 20th April, Rostock-Warnemünde, Germany.
4. "In situ space and time resolved x-ray absorption spectroscopy: dynamic structure of platinum during kinetic oscillations of CO oxidation", XAFS 14, 14th International Conference on X-ray Absorption Fine Structure, **2009**, 26-31 July, Camerino, Italy.

Poster

1. "Generating highly active sites during oxidation of carbon monoxide", SCS Fall Meeting, **2008**, 11th September, Zurich, Switzerland.
2. "Dynamic Structure of supported platinum catalysts during oxidation of carbon monoxide", SCS Fall Meeting, **2009**, September 4, Lausanne, Switzerland.
3. "Dynamic Structure of supported platinum catalysts during oxidation of carbon monoxide: kinetic oscillations and structural changes in a single reactor", EuropaCat IX Congress, **2009**, August 31-September 4, Salamanca, Spain.
4. "In situ studies using hard X-rays", GRC Conference, Catalysis, **2010**, June 27-July 2, New London, USA.

Publications

Curriculum Vitae

Name	Jagdeep Singh
Date of Birth	03.10.1983
Nationality	Indian

2000 – 2004	Bachelor of Engineering in Chemical Engineering
	Thapar Institute of Engineering and Technology, Patiala, India
	Bachelor's Thesis: "Study of isomerization behavior of n-hexane over solid acid catalysts"
2004 – 2006	Master of Technology in Chemical Engineering
	Indian Institute of Technology, Roorkee, India
	Master's Thesis: "Hydroisomerization of n-Paraffins over metal loaded mesoporous molecular sieves"
	Supervisors: Prof. I.M. Mishra and Prof. W. Reschetilowski
2006 – 2010	Doctoral studies at Institute for Chemical and Bioengineering, ETH Zurich, Switzerland
	Supervisor: Prof. Dr. Jeroen A. van Bokhoven

Curriculum Vitae

Acknowledgements

Acknowledgements

Evalyn, for her enormous efforts and dedication in her Master thesis project, which contributed a lot to my thesis.

Nadiya, for her all-time help during my PhD and for being my German-English translator.

Gianluca, Sahil and Javier for helping me with data analysis.

Rahul and Lia for being nice friends and easy-going flatmates.

Gabriele, Jose, Eduardo, Nico, Ivan, Manoj, Rochit, Shilpi, Asif, Ela, Anna, Mimo, Alex, Cico, Ma, Srikant, Miriam, Anja, Laura for their friendship and wonderful time that I spent with them in Switzerland. All my other friends, with whom I had a great time.

Sinha, for his precious friendship and advices at different stages of my life.

All people from my dance groups in Switzerland. I had great fun with you people.

Aman didi and Amrit Bhaji for their great support during my stay in Switzerland.

All my colleagues in Jeroen's group.

It is very hard to express my feelings in proper words for my parents who have always encouraged me in all my endeavours. I am grateful to all my relatives, specially my sweet sister, Neetu, and my cousin Babloo. Above all, I want to express my humble and wholehearted prostration before GOD for sprinkling his unprecendented favor upon me.

Acknowledgements